5-2010

Examination of Deformation in Crystalline Rock From Strike-Slip Faults in Two Locations, Southern California

David H. Forand
Utah State University

EXAMINATION OF DEFORMATION IN CRYSTALLINE ROCK FROM STRIKE-SLIP FAULTS IN TWO LOCATIONS, SOUTHERN CALIFORNIA

by

David H. Forand

A thesis submitted in partial fulfillment
of the requirements for the degree

of

MASTER OF SCIENCE

in

Geology

Approved:

_____	_____
Dr. James P. Evans Major Professor	Dr. Susanne U. Janecke Committee Member
_____	_____
Dr. Mary S. Hubbard Committee Member	Dr. Byron R. Burnham Dean of Graduate Studies

UTAH STATE UNIVERSITY
Logan, Utah

2010

ABSTRACT

Examination of Deformation in Crystalline Rock From Strike-Slip Faults In Two Locations, Southern California

by

David H. Forand, Master of Science

Utah State University, 2010

Major Professor: Dr. James P. Evans
Department: Geology

Damage zones adjacent to or associated with faults are important to the geologic community because of their implications to hazards and their ability to preserve evidence for, and show history of, slip, fluid flow, and deformation associated with large strike-slip faults. We examine two fault zones in southern California where fault zone damage is expressed. We revisit the drilled crystalline core from the Cajon Pass California drill hole, 4 km northeast of the San Andreas fault (SAF), and 1 km north of the Cleghorn fault, to perform a systematic structural analysis of deformation and alteration associated with strike-slip faulting at the site. The core preserved 19 fault zones, 11 of which were not previously identified. The most significant fault is a fully intact steep-dipping fault zone at 3,402 m depth with potassium feldspar and epidote alteration. This fault correlates well with the nearby left-lateral Cleghorn fault. The extent of deformation varies within the core, and is controlled by the size of the fault zones intersected by the

core. The extent of deformation varies and is controlled by the size of the faults the core intersected.

We also examined the nature of right separation across the Clark fault damage zone along the Santa Rosa segment using a marker assemblage of biotite, hornblende-bearing tonalite - marble - bearing metasedimentary rocks - migmatite located in Coyote Mountain and the southeast Santa Rosa Mountains. Separation measured from this study is 16.8 km + 3.67 km / -6.03 km. Our measurement uses the updated location of the Clark fault in Clark Lake Valley and matches a distinctive lithologic contact across the fault instead of matching the diffuse western boundary of the Eastern Peninsular mylonite zone as previously used. We calculate the errors associated with projecting the contacts across Quaternary cover to the trace of the Clark fault, and consider a range of projections. Additional strain may have been accommodated in folds and small faults within the damage zone of the San Jacinto fault zone. Two large map-scale folds deform the marker assemblage near the San Jacinto fault zone and we tested whether Cretaceous ductile deformation or brittle late Quaternary right slip produced the folds.

(286 pages)

ACKNOWLEDGMENTS

This thesis is a labor of love. There are many people that contributed in one way or another to the completion of this thesis. I would first like to thank Jim Evans. I first met Jim in the summer of 2004 when he gave me the opportunity to work with him as an intern with SCEC. Two years later, when I started applying to graduate school, Jim graciously and enthusiastically granted me another opportunity to work with him as a graduate student. The experience has been wonderful and Jim continually went beyond the role of mentor. Susanne Janecke deserves as much praise as Jim for her role as my "unofficial" advisor. She was my advisor for the work that was conducted in the Anza Borrego Desert State Park (Chapter 3). Her patience, support, and detailed input proved to be invaluable. Rounding out the trifecta of my thesis committee was Mary Hubbard, who provided great feedback both in the review of this document and as research was being conducted.

Eric Mustonen, Ana Hodgson, Aurora Bouchier, and Jonathan Caine all provided me with housing while conducting field work, as well as companionship and the occasional meal! Their support was integral to the completion of this thesis. Jonathan Caine and William Christiansen provided me with the lab and materials to epoxy core at the USGS office in Lakewood Colorado.

Many thanks are deserved by my fellow graduate students with whom I shared an office, including Sarah Springer, Ben Belgarde, Adam Majeski, Dustin Keele, and Kelly Bradbury. Their companionship and friendship only enhanced my experience at Utah State. Thanks to Amanda Schulz for teaching me GIS and answering my questions. Lori Hirschi, Jean Daddow, and Marsha Hunt all provided assistance when navigating through

the graduate school process as well as fantastic administrative support. Thanks to all of the other grad students, faculty, and staff in the USU geology department. You have all made my years at USU memorable.

Many, many thanks are due to my girlfriend Elissa for her uncompromising support, her willingness to listen to me rant about geology, and her patience to proofread early drafts of this document. She has added so much to this thesis in ways that are unquantifiable.

This project was funded by the Society of Petrophysicists and Well Log Analysts, ExxonMobil, and the Perter K. McKillop Scholarship and separate Southern California Earthquake Center grants awarded individually to Susanne Janecke and Jim Evans.

Thanks Everyone!

Dave Forand

“I arise in the morning torn between a desire to improve the world and a desire to enjoy the world. This makes it hard to plan the day.”

E.B. White

“So are you enjoying or improving today?”

-Kelly Bradbury

CONTENTS

Page

LIST OF TABLES

LIST OF FIGURES

CHAPTER 1

INTRODUCTION

Damage zones adjacent to faults are important because of their implications to hazards and their ability to preserve evidence for, and show history of, slip, fluid flow and deformation associated with large strike-slip faults. Damage zones are typically characterized by an increase in subsidiary faulting, fracturing, mineral alteration, and/or veins as compared to the undeformed host rock (Chester and Logan, 1987; Chester et al., 1993). Analysis of these zones can be used to examine how energy is released when an earthquake ruptures and deforms the host rock immediately surrounding a fault. Deformation in damage zones can be examined to understand strain distribution associated with faults. Structures that develop in damage zones can give valuable information about fault propagation and growth, fluid flow, and earthquake initiation and termination (Kim et al., 2004).

Damage zones form adjacent to strike-slip, reverse, and normal faults (Kim et al., 2004). Damage zones are not just outcrop-scale features at different structural levels on the surface of the earth, but can also be documented at micro-, meso-, and macro-scales in the subsurface. Drilled core together with surface mapping are excellent ways to document damage zones. Core retrieved from depth represents deformation and deformation processes at depth, whereas surface mapping of damage zones can constrain their lateral extent as well as identify large structures that may not be observable in micro- and meso-scale studies of core. Integrated studies of damage zone at a variety of scales better constrain how deformation is being accommodated adjacent to faults.

The focus of this thesis is to examine damage zones and their associated structures in two locations in southern California along major strike-slip faults developed in crystalline rock (Figure 1-1). Surface exposures of damage zones at the map scale and drilled core from 3.5 km depth were studied. I examined core from the Cajon Pass Deep Drill Hole (CPDDH) project, a drill hole along the San Andreas and Cleghorn faults in the central Transverse Ranges. I also examined areas surrounding the Clark Fault, part of the San Jacinto fault zone located along the eastern Peninsular Ranges, Southern California were mapped to examine the damage zones and determine separation.

This thesis is divided into two chapters, each focusing on a unique structural problem in southern California. The second chapter, titled "Revisiting the Cajon Pass Core: What Can a Systematic Structural Analysis Reveal About Faulting at Depth Along the San Andreas Fault?," is a systematic structural analysis of core retrieved from the Cajon Pass Borehole. The third chapter in this thesis is titled "Separation Across the Clark Fault, and Structural Characterization of the Clark and Coyote Creek Faults, Clark Valley, Coyote Mountain, Southeast Santa Rosa Mountains, California," and determines separation of the Clark fault in Clark Valley using a unique assemblage of biotite-hornblende bearing tonalite – marble - migmatite and quantifying unaccounted strain in the damage zone.

1-1. Cajon Pass

The Cajon Pass, southern California, lies between the San Gabriel and the San Bernardino Mountains (Figure 1-1). The right-lateral strike-slip San Andreas fault in

Cajon Pass strikes N60ºW, and there are many other subsidiary faults in the area, including the steeply dipping (85º-90º N) left-lateral strike-slip Cleghorn fault.

In 1983 a 1.7 km deep oil and gas exploration well was drilled in the eastern portion of the Cajon Pass by the Arkoma Corporation. Later, in 1986, a second borehole was drilled through the combined efforts of the Deep Observation and Sampling of the Earths Continental Crust, Inc. (DOSECC) and the United States Geological Survey (USGS) 50 m to the north of the Arkoma well. Often referred to as the Cajon Pass Deep Drill Hole (CPDDH), this borehole was drilled approximately 4 km northeast of the San Andreas fault to search for mechanical or thermal features that might be used to infer the shear stress at depth, measure the states of stress during slip events, evaluate the strength of faults, examine processes controlling crustal deformation adjacent to transform margins, and constrain energetics and dynamics of plate motion (Zoback and Lachenbruch, 1992). The CPDDH was drilled to a depth of 3.5 km. Data from the borehole includes in-situ stress measurements, geochemical and geophysical logging, examination of the cuttings, and 53 spot cores for a total length of 128 m over a depth range from 265 to 3,507 m. Though several lithologic studies were conducted on the core by Silver and James (1988), Anderson et al. (1988 a and b), Silver et al. (1988), Vernik and Nur (1992), and Pratson et al. (1992), no systematic structural analysis of the core was performed.

Comprehensive structural analysis provides many insights into faulting processes. In particular, revisiting the Cajon Pass core was of interest because existing descriptions of core did not describe or interpret deformation processes as a function of depth or a function of the proximity to large faults. The distinction between lithologic and structural

analysis is important when understanding deformation processes. Existing lithologic columns are restricted because they were based on the rocks' characteristics in hand sample, viewed under low-power magnification, or based on borehole logging tools. Structural analysis of the core provided insight by systematic investigation of internal structures to determine deformation history. This included identification of minerals and mineral alteration due to fluids, and microstructural, as well as microtectonic analysis.

1-2. Clark Fault

The San Jacinto fault zone, southern California, is approximately 300 km long, and represents the most seismically active fault in the San Andreas fault system in southern California (Thatcher et al., 1975; Sharp, 1967). The San Jacinto fault zone accommodates between 19 and 29 km of right separation of the transform plate boundary between the North American and Pacific plates (Bartholomew, 1970; Sharp, 1967; Dibblee, 1954; Hill, 1984; Sanders, 1989; Revenaugh, 1998; Janecke et al., 2005). The San Jacinto fault zone consists of several dextral strike-slip faults that together accommodate the plate motion in southern California. One of the longer faults in the zone is the Clark fault.

The Clark fault is a 145-150- km long active oblique dextral strike-slip fault with a minor southwest-down component of slip (Belgarde, 2007). This fault contains seven distinct segments from north of Hemet, California to the Extra fault in the southeast (Sharp, 1967; Sanders, 1989; Kirby et al., 2007). The Anza segment of the Clark fault has 23 km of right separation based on displacement of Cretaceous intrusive rocks (Sharp, 1967). The Clark fault trends west-northwest and cuts across metasedimentary and

plutonic rocks of the Peninsular Ranges and late Cenozoic sedimentary rocks of the Salton Trough (Sharp, 1967).

The two segments of the Clark fault that are of interest to this study are the Clark Valley and Santa Rosa segments (Sanders, 1989). The Clark Valley segment is bounded on its northwest end by a 1 km step and 14º bend to the Horse Canyon segment to the northwest (Sanders, 1989). Towards the southeast, along the Santa Rosa segment, the right separation was thought to decreases to approximately14.5 km (Sharp, 1967; Janecke et al., 2005). Combined, the Santa Rosa and Clark Valley segments are approximately 25 km long (Sanders, 1989).

The significance of working in this area is two-fold: 1. Displacement has not been measured in this area since Sharp (1967) and Bartholomew (1970), except in an abstract by Janecke et al. (2005). 2. Recalculating displacement not only has implication for the geologic community but also to the populations living in proximity to these active faults. Work along the Clark and Coyote Creek faults in the Coyote and the Santa Rosa Mountains can be used to determine a more precise lifetime slip rate across the Clark and Coyote Creek faults based on the total accumulated strain of the entire San Jacinto fault zone and prior age estimates. A marble–rich interval located in the Santa Rosa and Coyote Mountains provides exposures that were used to measure right separation and strain in the damage zone of these faults and the total right separation across the Coyote Creek and Clark strands of the San Jacinto fault zone.

Deformation, smaller subsidiary faults, and damage zone width were also explored and noted in each location along with the lithology of rock units, the strike and dip of foliation, and orientation of lineations, if present. Quaternary fault scarps located in

the areas surrounding each focus area were also mapped, as were relative ages of alluvium. The Clark fault in Clark Lake Valley, along the Santa Rosa Mountain northwest to Rockhouse Canyon, was also examined using imagery and spot checks in the field.

References

Anderson, R.N., Broglia, C., Pezard, P.A., and Williams, C.F., 1988a, Lithostrarigraphy determined from discriminate analysis of geochemical well logs from the Cajon Pass scientific drillhole, California: Geophysical Research Letters, v. 15, no. 9, p. 957-960.

Anderson, R. N., Dove, R. Silver, L., James, E., and Chappell, B., 1988b, Elemental and mineralogical analyses using geochemical logs from the Cajon Pass scientific drillhole, California, and their preliminary comparison with core analyses: Geophysical Research Letters, v. 15, p. 969–973.

Bartholomew, M.J., 1970, San Jacinto fault zone in the Imperial Valley, California: Geological Society of Bulletin, v. 81, p. 3161-3166.

Belgarde, B.E., 2007, Structural characterization near the SE end of the Clark fault, Salton Trough California [m.s. thesis]: Logan, Utah State University, 223 p.

Chester, F.M., and Logan, J.M., 1987, Composite planar fabric of gouge from the Punchbowl Fault, California: Journal of Structural Geology, no. 9, p. 621-634.

Chester, F.M., Evans, J.P., and Biegel, R.L., 1993, Internal structure and weakening mechanisms of the San Andreas Fault: Journal of Geophysical Research, v. 98, no. B1, p.771-786.

Dibblee, T.W., 1954, Geology of the Imperial Valley region, California, *in*: Jahns, R.H., (ed.), Geology of southern California, California Division of Mines Bulletin, v. 170, p. 21-28.

Hill, R.I., 1984, Petrology and petrogenesis of batholithic rocks, San Jacinto mountains, southern California, [PhD thesis]: Pasadena, California Institute of Technology.

Janecke, S.U., Kirby, S.M., Langenheim, V.E., Steely, A.N., Dorsey, R.J., Housen, B., and Lutz, A., 2005, High geologic slip rates on the San Jacinto fault zone in the SW Salton Trough, and possible near-surface slip deficit in sedimentary basins: Geological Society of America Abstracts with Programs 37, p. 257.

Kim, Y.S., Peacock, D.C.P., and Sanderson, D.J., 2004, Fault damage zones: Journal of Structural Geology, no. 26, p. 503-517.

Kirby, S. M., Janecke, S. U., Dorsey, R. J., Housen, B. A., Langenheim, V. E., McDougall, K. A., and Steely, A. N., 2007, Pleistocene Brawley and Ocotillo Formations: evidence for initial strike-slip deformation along the San Felipe and San Jacinto fault zones southern California: Journal of Geology 115, 43-62.

Pratson, E. L., Anderson, R. N., Dove, R. E., Lyle, M., Silver, L. T., James, E. W., and Chappell, B. W. 1992, Geochemical logging in the Cajon Pass drill hole and its application to a new, oxide, igneous rock classification scheme: Journal of Geophysical Research, v. 97 no. B4, p. 5167–5180.

Revenaugh, J., 1998, Seismic estimation of cumulative offset on the San Jacinto fault zone: EOS, Transactions, American Geophysical Union, v.79, F593.

Sanders, C. O., 1989, Fault segmentation and earthquake occurrence in the strike-slip San Jacinto fault zone, California. *in*: Schwartz, D. P.; Sibson, R. H. (eds.) Proceedings of conference XLV; a workshop on fault segmentation and controls of rupture initiation and termination, U. S. Geological Survey Open-File Report OF 89-0315, p. 324-349.

Sharp, R.V., 1967, San Jacinto fault zone in the Peninsular Ranges of southern California: Geological Society of America bulletin, v. 78, p. 705-729.

Silver, L.T., and James, E.W., 1988, Geologic setting and lithologic column of the Cajon Pass deep drillhole: Geophysical Research Letters, v. 15, no. 9, p. 941-944.

Silver, L.T., James, E.W., and Chappell, B.W., 1988, Petrological and geochemical investigations at the Cajon Pass deep drillhole: Geophysical Research Letters, v. 15, no. 9, p. 961-964.

Thatcher, W., Hileman, J.A., and Hanks, T.C., 1975, Seismic slip distribution along the San Jacinto fault zone, southern California and its implications: Geological Society of America Bulletin, v. 86, p. 1140-1146.

Vernik, L., and Nur, A., 1992, Petrophysical analysis of the Cajon Pass scientific well: implications for the fluid flow and seismic studies in the continental crust: Journal of Geophysical Research, v. 97, no. B4, p.5121-5134.

Zoback, M.D., and Lachenbruch, A.H., 1992, Introduction to special section on the Cajon Pass Scientific Drilling Project: Journal of Geophysical Research, v. 97, no. B4, p. 4991-4994.

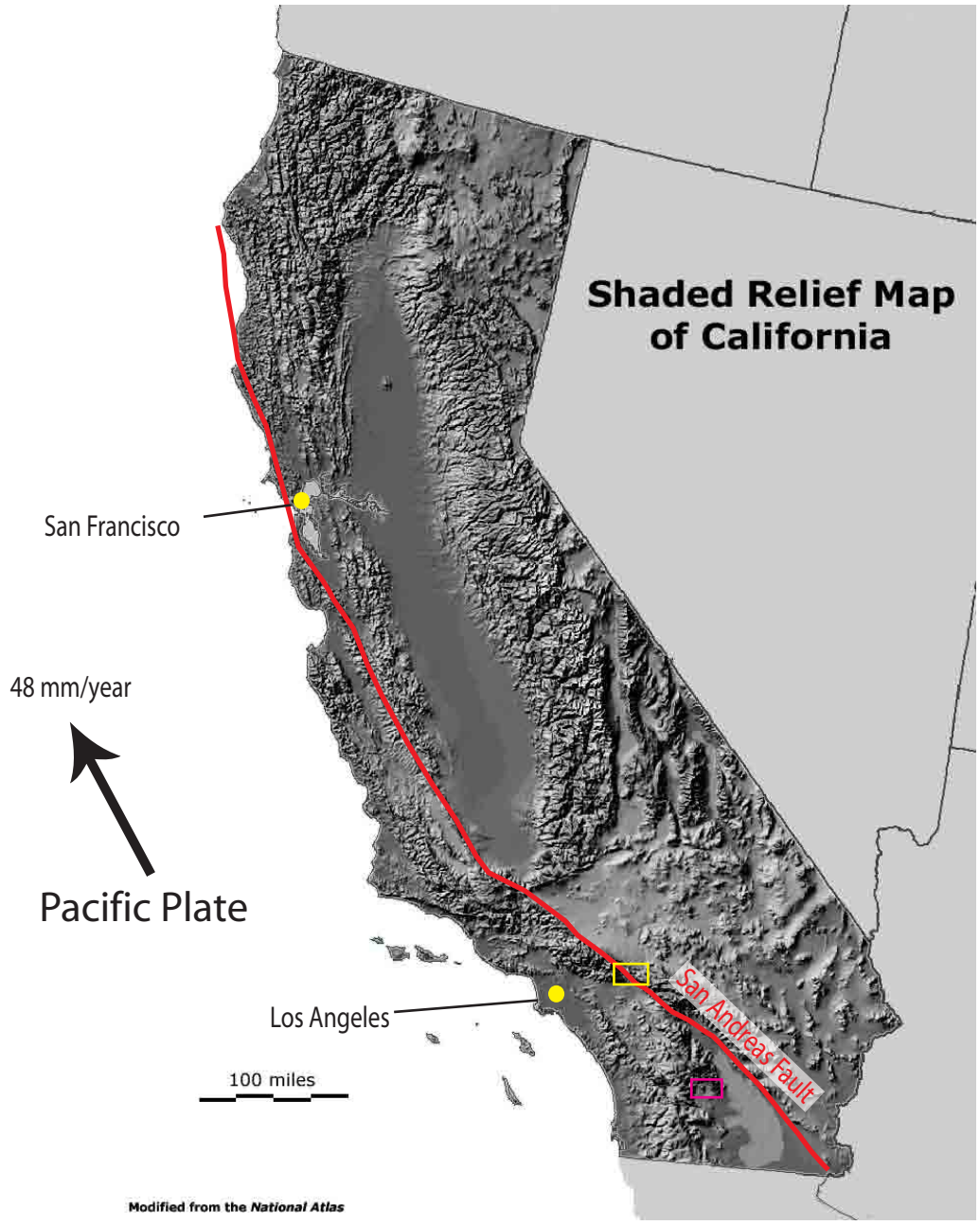

Figure 1-1. Shaded relied map of California showing the location of the San Andreas Fault, the direction and slip rate of the Pacific Plate. The yellow box marks the location of the Cajon Pass. The pink box marks the location of Coyote Mountain and the SE Santa Rosa Mountains. Image modified from *National Atlas.Gov*.

CHAPTER 2

REVISITING THE CAJON PASS CORE: WHAT CAN A SYSTEMATIC STRUCTURAL ANALYSIS REVEAL ABOUT FAULTING AT DEPTH ALONG THE SAN ANDREAS FAULT?

Abstract

We revisit the drilled crystalline core from the Cajon Pass, California drill hole, 4 km northeast of the San Andreas (SAF), and Cleghorn faults, to perform a systematic structural analysis of deformation and alteration associated with strike-slip faulting at the site. Previous lithologic descriptions of the core did not incorporate descriptions or interpretations of deformation processes at depth. The core and outcrop observations provide a sampling of a 4.5 km vertical column adjacent to the SAF. Shallow rocks in the borehole are predominantly sandstones and augen granites, with few fault and fracture zones. Below 500 m depth in the core, gneisses, granite diorites, and granite gneisses dominate, and intense faults and fracture zones are present. The extent of deformation varies within the core, and is controlled by the size of the fault zones intersected by the core. Distribution of faults in the core has a general increase with depth, and fractures within the core have greater populations around fault zones. Despite more faults located at depth, the size of the faults vary and not all fractures are fault related resulting in the highest distribution of fractures clustering around a fault at 2500 m. Microstructures in these fault zones primarily include shear fractures containing a matrix of laumontite with angular to sub-angular clasts within the matrix and may record evidence of seismic stress cycles. Predominantly laumontite signatures on X-ray diffraction analysis of the

structures from the core are indicative of moderate to high temperature fluid interacting with the rocks. The core preserved 19 fault zones and 11 of them were not previously identified. The most significant is a fully intact steep dipping fault zone at 3,402 m depth with potassium feldspar and epidote alteration. This fault correlates well with the nearby left-lateral Cleghorn fault. The San Andreas Fault most likely has an influence on the formation of structures seen in the borehole and core, but the proximity of the Cleghorn fault to the borehole make for a more compelling argument. These data also has significance to testing the theory of a moderately dipping San Andreas Fault in the area of the Cajon Pass. The absence of Pelona Schist ant the deepest part of the hole indicates that the SAF, if it dips northeast, must be steeper than 45°.

2-1. Introduction

The Cajon Pass in southern California lies between the San Gabriel and the San Bernardino Mountains (Figure 2-1). The pass serves as a major corridor for the transport of people and goods in and out of the Los Angeles Basin, and has geologic significance because the San Andreas Fault strikes through it (Figure 2-2). The right-lateral strike-slip San Andreas Fault in Cajon Pass strikes N60ºW, and there are many other subsidiary faults in the area, including the steeply dipping (85º-90º N) left-lateral strike-slip Cleghorn fault (Figure 2-2). The Cleghorn fault is concealed in the Cajon Pass, but in the San Bernardino Mountains it is identified by the offset of folds and faults and offset Quaternary terrace deposits and stream beds (Meisling and Weldon, 1982, 1989).

In 1983 a 1.7 km deep oil and gas exploration well was drilled in the eastern portion of the Cajon Pass by the Arkoma Corporation. In 1986, a second borehole was

drilled through the combined efforts of the Deep Observation and Sampling of the Earths Continental Crust, Inc. (DOSECC) and the United States Geological Survey (USGS) 50 m to the north of the Arkoma well. Often referred to as the Cajon Pass Deep Drill Hole (CPDDH), this borehole was drilled approximately 4 km northeast of the San Andreas Fault to search for mechanical or thermal features that might be used to infer the shear stress at depth, states of stress during slip events, strengths of faults, processes controlling crustal deformation adjacent to transform margins, and the energetics and dynamics of plate motion (Zoback and Lachenbruch, 1992). One of the main conclusions from this drilling project was that the San Andreas Fault was weakly loaded in southern California, with the σ_{Hmax} oriented nearly normal to the trace of the fault (Zoback and Healy, 1992; Shamir and Zoback, 1992). This conclusion is controversial because σ_{Hmax} is predicted to be 30° from the trace of the fault according to Anderson theory of mechanics (Anderson, 1905, 1951).

The CPDDH was drilled to a depth of 3.5 km. *In-situ* stress measurements, geochemical and geophysical logging, examination of the cuttings, and 55 spot cores for a total length of 125.4 m over a depth range from 265 to 3,507 m were recovered from this borehole. No records were found to determine why core was acquired at the chosen depths. Several lithologic studies described the core (Silver and James, 1988; Anderson et al., 1988 a and b; Silver et al., 1988; Vernik and Nur, 1992; Pratson et al., 1992) but no systematic structural analysis of the core was performed. The only structural analysis focusing on fractures in the borehole used a teleview log and was conducted by Barton and Zoback (1992). Fractures and structures in the borehole and borehole electrical images and electrical resistivity of the upper 1,829 m were analyzed by Pezard and Luthi

(1988) and Pezard et al. (1988). This study is the first comprehensive analysis of the entire crystalline core.

2-1.1. Tectonic Setting and History

The San Andreas Fault initiated approximately 25 Ma as a result of the change in motion of the North American and Pacific plates (Atwater and Molnar, 1973; Dickinson, 1981; Irwin, 1990). The 1100-km long, right-lateral fault represents the modern transform plate boundary along the west coast of North America and produces large earthquakes as evidenced by major surface rupturing earthquakes in 1857 and 1906. The Mojave segment of the San Andreas Fault, northwest of the borehole (Figure 2-2, Figure 2-3, Figure 2-4) is currently moving 20-40 mm/year (Weldon et al., 2002) and the San Bernardino segment southeast of the borehole is moving 24 ± 4 mm/year (Weldon and Seih, 1985). In the Cajon Pass, the San Andreas Fault strikes 302° and is the largest fault in the area.

The creation of the Cajon Pass is attributed to erosion of fault rocks between the adjacent uplifting San Bernardino and San Gabriel Mountains. A major episode of late Miocene uplift along the Squaw Peak and Cedar Springs thrust systems produced the ancestral San Bernardino Mountains (Meisling and Weldon, 1989). At this time the San Gabriel fault system was the active part of the San Andreas transform system.

Two additional phases of tectonic activity occurred in the Quaternary in the northwest San Bernardino Mountains. The first phase of uplift in the early Pleistocene affected a broad area and was due to slip across a hypothesized deep crustal detachment ramp (Meisling and Weldon, 1989). The second phase of uplift began in Mid Pleistocene

time with the uplift of the western portion of the San Bernardino Mountains. When this phase of Quaternary uplift diminished, the location of uplift shifted to a narrow area along the San Andreas Fault and is thought to be due to a northeast step at depth of the San Andreas Fault, which may have resulted from the San Andreas Fault's intersection with the nearby Cucamonga and San Jacinto faults (Weldon, 1986; Kenney, 1999).

The structure in the Cajon Pass region is complex, recording contractional and strike-slip deformation (Weldon, 1986). Based on paleoseismology and geomorphology, Weldon (1986) determined the long-term slip rates of the SAF in the Cajon Pass to be on average 24.5 ± 3.5 mm/yr over the past 14,400 years. Recent paleoseismic work on the San Andreas Fault in Wrightwood, CA (Weldon et al., 2002) have determined a long term slip rate of 20 to 40 mm/yr and confirmed ruptures in 1812 and 1857.

The Cleghorn fault (Figure 2-2, 2-3, and 2-4), in the Cajon Pass, is a steeply dipping (70˚–90˚), left-lateral strike-slip fault. It formed with the Cedar Springs fault system in late Miocene as a south-down reverse fault, and accumulated approximately 300 m of vertical separation (Meisling and Weldon, 1989). The fault was then reactivated as a left-lateral strike-slip fault in the Quaternary based on offset of older folds, faults, and disturbed alluvial fans (Meisling and Weldon, 1989). The fault is predicted to preserve both dip slip and strike-slip slickenlines. At the surface the Cleghorn fault juxtaposes deeper granitic rocks on the Crowder Formation and exhibits an asymmetry of the fault core (Jacobs, 2005). In areas the fault consists of a 2 cm thick foliated, maroon clay layer that is localized next to the Crowder Formation with a total fault core thickness of 32 cm (Jacobs, 2005).

2-1.2. Questions Posed

The study examines drillcore of crystalline rocks acquired in the CPDDH project from 1986-1989. Outcrops of the nearby left-lateral strike-slip Cleghorn fault are examined as well. The core was than combined with outcrops along the Cleghorn fault to examine an approximately 4.5 km depth range of damaged rock in the Cajon Pass area near these two major strike-slip faults. The specific questions for this study are:

1. Does deformation vary with depth or with respect to fault zones? If so, how?
2. How does deformation at depth correlate to any faults exposed on the surface?
3. What is the nature of deformation textures and alteration in cored faults?
4. How does deformation at depth compare with nearby exhumed faults?
5. Do the data from the Cajon Pass Borehole support a shallowly dipping San Andreas Fault as hypothesized by Fuis et al. (2007)?
6. What is the primary control of damage observed in the core?

2-1.3. Significance of This Study

Comprehensive structural analysis provides many insights into faulting processes. In particular, revisiting the Cajon Pass core is of interest because existing descriptions of core do not describe or interpret all deformational features that are present. The distinction between lithologic and structural analysis is important when understanding deformation processes at depth. Existing lithologic columns are restricted, and were based on the rocks' characteristics in hand sample or under low-power magnification. Structural analysis of the core will provide insight by systematic investigation of internal

structures to determine deformation history. This includes identification of minerals and mineral alteration due to fluids and microstructural and microtectonic analyses.

2-1.4. Prior Work

Fifty-five spot cores totaling in 125.4 m were retrieved from the Cajon Pass (Pratson et al., 1992; this study). Of the 55 cores, 50 are of crystalline rock, comprise 109.3 m and are currently warehoused at the USGS Core Research Center in Denver, Colorado. Spot cores vary in length but average 10 m long, though actual recovery varies from core to core (Appendix A). The core consists of deformed and undeformed gneisses, granites, diorites, and granodiorites.

Numerous stress, geophysical, and laboratory studies were conducted on the Cajon Pass core. The microstructural analyses performed focused on the orientations of microfractures in a small subset of samples in two orientated cores at 745 m and 1,284 m depth, defining 3 distinct sets at 40°-50°, 68°-76°, and 332°-346° (Wang and Sun, 1990). Aseismic fracturing was described and interpreted throughout the entire core as the result of slow deformation from dilatancy, extension, and shear fractures (Blenkinsop and Sibson, 1992). Petrophysical analysis focused on elastic properties, density, porosity, permeability, and petrophysical classification (Vernik and Nur, 1992). Vernik and Nur (1992) also identified faults that have been altered in the zeolite facies of metamorphism resulting in an increased permeability. They concluded that the intact core at depth is free of fluid fill micro cracks and is in agreement with in situ sonic velocities. X-ray fluorescence (XRF) of 22 of the spot cores determined major element abundances (Pratson et al., 1992). Furthermore, Pratson et al. (1992) combined XRF with

geochemical well logs to determine a comprehensive lithologic column of the borehole from 500 m to 3,430 m depth and are discussed in section 2-3.1. Anderson et al. (1988a) used geochemical tools to make continuous measurements of major and trace elements in the well down to 1800 m and interpreted lithologies. Silver et al. (1988) performed whole-rock chemical analysis on 7 cores from 525.57 to 1,741.35 m depths. Silver et al. (1988) examined 120 thin sections for textural structures and mineral abundances. Major and trace element, and isotopic analyses were performed on a small subset of samples to identify lithologies. Zircon dating was performed on the cores from 1,352.9 m to 1,353.3 m and interpreted to be 77.3 ma by Silver et al. (1988).

However, no systematic structural analysis of the core has been performed and no attempts have been made to systematically correlate structures, lithology, geochemistry, and geophysical data with petrophysical studies. In addition, overview studies and summaries by Zoback et al. (1988), Silver and James (1988), and Zoback and Healy (1992), as well as many others, often present data in extremely small figures that are poorly labeled, and did not bring together available lithologic, structural, and geophysical datasets for a comprehensive interpretation.

Barton and Zoback (1992) conducted a statistical analysis of macrofractures in the borehole using borehole televiewers and compared fracture orientations and distributions with those of previous workers such as Vernik and Nur (1992), Blenkinsop and Sibson (1992), Blenkinsop (1990), Wang and Sun (1990), Vincent and Ehlig (1988), but none of their data cover the entire core data set, and most are limited to the core from the first phase of drilling, which went to a depth of 2115 m. This study incorporates our systematic analysis of the entire crystalline core data set, integrates data from previous

workers, and compares results to the fracture analysis presented by Barton and Zoback (1992).

Silver and James (1988), Vincent and Ehlig (1988), Blenkinsop (1990), Blenkinsop and Sibson (1992), Barton and Zoback (1992), Vernik and Nur (1992), Pratson et al. (1992), Vernik and Zoback (1992), Shamir and Zoback (1992), and Zoback and Healy (1992) identified fault zones within the core from geophysical logging tools, cuttings, and basic core observations. Blenkinsop and Sibson (1992), and Vernik and Nur (1992) described the architecture of some of the fault zones, but their analyses were incomplete in some aspects. Our study has faults and fault zones that had not been previously identified. Our systematic analysis of the entire crystalline core combined with the aforementioned studies makes for a complete structural analysis of the Cajon Pass core and includes an analysis of newly identified fault zones within the core as well as possible correlations with faults mapped on the surface and implications for other studies conducted within the area.

Seal and Barth (2007) have conducted detrital zircon dating on the crystalline rock from the Cajon Pass borehole. They identified two distinct pluton suites based on the ages of gneiss and granitic granodiorite and tonalite. The granodiorite samples were collected from 1,023.3 m, 1,351.5 m, and 2,427.6 m depth; the gneiss sample was collected from 1,655.3 m; and the tonalite sample was collected at 3,019.0 m depth. The upper pluton samples show that it emplaced at 151.3± 1.3 Ma. A younger granodiorite pluton was emplaced at 78.9 ± 1.3 Ma to 81.3± 0.8 Ma adjacent to the first and incorporated zircons from the older pluton. The bottom-most sample returned dates of

1,625 ± 12.5 and 1,739.0 ± 10 Ma, possibly due to material incorporated into the melt from a source deeper than the core or from a preexisting pluton.

Jacobs (2005) performed surface studies along the Cleghorn fault. He focused on fault structures and compositions including mesoscopic fault zone geometry, the nature and extent of fault core and damage zone, and fault kinematics within the San Bernardino Mountains. His work on the Cleghorn fault did not continue west of Cleghorn Mountain. Exposures west of Cleghorn Mountain can be used to correlate structures on the surface with faults seen in the core and serve as a proxy of strain and damage differences between the core and the surface. By incorporating the surface exposures of faults described by Jacobs, the total depth range of the fault-related damage examined extends to 4.5 km.

2-2. Methodology

Multiple methods were applied to address the questions posed here. Mesoscopic examination and logging of the Cajon Pass core was carried out to define first order observations of the core including basic lithologies, fault locations and depths, evidence of fault slip, fault dip, and sense of slip, fractures, and alteration seen as the result of fault slip within the core. Petrographic and microstructural analyses of deformation attributes in thin sections obtained from core include lithological descriptions, analysis of textures, and interpretations of deformation mechanics. Geochemical characterization of rocks was performed using X-ray diffraction (XRD) and X-ray fluorescence (XRF) analyses. The XRD was used to determine the composition of fault or fracture fills in the core. The

XRF analysis was used to examine compositional changes across some faults in the core. Samples were collected for future stable isotope analyses and 40Ar/39Ar dating.

The petrological, geochemical, and structural data were combined with compressional (V_p) and shear (V_s) sonic velocity geophysical log data, as well as porosity, resistivity, and gamma logs. This data was analyzed and compared with core data to determine how geophysical data may relate to deformation mechanics and to examine geophysical data in order to infer physical properties of deformed rocks. Furthermore, wireline logs were correlated to the drilled core in an attempt to validate the accuracy of the different sets of data. Detailed mapping of small faults and deformation zones located within the cores was also performed.

2-2.1 Field Methods

The Cajon Pass and surrounding faults used in this study lie within two 7.5 – minute USGS topographic quadrangles: Cajon and Silverwood Lake. The main focus of this aspect of the study is to identify, describe, and sample faults near Cajon Pass in the western San Bernardino Mountains. Faults were located in the field using geologic maps of Weldon (1986), Meisling (1984), Morton and Miller (2003), Jacobs (2005), and Meisling and Weldon (1982, 1989) as well as from reconnaissance mapping and analysis of air and satellite imagery. A Garmin eTrex Venture CX model GPS was used to record the locations in North American Datum (NAD) 27 UTM projection. UTM locations, specific site details, written descriptions, and site identification numbers were recorded. Detailed outcrop sketches were made to record fault geometries, offsets, and cross-cutting relationships of faults, fractures, and veins. The attitude of the bed as well as

faults and fault stria were collected using a Brunton compass. Photographs were taken using an Olympus Stylus 710 digital camera. Photograph dates and numbers were recorded to correspond with specific sites. Written descriptions of sites include lithologies and orientations of foliations and structural features. An outcrop-specific, systematic (i.e. non-random) sampling plan was developed to representatively sample the damage zone rock and fault core at the fault zones studied. A total of 8 samples were collected during field work over 2 days. Samples collected at the surface for this study and samples of the Cleghorn fault collected by Jacobs (2005) were then compared with samples and results from 480 to 3,506 m depth in the Cajon Pass core, effectively forming an approximately 4.5 km deep record of damage along major strike-slip faults in southern California.

Data collection locations were determined using air photos of the Cleghorn fault in the area of the Cajon Pass and in the San Bernardino Mountains. Jacobs (2005) noted and mapped faults and damaged zones of the Cleghorn fault in the San Bernardino Mountains and described thin sections of the damage zone but did not continue along the fault westward past Cleghorn Mountain. Some of the Pass and surrounding areas have been mapped by Weldon (1986) and Miller and Weldon (1992) and some exposures of the Cleghorn fault have been examined by Jacobs (2005).

2-2.2. Core Logging Methods

Detailed logging of the entire crystalline core was conducted as part of the systematic structural analysis of the Cajon Pass core. In general, the methods outlined in Blackbourn (1990) were followed. These include making note of depths, core position,

rock name, color, fabric, texture, weathering, tectonic structures, veins and mineralization (Blackbourn, 1990). Logging was also used to determine lithologic changes, presence of faults and fractures, orientation of faults and fractures, foliation attitudes, geometries and architecture of fractures, faults, and fault zones. Descriptions were written for each core and measurements were taken of fracture depth, length, and dip angle. Fracture type, such as open, closed and drilling induced, was also recorded. All archived core as well as sample locations were photographed.

2-2.3. Core Condition and Previous Samples

Recovery of the core ranges from excellent (fully intact) to very poor (low percentage of recovery, where core was reduced to rubble). Upon retrieval, the core was cut into slabs. For core 4 ½" in diameter or less; a 1 ¼" thick slab was cut along the full length of the core and archived. The remainder was designated as the sample set. For cores greater than 4.5" diameter, two slabs were cut. A 1.25" thick slab was cut first for archive and second 1.25" slab was cut as a "working set" for drill site examination. The remainder was designated as the sample set. Both archive sets were cut 180° from a red and black marker reference and the working set was cut 90° from the marker reference after the archive set (Figure 2-5).

Some previous samples taken from the sample core are marked by workers in pencil on the core boxes or by small Styrofoam bricks. Appendix B is a record of all previous samples removed from the core that were marked on the core. This appendix represents only some of the previous samples, as not all workers left notes of sample

locations (Figure 2-5). Previous workers more densely sampled some areas of the core than others.

2-2.4. Core Maps

Detailed 1:1 trace maps of the core were produced for 5 spot cores. The purpose of these maps is to characterize the lithologic and mesoscopic scale structures observed on the core surface. Mapping was performed by wrapping Mylar or thin clear plastic sheets around the core and tracing out lithologic changes, fractures, and faults with permanent markers. When unwrapped, these maps have a record of all deformation and lithologic changes, as well as distribution of damage within each spot core. The core maps were used in conjunction with logging of the core.

2-2.5. Review of Borehole Geophysical Logs

Original wireline log data were not reviewed for this study because we were unable to attain the original or digital files. Logs previously published by Barton and Zoback (1992) were primarily used along with data published in Blenkinsop and Sibson (1992), Vernik and Nur (1992), Vincent and Ehlig (1988), Blenkinsop (1990), Silver and James (1988), Pratson et al. (1992), Vernik and Zoback (1992), Shamir and Zoback (1992), and Zoback and Healy (1992). The published logs were reviewed and attempts were made to correlate Vp and Vs responses, as well as porosity, resistivity, and gamma logs, to faults and fault zones identified in the core. Typically high values of porosity, shear velocity, compressional velocity, and resistivity can be indicative of the presence of fault zones. This data was also used to determine damage zone thickness and to infer competency contrasts of structures and host lithology.

2-2.6. Laboratory Methods

2-2.6.1. X-ray diffraction

Samples for X-ray diffraction (XRD) analysis were chosen based on their macroscopic appearance during logging of the core. Features such as fractures with mineral fills, faults showing evidence of gouge production, and host samples were chosen. Samples from field observations along subsidiary faults to the Cleghorn fault within the Cajon Pass were also analyzed.

Samples analyzed with X-ray diffraction (XRD) were crushed in a Rocklabs grinding mill in a Saylon (lightweight ceramic) head for an average of 3 minutes, depending on the hardness of the sample. This process reduced the sample to a fine powder. The powder was then sieved through a 125 mesh sieve to insure uniform grain size. Any grains that did not pass through the sieve were crushed by hand with a mortar and pestle until they were able to pass the sieve. After all of the material was sieved, the sample was shaken to insure homogeneity and mounted in aluminum holders for XRD analysis. All samples were analyzed using a Philips X-Pert PRO PANalytical machine with the accompanying X-Pert Highscore software for result interpretation. A total of 33 samples were analyzed. The diffractometer scanned each sample from 5-65° at a speed of 0.04° per second. X-rays were produced with a copper tube at 40 amps with accelerating voltage of 45 Kv. Results are tabulated in Appendix E and Table 2-3.

2-2.6.2. X-ray fluorescence

X-ray fluorescence (XRF) was performed on 19 samples from the Cajon Pass core. The XRF analysis was used to determine compositional changes across faults in the

core and to determine bulk mineralogy of the host rock. All 19 samples were sent to ALS Chemex, located in Reno, Nevada. The steps for XRF preparation were:

1. Samples dried at 110-120° C.
2. Samples were crushed using either an oscillation jaw crusher or a roll crusher so that >70% of the sample passed through a 2 mm (10 mesh) screen.
3. Samples then pulverized using a ring mill such that >85% of the sample passed through a 75 microns (200 mesh) screen.
4. Samples were then fused using a lithium borate fusion. The melt was poured into a mould and cooled to yield a solid glass disk.
5. The disks were analyzed in XRF machine.

The samples were analyzed for the elements SiO_2, Al_2O_3, Fe_2O_3, CaO, MgO, Na_2O, K_2O, Cr_2O_3, TiO_2, MnO, P_2O_5, SrO, BaO, and Loss Of Ignition (LOI). All elements and LOI have a detection limit of 0.01%. Results are in Appendix F.

2-2.6.3. Thin sections

To describe and understand the microscopic processes occurring throughout fault zones captured by the core, 51 thin section billets were prepared at Utah State University, and then completed by Quality Thin Section. The steps for billet preparation were:

1. Coat sample with two-part Petropoxy 154 (resin and agent 154).
2. Vacuum samples and recoat until fully impregnated.
3. Cure samples at 135° C for 4-6 hours.
4. Cut samples into specified billet size using wet rock saw and allow to dry at room temperature for at least 24 hours.

All but 7 samples were epoxied using Petropoxy 154. The remaining samples were epoxied using Buehler Epothin hardener 20-8142.016 and resin 208140-032, vacuumed and allowed to cure at room temperature for 48 hours at the USGS Central Region Office in Lakewood, CO. Upon return to Utah State University, optical microscopy analysis and digital photography was performed using the completed thin sections.

2-3. Results

A generalized lithologic column derived from both geophysical borehole measurements and core and cuttings data based on Vernik and Zoback (1992) is shown in Figure 2-6. Figure 2-6 also shows the location of spot core recovered during drilling. A total of 125.4 m of spot core was retrieved, of which 108 m are in crystalline rocks from depths 480 to 3,506 m. From this core, a total of 142 samples were cut, the majority limited to 1 cubic inch. Of 142 samples, 51 were cut into thin sections, 19 were used for XRF analysis, and 33 were used for XRD analysis (Appendix C). All samples were photographed using a high-resolution digital camera. Core, segment, and depth data were recorded when available.

Twenty-one faults were sampled, either partially or wholly, by the core and were logged in this study. Of the 21 cored faults, 11 are newly identified in this study. The newly identified faults are described below.

2-3.1. General Observations of Rock Types and Structures

The borehole intersected 497 m of sedimentary rocks and 3,000 m of older basement rocks. The Miocene Cajon Formation overlays Cretaceous and older crystalline basement complexes in the borehole. The Cajon Formation is a buff arkosic sandstone,

locally pebbly to conglomeratic with reddish and greenish siltstone and claystone. Lithic clasts include granite, gneiss, schist, and volcanic fragments (Silver and James, 1988). The Cajon Formation was not examined. The basement complex is comprised of various types of granite, granodiorite, tonalite, monzonite, diorite, and small amounts of syenite and gabbro (Pratson et al., 1992). Pratson et al. (1992) determined these variations using an oxide classification scheme of the borehole from wireline tools and used some of the core as quality control. There interpretation and classification of basement rock differs from that of Silver and James (1988), Anderson et al. (1988 a and b), Silver et al. (1988), Vernik and Nur (1992), Vernik and Zoback (1992), and Barth and Dorais (2000), classified the crystalline basement as a combination of gneissic granodiorite, gneissic granite, paragneisses, migmatitic granodiorite, granite, migmatitic diorite, and gneissic diorite (Figure 2-7).

Though there are different basement rock types, the units can be combined and simplified into four distinct assemblages. Assemblage one is sandstone; assemblage two is gnessic granitic rocks; assemblage three is comprised of migmatitic rocks; and assemblage four is an interlayering of assemblage two and three with some gneissic diorites (Figure 2-8).

Structures observed in the core include faults, mode I fractures and mode II fractures. This, combined with fairly friable material, reduced the quality of sample and archived slabs of core in places. In locations where faults were observable in the core and sample core was available, samples were collected for further analysis. Measurements of fault and fracture type, frequency, and lengths are limited to exposure within the core. The dips of faults and fractures were also measured. For example, a steeply dipping

fracture that cuts through the center of the core will be a greater length than a horizontal fracture

2-3.2. Faults in the Core

Previously a total of 26 fault zones of varying thicknesses were identified and recorded in the borehole from a combination of partial core studies, examination of cuttings, and borehole geophysical log interpretation (Blenkinsop and Sibson (1992), Barton and Zoback (1992), Vernik and Nur (1992), Vincent and Ehlig (1988), Blenkinsop (1990), Silver and James (1988), Pratson et al. (1992), Vernik and Zoback (1992), Shamir and Zoback (1992), and Zoback and Healy (1992). Eleven new fault zones were identified in core, described, and interpreted in this study bringing the total to 37. Previously published core studies and geophysical log data were used to augment our descriptions and interpretations. Of the 26 previously identified fault zones, only 10 were cored or had portions of their damage zones cored. Appendix H contains photographs of the 10 faults.

The newly identified fault zones range from 0.5 to 20 m (Figure 2-7) in apparent thickness, though this number has a large error associated with it due to the limitations of the short spot cores and variable quality of recovery. In hand samples the faults typically appear as well-defined zones of varying thicknesses and contain a shear fracture-fill ranging from pink to white to pale green. Open or closed fractures, either individually or combined, populate the areas surrounding the faults. Most slip surfaces appear to have a damage zone associated with them. The damage zone thickness varies from fault to fault, and the extent of the measured damage depends on the size of the fault where it could be

quantified. Compressional- and shear-wave velocity, porosity, and fracture distribution logs published by Barton and Zoback (1992) aided in the measurements of the width of damage zones. The newly identified fault zones are minor in size and offset compared to large fault zones detected previously by various logging tools. Please refer to Table 2-1 for the descriptions of the identified faults in the core.

2-3.2.1. Microstructure analysis

The purpose of this section is to present the results of core and optical microscopy observations of all the newly identified fault zones from the core. The analysis of the 51 thin sections emphasizes the fault zones captured by the core. Appendix D contains a summary of observations from all thin sections. Thin sections were cut to characterize the microstructures in the core and to relate them to mesoscopic-scale deformational features observed in hand samples of the core.

2-3.2.2. Descriptions of newly identified faults

Fault at 1138 - 1140 m

This fault is situated in a leucocratic granite gneiss with large potassium feldspar crystals on both sides of the fault. Some of the rocks surrounding this fault are well foliated. The fault is poorly preserved (Figure 2-9). The entire fault zone was broken and rock chips are in a plastic bag and the original thickness is unknown. The rubble contains pink to white chunks and there is no measurable offset, sense of movement and dip measurable from the vertical axis of the core. There are a few mostly open fractures in the intact core surrounding the fault, with some gray mineral fill in the closed fractures.

In thin section, this is a small fault with laumontite fill. The laumontite zone is well defined with distinct boundaries between the laumontite matrix and the microbreccia. The microbreccia is asymmetric, and not always present along the laumontite boundary. Grain fragments within the matrix all have a similar orientation with their Y-axes aligned with flow. Perpendicular to the main laumontite zone, open fractures extend into the host rock and large grain laumontite has precipitated in them. The fault reflects at least four distinct episodes of deformation (Figure 2-9). The very center has large laumontite growths; fine grain laumontite surrounds larger laumontite. Discrete slip surfaces bound the laumontite zone. Outside of the main laumontite zone, the host rock is comprised of fractured grains with smallest grains closer to the main zone. Larger grains are farther away from the fault zone.

Fault at 1354 - 1355 m

This fault is located in a black and white leucocratic granodiorite. The core from this fault is intact. The fault is narrowly defined, making a core-fault angle of approximately 75°, (Figure 2-10), and contains a 2-cm thick white to pale green zone with a pink alteration halo. A poorly developed slip surface is observed in the core showing mixed mode slip vectors. Parts of the fault are friable with a clay-gouge type material. There are very few fractures in the core, with the damage zone confined to the area of the main fault.

The thin section of the fault at 1354 - 1355 m has shear fractures with two phases of laumontite precipitation within the shear fractures, and no clear sense of slip. The first phase of laumontite in the shear fractures exhibit a fine-grained matrix, with what appears

to be a secondary precipitate of a comparatively larger grain laumontite within the matrix. This could be due to reactivation of the shear fracture after precipitation of initial laumontite. This would explain the creation of the fine grain laumontite matrix. Etched calcite is present along the boundaries of the fault. Small mode I fractures as well as fractured grains surround the main structure (Figure 2-11).

Fault at 1499 - 1501 m

The fault at 1500 m is in a well-to-moderately foliated gray diorite and amphibolitic gneiss, and contains a narrowly defined shear zone. A small shear zone cuts the core almost horizontally and is green to red due to the presence epiodite and hematite. It has some slickenlines (Figure 2-12) on an internal chunk of core. The slip direction appears to be dip slip, but because this section of the core is poorly preserved, confidence is low. Horizontal open fractures are present in the area.

The shear zone is not as well developed as other samples, and is identified by a change in grain size and has a strong alignment of biotite. Two episodes of deformation are recorded. There is a fine-grained laumontite matrix zone with large growth laumontite grains in the center of the shear zone. Localized slip surfaces appear at some edges of the shear zone. Grains surrounding the shear zone are fractured (Figure 2-13).

Fault at 1900 – 1906 m

This fault dips 30° and is in a white to gray granite–granodiorite that transitions to dark gray granitic gneiss, and contains many pink to buff feldspars on either side of the fault. The protolith is highly damaged. Zones of white to light gray zeolotic alteration with (Figure 2-14), and fractures and friable rock surrounding the zeolites are present.

There are many fractured grains, but no offset or slicks seen, and the alteration zone makes a shallow angle with the core axis. The core contains some open horizontal fractures with a few small zeolitic fill fractures throughout.

The microstructures at this depth are limited to laumontite and calcite filled fractures. The host rock surrounding the fractures is intact and displays repeated deformation. Some fractured grains and twinned calcite are present. Deformation is confined to the area of the main fracture, and no reduction in grain size is observed (Figure 2-15).

Fault at 1981 – 1982 m

The fault at 1982 m (Figure 2-16) is developed within a gray granite to granodiorite that has some weak foliations throughout. A well-defined small fault dips 70° and contains ~4 mm thick gouge zone of possible chlorite and epidiote. A pink alteration halo surrounds the fault. A similar fault is observed 0.3 m deeper. Slickenlines observed on both faults appear predominantly dip-slip based on the direction of slicks on the dipping fault. There are some white zeolite filled fractures that are dipping more shallowly in the vicinity of the faults.

Fault at 2070 - 2080 m

A gray to black highly alterated granodiorite is the host lithology for this fault. The rock (Figure 2-17) is moderately to well foliated, and alters from fine to coarse crystalline. It contains no clear fault or slip surface. No slicks were observed. Alteration observed is green to white and marked by a drastic change in grain size. A separate 4 mm

thick alteration zone is dipping 50°. Poor recovery of this core limits the interpretation and description.

Thin sections from this area contain shear fractures with multiple episodes of movement observed (Figure 2-18). Areas of different styles of deformed rocks are present, and these areas may be the result of multiple episodes of fractures combined with pulses of fluid flowing through the system. The innermost area of the encompassing shear fracture zone contains a fine-grained matrix of laumontite with some possible rotated and elongated grains scattered throughout. A clay gouge zone (Figure 2-18) is in the very center of the laumontite matrix. The second innermost area has a larger grain matrix than the inner area, but appears to be the same material. The outermost area inter-fingers with the 2nd zone and contains larger fractured grains, some of which may be calcite. Microcracks as described by Blenkinsop and Sibson (1992) are also present throughout the thin section, but do not cross the main shear zone. The damage is well defined and does not appear to extend into the host rock.

Fault at 2110 - 2122 m

The fault is located in a dark gray gneissic granodiorite to light gray to white leucocratic granite. Because the fault core is in loose chunks in a bag, the dip, and the width are undeterminable (Figure 2-19). The fault is white, and the color contrast with the surrounding darker rock is sharp. Another small fault may be located ~ 0.5 m above and contains a poorly developed white to pale green zeolite alteration. Horizontal sub-parallel fractures dominate the core around the fault.

Fault at 2232 - 2252 m

A dark gray to black fine crystalline gneiss with bands of granite gneiss is the host rock in which this fault is located. The core is highly fractured (Figure 2-20) with a well-defined shear zone containing both a white chlorite to zeolite alteration fault as well as a green fault that appear to be dipping 90° and 70°, respectively. There is offset within the shear zone of approximately 4 cm, in the intact core, but more may be present. Because of the fragmented core, there is no discernable type fault type. Slicks were not observed. Some open horizontal fractures are present in the area.

Thin fractures with laumontite fill are present. Some brittle reductions in grain size are seen near veins and fractured grains (Figure 2-21). Some areas of the veins are larger fibrous laumontite growth minerals, but areas surrounding the larger grains are of a near uniformly fine-grained matrix. The uppermost area of the thin section contains deformed twinned calcite with dissolved areas within and around the grain. There is no clear sense of movement along any of the structures in the thin section. Some pyrite is seen in the thin section as well.

Fault at 2317 - 2350 m

This fault (Figure 2-22) is in a medium crystalline leucratic poorly foliated granite that contains medium pink potassium feldspar porphyroclasts. No slip surface is observed, but the core has a high density of vertical to sub vertical, ~1 mm wide, mostly white fractures that extend the length of the segments. This is most likely part of the damage zone, and fault was not preserved in the core due to poor recovery.

Laumontite filled mode I fractures dominate the thin sections from this fault zone (Figure 2-23). The widest parts of the fractures have clear evidence of laumontite growth and show evidence for a volume increase as well as brittle deformation of some of the surrounding grains. Microcracks are also present in thin section. The host rock is intact and undeformed. There is no change in grain size in the vicinity of the fractures, and no fractured grains.

Fault at 2735 - 2755 m

This fault (Figure 2-24) is in a medium crystalline, highly deformed gray granodiorite. A 2-cm wide, 11.5-cm long, vertical to moderately dipping fault contains clay gouge, with well-developed foliations in the core. The surrounding fault dips approximately 60° and has green (epidiote, chlorite) alteration zone mixed with some pink alteration. Smaller faults are also present in the core slice containing similar composition. The core is highly fractured and the rubble has a similar appearance to the host rock with narrow bands of white to pink zeolite alteration. The faults appear to be dip slip and are of an unknown thickness.

Laumontite-filled shear fractures are present throughout this area (Figure 2-25). In some areas three distinct episodes of deformation are present within the laumontite fill and are recognizable by the differences in grain size and shape. The host rock surrounding the shear fractures highly deformed and contains fractured grains and variations in grain size, with isolated areas of grain size reduction. Some large quartz veins are present in the area as well. The quartz veins have an abrupt termination and the

grains immediately surrounding the quartz vein are fractured or plastically deformed. Small dilatant laumontite veins are also present in some of the surrounding grains.

Fault at 2852 - 2853 m

A gray medium to coarse-grained, poorly foliated, highly fractured granodiorite (Figure 2-26) is the host rock for this fault. No clear fault is observed, but the core contains a small zone of ~1 cm thick zeolite alteration in a zone of fractures. Red and green alteration dominate the area. A large number of horizontal fractures are littered throughout the core.

Small, narrowly defined shear fractures are present in thin section. Sections of the shear fracture are red (Figure 2-27) and surrounded by a laumontite matrix. There is a distinct reduction in grain size along the shear fracture. In areas the laumontite matrix appears to have captured angular fragments of the host rock. Some calcite appears to have precipitated around the shear fracture. Fracture grains, twinned calcite, and microcracks are present. Some small mode I fractures are present with laumontite fill in the area.

Summary

In the newly identified faults, most lack sense of slip indicators. The faults were identified by their alteration zones, surrounding gross increase in the intensity of fractures surrounding alteration zones, and the decrease in competence of the host rock. The transition in rock competence from protolith to fault ranges from gradual to sharp and can result in poor recovery and preservation of the faults that have been drilled. This is

problematic when determining original orientation of the identified faults, as well as collecting samples that accurately represent the fault.

Of the 37 faults identified, only four appear (2500, 2800, 3200, and 3400 m depth) to have damage zones greater than or equal to approximately 10-20 m wide. These wider fault zones were identified using a combination of velocity logs, core, cuttings, and fracture frequency plots. Of these four faults, two were partially cored and preserved. The core from the fault zone at 3,400 m depth is a fully intact core containing a moderately dipping fault with a well-developed alteration zone with a green to gray to pink alteration throughout (Figure 2-40). The fault preserves no indication of the amount of offset, but shear sense indicators show a predominantly dip slip fault. Wireline tools did not show as strong a response for this fault zone as some of the others (Barton and Zoback, 1992) (Figure 2-34).

The fault zone at 2,800 m depth is in a leucratic granitic biotite hornblende gneiss that at hand sample inspection does not have any identifiable fault zones or fault traces. The core is highly fractured, but some of this core has poor recovery and thus cannot be described as well as some of the other faults.

Competence contrasts in the host lithologies are also recognizable in wireline log data. In particular, the fracture aperture and orientation derived from down-hole televiewer data recorded areas of competency contrast, as rocks weakened by seismic movement are more prone to collapse and create a larger aperture (Barton and Zoback 1992). All of the areas of large apparent aperture of fractures recorded by the down-hole televiewer correlate well with faults observed in the core or interpreted by previous workers using a variety of wireline logs (Silver and James, 1988; Vincent and Ehlig,

1988; Blenkinsop, 1990; Barton and Zoback, 1992; Blenkinsop and Sibson, 1992; Pratson et al., 1992; Shamir and Zoback, 1992; Vernik and Nur, 1992; Vernik and Zoback, 1992; Zoback and Healy, 1992).

The absolute orientations of faults in the core are undeterminable because the core was not oriented when drilled. Pezard et al. (1988) have reoriented the core from 521 to 1500 m depth using the borehole televiewer, but the warehoused core had no indications of orientation. Attempts to reorient the core based on correlating measured fracture dips from the core with the fracture dip and dip direction in borehole televiewer data (Barton and Zoback, 1992) was unsuccessful due to the highly variable orientations and distributions of fractures.

The mean dip of the newly identified faults is 55.8° and the mean dip of all of the faults is 52.1°. Table 2-1 shows the dips relative to the core axis of all faults captured by the core individually.

2-3.2.3. Microstructure summary

Microstructural damage varies in thickness throughout the core, but regardless of width, some common features exist in the core samples. Laumontite is the predominant mineral in all of the microstructures, regardless of the mode of fracture (mode I, II) or possible micro fault. There are varying amounts of secondary alteration of laumontite, with some shear fracture zones (small faults) displaying more than one episode of laumontite precipitation within the same defined fracture. The near ubiquitous abundance of laumontite fill in the damage zones suggests that a moderate to high temperature fluid interacted with rocks in these damage zones, was present during the faulting process

(James and Silver, 1988; Vincent and Ehlig, 1988), or entered at some point after damage occurs. Larger shear fracture zones have fine grain lineations located in the laumontite matrix that may represent micro slip planes, or an ultracataclasite zone. Some of the microstructures from the Cajon Pass do show evidence of repeated stress/strain cycling, based on evidence of undeformed laumontite crystals surrounded by a matrix of fine-grained and fractured laumontite.

2-3.2.4. Other faults

The other faults examined in thin section contained similar microstructures as described in the samples above. In general, wider shear fracture zones contained greater damage then smaller ones, though they nearly all displayed various styles of fractures and laumontite growth. Also, grain-size reduction, microfractures, and mineral alteration, to varying degrees, is seen throughout the majority of samples.

2-3.3. Fractures in the Core

Fractures are present throughout the core and range in orientation relative to the axis of the core, thickness, aperture, and fill material. All filled fractures are either mode I or shear fractures. Many mode I fractures that contain no fracture fill within the core are suspect as they could be drilling induced, formed after coring, or formed during transport. Drilling induced fractures commonly show a unique orientation within the core and are sub-parallel to the core axis or perpendicular to it (Kulander et al., 1990). The clockwise rotation of the drill bit may also cause chipping along the margin of the core (Kulander et al., 1990), and improper or aggressive handling of the core may induce fractures.

Fractures observed in the core have either a light pink, gray, or white fill, if they are not open. The color of the fracture fill does not appear to be dependent on fracture aperture, dip, or host lithology. In hand sample, the fill appears to be a fine grain matrix of material in a well-defined zone bounded by the fracture walls despite color (Figure 2-28). Gradational zones surrounding fractures are lacking, though a slight halo surrounds some of the mostly vertical fractures that contain a white fill. The fracture fill was not identifiable in hand sample, but XRD analysis was able to characterize the material as mostly zeolites (discussed in the XRD section below).

A total of 329 fractures were measured in the core. Based on mesoscopic review of the core, most of the fractures appear to be mode I, though the lack of core in some sections limits this interpretation. The fractures range in dip relative to the axis of the borehole, with the majority of the fractures dipping between 30° and 75°. Though most of the fractures dip moderately, long, continuous, vertical or nearly vertical fractures are present in some core segments. These fractures usually range from 1-2 mm wide and contain a white material fill. They are observed in swarms or closely spaced, sub-parallel fractures with anywhere between 5 and 15 present. Of the 329 fractures measured, the majority of the fractures are between 2050 m-2500 m. It is important to remember that the measurements from this study are strictly from the crystalline spot core, which represents only 3.57% of the total depth of the borehole. Thus, complications of fracture data may not be representative. Nevertheless, this finding of concentrated fractures between 2050 m – 2500 m is in agreement with fracture studies from Barton and Zoback (1992).

Because the core is unoriented, fracture sets were identified solely from their dip relative to the axis of the core. The fracture analysis identified two distinct sets at 30° and 65° to the core axes.

2-3.4. Geochemical Analyses

2-3.4.1. X-ray diffraction

X-ray diffraction (XRD) (n=33) results typically show granite to granodiorite mineralogies for the host rock (Table 2-3). This is in agreement with thin-section analysis as well as mesoscopic core observations. The typical protolith mineralogy is: quartz, albite, anthorite, christobolite, orthoclase, microcline, with minor amounts of biotite, phlogopite, chalcopyrite, graphite, and magnesiohornblende. Quartz and albite are present in nearly every sample. Albite is the primary plagioclase in most samples. Anthorite and christobolite are also present in many of the samples. Orthoclase and microcline dominate the potassium feldspars recognized in analysis. Micas are rare, but include biotite and phlogopite when present. Mafic minerals such as chalcopyrite, graphite, and magnesiohornblende are present in some of the samples, but make up less than 15% of all XRD analysis conducted for this study (Table 2-3).

Alteration zones are predominantly comprised of laumontite, with illite and nontronite rarely present. The XRD analysis of samples taken from the fault zones or damage zones of both the newly identified faults and those previously identified was predominantly laumontite in addition to the host rock minerals. Laumontite ($Ca(AlSi_2O_6)2•4H_2O$) is a zeolite that is indicative of thermal fluids ranging from 30° C to 450° C as experimentally derived by Ghobarker and Schaf (1998). Blenkinsop and

Sibson (1992) determined the chemical reactions that led to the breakdown and alteration of protolith minerals includes:

$$Na^{+} + H_4SiO_4 + NaAlSi_3O_8 \bullet CaAl_2Si_2O_2 = 2NaAlSiO_3O_8 + Al^{3+} + Ca^{2+} + 4OH^{-}$$

(Plagioclase) (Albite)

Which leads to these reactions in the formation of laumontite and calcite:

$$2Al^{3+} + Ca^{2+} + 8OH^{-} + 4SiO_2 = CaAl_2Si_4O_{12} \bullet 4H_2O$$

(Laumontite)

$$Ca^{2+} + CO^{2-}_3 = CaCO_3$$

(Calcite)

In situ laumontization can also occur by the hydration reaction from plagioclase (Boles and Coombs, 1977):

$$NaAlSi_3O_8 \bullet CaAl_2Si_2O_2 + 2SiO_2 + 4H_2O = NaAlSiO_3O_8 + CaAl_2Si_4O_{12} \bullet 4H_20$$

(Plagioclase) (Albite) (Laumontite)

The stability field of laumontite has been defined by various workers to be somewhere between 90° – 280° C (Zen and Thompson, 1974; James and Silver, 1988; Vincent and Ehlig, 1988; Blenkinsop and Sibson, 1992). James and Silver (1988) determined that laumontite is actively forming ~2.1 km depth based on halos surrounding laumontite grains. They than calculated the low-end stability to be ~ 90° C to 250° C. Vincent and Ehlig (1988) used a laumontite stability of 190 - 250°, as determined from Zen and Thompson (1974), Finally, Blenkinsop and Sibson (1992) have synthesized all of the above data and states that the temperature range of deformation is 90º-250º based on the stability limits of laumontite in the Cajon Pass as calculated by the above mentioned workers.

The stability field of laumontite plus albite, as determined by Zen and Thompson (1974) and Turner (1980), lies between 190 - 250° C at 0.2 to 0.8 kb water pressure. Water pressure at the borehole was determined to be 0.24 to 0.34 kb, and the equilibrium temperature gradient of ~37 C/km (calculated from Sass et al., 1992; Lachuenbruch and Sass, 1988) are consistent with the creation of laumontite throughout the crystalline core.

In hand samples from the core, laumontite is white to pale green to light pink and is softer than the unaltered rock. White laumontite can be indicative of either dehydration of laumontite after its precipitation or a pure sample of the mineral (REF). It is unknown if the white samples observed and collected from the core are representative of a pure mineral or from dehydration. The core has been warehoused for 20 years and either reason could explain the color. Impurities likely explain color variations in the laumontite.

Of note is the near absence of clay signals or patterns in the XRD analysis and thin section analyses. Clay minerals were not readily identified during logging of the drill core and the lack of clay minerals may be the result of several processes.

1. Little clay in the sampled rocks because conditions did not favor its formation.
2. Any clay present in the fault zones was washed away with the drilling fluid during coring.
3. None of the fault cores as defined by Chester et al. (1993) were cored, and clay minerals are not typically present outside of the fault cores.
4. Clays were continually being removed from the fault systems because of high fluid flow within the rock.

2-3.4.2. X-Ray Fluorescence

X-ray fluorescence (XRF) analysis was performed on 19 samples across five fault zones and protolith from various depths in the core. Principal component analysis (PCA) was performed on all of the samples and an eigenvector method was used to reduce the data on all oxides and loss of ignition (LOI) to identify the significant variables for each that have the most weight in defining the geochemistry of the sample. The longer the length of the eigenvector after the PCA analysis, the more important the variable is in defining the composition of the sample (Appendix G). After PCA was conducted, plots were made of all of the variables with respect to the damage zone. Emphasis was placed on the significant variable identified from the PCA. These plots show the geochemical differences between undeformed rock and damage zone rock.

The whole-rock geochemical data are percentages of a total sum, which comprise a closed data set. This means that if one variable changes, the others must change, even if the absolute abundances are no different. To correct this, a log 10 transformation was performed on the data to convert it to an open data set. The data were also centered and standardized prior to conducting the PCA. After the PCA, the results were plotted and more that 70 % of the variation of each of the fault zones can be represented on two axes of the plot (Figure 2-29).

PCA was performed on all 19 samples and it was determined that SrO, Na_2O, BaO and K_2O are significant in defining the Cajon Pass core fault zones whole-rock geochemistry. Comparison of all oxides with emphasis on the significant variables in the protolith and damage zone rock was used to examine changes and differences in the damage zone rock and the protolith.

Damage zone rocks and undeformed host rock were collected from four faults in the core. For all of the faults two samples were collected: a damage zone sample and a host rock sample. These two samples were used to compare the variable changes (oxides) from undamaged host rock to damage zone rock.

1499 – 1501 m

Comparisons of weight percent of oxides in the damage zone and protolith reveal that Al_2O3, Fe2O3, MaO, MgO, and Na_2O show the largest depletion in the damage zone, as do all of the other oxides with the exception of K_2O and SiO_2 (Figure 2-30). The increase in K_2O can be explained by the creation of phlogopite. The increase in SiO_2 may be due to a slight increase in the quartz content of the damage zone as result of fluid interaction. The decrease in all other oxides may be due to the transport of soluble elements out of the damage zone.

2232 – 2252 m

XRF results from this fault zone show an increase in Al_2O_3, Fe_2O_3, MaO, MgO, and Na_2O as well as all of the other oxides except SiO_2 and LOI (Figure 2-31). The slight decrease of SiO_2 may be related to fluid transporting it out of the damage zone. The enrichment of K_2O can be attributed to the alteration of feldspar of phlogopite, where as the increase in Al_2O_3, Fe_2O_3, MaO, MgO, and Na_2O is the result of the formation of albite and the presence of magnesiohornblende in the damage zone rock.

2317 – 2350 m

Comparisons of weight percent of oxides in the damage zone and protolith reveal that there is very little change in the geochemistry between the two. The damage zone is

marked by a slight decrease in all oxides (Figure 2-32), with the exception of K_2O. The increase in K_2O may be due the alteration of feldspars. The similarity of the two samples suggests that the samples were collected outside of the damage zone and are not representative of faulting at depth.

2852 – 2853 m

The whole rock chemical analysis shows an increase in Fe_2O_3, CaO, K_2O, and MgO, a significant decrease in Na_2O, and a slight decrease in all other oxides (Figure 2-33). The increase in Fe_2O_3, CaO, MgO, and K_2O is most likely due to the presence of fluorannite, laumontite, and nontronite. The decrease in Na_2O may be due to the dissolution of albite. The remaining oxides and LOI show little variation from protolith to damage zone.

2-3.5. Relationship Between Faults in the Core and Wireline Log Data

Wireline log data was used to aid the interpretation of faults identified from the core analysis Figure 2-34. Relating the log data to the core is difficult because of the small size and small offset of the newly identified faults as well as the sampling set of the logging tools, specifically in regards to the shear (Vs) and compressional (Vp) logs. Typically, larger fault zones mostly identified by previous workers (Barton and Zoback, 1992; Blenkinsop and Sibson, 1992; Vernik and Zoback, 1992) were marked by drastic increases in Vs and Vp values, though this is not consistent (Table 2-2). Correlations are also present between the fracture distribution and fracture aperture logs and fault zones. The largest fault zones as determined by wireine log data are at 2439-2526 m and 3180-

3204 m depths have the largest fracture aperture. This is likely due to the collapsing of the sidewall because of lack of rock competency. Fracture frequency tends to increase in the vicinity of most fault zones. Similarly, the larger fault zones do not show a high fracture frequency because of sidewall collapse. A few of the newly identified faults also had measurable fault and damage zone thicknesses.

2-3.6. Field Studies of the Cajon Pass Rock and Exhumed Faults in the Western San Bernardino Mountains

Rocks and outcrops from the Cajon Pass were examined and sampled to use as a comparison to fault rocks from the Cajon Pass core itself. Field reconnaissance and data collection was conducted in the area of Cajon Pass, with emphasis on the Cleghorn fault and the Cleghorn fault zone. This fault is of interest because of its proximity to the borehole, its length and its dip toward the borehole. Previous samples from the Powell Canyon fault were also examined Jacobs (2005).

Fieldwork in Cleghorn Mountain, and Cleghorn Pass was chosen because they are west of the westernmost border of the Cleghorn fault that was examined by Jacobs (2005). Mapping the fault westward toward the borehole would allow for a better correlation and comparison of fault rocks at depth from the core. Unfortunately, the lack of access and the danger resulting from widespread wildfires in October 2007 limited field work and sample collection in the area.

Samples were collected from a small thrust fault on the north side of Cleghorn Mountain. This small fault branches off the area around the Cleghorn fault to the Powell Canyon fault. The fault is in a pink to buff to white granodiorite containing quartz,

feldspar, biotite, and hornblende. The rock is mostly white but transitions to a pink-buff tone in the vicinity of the fault. The fracture distribution appears to increase in the pinker rocks, though this varies. There are two faults in this area: one vertical and one dip slip horizontal fault (Figure 2-35).

2-3.6.1 Microstructure analysis

Of the five thin sections cut from the outcrops of fault areas exposed in the Cajon Pass area for this study, only one has microstructural damage. In thin section, the rocks are surprisingly undeformed, unfoliated, and intact. One sample that was collected from the area of the fault core contains some mode I fractures with laumontite fill and many open mode I fractures. The laumontite filled mode I fractures are very similar in appearance to the ones observed throughout the core at depth. The remaining samples contain only mode I fractures despite their proximity to the fault zones. The high density of open fractures suggests limited fluid-rock interaction in this system. It may also suggest that the fault is acting as a conduit to flow, and that precipitation of laumontite is only occurring within the fault core areas. If fluid were interacting with the host rock, and not the damage zone, one would expect more laumontite growth in the fractures away from the fault core and none within the fault core.

2-4. Discussion

2-4.1. Fracture Distribution in the Core

Previous work on the mesoscopic fractures is primarily restricted to Barton and Zoback (1992). Their study was focused on fracture orientation data gathered using a borehole televiewer. The fracture data was statistically analyzed and compared with more

limited studies of fractures in the core Vernik and Nur (1992), Vincent and Ehlig (1988), Wang and Sun (1990), Blenkinsop and Sibson (1992), and Blenkinsop (1990).

This study's fracture results (n=329) are in general agreement with Barton and Zoback (1992), (n=~5000) despite a large difference in the amount of data points. Based on the data collected by this study in addition to data from Barton and Zoback (1992), Vernik and Nur (1992), Vincent and Ehlig (1988), Wang and Sun (1990), Blenkinsop and Sibson (1992), and Blenkinsop (1990), the fracture density increases with proximity to fault zones, with larger fault zones at 2,500 m having the highest fracture distribution. Our data (Figure 2-36, Figure 2-37) and that of Barton and Zoback (1992) show similar evidence to this. Despite that fracture intensity is spatially related to fault locations, histograms of faults versus depth show that fault frequency statistically increases with depth as well as apparent aperture of fractures. Though more faults may be located at depth, the size of the faults vary and not all fractures are fault related, thus explaining why fractures have a different distribution than faults.

2-4.2. Distribution of Faults in the Core

For the total population, fault frequency increases with depth plus a marked low at ~2000 m (Figure 2-38). Though the fault cores and damage zones vary in thickness; the three largest fault zones are located at 2,500, 3,200, and 3,400 m depth. Faults with dips of 50°-90° are the most common with a mode of 70° ± 5° (Figure 2-38b).

There is no dominant dip of faults observed in the core, nor is there any significant change of fault dip versus depth. Of the 21 faults captured in coring, only 12 had good recovery and measurable dip. The other faults were identified from the high

density of damage and loss of competence of the core. Dips ranged from shallowly dipping (0-15°) to 90°. There does appear to be a slight increase in the dip of faults in the deepest sections of the core, but overall trends are not discernible.

2-4.3. Overall Trends and Distribution of Damage in the Core

We compared the distributions of fractures and faults from the core, to show whether the fracture positions in the core correlates to the vicinity of faults and fault zones. More fractures populate the area surrounding faults and fault zones. The frequency of faulting increases with depth, as discussed above, but fracture density does not necessarily increase with depth. This is due to the variation in size of the faults captured by the core and borehole and the presence of fractures likely not related to faulting. There may also be an anticorrelation of faults and fractures in areas, particularly near 2400 m depth. This area has a high fracture density, but is an area of few faults. Perhaps fractures evolve into faults and thereby reduce their frequency. The sizes of the faults do not appear to be depth dependent (Figure 2-38).

The types and styles of structures do not have any discernable trend throughout the core. Both meso- and microstructures of similar styles are observed throughout. The scales of these structures vary by location, but in general the density of larger structures coincides with fault zone locations. Fracture fill and alteration does not appear to have any variation with respect to depth. The predominant alteration mineral is laumontite, as discussed above and below. The dip of these structures varies from 30° to 60°. Steep and low angle fractures and faults are observed, with the majority of the faults having a similar dip, and the fractures display a wide rage of dips. Most notable are sets of vertical

to near vertical fractures, with a laumontite fill in many of the cores. These fractures are likely not related to faulting.

2-4.4. Correlating Faults in the Core with Faults on the Surface

Attempts to correlate newly identified fault zones observed in the borehole and the core with faults mapped on the surface have been unsuccessful. The unoriented core does not allow for the projection of any measured fault dip because of the unknown strike. Likewise, the borehole logging data has a considerable amount of variance with its correlation between fracture dip and strike. Furthermore, no new faults identified by this study are likely to have a mappable surface trace based on their small size. Larger fault zones identified previously and located at 2500 m, 3200 m, and 3400 m are the largest fault zones intersected by the borehole, and are the best candidates for surface correlation.

Though 37 faults of varying size and at varying depths were intersected by the borehole, the likelihood of all of them being exposed or having traces at the surface is small. Many of the faults captured are thin, but several larger faults are candidates. We attempted to correlate all of the observed faults with the surface despite the high uncertainty that all of the faults would have surface expressions. These attempted correlations assume a planar fault surface. Larger faults identified by wireline log data may also correlate with surface traces, but lack of core make confident correlation impossible. Barton and Zoback (1992) approximated the orientations of all major fault zones from depths 1,750-3460 m and determined that they strike NNW, dipping to the west.

Fault correlations and extrapolations to the surface were conducted using right triangle geometry. The equation used is:

$$\tan \theta \bullet \text{adjacent} = \text{radius}.$$

Theta is determined with the equation:

$$180° - (\text{dip of fault} + 90°)$$

This equation is used because the radius was can then be projected from the location of the borehole to determine possible surface locations of faults observed at depth. The method assumes that topography in the immediate area of the borehole is flat, and that there is no variation in dip along the fault.

Of all of the faults, the fault zone at 3200 m depth has is the most likely to correlate to a surface fault (Figure 2-39). The cored fault dips approximately 75°, (Figure 2-40) and projects upward to the nearby left lateral strike-slip Cleghorn fault. The surface trace of the Cleghorn fault has a dip that ranges from 70° to vertical (Meisling, 1984) and is located approximately 1.5 km away from the borehole. The trace of the Cleghorn fault is concealed in this location, and thus approximate, and the associated error with it and changes in dip degree at depth allow for this correlation to be acceptable.

2-4.5. Stress Measurements

Stress measurements from the borehole at 3398 m, approximately 4 m above the fault zone at 3400 m, have a horizontal maximum stress orientation of 127 ± 21° degrees (Shamir and Zoback, 1992) and the average stress orientation for the borehole from 1750 to 3460 m depth is 57 ± 19°. Both of these measurements are based on orientation and distribution of borehole breakouts (Shamir and Zoback, 1992). The overall average of

maximum horizontal stress in the borehole provides a left-lateral sense of strike-slip movement on a northwest striking fault, but at a slightly higher angle (60°) than what is predicted in Anderson theory of mechanics (30°). This is in general agreement with the predicted maximum horizontal stress for the left-lateral, northwest striking Cleghorn fault (Figure 2-2). The influence and implications of the Cleghorn fault on stress magnitude and orientation measurements has been discussed in detail by Zoback and Healy (1992), Scholz and Saucier (1993), and Scholz (2000).

The 127 ± 21° stress orientation measurement in the immediate vicinity of the fault at 3402 m is puzzling but occurs in 3 of 14 stress measurements (Figure 2-34). This measurement is anomalous in comparison to the other 17 measurements from the entire borehole breakouts by Shamir and Zoback (1992). This particular orientation plots at a low angle to both the trace San Andreas and Cleghorn faults and displays a right-lateral strike movement (Figure 2-34). Perhaps this orientation is due to the proximity to nearby faults or the rocks in the area highly damaged in sections that there are too many faults resulting in stress variations.

The data presented in this study has implications for previous interpretations of the orientations of σ_{Hmax} along the San Andreas Fault in southern California. One of the main conclusions of the Cajon Pass Project was the interpretation of a weak San Andreas Fault based on σ_{Hmax} oriented normal to the trace of the fault Zoback and Healy (1992). This interpretation has been controversial. Scholz and Saucier (1993) and Scholz (2000) argue that the stress orientations measured in the Cajon Pass borehole are really reflective of a stress reorientation around the Cleghorn fault, and thus do not accurately represent the stress around the SAF. Focal mechanisms have also been interpreted (Hardebeck and

Hauksson, 1999) to show σ_{Hmax} at an intermediate angle (30°-60°) in southern California, contrary to conclusions by Zoback and Healy (1992).

2-4.6. Microstructure Analysis

Microstructures observed in the core are generally similar to fractures, microcracks, cataclasis, and veins described by Blenkinsop and Sibson (1992) and James and Silver (1988) and fault related rocks investigated by Vernik and Nur (1992). Blenkinsop and Sibson (1992) however concluded that microstructures do not show obvious evidence for repeated stress or strain cycling, but some thin sections examined here in the vicinity of fault zones clearly show otherwise. Some thin sections show evidence for up to five different episodes of deformation as well as distinguishable relative ages (Figure 2-18). Distinguishable and different deformation episodes in thin section often include dilatant texture formed from the *in situ* alteration of plagioclase feldspar grains, fracture grains and microcracks, grain-size reduction from shear movement, with the smallest grain size concentrated in the center of any fracture of shear zone, the presence of cataclasite and ultracataclasite, localized slip concentrated on surfaces either in the center or on the edges of shear fractures, and developed gouge zones. Apparent chemical alteration from the introduction of fluids is also observed as evidence by the presence of large growth laumontite and calcite grains as well as replacement of albite into laumontite.

Blenkinsop and Sibson's (1992) conclusions and descriptions are observed in this study in core samples both away from and near fault zones, and likely record crustal deformation associated with uplift of the area as described by Silver and James (1988)

and Meisling and Weldon (1989). Likewise, Blenkinsop and Sibson only examined thin section from the oriented section of the core from 521 to 1744 m depth, as well as at depths of 1897, 2244, and 2799 m. Vernik and Nur's (1992) descriptions of laumontite protocataclasite dominated fault-related rocks are also present throughout, but their description and interpretations lack relative age identifications.

2-4.7. Significance of Laumontite in Fault Zones and Damage Zones in the Core

The ubiquitous laumontite and the lack of clay minerals (<5%) within the core is significant for several reasons. The presence of laumontite indicates a moderate to high temperature fluid in the system 90°C-250°C (James and Silver, 1988; Vincent and Ehlig, 1988; Blenkinsop, 1990; Blenkinsop and Sibson, 1992). Because nearly 100% of the structures throughout the core have laumontite fill in them, warm fluids were most likely present throughout the deformational history of the core at all the depths. Perhaps elevated pore fluid pressure created the mode I fractures observed throughout the core (Blenkinsop and Sibson, 1992).

For the upper 2.4 km of core, James and Silver (1988) determined a zonation of laumontite from 600 to 1885 m and 2080 to 2524 m depth and stilbite from 1885 to 2080 m depth, but used a limited sample set. XRD analysis from this study does not support their conclusion. XRD results from this study (Table 2-3) from the entire core as well as from 1885-2080 m depth show laumontite as the predominant zeolite, with stilbite recognized in only one sample.

James and Silver (1988) conclude, in part based on field work by Vincent and Ehlig (1987, 1988), that the San Andreas Fault in the Cajon Pass may act as a locus to

zeolitization. The identification of laumontite in samples from the San Bernardino Mountains (Jacobs, 2005; this study) and the conclusion of this study that most of the faults in the Cajon Pass core are likely northeast of the Cleghorn fault and in its hanging wall suggests that the San Andreas Fault and perhaps the Cleghorn fault are controlling the zonation and precipitation of laumontite, and may also control fluid flow in the Cajon Pass area. Locally, within the core, faults and fractures are likely controlling the geometry and extent of laumontite. The relative weakness of laumonite (hardness = 3.5-4) combined with possible continuous deformation in the Cajon Pass may be responsible for the creation of the laumonite matrix observed in many of the thin sections.

2-4.8. Adding to the Total Vertical Column of Damage in the Cajon Pass

The location of the Cajon Pass borehole is ideal for analyzing and comparing nearby faults and fault rocks in the San Bernardino Mountains at different crustal levels. This analysis and characterization effectively increases the total vertical column of damaged fault rock in the area from the surface to approximately 4.5 km depth. The depth is derived from the addition of the total depth of the Cajon Pass borehole plus the maximum elevation range over which fault rocks of the Cleghorn fault are exposed in the San Bernardino Mountains. Constructing a vertical column such as this allows for a more complete characterization of the changes of fault and off fault damage along major strike-slip faults. Faults and fault rock descriptions similar to this study have been documented by Jacobs (2005), Anderson et al., (1983), and Weldon (1986) in the San Bernardino Mountains.

The Cleghorn fault is of particular interest because of its size and proximity to the CPDDH. The fault was examined in detail by Jabobs (2005) in the area of Cleghorn Mountain and extending east past Silverwood Lake (Figure 2-41). Jacobs' (2005) thin sections of the Cleghorn fault damage zone are characterized by shattered grains in a clay-rich microbreccia matrix and by many fractures, some with calcite and microbreccia fill. Veins in the area display evidence of multiple episodes of fluid interaction. XRD analyses from rocks along the Cleghorn fault are characterized by albite, orthoclase and microcline, with clays consisting of kaolinite, palygorskite, and montmorillonite.

Clays are more abundant in samples collected from fault exposures in the San Bernardino Mountains than from samples from of core. Thin sections from the San Bernardino Mountains are characterized by similar structures regardless of their locations. Other faults in the western San Bernardino Mountains examined by Jacobs (2005) include the Eastwood, Crass Valley, and Powell Canyon faults as well as some unnamed faults in the area. XRD analyses of these other faults have strong laumontite signatures, are in similar host lihologies, and all have similar microstructural deformation.

Regardless of location in the 4.5 km depth column, microdeformational styles and XRD signatures of fault zones are similar. Clays are more predominant in faults sampled at the surface in the San Bernardino Mountains (the upper 1 km of the column), and may be indicative of clay stability at varying depths. At shallower depths, lower pressures, and lower temperatures, with little fluid present, clay alteration is expected to be more abundant. Oppositely, at greater depths and higher temperatures clays are less stable. With the addition of a fluid, laumontite not only is precipitated in mode I fractures but

also in fault planes. In contrast to studies of clay rich strike-slip faults by Evans et al. (1997), Caine et al. (1996), and Chester and Logan (1987), we document that clays are nearly absent in the Cajon Pass core. Therefore deformation and faulting in the Cajon Pass core likely formed at high temperature and greater depths than the faults studied by Evans et al. (1997), Caine et al. (1996), and Chester and Logan (1987).

Thermochronologic evidence for < 2 km of uplift of the San Bernardino Mountains since 18 Ma support of this hypothesis (Spotila et al., 2002; Blythe et al., 2002). We thus infer that before 12 Ma, and before uplift and erosion of the San Bernardino Mountains, faulting in the upper 2-3 km of crust created clay-rich fault zones. Uplift, and erosion of the San Bernardino Mountains after 12 Ma commenced at a rate of less than or equal to 0.09 km/Ma (Blythe et al., 2002). Uplift continued along with faulting, exhumation, and erosion continued. Clay rich faults and damage zone rock previously at shallow (~ < 1km) depths in the Cajon Pass were eroded away, whereas clay rich faults in the San Bernardino Mountains were better preserved. The faults remaining in the Cajon Pass at depth have mostly laumontite mineralogy's are preserved and are record of faults originating at a greater depth.

2-4.9. What is the Primary Control of Damage in the Cajon Pass Core?

Three models are proposed here for the source of damage observed in the Cajon Pass core. Two major strike-slip faults in the area of the borehole may be controlling damage observed in the core. The right lateral San Andreas Fault, 4 km away, as well as the left-lateral Cleghorn fault, approximately 1 km away, may have produced the damage within the borehole and core. Three models are presented:

1. The Cleghorn fault is the main control of damage.
2. The San Andreas Fault is the main control of damage.
3. A combination of both the San Andreas and Cleghorn faults are controlling damage in the core.

Based on the structural analysis of the core and the incorporation of the wireline log data, we propose Model 1 as the most reasonable model. The 70° dip of the major fault zone at 3402 m depth projects almost perfectly to the surface trace of the 70-90° dipping Cleghorn fault. The extensive damage around the fault at this depth also supports the interpretation.

Model 3 is also realistic, given the possible low dip of the SAF. It is not unreasonable to think the San Andrea fault, being the largest structure in the area, plays an important role in the formation of damage in the Cajon Pass. Uncertainties with Model 2, particularly the actual dip of the San Andreas Fault in the area, leads to a low confidence level, and thus this model is less likely.

The core contacts 3 to 4 about 500 m to 1200 m thick packages of similar rocks (assemblages1-4). 2 and 3 may be linked and consists of gneissic granites and migmatitic gnessic granites 1 are sandstone, 4 is the most heterogeneous. If the SAF cuts the borehole, San Gabriel Mountains basement would be present below the fault in the core. The San Gabriel basement has abundant tonalite where as the San Bernardino mountains do not (Morton and Miller; 2003, Morton and Miller, 2006). Also, the Pelona schist is diagnostic of the San Gabriel fault block. None of these distinctive lithologies are present in the Cajon Pass borehole (Figure 2-7). Thus we conclude that all the rocks are from the

San Bernardino Mountain block and are northeast of and above the SAF. This eliminates the possibility of a dip of less than 45°for the SAF in this region.

2-4.10. Faults at Depth and Correlations with the Fuis Hypothesis

Recent work by Fuis et al. (2007, 2008) has challenged the notion that the San Andreas Fault is a vertical or near vertical fault, but rather has variation in dip and dip direction, creating a propeller like shape (Figure 2-42). Using gravity, magnetic, seismic data, microseismic data, and seismic imaging, Fuis et al. (2007, 2008) have determined dip, dip direction, and maximum depth constraint in km for the San Andreas Fault in southern California. Based on their studies, the SAF could be dipping as shallowly as 37° beneath the Cajon Pass area to the northeast, though the dip may be conservatively closer to approximately 45° (V. Langenheim, personal communication, 2007). A magnetic anomaly in the Cajon Pass is interpreted by Fuis et al. (2007, 2008) as the result of a large dipping fault (SAF). If so magnetic anomaly modeling suggests a fault dip in this location of about 37° (Figure 2-42).

We present a range of hypotheses for these results (Figure 2-43). Four cross sections perpendicular to the SAF and Cleghorn fault and intersect the CPDDH (Figure 2-43). The cross sections show the SAF dipping 90°, 60°, 45°, 37° and in the direction of the borehole, as well as the spatial relationship between the two. If the fault dips 45° or less, it is possible that the damaged rock from the bottom of the borehole could be SAF related fault rock. The three models presented here do not take into account the geometry of the nearby Cleghorn fault and its relationship to the borehole. The Cleghorn fault is discussed in more detail in section 2-4.9.

The implications of a shallowly dipping fault are far reaching in the geologic and geophysical community. If indeed the SAF is determined to have an approximate 45° dip as described above, the interpretations of stress measurements would have to be reexamined to account for the structure. Presently accepted measurements and interpretations are based on a vertical or nearly vertical dipping San Andreas Fault (Zoback and Healy, 1992; Shamir and Zoback, 1992), but with a shallow fault, interpretations will change. Also, seismic hazard analysis would have to be reevaluated for possible shaking scenarios for the densely populated area of southern California.

Other implications for the shallowly dipping San Andreas Fault are the interpretation of stress orientations along the fault. As stated in the Stress Measurments section, various interpretations have been suggested for stress data along the San Andreas Fault. Focal mechanisms used by Hardebeck and Hauksson (1999), and Hardebeck and Michael (2004) interpreted as σ_{Hmax} having an intermediated angle. If this interpretation is correct, then there is little stress paradox.

Stress orientation interpretations by Zoback and Healy (1992) and Scholz (2000, 2006), do not support or consider a dipping San Andreas Fault. Scholz interprets the σ_{Hmax} orientation is reflective of the Cleghorn fault, and thus accurate. On the other hand, Zoback and Healy interpret the σ_{Hmax} orientations as a weak fault.

2-5. Conclusions

Based on the structural analysis conducted on the crystalline core from the Cajon Pass, 11 new faults were identified in the Cajon Pass Core. By combining the detailed analysis of the core with wireline log data and previously published core analysis, an

organized and complete distribution of deformation in the core as well as the borehole can be determined. The majority of the faults captured by the core are small (~9 m thick average of fault and damage zone), and contain laumontite precipitation and alteration. The faults range in dip, have a small fault core, and uncertian offset. This is due to the limited core available as well as the small sample size.

The answers to the questions posed at the start of this study:

1. Deformation varies complexly with respect to depth or fault zones. Styles, geochemical features of fault zone, and microscopic features do not vary with respect to depth or to fault zones. The extent of deformation varies within the core, and is controlled by the size of the fault zones intersected by the core. The frequency of faults in the core increases 5-fold with depth, and fractures within the core have greater populations around fault zones, however, statistically, the fracture density does not increase in depth because of the presence of non-fault related fractures. This may be due to the variation in the size of the fault zones, with larger fault zones having a higher and wider fracture density than smaller ones or fault zones forming out of fractures. Another potential reason for this is that some faults could be inactive dip slip faults from older deformational events with some later strike-slip reactivation, thus increasing the fracture density in areas.
2. We propose that the fault zone intersected by the core at 3402 m (Figure 2-44) directly correlates with the nearby left-lateral strike-slip Cleghorn fault. The Cleghorn fault dips approximately 70 –90° to the northeast and is located approximately 1 km to the west of the borehole. The range of dip, combined with

the concealed nature of the fault, allow for a reasonable projection. This correlation suggests that all but the lower ~ 100m of the borehole are in the hanging wall of the Cleghorn fault and therefore separated from the SAF by a major active fault. The Cleghorn fault probably produced the fault rock in the lower 250-300 m of the borehole (Figure 2-44).

3. Microstructures in these fault zones primarily include shear fractures containing a matrix of laumontite with angular to sub-angular clasts within the matrix. Sense and amount of movement is not always discernable, but the microstructures in the vicinity of the fault zones may record evidence of seismic stress cycles. Evidence for this includes their damage zone alteration, style and types of fracture fillings, and textures. Intense microstructural damage, grain size reduction, fractured and cracked grains, and secondary mineral precipitation characterizes these damage zones. Samples in other parts of the core are more likely created by distributed crustal deformation occurring around the pass, such as the antiforms being created in the area (Weldon, 1986); though at some depths, the core in undeformed. Predominant laumontite minerals in the fault and damage zones are indicative of moderate to high temperature fluid interacting with the rocks. The small size of the faults observed as well as the laumontite signature can be interpreted as fluid interaction occurring as faults are rupturing or shortly thereafter. Fracture fills, both in and out of the damage zones, also predominantly return laumontite signatures. Therefore, the fluid column throughout the core, with the exceptions of some depths, has relatively low salinity, is alkaline, and Na-SO_4 type (Kharaka et al. 1988) and is within the temperature range to precipitate laumontite after an

increase in pore space following deformation. It is not known if fluid pressure is propagating fracture growth, but Blenkinsop and Sibson (1992) suggest that pore fluid pressure probably remained above hydrostatic pressure, and thus aided in the propagation of extensional fractures.

4. Comparisons of faults at depth with faults examined by Jacobs (2005) in the San Bernardino Mountains show that faults at depth within the core are predominantly laumontite, whereas faults examined at the surface in the San Bernardino Mountains contain more clays than laumontite. Microstructural deformation styles are similar regardless of the amount of clay present. The variation in laumontite content is hypothesized to be due to a combination of differences in water-rock interaction, lack of stability of clay at deeper crustal levels, and the considerable uplift and weathering of the San Bernardino Mountains as described by Spotila et al., 2002 and Blythe et al., 2002. Also, uplift is required to explain the lack of clay in fault zones and dominance of laumontite from 500 m to 3500 m.
5. Data presented here were used to test the Fuis hypothesis (2007, 2008) of a gently to moderately dipping San Andreas Fault in the area of the Cajon Pass. The data do not preclude a northeast dipping SAF, but appear to rule out a dip less than 45° because there are no demonstrable rock types from southwest of the SAF in the core. Furthermore, the dip of the Cleghorn fault and dip of a major fault at 3402 m depth matches within error and projects towards one another.
6. Two nearby faults, the San Andreas and the Cleghorn faults, are the two most suspect to controlling the damage observed at depth in the core. Examination of the physical damage in the core, wireline log data, and models of dipping faults

presented by Fuis et al. (2007, 2008) allow for a robust interpretation of the source of damage in the core. The results of this work indicate that the Cleghorn fault may be the main source of damage seen in the core, and that a fault zone captured in a spot core at 3402 m is likely a major strand of the Cleghorn fault. Subsequently, stress measurement interpretations from deep within the borehole are likely to reflect stresses around the Cleghorn fault.

References

Anderson, E.M., 1905, The dynamics of faulting: Transactions of the Edinburgh Geological Society, no. 8, p. 387-402.

Anderson, E.M., 1951, The dynamics of faulting and dyke formation with applications to Britain: Oliver and Boyd, Edinburgh.

Anderson, J. L., R. H. Osborne, and Palmer, D.F., 1983, Cataclastic rocks of the San Gabriel fault – an expression of deformation at deeper crustal levels in the San Andreas fault zone: Tectonophysics, v. 98, p. 209-251.

Anderson, R.N., Broglia, C., Pezard, P.A., and Williams, C.F. 1988a, Lithostratigraphy Determined from Discriminate Analysis of Geochemical Well Logs from the Cajon Pass Scientific Drillhole, California: Geophysical Research Letters, v. 15, no. 9, p. 957-960.

Anderson, R. N., Dove, R. Silver, L. James, E. and Chappell, B. 1988b, Elemental and Mineralogical Analyses Using Geochemical Logs from the Cajon Pass Scientific Drillhole, California, and their Preliminary Comparison with Core Analyses: Geophysical Research Letters, v. 15, p. 969–973.

Atwater, T., and Molnar, P., 1973, Relative motion of the Pacific and North American plates deduced from sea-floor spreading in the Atlantic, Indian, and South Pacific Oceans, *in* Kocvach, R.L., and Nur, A., eds., Proceedings of the conference on tectonic problems of the San Andreas fault system: Stanford, California., Stanford University Publications in the Geological Sciences, v. 13, p. 136-148.

Barth, A.P., and Dorais, M.J., 2000, Magmatic anhydrite in granitic rocks: first occurrence and potential petrologic consequences: American Mineralogist, v. 85, p.430-435.

Barton, C.A., and Zoback, M.D., 1992, Self-similar distribution and properties of macroscopic fractures at depth in crystalline rock in the Cajon Pass scientific drill hole: Journal of Geophysical Research, v. 97, no. B4, p.5181-5200.

Blackbourn, G.A., 1990, Cores and Core Logging for Geologists: Whittles Publishing Limited, Scotland, UK, 113 p.

Blenkinsop, T.G., 1990, Correlation of paleotectonic fracture and microfracture orientations in cores with seismic anisotrophy at Cajon Pass drill hole, southern California: Journal of Geophysical Research, v. 95, no. B7, p. 11143-11150.

Blenkinsop, T.G., and Sibson, R.H., 1992, Aseismic Fracturing and Cataclasis Involving Reaction Softening Within Core Material From the Cajon Pass Drill Hole: Journal of Geophysical Research, v. 97, no. B4, p. 5135-5143.

Boles, J.R., and Coombs, D.S., 1977. Zeolite facies alteration of sandstone in the Southland syncline, New Zealand, American Journal of Science, v. 77, p. 982-1012.

Blythe, A.E., House, M.A., and Spotila, J.A., 2002, Low-temperature thermochronology of the San Gabriel and San Bernardino Mountains, southern California: constructing structural evolution, in Barth, A., ed., Contribution to crustal evolution of the southwestern United States: Boulder, Colorado, Geological Society of America Special Paper 365, p. 231-250.

Caine, J.S., Evans, J.P., and Forster, C.B., 1996, Fault zone architecture and permeability structure: Geology, v. 24, no. 11, p. 1025-1028.

Chester, F.M., Evans, J.P., and Biegel, R.L., 1993, Internal structure and Weakening Mechanisms of the San Andreas Fault: Journal of Geophysical Research, v. 98, no. B1, p.771-786.

Chester, F.M., and Logan, J.M., 1987, Composite Planar Fabric of Gouge from the Punchbowl Fault, California: Journal of Structural Geology, no. 9, p. 621-634.

Dickinson, W.R., 1981, Plate tectonics and the continental margin of California, in Ernst, W.G., ed., The geotectonic development of California, (Ruby volume 1): Englewood Cliffs, N.J., Prentice-Hall, p. 1-28.

Evans, J.P., Forster, C.B., and Goddard, J.V., 1997, Permeability of fault-related rocks, and implications for hydraulic structure of fault zones: Journal of Structural Geology, v. 19, p. 1393-1404.

Fuiss, G.S, Scheirer, D.S., Langenheinm V.E., and Kohler, M.D., 2007, The San Andreas fault in southern California is almost nowhere vertical-implications for tectonics: Geological Society of America Abstracts with programs, v. 39, no. 6, p.279.

Fuiss, G.S., Scheirer, D.S., Langenhein, V.E., Kohler, M.D., 2008, The San Andreas Fault in southern California has a “propeller” shape-implications for tectonics and seismic hazard: Geological Society of America Abstracts with programs, v. 40, no. 6, p.326.

Ghobarker, H., and Schaf, O., 1998, Hydrothermal synthesis of laumontite, a zeolite: Microporous and Mesoporous Materials, v. 12, is. 1-2, p. 55-60.

Hardebeck, J.L., and Hauksson, E., 1999, Role of fluid in faulting inferred from stress field signatures, Science, v. 285, p. 233-236.

Hardebeck, J.L., and Michael, A. J., 2004, Stress orientations at intermediate angles to the San Andreas fault, California: Journal of Geophysical Research, V. 109, no. 11, p. 11303.

Iwrin, W.P., 1990, Geology and plate-tectonic development, in Wallace, R.E., ed., The San Andreas fault system, California: USGS professional paper 1515, p. 61-81.

Jacobs, J.R., 2005, Examination of exhumed faults in the western San Bernardino Mountains, California: implications for fault growth and earthquake rupture. [m.s. thesis]: Logan, Utah State University, 226 p.

James, E.W., and Silver, L.T., 1988, Implications of Zeolites and their zonation in the Cajon Pass deep drillhole: Geophysical Research Letters, v. 15, no. 9, p. 973-976.

Kenney, M.D., 1999, Emplacement, Offset History, and Recent Uplift of Basement within the San Andreas Fault System, Northeast San Gabriel Mountains, [Ph.D. Dissertation]: Eugene, University of Oregon, 279 p.

Kharaka, Y.K., Ambats, G., Evans, W.C., and White, A.F., 1988, Geochemistry of water at Cajon Pass, California: preliminary results: Geophysical Research Letters, v. 15, no. 9, p. 1037-1040.

Kulander, B.R., Dean, S.L., and Ward, B.J., 1990, Fractured core analysis: interpretations, logging, and use of natural and induced fractures in core: The Association of American Petroleum Geologist Series, no. 8, The American Association of Petroleum Geologists, Tulsa, Oklahoma, 148 p.

Lachenbruch, A.H., and Sass, J.H., 1988, The stress heat-flow paradox and thermal results from Cajon Pass: Geophysical Research Letters, v. 15, no. 9, p. 981-984.

Meisling, K.E., 1984, Neotectonics of the north frontal fault system of the San Bernardino Mountains, southern Claifornia: Cajon Pass to Lucerne Valley, [Ph.D. Dissertation]: Pasadena, California Institute of Technology, 394 p.

Meisling, K.E., and Weldon, R.J., 1982, The late-Cenozoic structure and stratigraphy of the western San Bernardino Mountains, *in* Sadler, P.M., and Kooser, M.A., eds., Late Cenozoic stratigraphy and structure of the San Bernardino Mountains, field trip 6 of Cooper, J.D., compiler, Geologic excursions in the Transverse Ranges, southern California: Geological Society of America, Cordilleran Section, 78th Annual Meeting, Anaheim, California Volume and Guidebook, p. 75-82.

Meisling, K.E., and Weldon, R.J., 1989, Late Cenozoic tectonics of the northwestern San Bernardino Mountains, southern California: Geological Society of America Bulletin, v.101, no.1, p. 106-128.

Miller, M., and Weldon, R.J., 1992, A lateral ramp origin for the north trending segment of the Squaw Peak fault, Cajon Pass, California: Journal of Geophysical Research, v. 97, p. 5153-5165.

Morton, D.M. (compiler), and Miller, F.K., (compiler), 2003, Preliminary Geologic Map of the San Bernardino 30' x 60' quadrangle, California: U.S. Geological Survey Open-File report 03-293, scale 1:100 000, 5 sheets.

Morton, D.M., (compiler), and Miller, F.K., (compiler), 2006, Geologic map of the San Bernardino and Santa Ana 30' x 60' quadrangles, California: Geological Survey Open-File report 2006-1217, scale 1:100 000, 4 sheets, 200 p. text.

Pezard, P.A., Anderson R.N., Howard, J.J., Luthi, S.M., 1988, Fracture distribution and basement structure from measurements of electrical resistivity in the basement of the Cajon Pass scientific drillhole, California: Journal of Geophysical Research Letters, no. 15, p. 1021-1204.

Pezard, P.A., and Luthi, S.M., 1988, Borehole electrical images in the basement of the Cajon Pass scientific drillhole, California; fracture identification and tectonic implications: Journal of Geophysical Research Letters, no. 15, p. 1017-1020.

Pratson, E. L., Anderson, R. N., Dove, R. E., Lyle, M., Silver, L. T., James, E. W., and Chappell, B. W., 1992, Geochemical logging in the Cajon Pass drill hole and its application to a new, oxide, igneous rock classification scheme: Journal of Geophysical Research, v. 97 no. B4, p. 5167–5180.

Sass, J.H., Lachenbruch, A.H., Moses Jr., T.H., and Morgan, P., 1992, Heat flow from a scientific research well at Cajon Pass, California: Journal of Geophysical Research, v. 97, no. B4, p. 5017-5029.

Scholz, C.H., 2000, Evidence for a strong San Andreas fault: Geology, v. 28, no. 2, p. 163-166.

Scholz, C.H., 2006, The strength of the San Andreas fault; a critical analysis: Geophysical Monograph, no. 170, p. 301-311.

Scholz, C.H., and Saucier, F.J., 1993, What do the Cajon Pass stress measurements say about stress on the San Andreas fault?: Journal of Geophysical Research, v. 98, p.17867-17869.

Seal, E. and Barth, A., 2007, A determination of the origin of granitic rocks of the Cajon Pass scientific drill hole, San Bernardino Mountains, Ca: Abstracts with programs, Geological Society of America, v. 39, no. 6, p. 318.

Shamir, G., and Zoback, M.D., 1992, Stress orientation profile to 3.5 km depth near the San Andreas fault at Cajon Pass, California: Journal of Geophysical Research, v. 97, no. B4, p.5059-5080.

Silver, L.T., and James, E.W., 1988, Geologic Setting and Lithologic Column of the Cajon Pass Deep Drillhole: Geophysical Research Letters, v. 15, no. 9, p. 941-944.

Silver, L.T., James, E.W., and Chappell, B.W., 1988, Petrological and geochemical investigations at the Cajon Pass deep drillhole: Geophysical Research Letters, v. 15, no. 9, p. 961-964.

Spotila, J.A., House, M.A., Blythe, A.E., Niemi, N.A., and Bank, G.C., 2002, Controls on the erosion and geomorphic evolution of the San Bernardino and San Gabriel Mountains, southern California, in Barth, A., ed., Contribution to crustal evolution of the southwestern United States: Boulder, Colorado, Geological Society of America Special Paper 365, p. 205-230.

Turner, F.J., 1980, Metamorphic petrology, 2nd ed.: McGraw-Hill, New York, 524 p.

Vernik, L., and Nur, A., 1992, Petrophysical analysis of the Cajon Pass scientific well: implications for the fluid flow and seismic studies in the continental crust: Journal of Geophysical Research, v. 97, no. B4, p.5121-5134.

Vernik, L., and Zoback, M.D., 1992, Estimation of maximum horizontal principle stress magnitude from stress-induced well bore breakouts in the Cajon Pass scientific research borehole: Journal of Geophysical Research, v. 97, no. B4, p.5107-5119.

Vincent, M.W., and Ehlig, P.L., 1987, Laumontite mineralization in rocks exposed north of the San Andreas fault at Cajon Pass, California: EOS Transactions, v. 68, p. 1495.

Vincent, M.W., and Ehlig, P.L., 1988, Laumontite mineralization in rocks exposed north of the San Andreas fault at Cajon Pass, southern California: Geophysical Research Letters, v. 15, no. 9, p. 977-980.

Wang, C.Y., and Sun, Y., 1990, Oriented microfractures in Cajon Pass Drill Cores: Stress Field Near the San Andreas Fault: Journal of Geophysical Research, v. 95, no. B7, p. 11135-11142.

Weldon, R.J., 1986, The late Cenozoic geology of Cajon Pass: Implications for tectonics and sedimentation along the San Andreas fault [Pd.D. thesis]: Pasadena, California Institute of Technology, 400p.

Weldon, R.J., Fumal, Powers, T.J., Pezzopane, S.K., Scharer, K.M., and Hamilton, J.C., 2002, Structure and earthquake offsets on the San Andreas fault at the Wrightwood, California, paleoseismic site: Bulletin of the Seismological Society of America, v. 92, no. 7, p. 2704-2725.

Weldon, R.J., and Sieh, K.E., 1985, Holocene rate of slip and tentative recurrence interval for large earthquakes on the San Andreas fault, Cajon Pass, southern California: Geological Society of America Bulletin, v. 96, no. 6, p. 793-812.

Zen, E., and Thomposn, A.B., 1974, Low grade regional metamorphism: mineral equilibrium relations: Annual Review of Earth and Planetary Sciences, v. 2, p. 197-212.

Zoback, M.D., Silver, L.T., Henyey, T., and Thatcher, W., 1988, The Cajon Pass scientific drilling project: phase 1: Geophysical Research Letters, v. 15, no. 9, p. 933-936.

Zoback, M.D., and Lachenbruch, A.H., 1992, Introduction to special section on the Cajon Pass scientific drilling project: Journal of Geophysical Research, v. 97, no. B4, p. 4991-4994.

Zoback, M.D., and Healy, J.H, 1992, In situ stress measurements to 3.5 km depth in the Cajon Pass scientific research borehole: implications for the mechanics of crustal faulting: Journal of Geophysical Research, v. 97, no. B4, p. 5039-5058.

Table 2-1. Summary of all faults identified in the core.

Fault Depth Range (m)	Cored (Y/N)	Core, Segment	Rock Description and Type	Fault Description and Type	Fault Zone and Damage Zone Thickness (m)	Dip of Fault When Measurable From Core (°)	Figure Number	ID'd By Whom
500-515	Y	5,11	White to green to gray strongly foliated granodiorite. Core ranges from poorly to well preserved.	Zone of pale green cataclasite deformation, zone extends throughout the core. Most well developed fault zone dips 60°. Cataclasite anatomists throughout the core between more developed zones. Red and green slicks are on some of the chunks in bags.	15	60	Appendix H	V&N
530-540	N				10			S&J
690-710	Y	7,2	Weakly foliated augen granite. Augens are pink to orange and fractured.	Zone of pale green cataclasite deformation, zone extends throughout the core. Most well developed fault zone dips 45°, less developed zones is approx 30°. Cataclasite anastomoses throughout the core between more developed zones.	20	45	Appendix H	S&J
850	Y	11,1	Gray medium crystalline granite with pink kspar, and minor amounts of biotite.	Fault zone is in chunks, cannot measure dip			Appendix H	V&N
1138-1140	Y	15,4-3	Leucocratic granite gneiss with some large spar crystals areas are well foliated	All of fault zone is in a bag. Well defined fault zone with no real measurable damage zone	2		Figure 2-9	DHF
1290-1315	Y	16,1	Dark gray gneissic granite/pargneiss with web of 1mm thick zeolite filled fractures	Highly fractured zone, no fault or slip surface observed.	25		Appendix H	S&J
1354-1355	Y	17,5, 1	Black and white leucocratic granodiorite with a weak to moderate foliation. Core is intact.	Narrowly define fault, dipping moderately to steeply, contains 2 cm thick white to pale green zone, with a pink alteration halo. Poorly developed slip surface seen. Parts of fault are weak with a clay gouge (green surface). Dips approximately 75°	1	75	Figure 2-10	DHF
1425-1450	N				25			S&J
1499-1501	Y	18,1	Gray dioritic and amphibolitic gneiss, well to moderately foliated contains narrowly defined shear area	Small shear zone, cuts core almost horizontally, shear zone is green to red in color (epiodite and hematite), has some slicks observed on internal chunk of core. Cannot determine slip direction	2	0	Figure 2-12	DHF
1900-1906	Y	26,6,5,3,2	White to gray granite-granodiorite, transitions to dark gray granitic gneiss contains much zeolite (?) alteration and pink to buff feldspar growth. Rock is highly damaged	Zone of white to light gray zeolotic alteration, with damage surrounding zeolites. Many fractured grains, no offset seen, alteration zone is slight dipping.	6	30	Figure 2-14	DHF

1981-1982	Y	28,1,2,3	Gray granite to granodiorite, some faint foliations throughout	Well-defined small fault dipping 70°. Contains ~4mm thick gouge zone of chlorite and epidiote? Pink halo alteration surrounds the fault. Similar fault is observed.3 m deeper; slicks on both appear predominately dip slip.	1	70	Figre 2-16	DHF
2070-2080	Y	33,1	Gray to black highly alterated granodiorite. Moderately to well foliated, alters from fine to coarse crystalline	Highly altered rock, contains no clear fault or fault trace. Alteration is green to white in color and marks a drastic change in grains size. Bad recovery limits interpretation.	10	50	Figure 2-17	DHF
2110-2122	Y	34,1	Dark gray gneissic granodiorite to light gray to white leucocratic granite.	Bag of fault zone rock, unable to determine dip, or width, another small fault may be located ~ 2 feet above contains a poorly developed white zeolotic alteration	12	15	Figure 2-19	DHF
2130-2140	N				10			Prat.
2153-2186	N				33			Prat.
2203-2226	N				23			Prat.
2232-2252	Y	36,1	Dark gray to black fine crystalline gneiss with bands of granite gneiss. Highly fractured	Well-defined sear zone containing both a white chlorite to zeolite alteration fault as well as a greener epidote? Alteration zone 2.4 cm away. No offset set seen, and unable to tell fault type	20	70, 90	Figure 2-20	DHF
2260-2292	Y	37, 4	Gray and white moderately foliated gneissic granodiorite. Highly fractured zone, and filed zone	No fault seen, but highly fractured. Fractures are <1mm thick and contain a white zeolite fill.	32		Appendix H	V&N
2317-2350	Y	38,1,2	Leucocratic granite, poorly foliated, medium crystalline, some pink kspar porphyroclasts	No large fault seen, but highly fractured. Fractures are <1mm thick and contain a white zeolite fill.	33		Figure 2-22	DHF
2439-2526	N				87			Prat.
2546-2556	N				10			Prat.
2570-2580	N				10			V&N
2608-2616	Y	43,1	White to gray granodiorite, varying grain sizes due to deformation	Marked grain size reduction and pink laumontite alteration and zoning. 5 near horizontal shear zones and one dipping moderately	8	27, 10	Appendix H	V&N
2627-2656	Y	44,1	Black and white gneissic granodiorite. Highly fractured, with much of the core in bags.	Dipping green cataclasite zone with web like geometry. Red hematite slicks seen in bag with fault/damage rock that is not intact	29	54	Appendix H	V&N
2735-2755	Y	46,7	Gray granodiorite, medium crystalline, highly deformed	2 cm wide vertical to moderately dipping fault. 11.5 cm long. Contains a hematite quartz clay gouge, with strong foliations. Surrounding fault is green (epidote, chlorite) alterations mixed with more pink alteration. Smaller faults are also present in the core slice containing similar composition.	20	60, 90	Figure 2-24	DHF
2779-2807	Y	47,1	Gray medium crystalline granite with some open fractures	White fault? Zone with pink halo, no offset seen, but shear structures around it? Incomplete section of core, Lots of open horizontal fractures	28	65	Appendix H	B&Z

2852-2853	Y	48,2	Gray medium to coarse poorly foliated granodiorite. Highly fractured	No clear fault seen, rock is highly fractured, contains small zone of ~1 cm thick of zeolite. Alteration in a zone of fractures. Areas contain greenish and reddish alterations throughout. Epidote and hematite.	1		Figure 2-26	DHF
3100-3124	N				24			V&N
3136-3150	N				14			V&N
3162-3172	N				10			Prat.
3180-3204	Y	51,3	Black and white gneissic granodiorite with a weak to moderate foliation. Interbedded with finer crystalline more mafic gneiss. Coarse pink kspar crystals are present in area. Core in well damaged and not preserved well.	Core is poorly preserved. Some chucks contain a green to rusty red slip surface. Many chucks have web like pink laumontite alteration, and in areas, chunks have a pink hue to them.	24		Appendix H	V&N
3219-3241	N				22			Prat.
3336-3359	N				23			Prat.
3390-3400	N				10			V&N
3402-3415	Y	53,4	Black and white gneissic granodiorite with a weak to moderate foliation. Interbedded with finer crystalline more mafic gneiss. Coarse pink kspar crystals are present in area. Core in well damaged and not preserved well.	One fully intact core with large fault dipping at 75° separating pink and light green alteration. The remainder of the core contains webs of pink laumontite alteration, with some light green alteration. Both open and filled fractures are present in the area.	13	75	Figure 2-40	B&Z
3421.6	N				Unknown			Prat.
3440	N				Unknown			V&N

ID'd By Whom Key
DHF = This Study
B&Z = Barton and Zoback, 1992
V&N = Vernik and Nur, 1992
Prat = Pratson et al., 1992
S&J = Silver and James, 1988

Table 2-2. Table of all wireline log signatures in faults zones from 1800 to 3420 m depth. (+) = positive response; (-) = negative response; (none) = no response above background. See Figure 2-33 for locations.

Fault Depth Range (m)	Compressional Velocity (Vp)	Shear Velocity (Vs)	Porosity	Resistively	Gamma
1900-1906	+	+	+	None	+
1981-1982	None	None	None	+	+
2070-2080	-	-	+	+	+
2110-2122	-	-	+	+	+
2130-2140	None	None	None	-	None
2153-2186	-	-	-	+	None
2203-2226	+	+	+	None	None
2232-2252	-	None	None	None	None
2260-2292	+	+	+	+	+
2317-2350	+	+	+	+	None
2439-2526	+	+	+	+	None
2546-2556	-	None	+	+	None
2570-2580	+	+	None	+	-
2608-2616	None	None	None	+	None
2627-2656	None	None	None	+	None
2735-2755	-	None	+	None	None
2779-2807	-	-	+	+	None
2852-2853	None	None	None	None	None
3100-3124	None	None	None	None	+
3136-3150	None	None	None	None	+
3162-3172	+	+	+	+	+
3180-3204	-	+	+	+	+
3219-3241	-	None	+	+	+
3336-3359	None	None	None	-	+
3390-3400	+	None	None	None	None
3402-3415	None	None	None	-	None

Table 3-2. Summary of XRD results for all samples.

Sample Number	Core	Segment Number	Depth (m)	Main Minerals
1710	5	11	521.21	Quartz, Anorthite, Albite, Enstatite, Kaolinite, Clinochlore, Biotite
2299.2	7	2	700.80	Nontronite, Albite, Anorthoclase
3362	14	1	1024.74	Laumontite, Chalcocite, Crsitobalite, Quartz
3736.7	15	3	1138.95	Laumontite, SiO2, Albite
4215.6	16	2	1284.91	Quartz, Laumontite, Lavendulan
4443.5	17	3	1354.38	Laumontite, Quartz, Calcite, Stilbite
18.1	18	1	-	Anorthite, Kailinite, Quartz, Cobalt phlogopite, Tremolite
4923.1	18	1	1500.56	Quartz, Laumontite, Phlogopite, Albite, Bobierrite
6181	25	1	1883.97	Laumonitie - leonhardite, SiO2, Cristobalite, Fluorannite
6243 Black	26	5	1900.12	Laumontite, Phlogopite, Quartz, Biotite, Cristobalite
6243 White	26	5	1900.10	Graphite, Quartz, Laumontite, Illite, Ankerite, Anorthoclase, Orthoclase, Augite, Slawsonite
6246.6	26	4	1903.96	Magnesiohornblende, Cristobalite, Albite, Phlogopite, Crossite
6254	26	1	1906.22	Laumontite, Tin Tetramethylamnonium Sulfide, Metavariscite, Halite
33.1	33	1	-	Quartz, Albite, Calcite, Stilbite
34.1	34	1	-	Laumontite, quartz, Cristobalite, Albite, Kyanite, Magnesiohor
34.1	34	1	-	Quartz, Albite, Orthoclase, Nontronite, Magnesiohornblende
6934	34	2	2113.48	Laumontite, quartz, zeolite, magnesiohornblende,
7380.1	36	1	2249.45	Magnesiohornblende, Albite, Phlogopite
7378.8	36	4	2249.06	Laumontite, Ferropargasite, Cristobalite, Chalcocite
7508	37	2	2288.44	Quartz, Laumontite, Laumontite, Weissbergite, Zeolite
7715.5	38	1	2351.68	Quartz, Orthoclase, Albite
7963.8	39	5	2427.37	Laumontite, Illite, low Quartz, Anorthite, Graphite, Actinolite
42.1	42	1	-	Quartz, Cristobalite, Nontronite, Albite
8557	43	1	2608.17	Laumontite, Quartz, Biotite, Anorthite
8645.1	44	1	2635.03	Quartz, Albite, Microcline
8996.4	46	7	2742.10	Quartz, Albite, Phlogopite, Zircon
9002.1	46	5	2743.84	Laumontite, Laumontite, Laumontite, Simplotite
47.1 W	47	1	-	Low Quartz, Zilica, Laumontite, Cristobalite
47.1 WO	47	1	-	Laumontite, Cristobalite, Quartz, Albite,
9361.5	48	1	2853.39	Low quartz, Albite, Fluorannite, SiO2, Albite, Nontronite
53.3	53	1	-	Chalcopyrite, Muscovite, Laumontite, almandine, Ferropargasite
11161.7	53	6	3402.09	Quartz, Albite, Laumontite, Terranovaite, Jianshuiite
11168	53	2	3404.01	Laumontite, Quartz, Albite

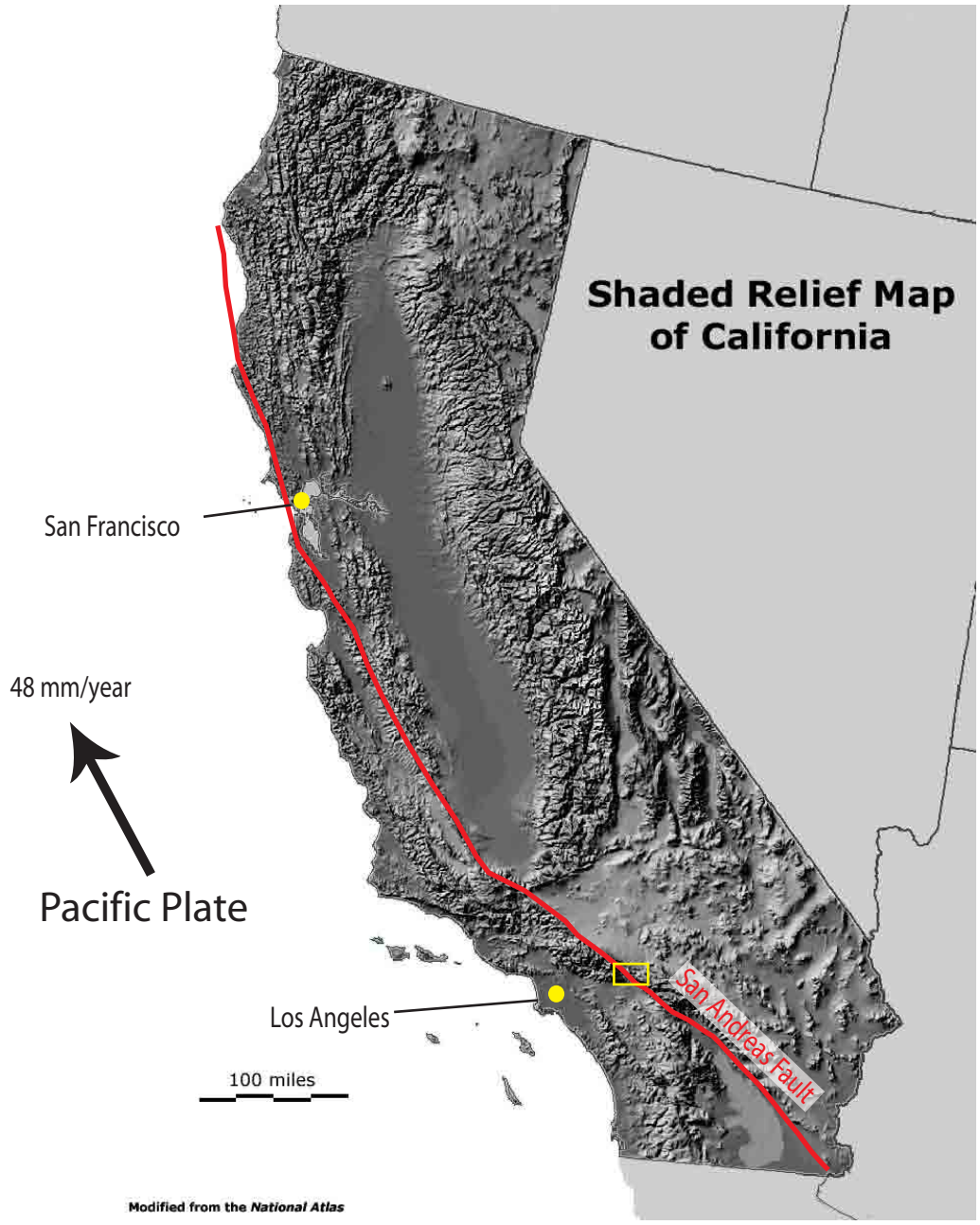

Figure 2-1. Shaded relied map of California showing the location of the San Andreas Fault, the direction and slip rate of the Pacific Plate. The yellow box marks the location of the Cajon Pass. A detailed map of the yellow box is shown in figure 2-2. Image modified from *National Atlas.Gov*.

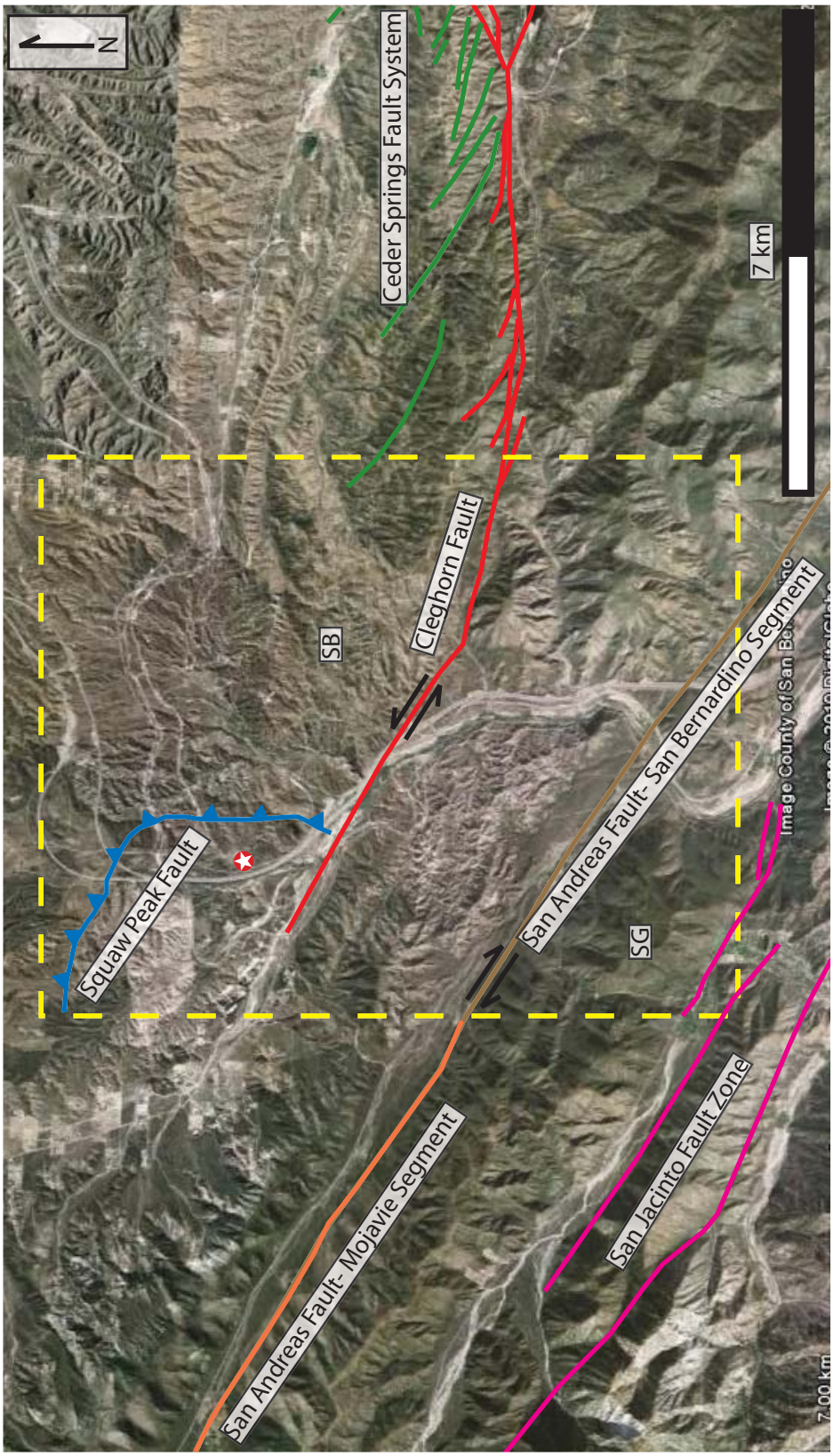

Figure 2-2. Google Earth image of the Cajon pass with major faults annotated in various colors. The red star represents the location of the Cajon Pass Borehole. The yellow box represents the location of the detailed map in Figure 2-3. SG= San Gabriel Mountains; SB= San Bernardino Mountains.

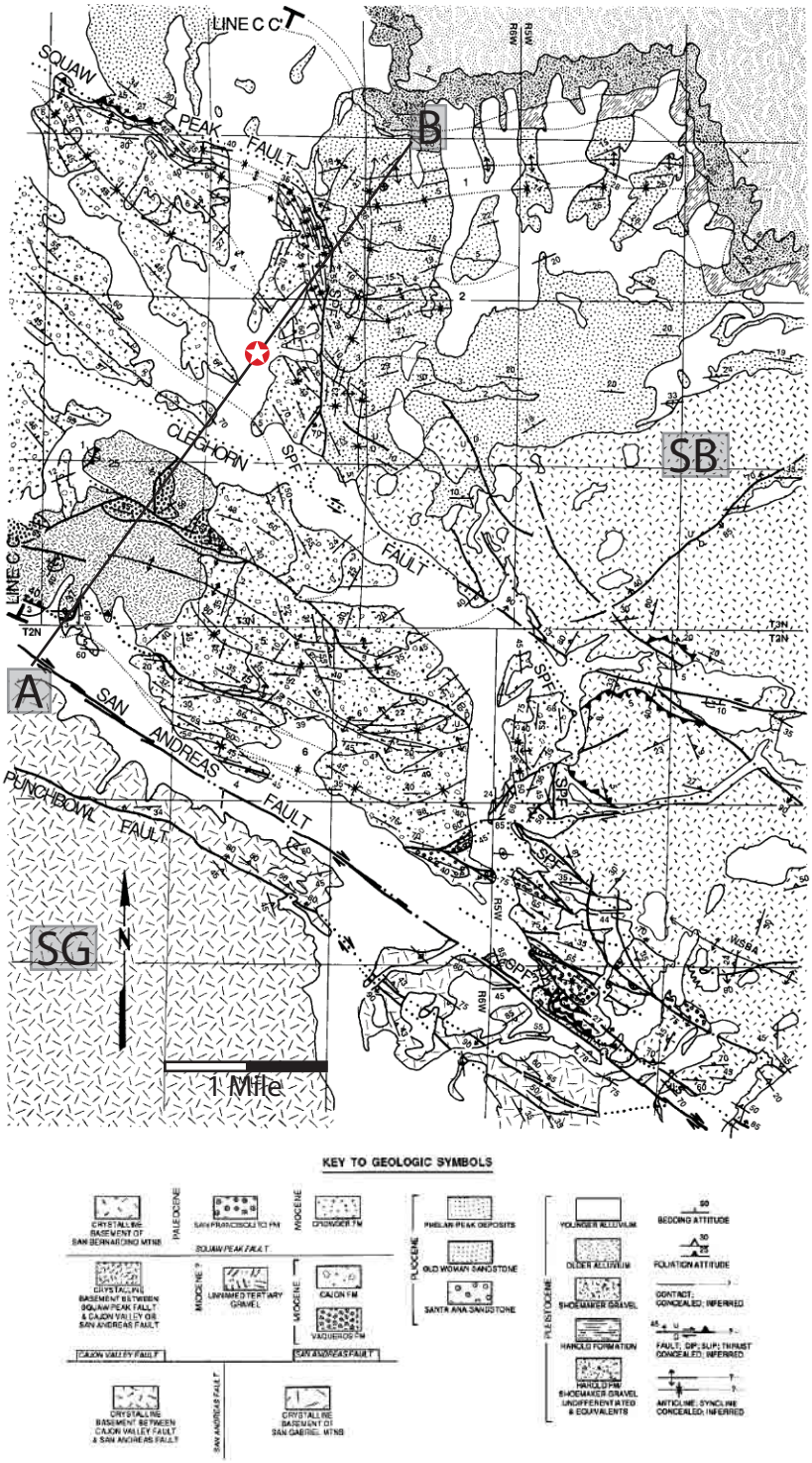

Figure 2-3. Geologic map of the Cajon Pass by Meisling and Weldon (1989). The red star marks the location of the Cajon Pass Borehole. Cross section line AB is displayed in Figure 2-4. SG= San Gabriel Mountains; SB= San Bernardino Mountains.

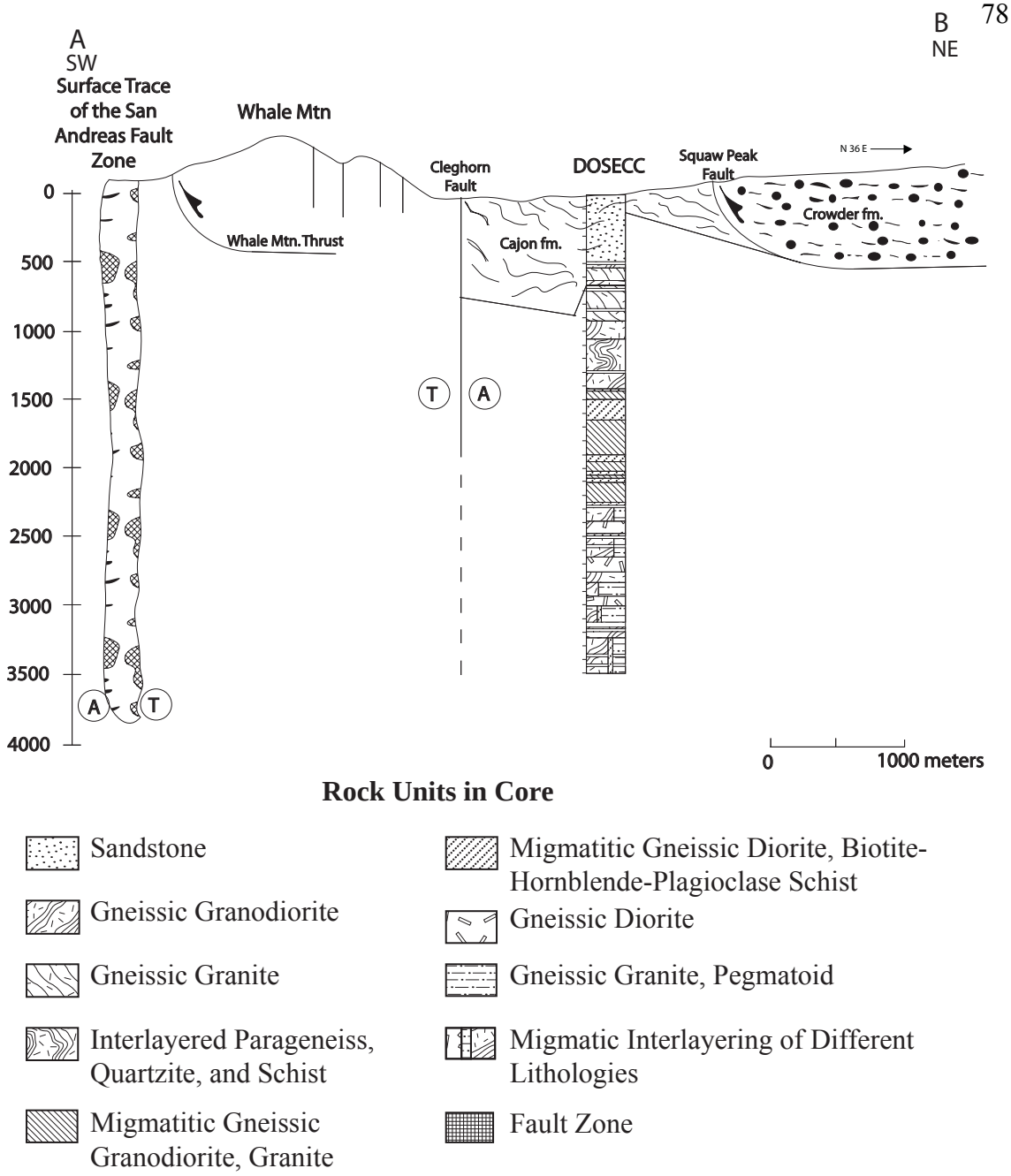

Figure 2-4. Simplified cross section of the Cajon Pass showing the relationship of the San Andreas fault, Whale Mountain thrust, Cleghorn fault, and Squaw Peak fault to the location of the borehole slightly modified from Zoback and Healy (1992). A lithologic column modified from Vernik and Nur (1992) has been placed on the location of the borehole. T and A denote towards and away motion on the strike-slip faults. Note the sense of movement is left-lateral, as opposed to the right lateral San Andreas Fault. Both faults are assumed to be vertical in this cross section. A modified version of this cross section (Figure 2-44) better explains the data and the results of this study.

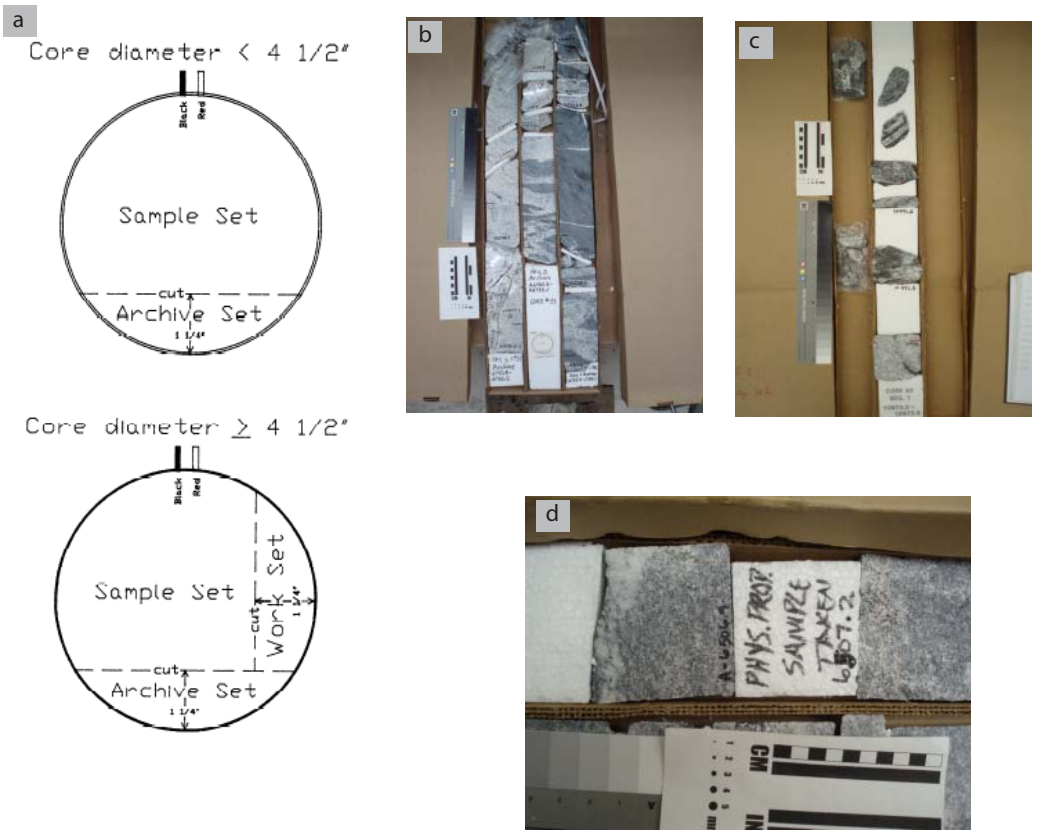

Figure 2-5. Schematic of core slabbing procedures, with photographs of core recovery and previous sample locations. (a) Schematic of core slabbing procedures (Campbell and Gay, 1989). (b) Photograph of archive slab with excellent recovery, and (c) with poor recovery. (d) Photograph showing a note at a location of a prior sample. Note the fractured segments separated by white styrofoam.

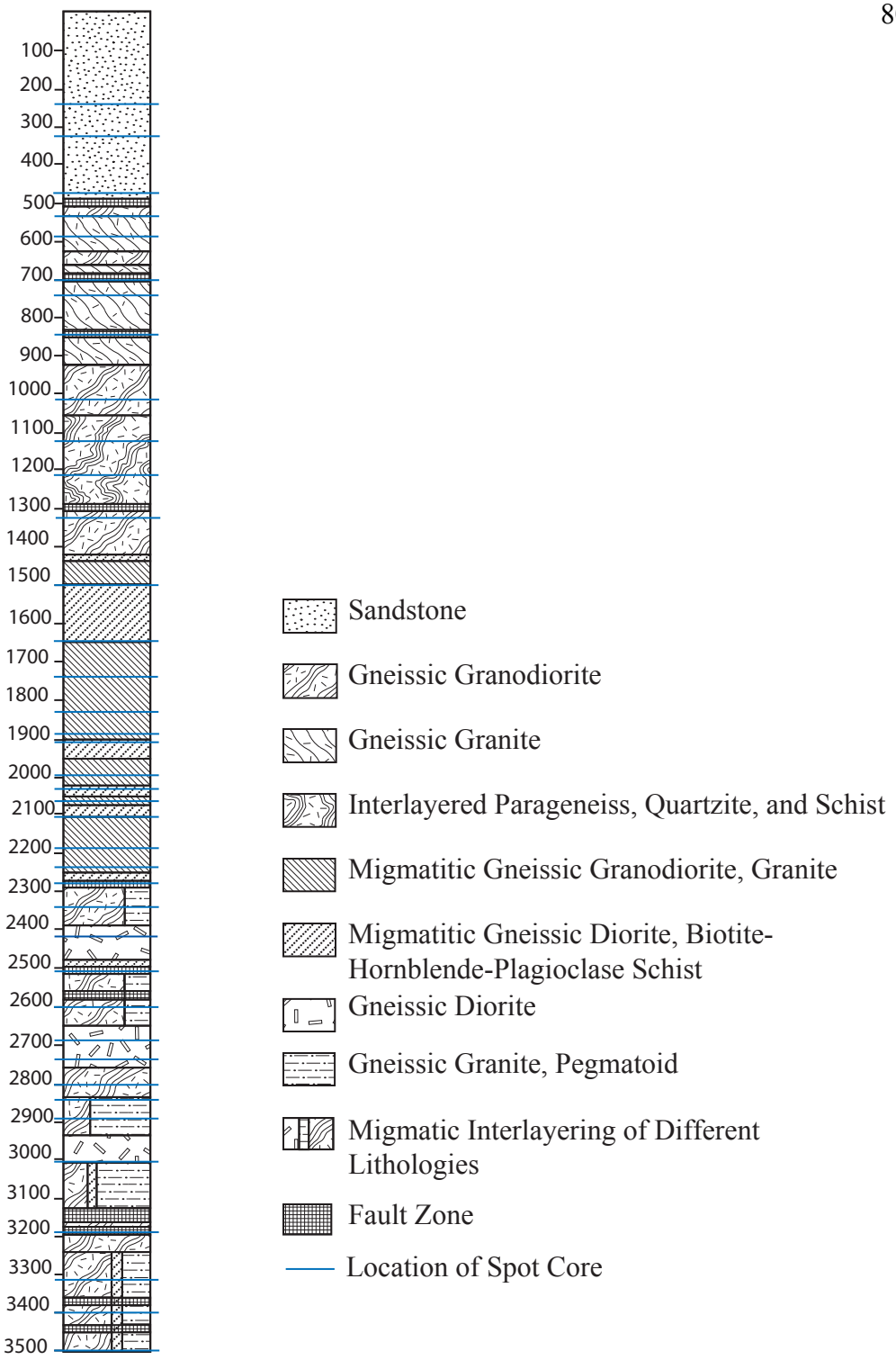

Figure 2-6. Lithologic column of the Cajon Pass Borehole as determined from core, cuttings, and wireline log data. The blue lines indicate the location of core recovered from the borehole. Lithologic column slightly modified in this work from Vernik and Zoback (1992).

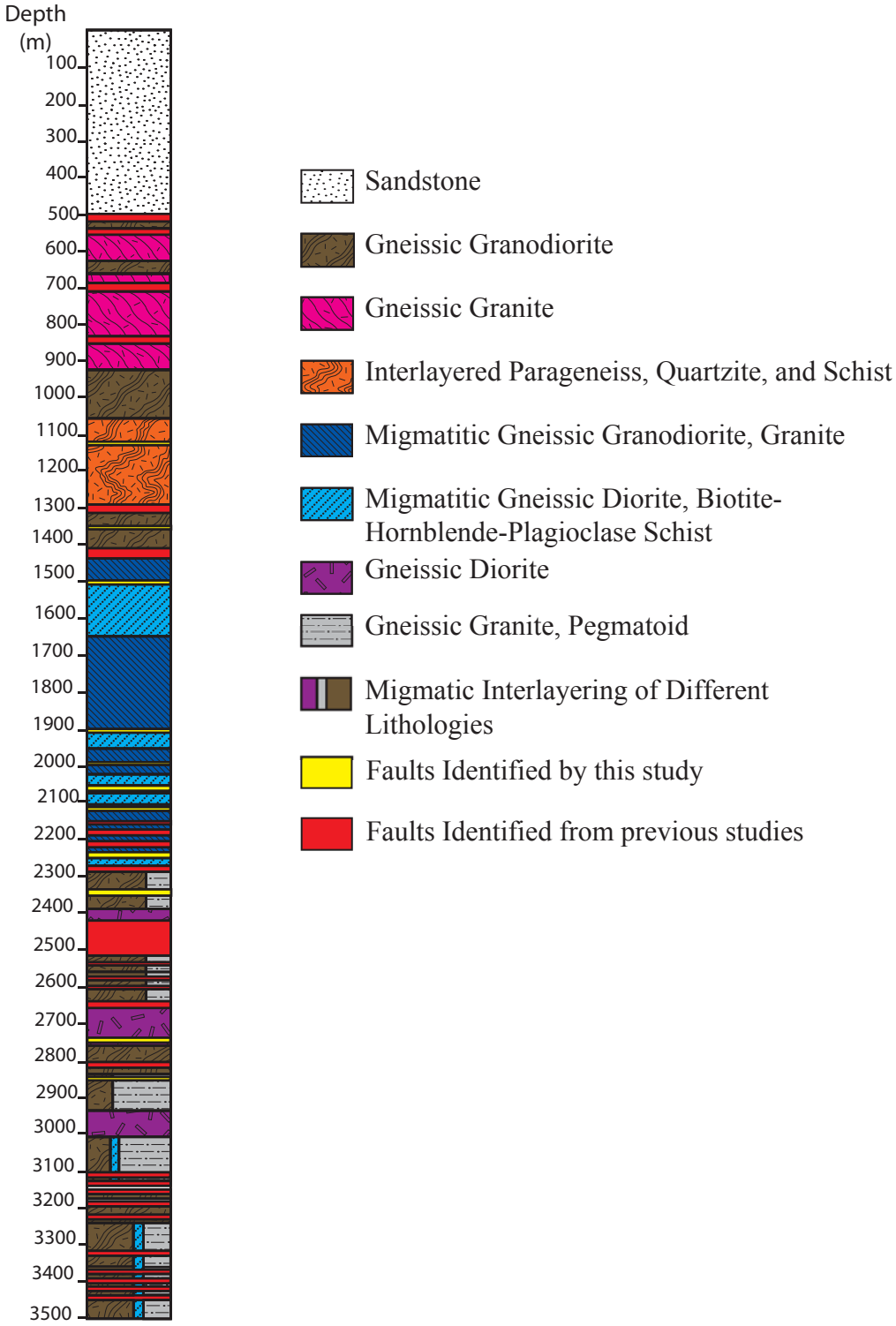

Figure 2-7. Revised lithologic column of the Cajon Pass Borehole from Vernik and Zoback (1992) as determined from core, cuttings, and wireline log data. The yellow boxes represent faults identified from this study and the red boxes represent faults identified by previous workers. Depth is in meters.

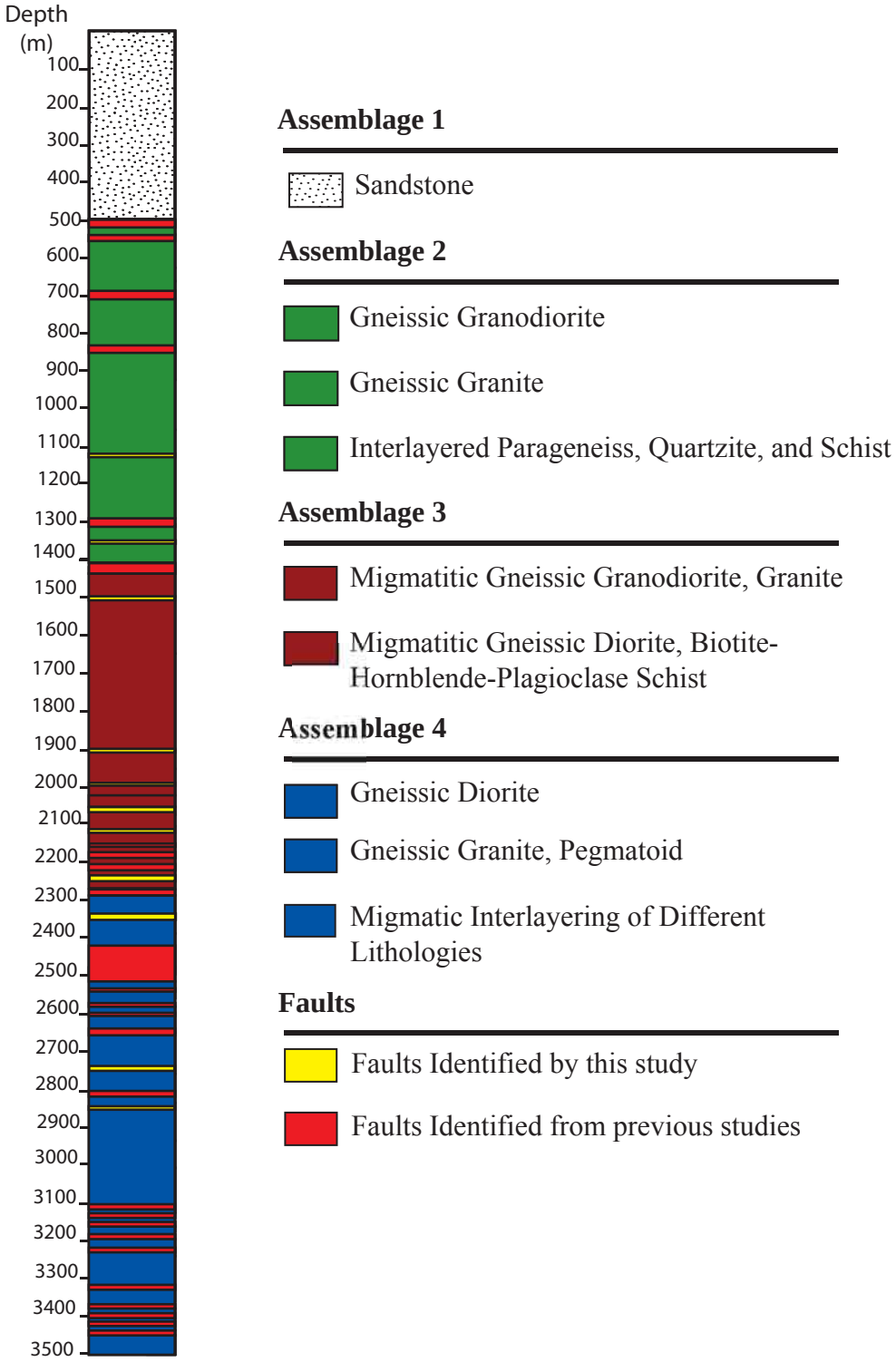

Figure 2-8. Simplified lithlogic column of the Cajon Pass Borehole modified from Vernik and Zoback (1992) as determined from core, cuttings, and wireline log data. Assemblage 1 is comprised of sandstone; assemblage 2 is gnessic granitic rocks; assemblage 3 is comprised of migmatitic rocks; and assemblage 4 is an interlayering of assemblage two and three with some gneissic diorites. The yellow boxes represent faults identified from this study and the red boxes represent faults identified by previous workers. Depth is in meters.

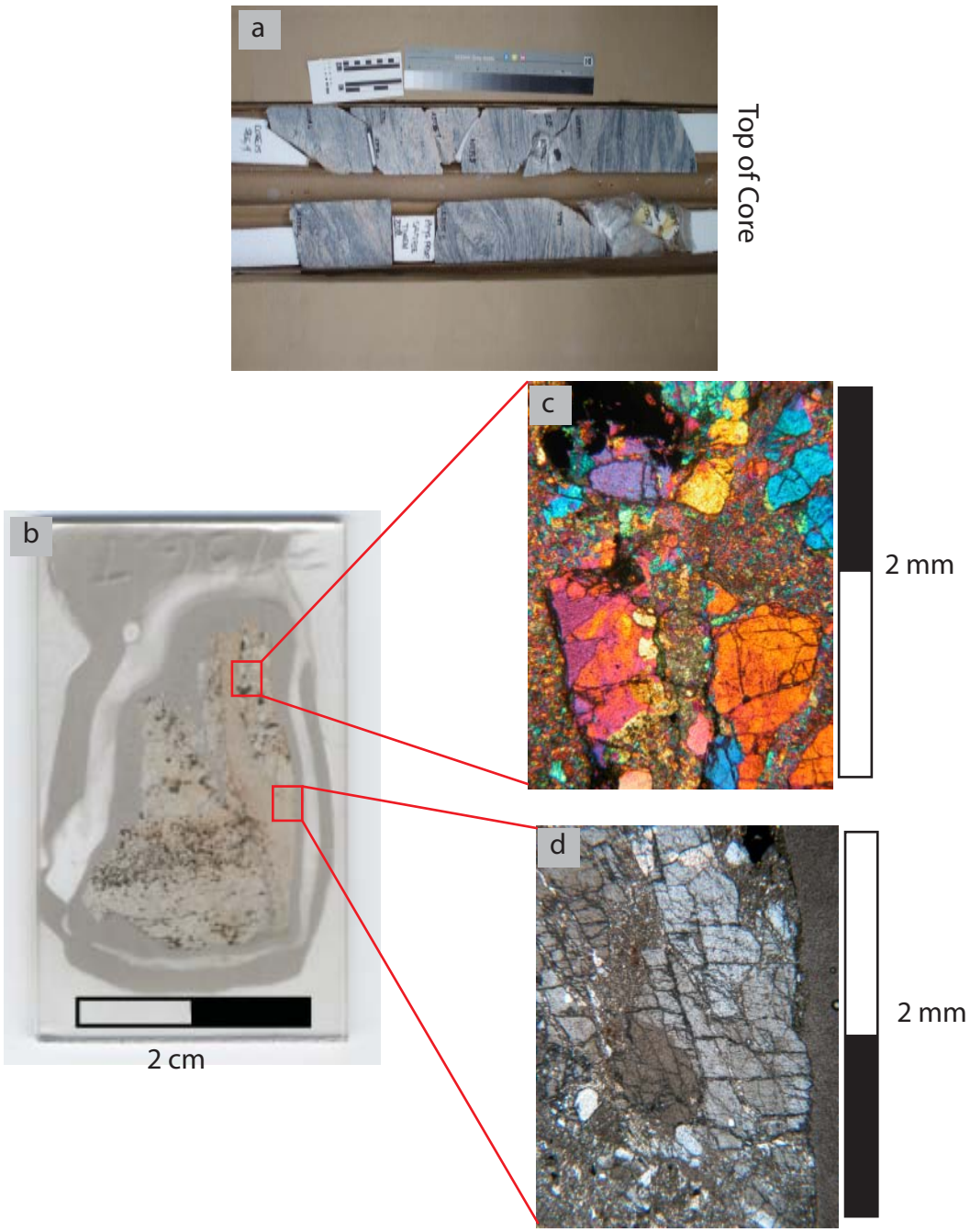

Figure 2-9. Photographs of the core and thin sections from the fault zone at 1138 – 1440 m depth in a Lleucocratic granite gneiss. (a) Photo of a portion of the archive slab. Note the fractured segments separated by white styrofoam. (b) Scan of a thin section from 1138 m depth. (c) Photomicrograph in CPL of a large shear zone with a laumontite matrix fill. (d) Photomicrograph in PPL of a portion of the laumontite shear zone and laumontite filled fractures creating a dilatant texture in grains near the shear zone. CPL = cross polarized light; PPL = plane polarized light.

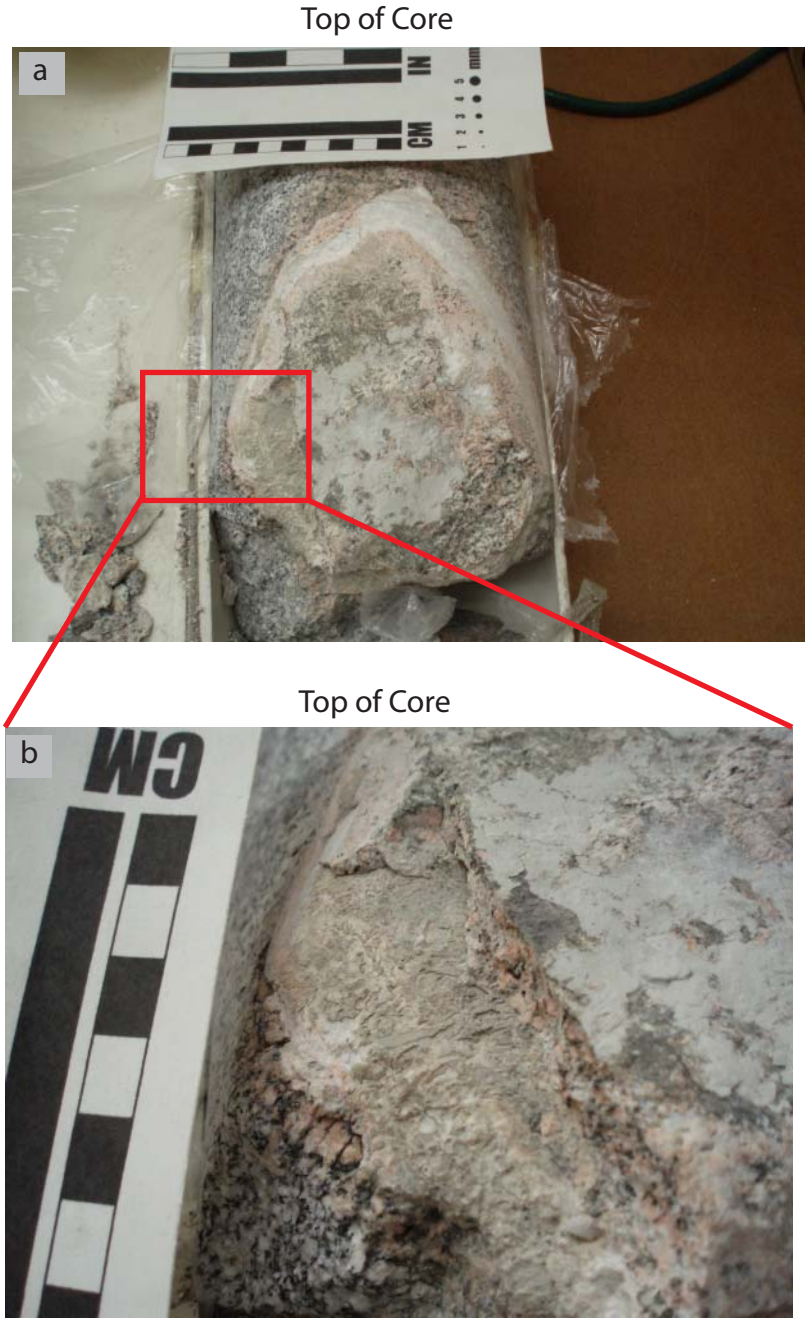

Figure 2-10. Photographs of the moderately dipping fault from 1354-1355 m depth (a) in a granodiorite. Note the intact nature of the core and localization of damage. A 2 cm thick dip slip surface is shown in photo (b), and fibrous pink to pale green laumontite in the fault surface.

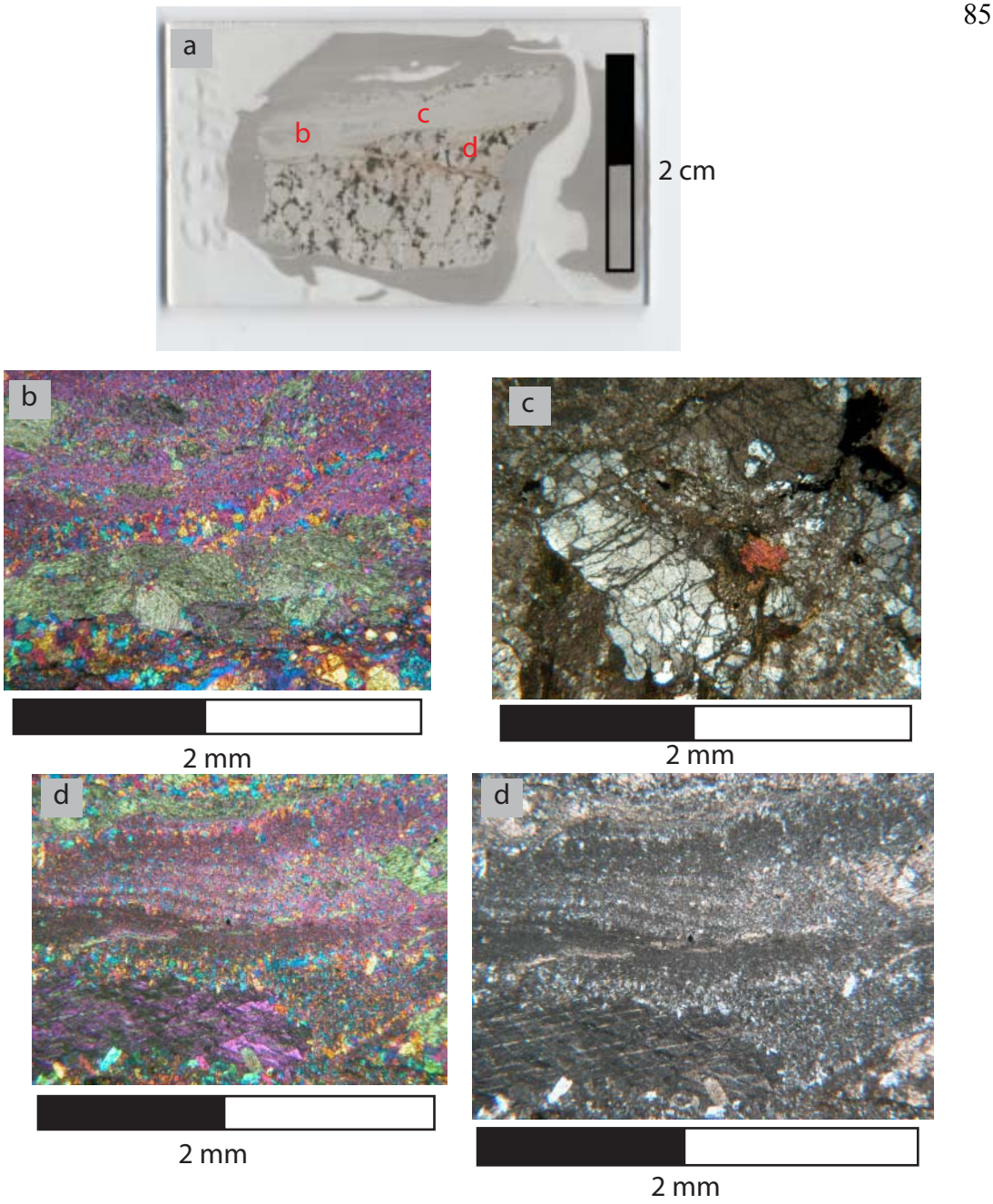

Figure 2-11. Thin Section Thin Section Microstructures of the fault zone at 1354 – 1355 m depth. (a) Scan of a thin section from 1354.3 m depth. The thin section is characterized by laumontite filled shear fractures of varying size and shattered grains of the protolith. Locations of photomicrographs are shown in red (b) Photomicrograph in CPL showing a shear fracture that has undergone transtension and precipitated fibrous laumontite in the center of the fracture. Etched calcite grains are also present in the laumontite matrix. (c) Photomicrograph in PPL showing shattered grains along the edges of the main shear zone. (d) Photomicrographs in CPL and PPL of the main shear zone showing a laumontite matrix fill, and recording multiple episodes of deformation. CPL = cross polarized light; PPL = plane polarized light.

Figure 2-12. Photographs of the some of the archive core from the fault zone at 1499-1501 m depth in a gray dioritic and amphibolitic gneiss (a). Note the fractured segments separated by white styrofoam. A foliated slip surface containing minor amounts of clay gouge and laumontite and poorly preserved slicks is shown in photo (b).

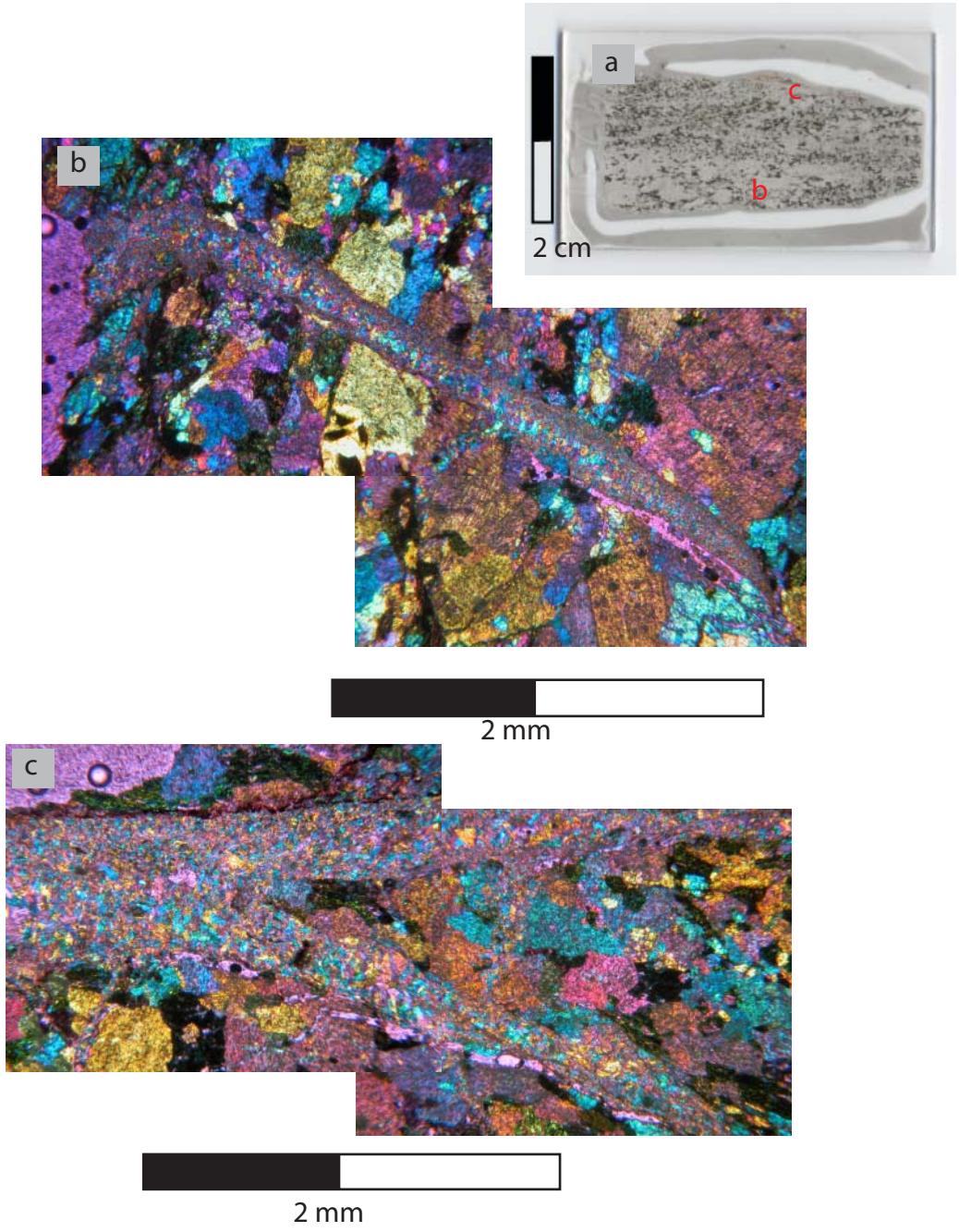

Figure 2-13. Thin section microstructures of the fault zone at 1499 – 1501 m depth. (a) Scan of a thin section from 1500.5 m depth. The thin section is characterized by laumontite filled shear fractures of varying size. Locations of photomicrographs are shown in red (b) Photomicrograph in CPL showing a shear fracture that has undergone transtension and precipitated fibrous laumontite in the center of the fracture. Note the offset grains along either side of the fracture. (c) Photomicrograph of laumontite shear zone with large protolith fragments entrained in the shear zone. A thin red gouge has developed along the top of the shear zone. CPL = cross polarized light.

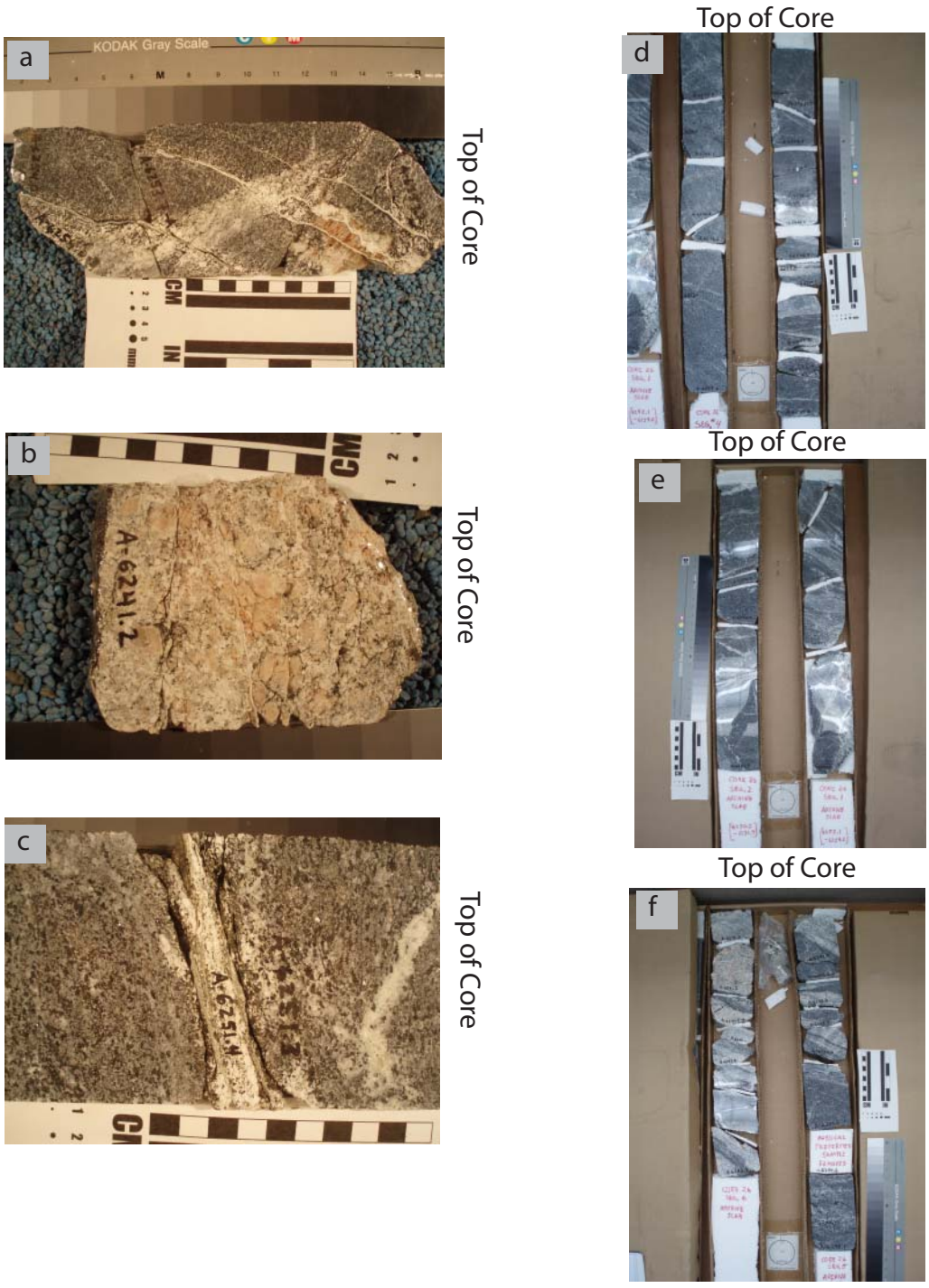

Figure 2-14. Photographs of some of the fault surfaces from fault zone 1900-1906 m depth in granite-granodiorite that transitions to a dark gray granitic gneiss. The archive slabs (d), (e), and (f) are highly fractured and in areas wrapped in plastic to prevent damage from handling. Fractured segments separated by white styrofoam. The protolith transitions from a gray –white granite to a dark granititic gneiss. The faults surfaces (a), (b), (c), are predominately laumontite. Notice that the fault surfaces range in dip from 30° to 60°.

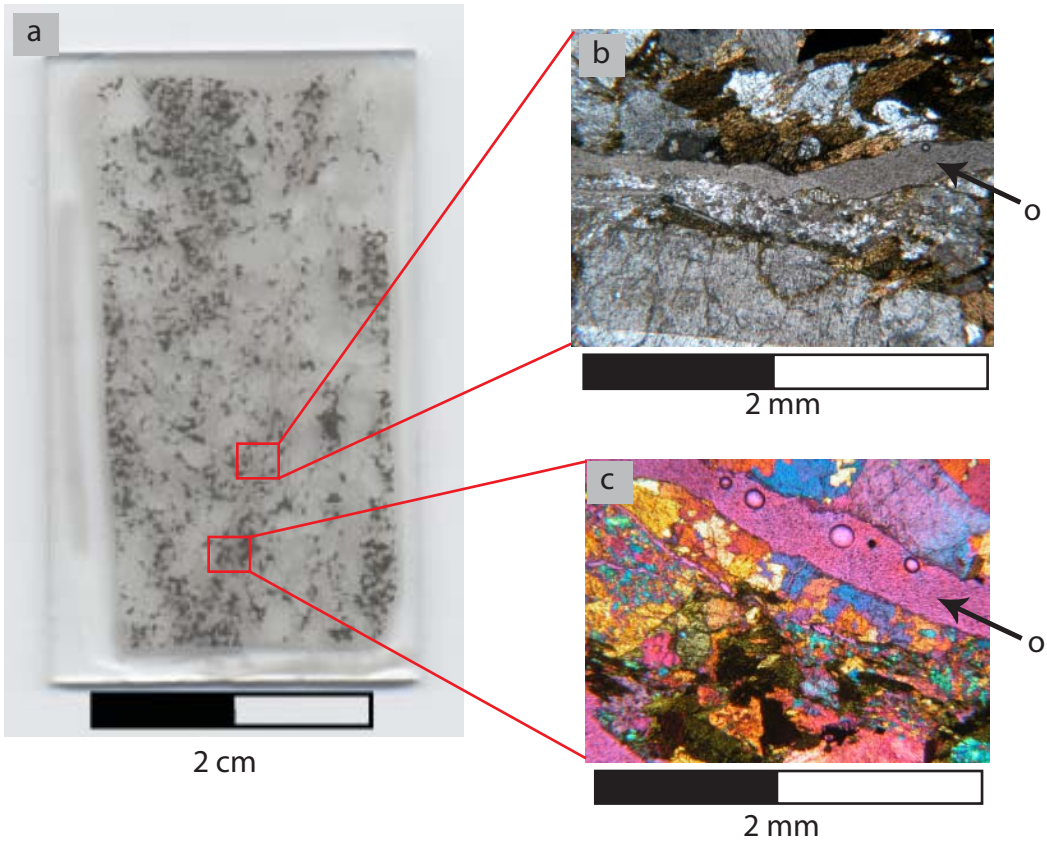

Figure 2-15. Thin section microstructures of the fault zone at 1900 – 1906 m depth. (a) Scan of a thin section from 1901.2 m depth. The thin section is dominated by a thin shear fracture with laumontie and calcite. Locations of photomicrographs are shown in red. (b) Photomicrograph in PPL showing the shear fracture that broke open (o). (c) Photomicrograph in CPL showing laumontite and calcite. CPL = cross polarized light; PPL = plane polarized light.

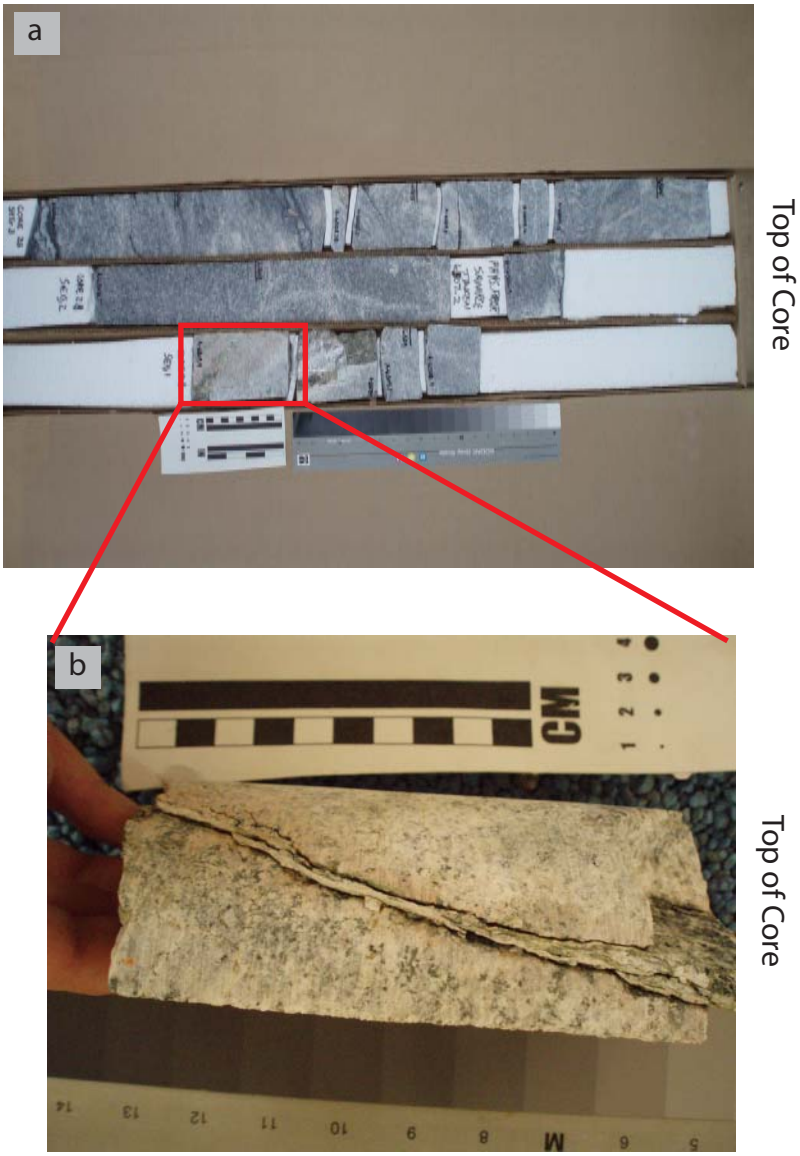

Figure 2-16. Photographs from the fault zone at 1981 – 1982 m depth in granite to granodiorite. Archive set (a) contains fairly intact core with a localized fault. Fractured segments separated by white styrofoam. (b) A 7 mm thick fault with a pale green to white alteration in its core and pink alteration extending into the host rock on the opposite side of the archived core in (a). Slicks are exposed on the alteration area.

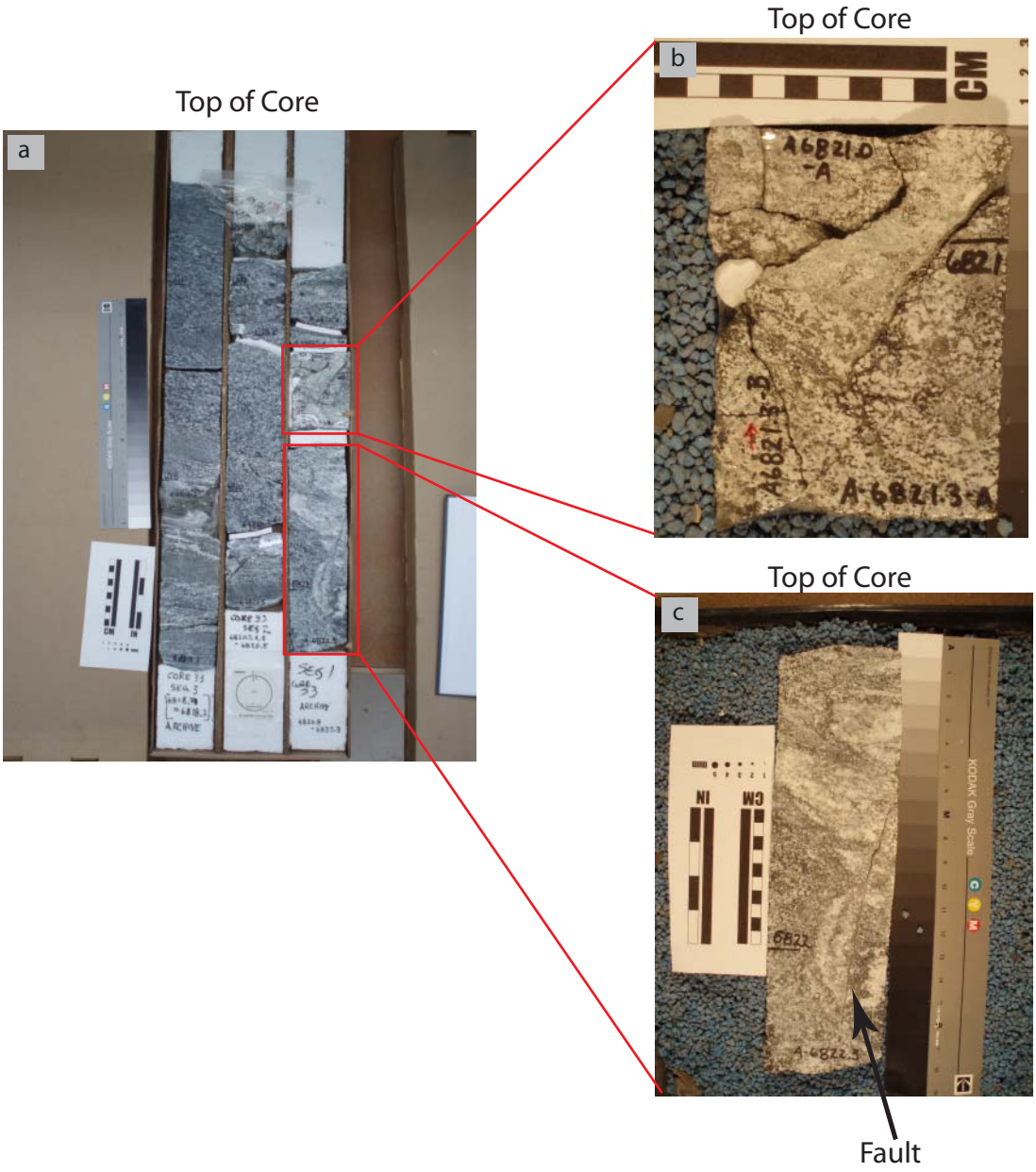

Figure 2-17. Photographs of the fault zone at 2070-2080 m depth in a granodiorite. (a) shows the archive set. Note the plastic bag with damaged rock from a small fault. Fractured segments separated by white styrofoam. (b) is a pale green zoelite rich fault. (c) is a steeply dipping filled fracture.

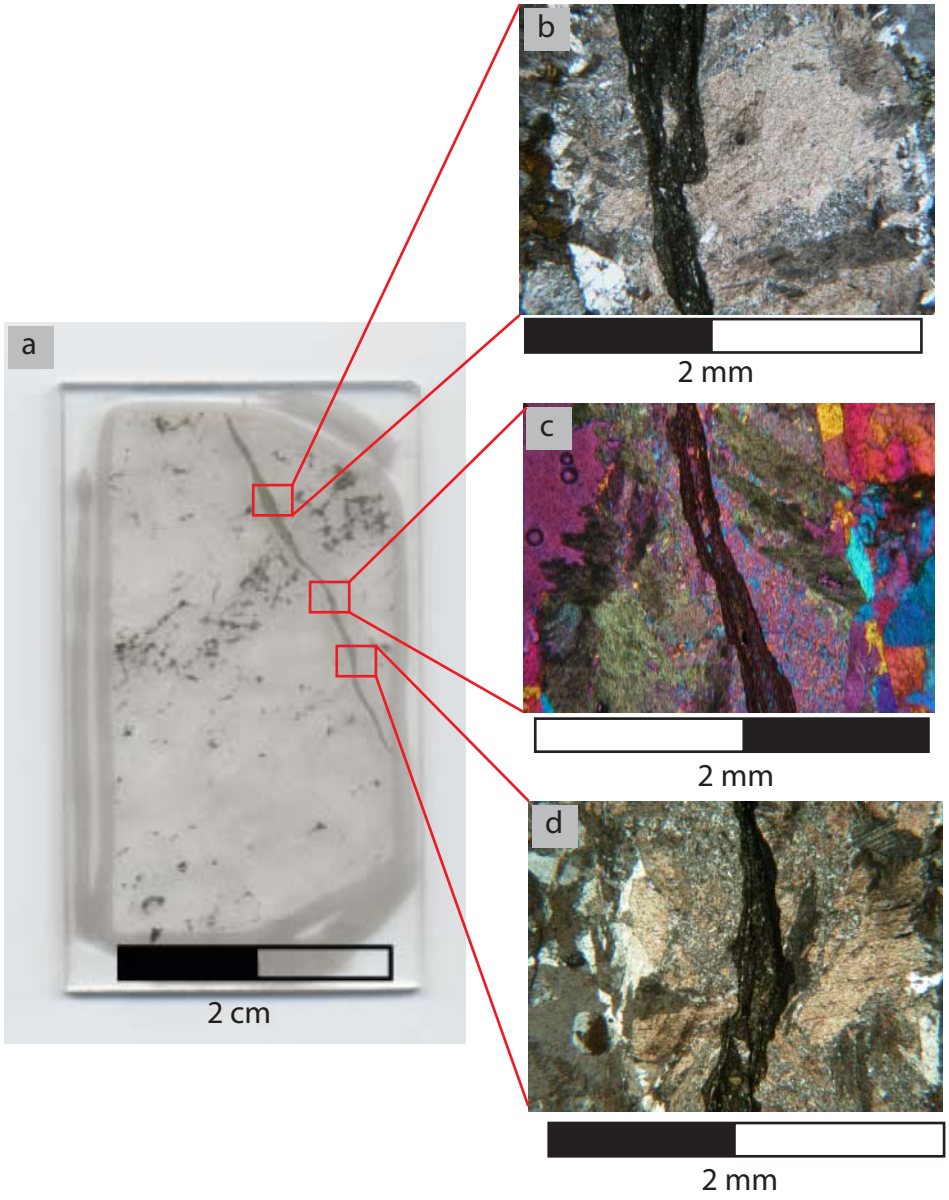

Figure 2-18. Microstructures of the fault zone at 2070 – 2080 m depth. (a) Scan of a thin section from Core 33, Segment 1. The thin section is dominated by a thin gouge zone, with laumontie and deformed calcite along the outer edges of the fault zone. Locations of photomicrographs are shown in red. (b) Photomicrograph in PPL showing the micro gouge zone with laumonite matrix. (c) Photomicrograph in CPL showing the gouge zone, laumontite matrix and calcite. (d) Photomicrograph in PPL showing the gouge zone and laumontite matrix. CPL = cross polarized light; PPL = plane polarized light.

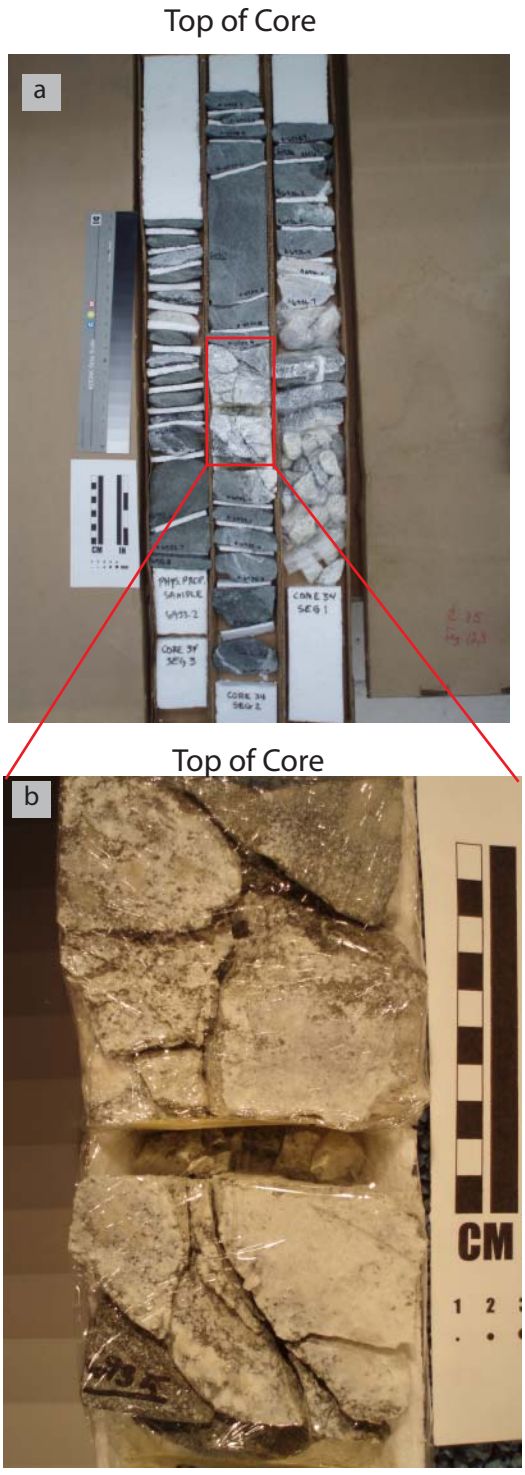

Figure 2-19. Photographs of the fault zone at 2110 – 2122 m depth in a gneissic granodiorite to leucocratic granite. (a) shows the archive slab from 2112.9 to 2114.7 m. Note the bags and wrapped damaged fault rocks as well as the intensity of drilling induced disk fractures. Fractured segments separated by white styrofoam. (b) shows a pale green laumontite slip surface and open fractures.

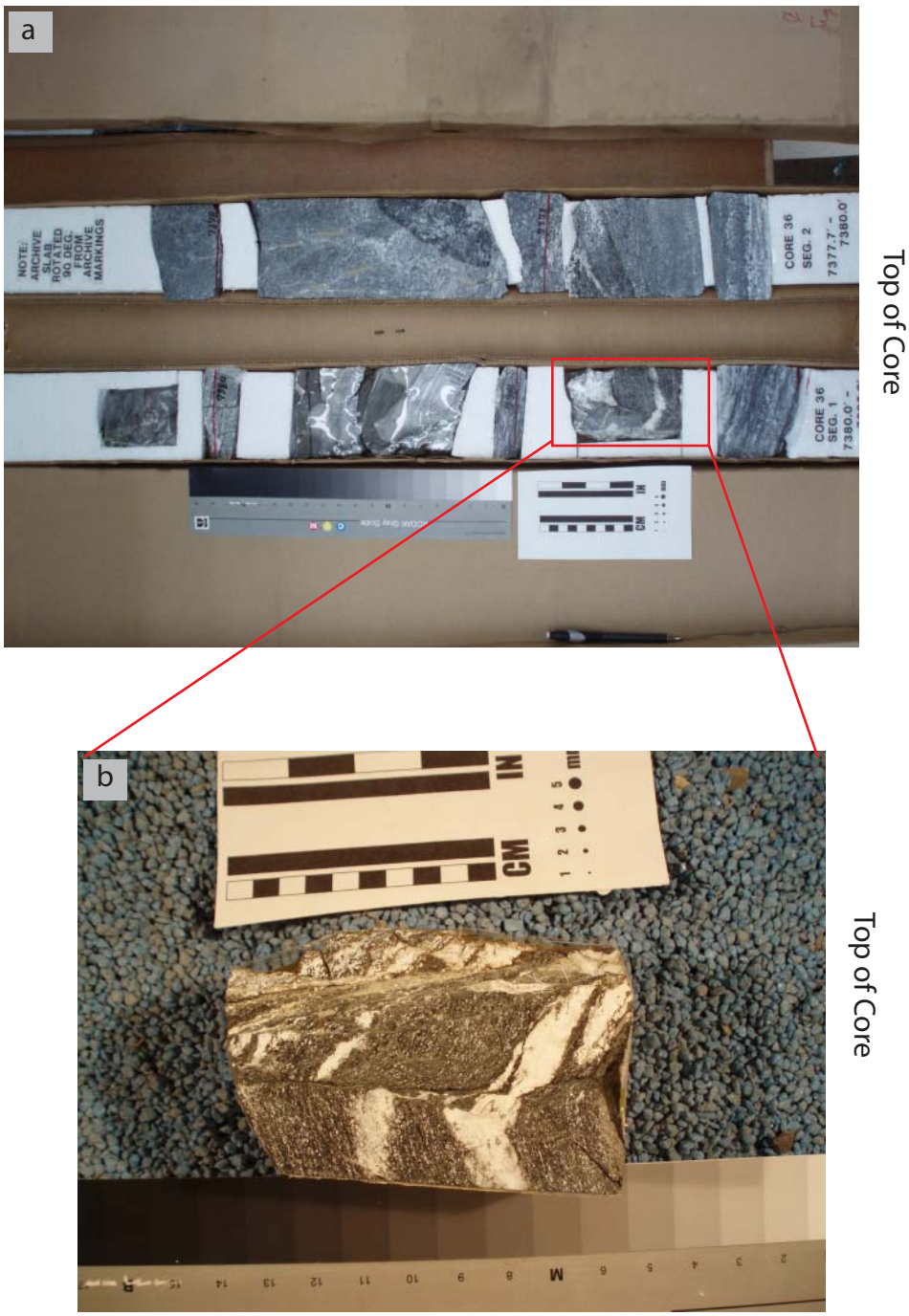

Figure 2-20. Photographs from the fault zone at 2232 – 2252 m depth in a fine crystalline gneiss. The archive core (a) is fractured and either wrapped or in a plastic bag. Fractured segments separated by white styrofoam. (b) is a strongly foliated fault with a pale green laumontite slip surface from the sample core from the same depth. A thinner fault in the gneiss has an apparent 1.5 cm offset.

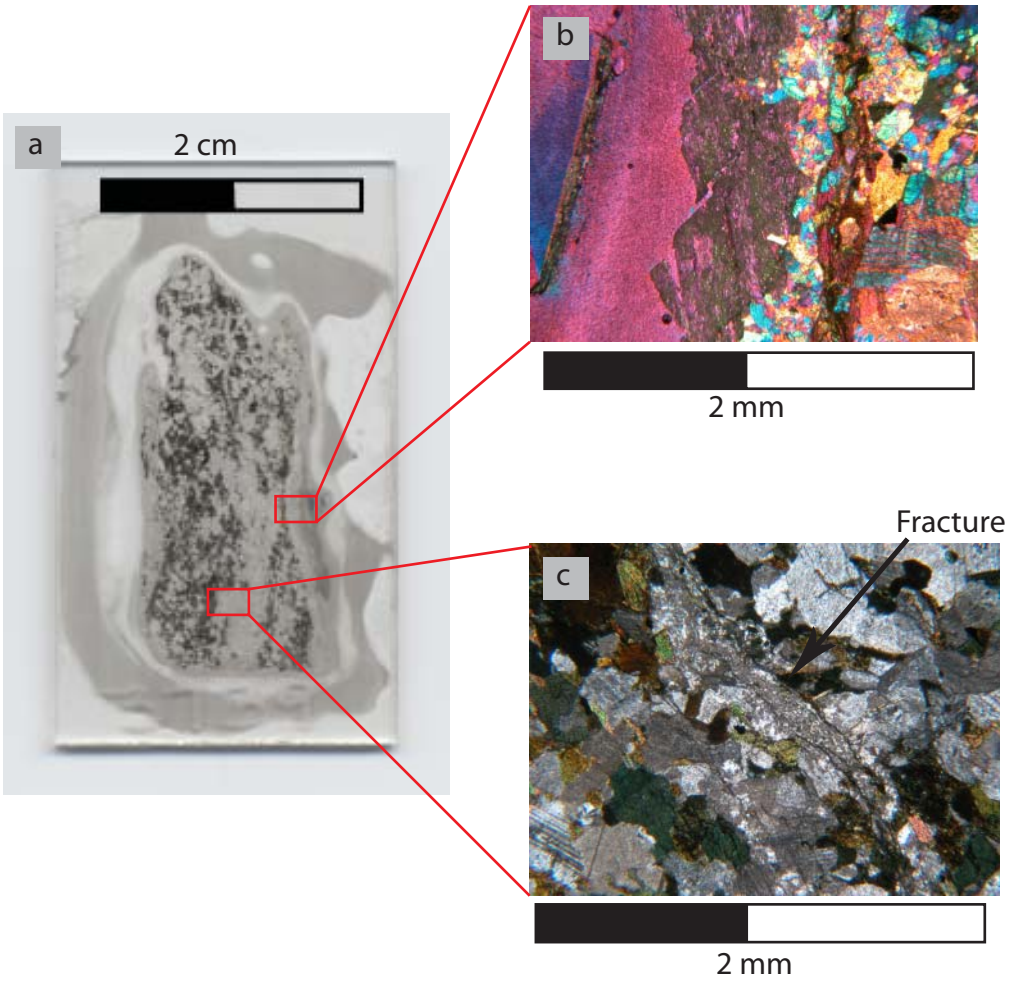

Figure 2-21. Microstructures of the fault zone at 2232 – 2252 m depth. (a) Scan of a thin section from 2249.1 m depth. The thin section is characterized by calcite and minor amounts of laumontite filled shear fractures of varying size and shattered grains of the protolith. Locations of photomicrographs are shown in red (b) Photomicrograph in CPL showing a portion of a shear fracture with etched calcite. (c) Photomicrograph in PPL showing a small laumontite filled fracture. CPL = cross polarized light; PPL = plane polarized light.

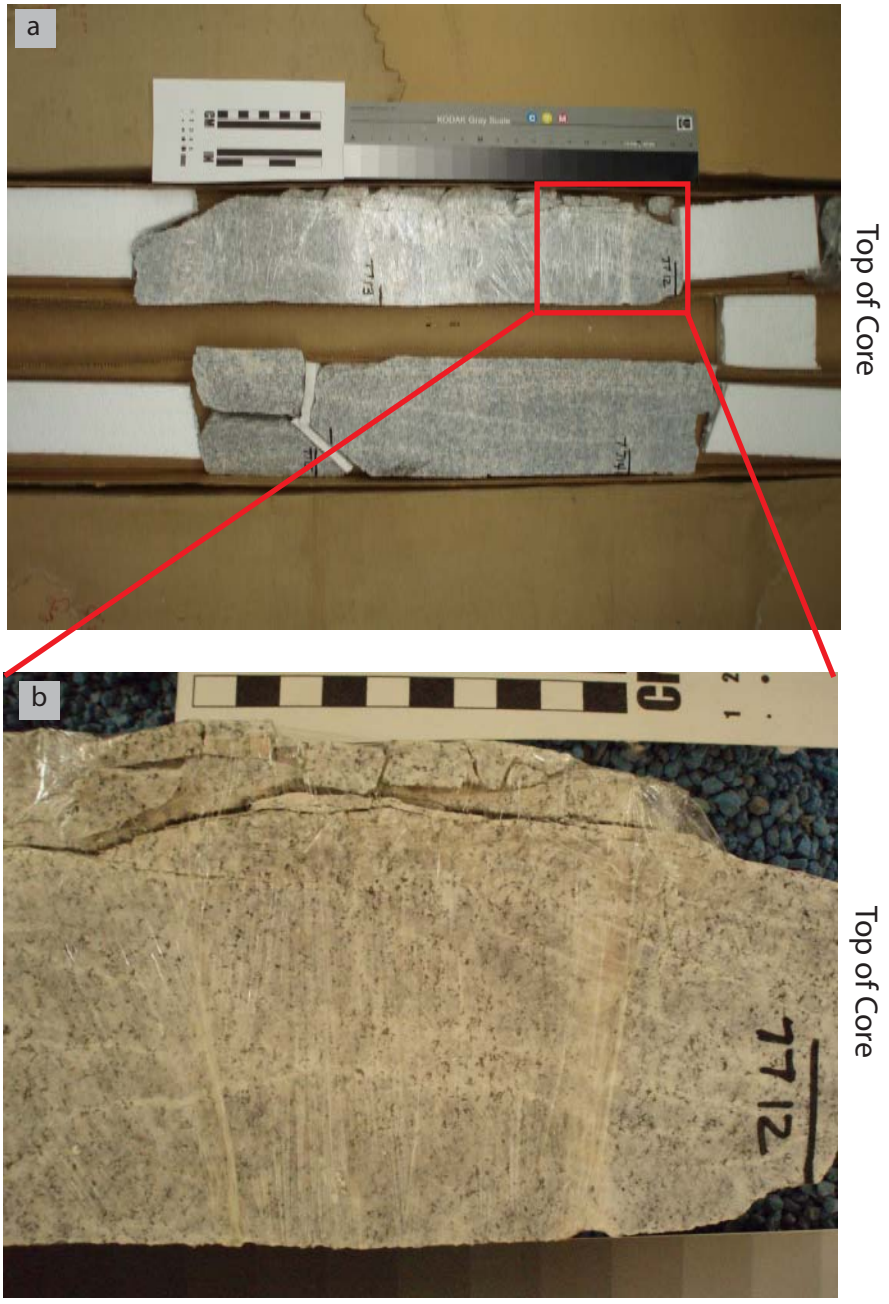

Figure 2-22. Photographs from the fault zone at 2317 – 2350 m depth in a leucocratic granite. The archive core (a) displays a nearly vertical small fault along one edge, as well as a high density of sub vertical, sub parallel white zeolite-filled fractures. Fractured segments separated by white styrofoam. (b) is a closer view of the fractures.

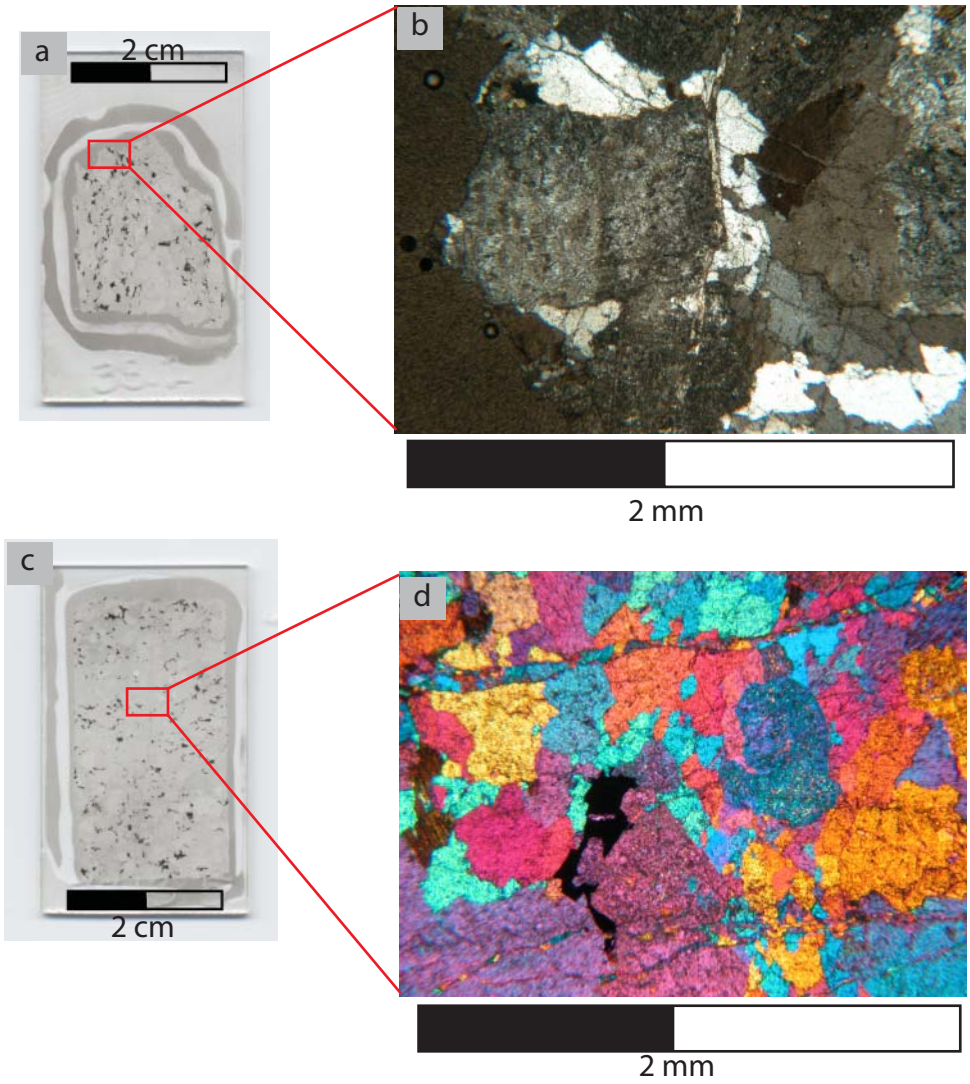

Figure 2-23. Microstructures of the fault zone at 2317 – 2350 m depth. (a) Scan of a thin section from core 38, segment 2 m depth. (b) Photomicrograph in PPL of mode I fractures with laumontite. (c) Scan of a thin section from 2350 m depth. (d) Photomicrograph in CPL of several parallel mode I fractures with a laumontite fill. A microcrack is seen towards the bottom of the photo. Locations of photomicrographs are shown in red. Both thin sections are characterized by parallel mode I fractures and microcracks. CPL = cross polarized light; PPL = plane polarized light.

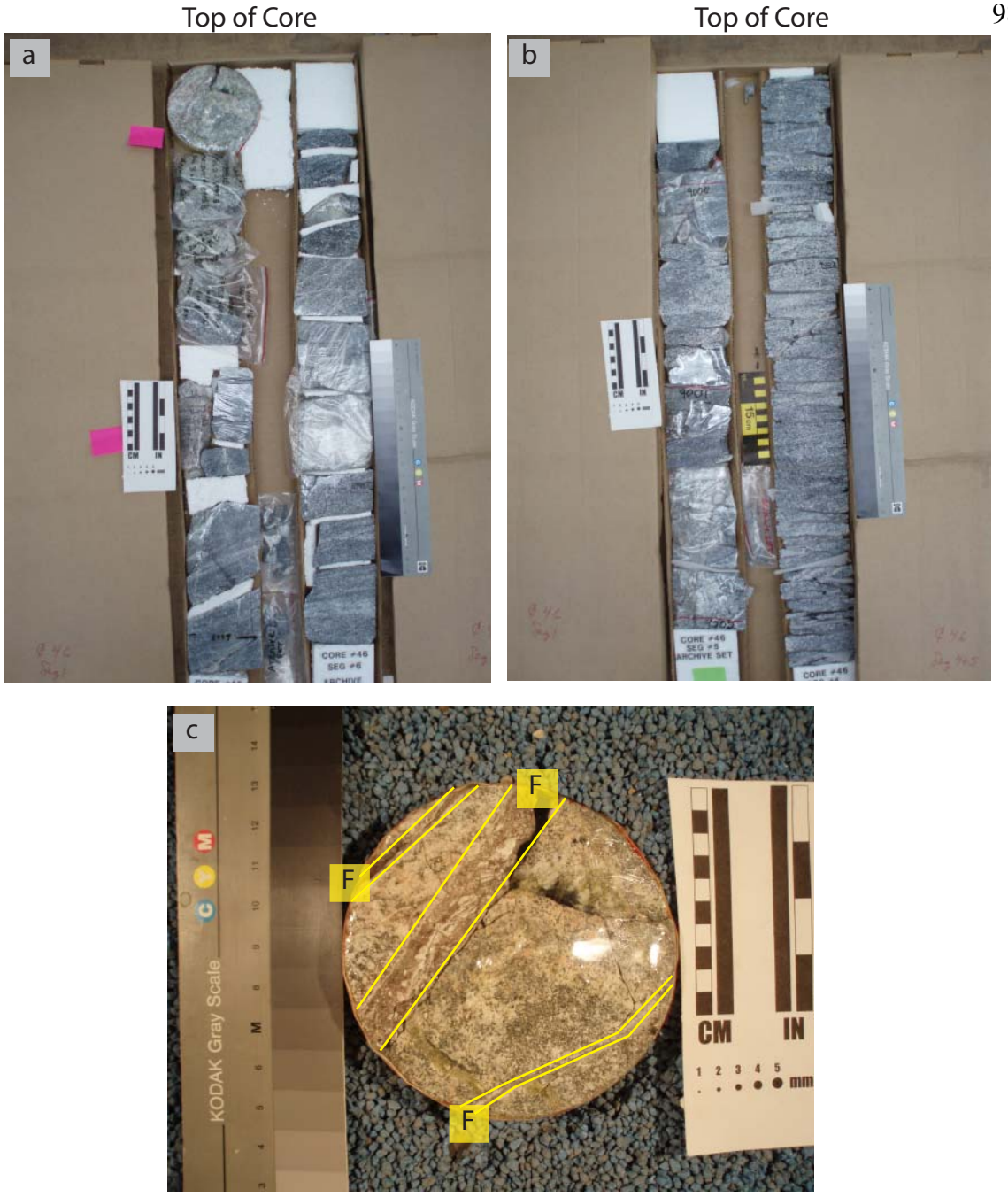

Figure 2-24. Photographs from the fault zone at 2735 – 2755 m depth in a granodiorite. The archive core (a) and (b) are populated with both natural and induced fractures. Much of the core is bagged or wrapped in plastic to prevent further damage from handling. Fractured segments separated by white styrofoam. Photo (c) is a cross section of the core (upper left of (a)) containing a steeply dipping fault, surrounded by epidiote, chlorite, and laumontite alteration. Smaller faults are also present in the core. F = fault.

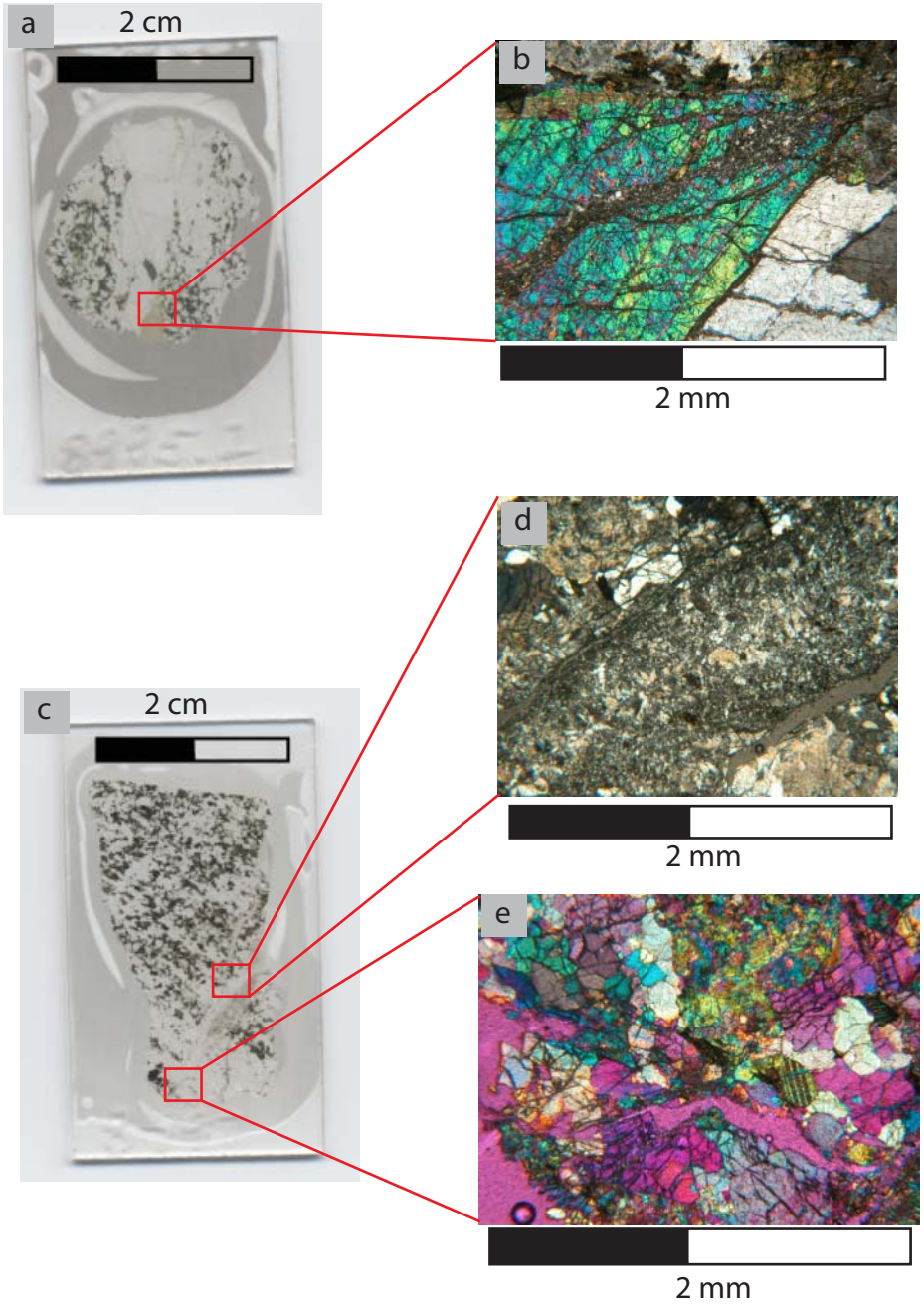

Figure 2-25. Microstructures of the fault zone at 2735 – 2755 m depth. (a) Scan of a thin section from 2741.7 m depth. (b) Photomicrograph in CPL showing the dilatant texture created from laumontite in a plagioclase grain. (c) Scan of a thin section from 2742.3 m depth. (d) Photomicrograph in PPL of a large shear zone with a laumontite matrix fill. The zone has evidence for four episodes of deformation. Open fractures probably formed during preparation to sample. (e) Photomicrograph in CPL of shattered grains near the shear zone from (d). CPL = cross polarized light; PPL = plane polarized light.

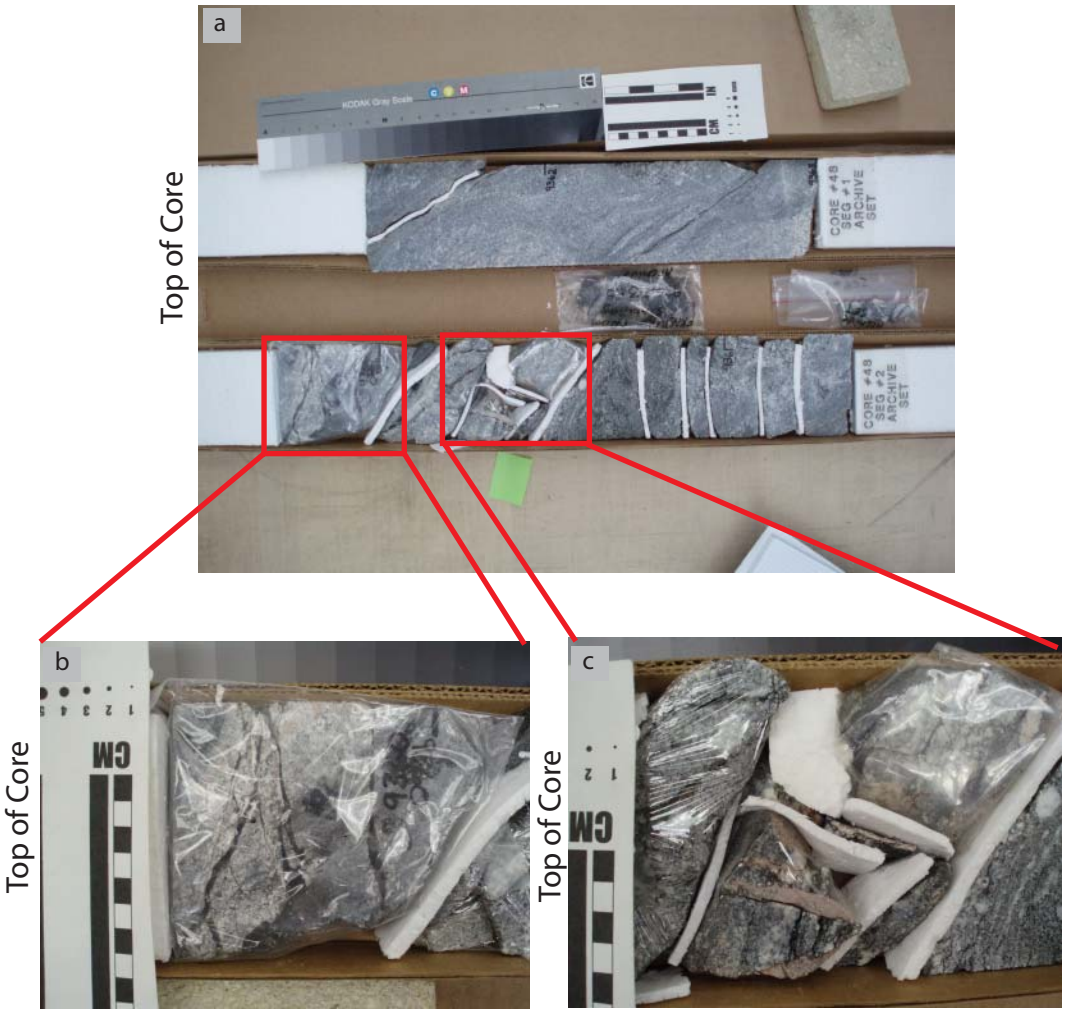

Figure 2-26. Photographs from the fault zone at 2852-2853 m depth in a poorly foliated granodiorite. Archive set (a) contains a highly fractured core with a zone of highly deformed rock that has bagged or wrapped in plastic. Fractured segments separated by white styrofoam. (b) contains a small bagged shear zone and (c) contains three approximately 6 mm thick pink laumontite shear zones.

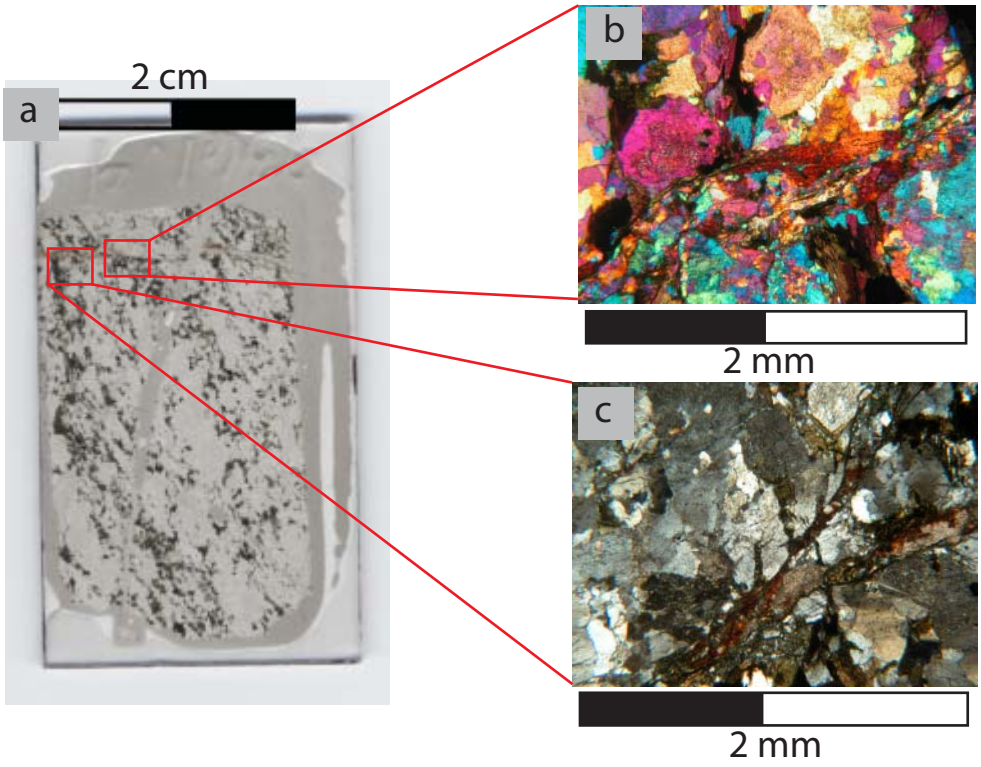

Figure 2-27. Microstructures of the fault zone at 2852 – 2853 m depth. (a) Scan of a thin section from 2853.3 m depth. (b) Photomicrograph in CPL showing small shear fractures with minor amounts of clay gouge. (c) Photomicrograph in PPL of small branching shear fractures with minor amounts of clay gouge. CPL = cross polarized light; PPL = plane polarized light.

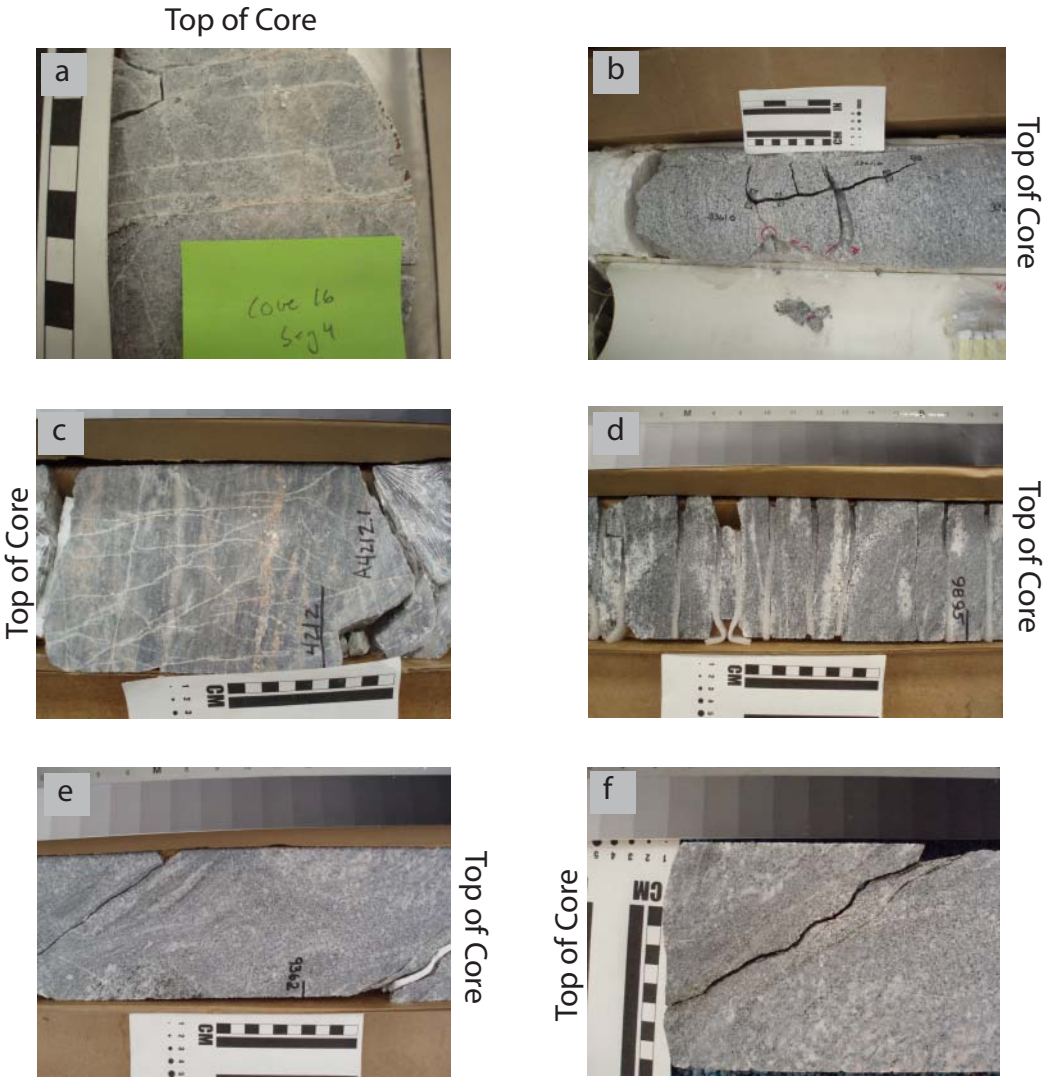

Figure 2-28. Photographs of typical fractures observed in the core. (a) Parallel white and pink zeolite filled fractures from 1284 m depth. (b) Induced and natural fractures from 1024 m depth. The induced fracture makes a right angle, and the natural fracture in perpendicular to the induced fracture. (c) Fracture web with white zeolite fill from 1284 m depth. (d) Induced disk fractures from 3016 m depth. (e) and (f) Dipping open fracture from 2854 m depth.

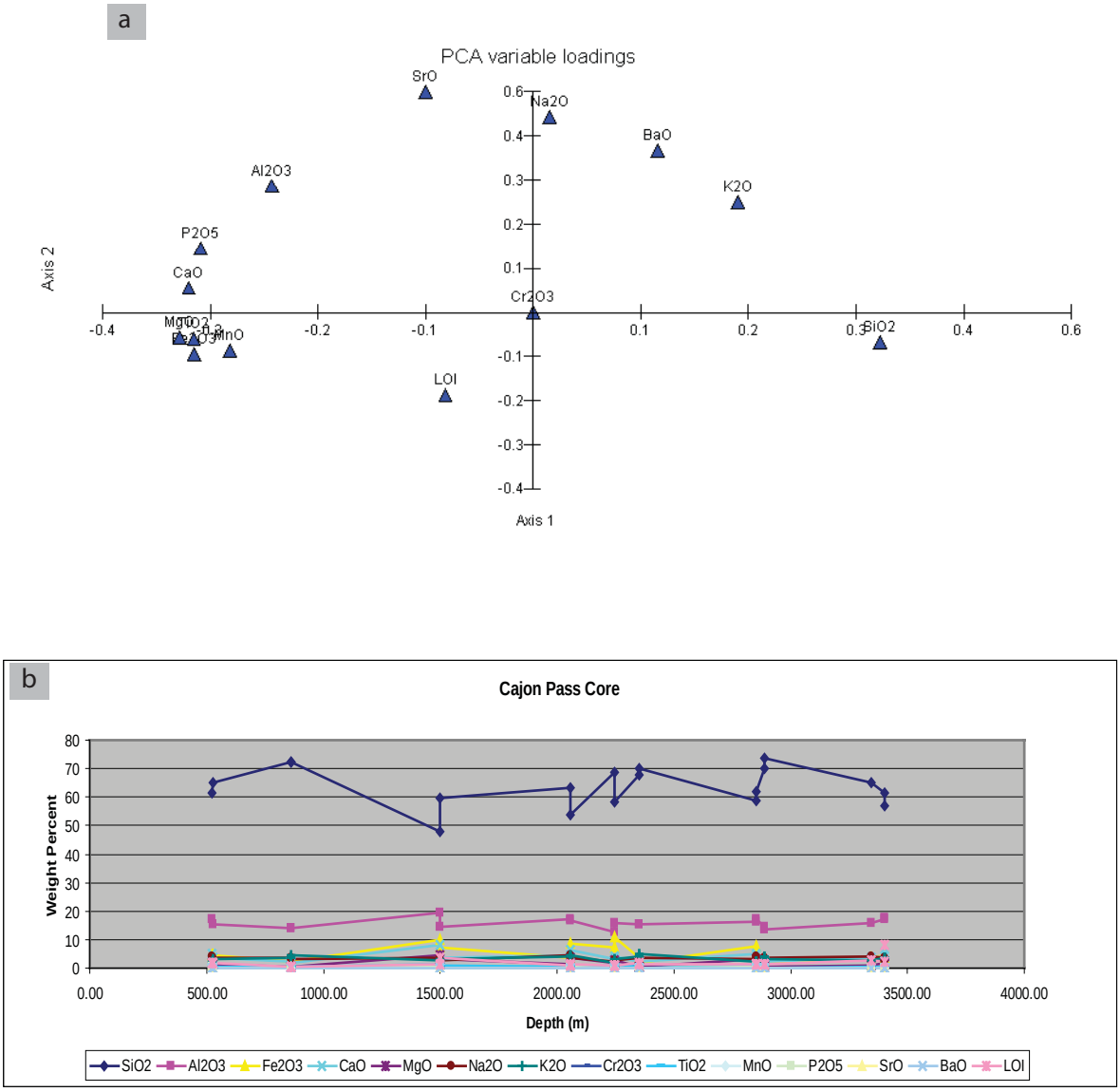

Figure 2-29. Whole rock geochemistry of all samples from the Cajon Pass core. (a) Principal Component Analysis of all oxides and LOI. The variables farthest away from the origin of the plot are the most significant. (b) Scatter plot of weight percent of all oxides and LOI vs. depth.

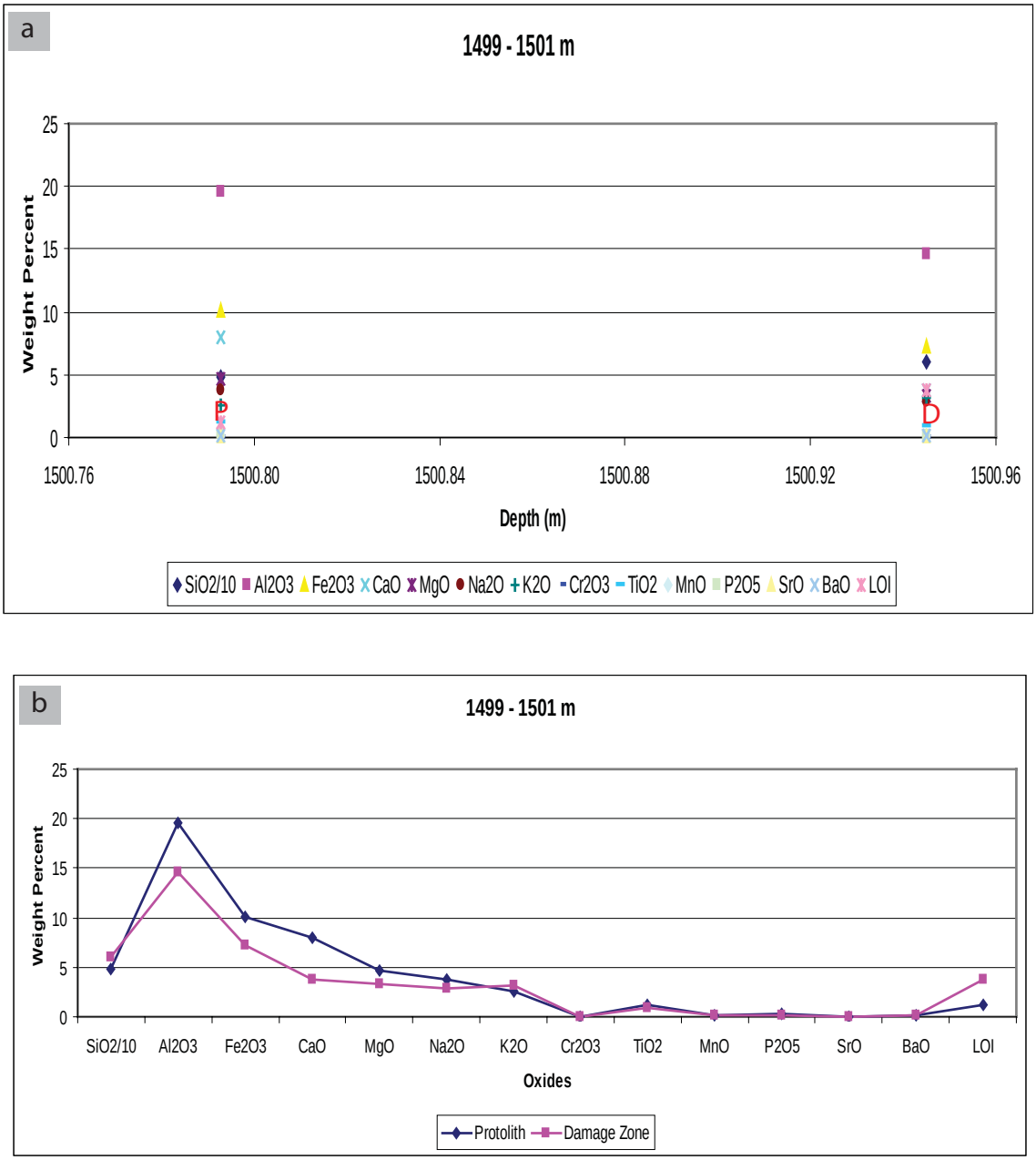

Figure 2-30. Whole-rock geochemistry of the 1499 – 1501 m fault zone. (a) Plot of weight percent of all oxides and LOI with respect to depth. D = damage zone, P = protolith. (b) Spider diagram of oxides and LOI in weight percent.

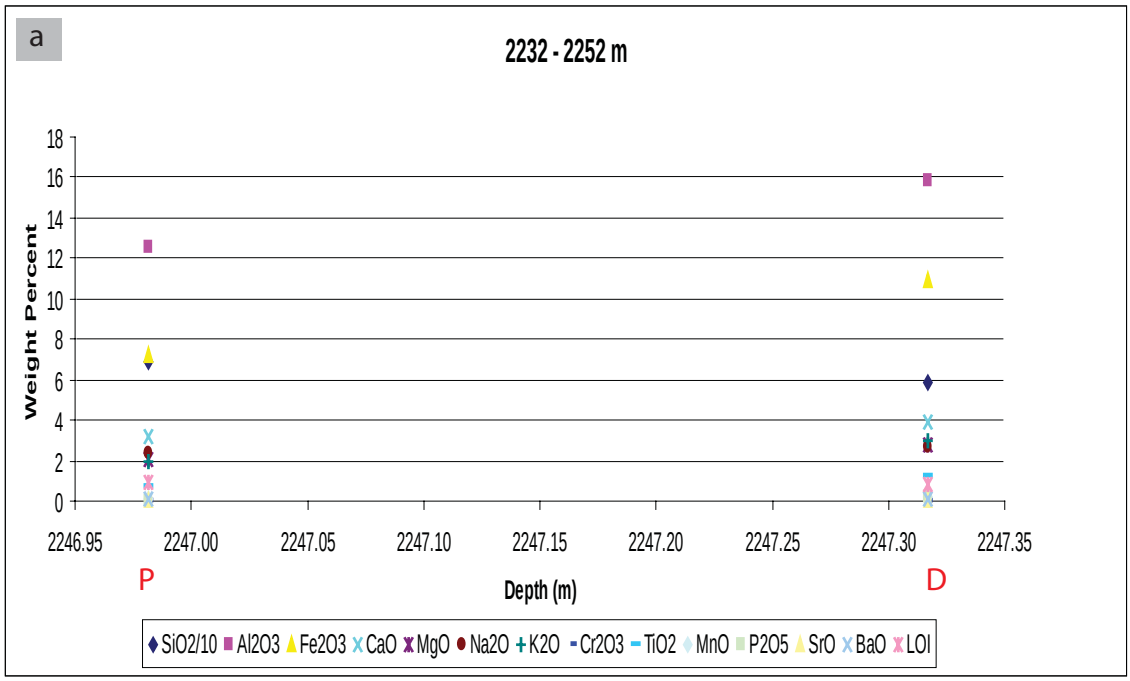

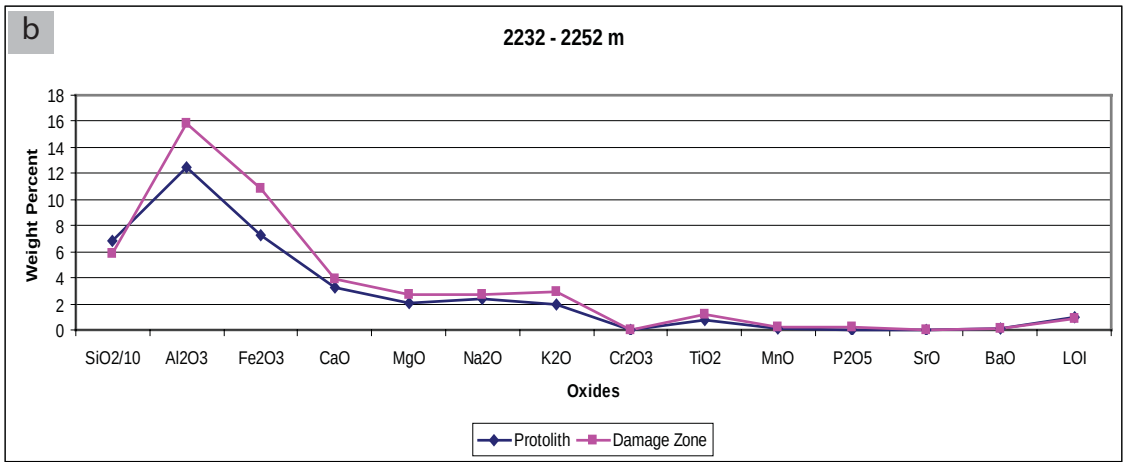

Figure 2-31. Whole-rock geochemistry of the 2232 – 2252 m fault zone. (a) Plot of weight percent of all oxides and LOI with respect to depth. D = damage zone, P = protolith. (b) Spider diagram of oxides and LOI in weight percent.

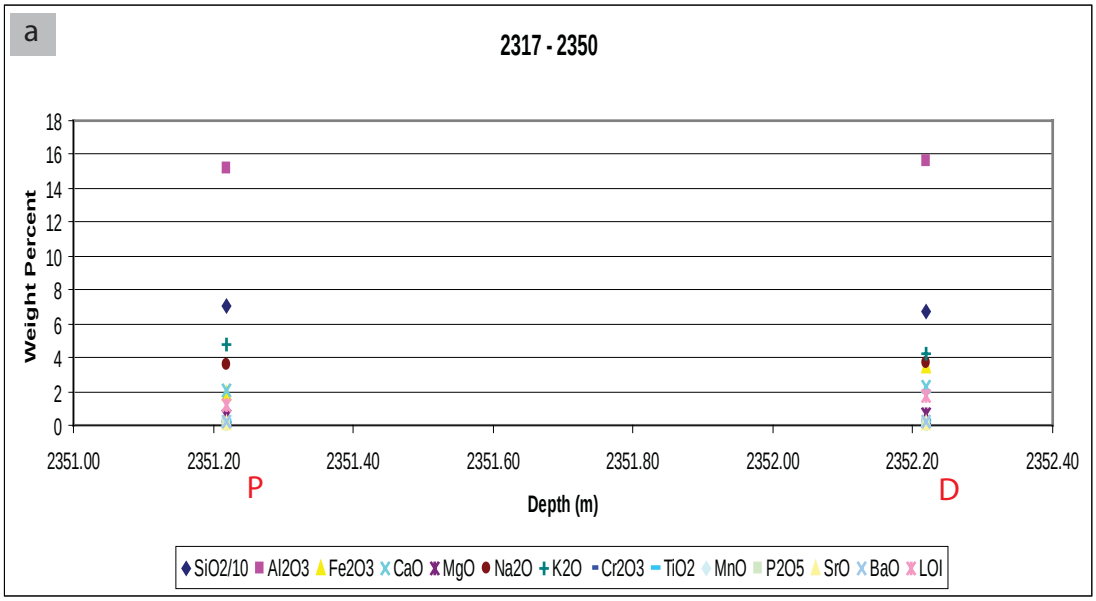

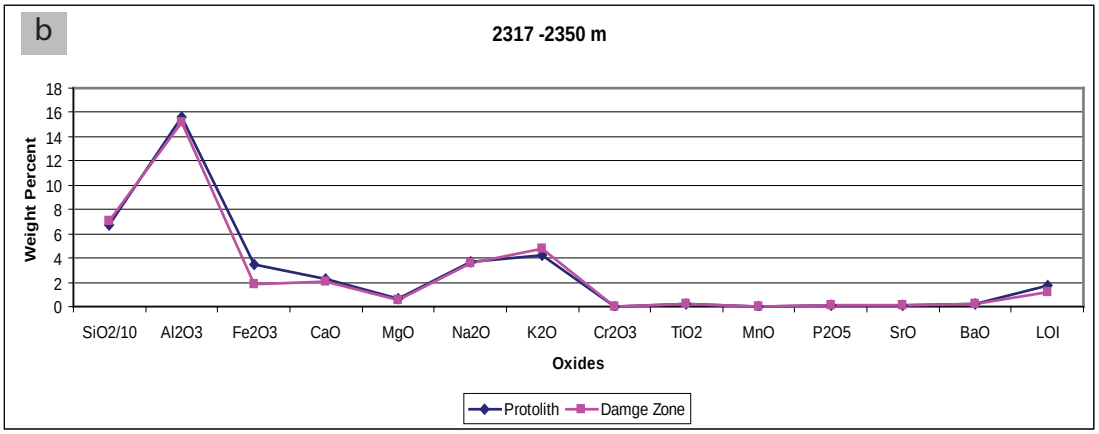

Figure 2-32. Whole-rock geochemistry of the 2317 – 2350 m fault zone. (a) Plot of weight percent of all oxides and LOI with respect to depth. D = damage zone, P = protolith. (b) Spider diagram of oxides and LOI in weight percent.

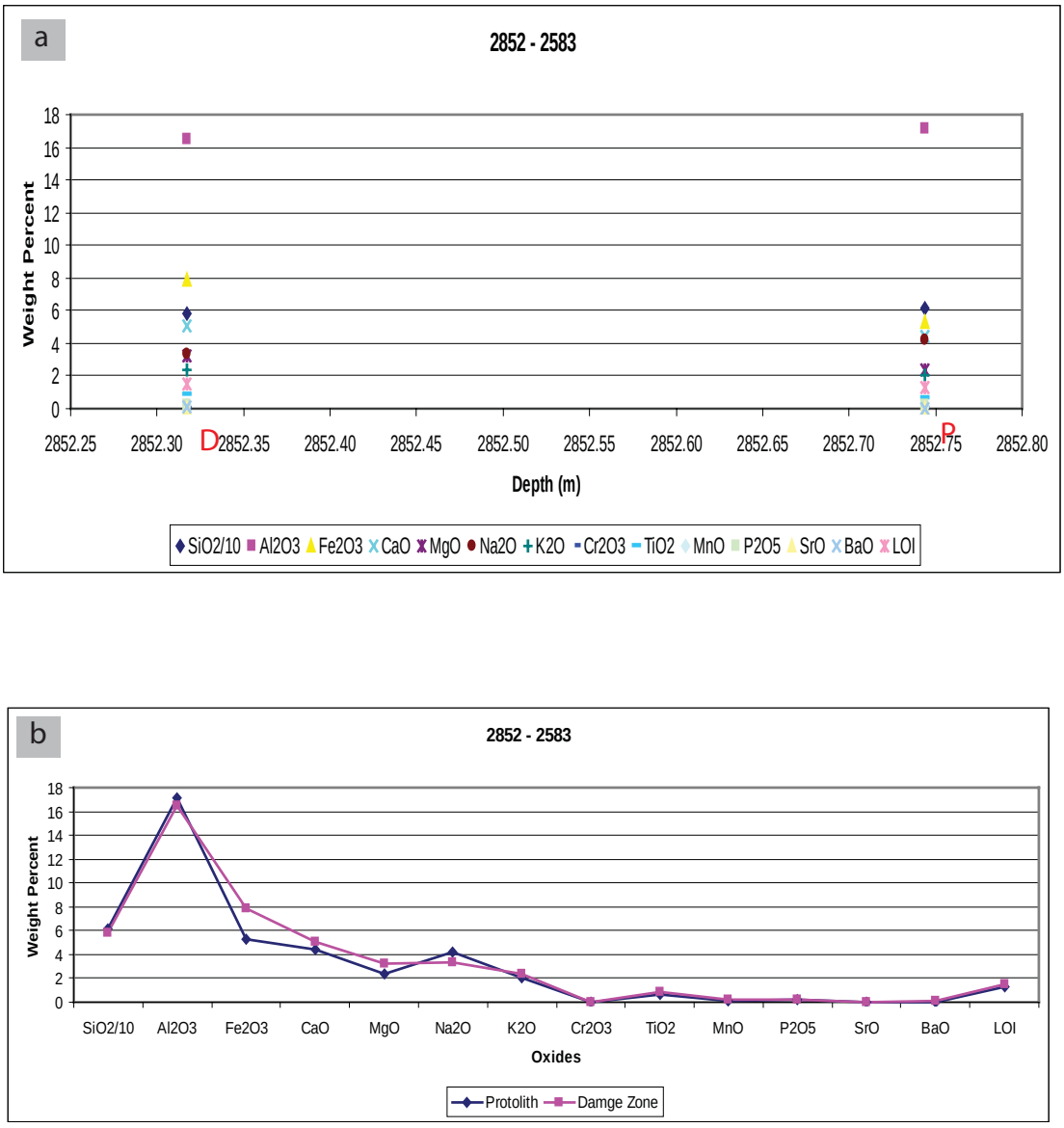

Figure 2-33. Whole-rock geochemistry of the 2852 – 2853 m fault zone. (a) Plot of weight percent of all oxides and LOI with respect to depth. D = damage zone, P = protolith. (b) Spider diagram of oxides and LOI in weight percent.

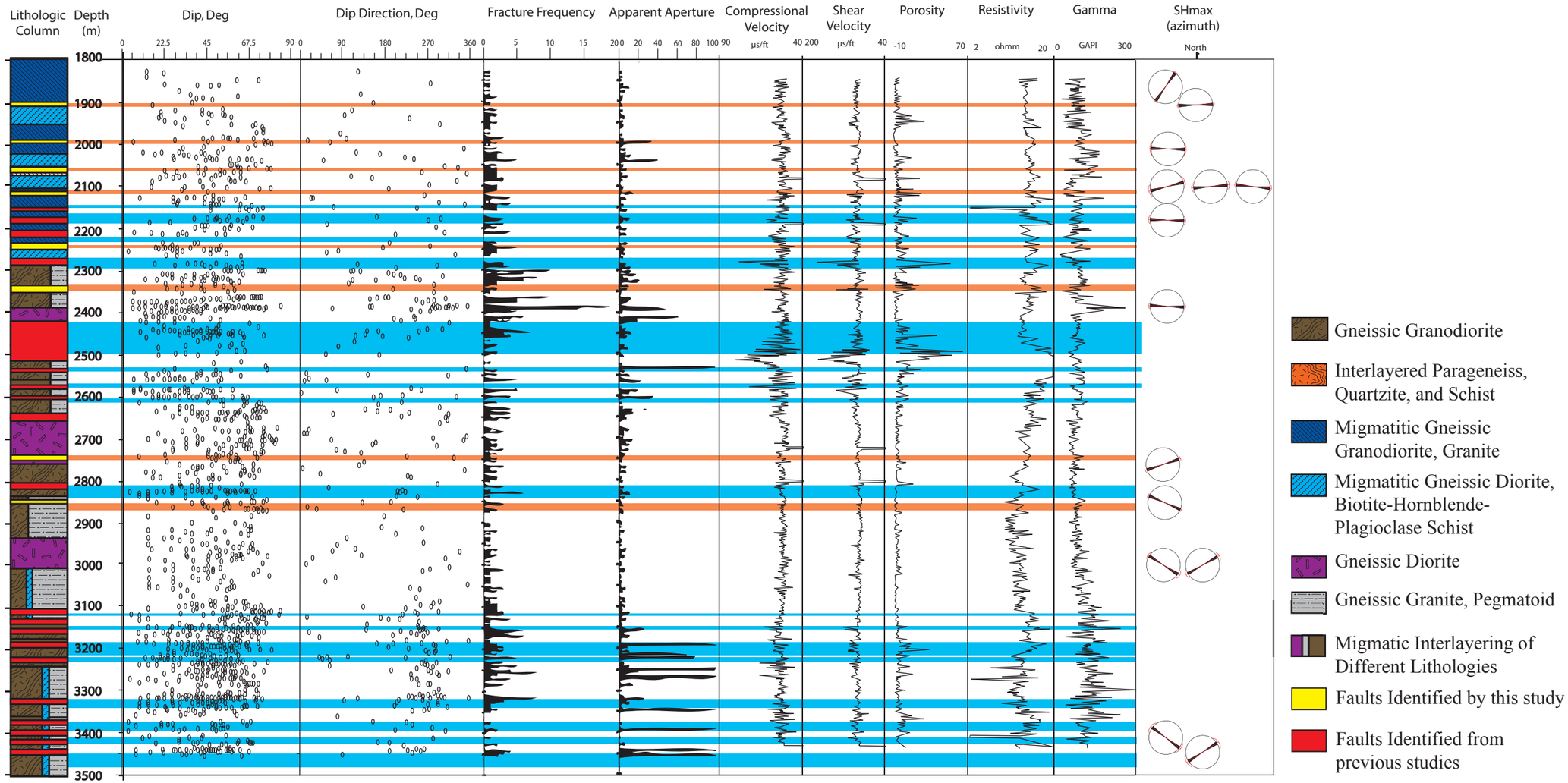

Figure 2-34. Lithologic column of the crystalline core and Cajon Pass borehole from depths 1800 m to 3500 m with wireline log data. Revised lithologic column of the Cajon Pass Borehole from Vernik and Zoback (1992) as determined from core, cuttings, and wireline log data. Dip degree, dip direction, fracture density, apparent fracture aperture, Vp, Vs, Porosity, Resistivity, Gamma logs are from Barton and Zoback (1992). σHmax from Zoback and Healy (1992). North is marked at the top of the column and the red lines around the circles represent associated error with each measurement. Orange lines mark locations of newly identified faults from this study. Blue lines represent previously identified faults. Positive and negative correlations of the faults with log data are displayed in Table 2-2. Location of the borehole is marked in Figure 2-2 and 2-3.

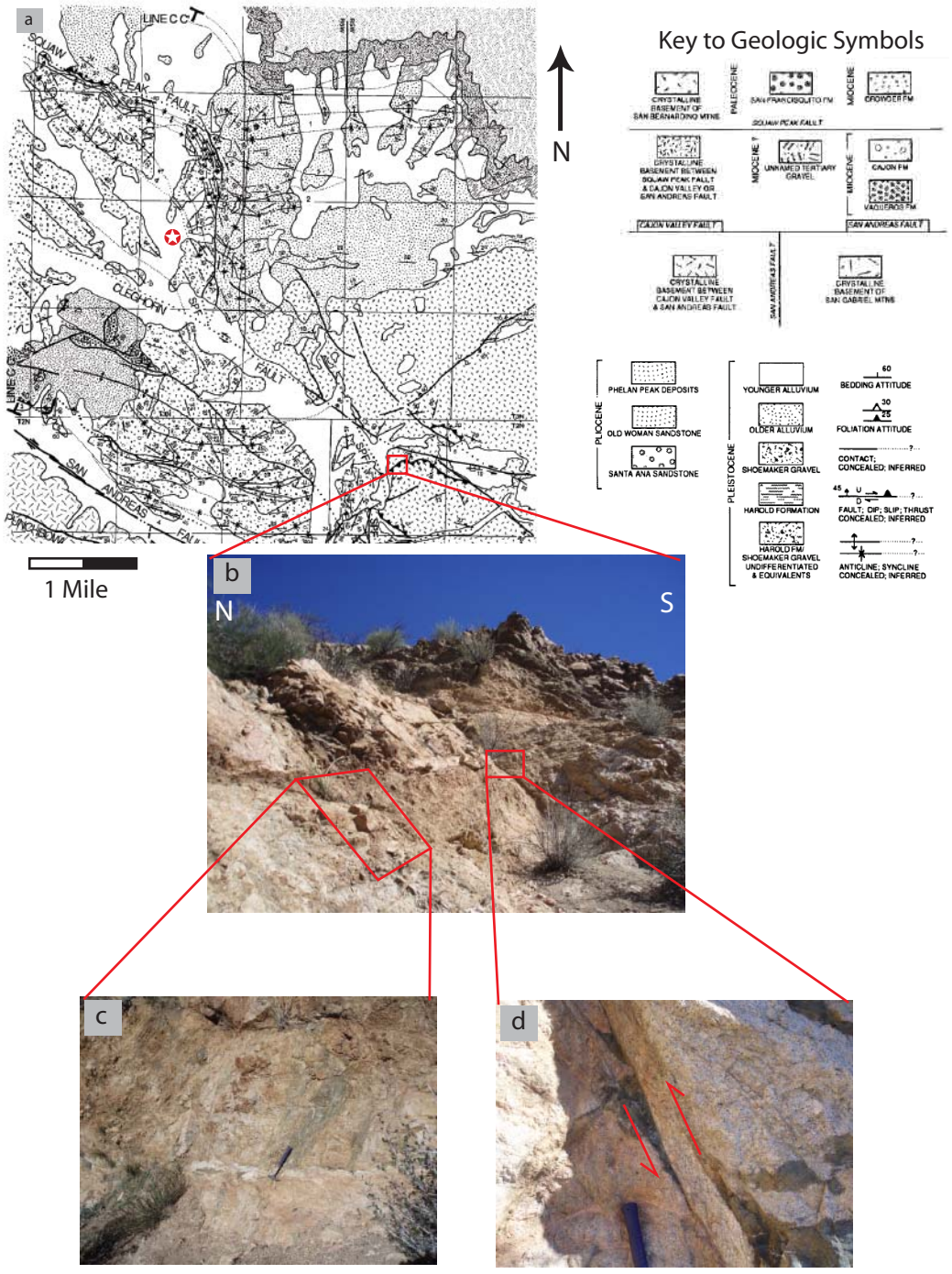

Figure 2-35. Photos of the field site in the Cajon Pass used in this study. (a) Portion of the geologic map of the Cajon quadrangle by Miesling (1984) showing the location of the borehole and the field site. (b) Overview photograph of the field area showing two dip-slip faults. (c) (d) Close up photographs of the two faults. Note the pink coloration of the host rock in the damage zone.

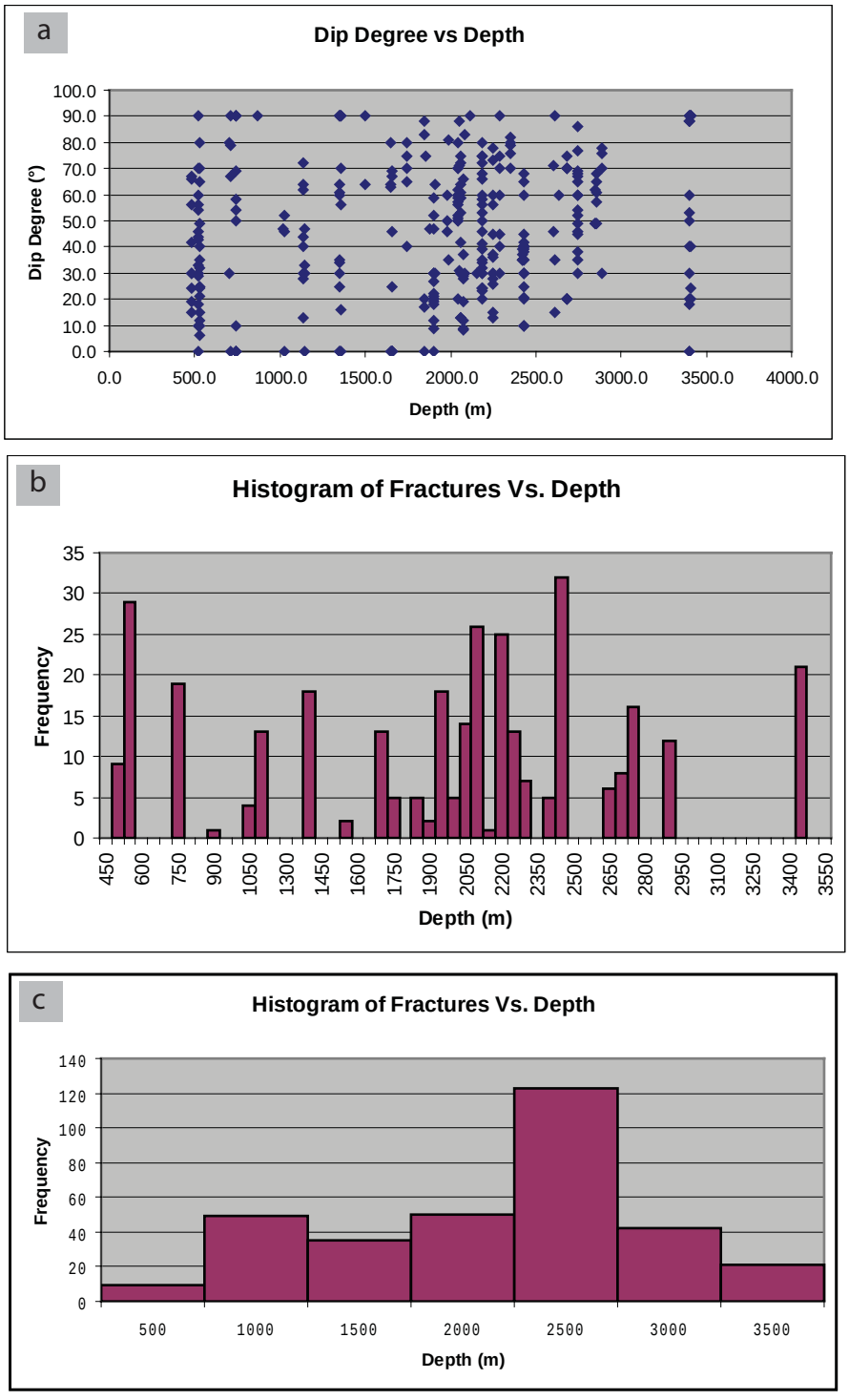

Figure 2-36. Graph and histogram of fractures and fracture dips vs. depth using all 329 fractures measured from this study. (a) is a plot of fracture dip vs. depth and (b) and (c) are histograms of fracture frequency vs. depth with different bin sizes. There is a strong correlation with range of fracture dips and the location of fault zones within the core. (a) and (b) have very similar geometries, as core segments with a high density of fractures (b) align well with the histogram.

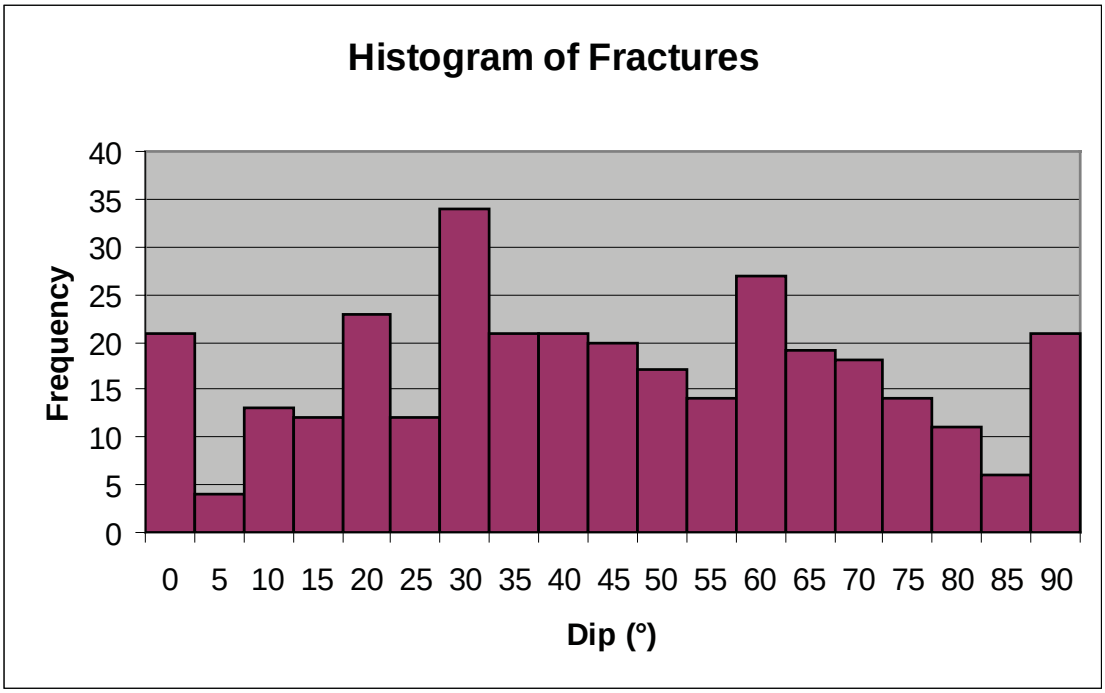

Figure 2-37. Histogram of all 329 fracture dips measured from core logged for this study. The mean of these fractures is 45°.

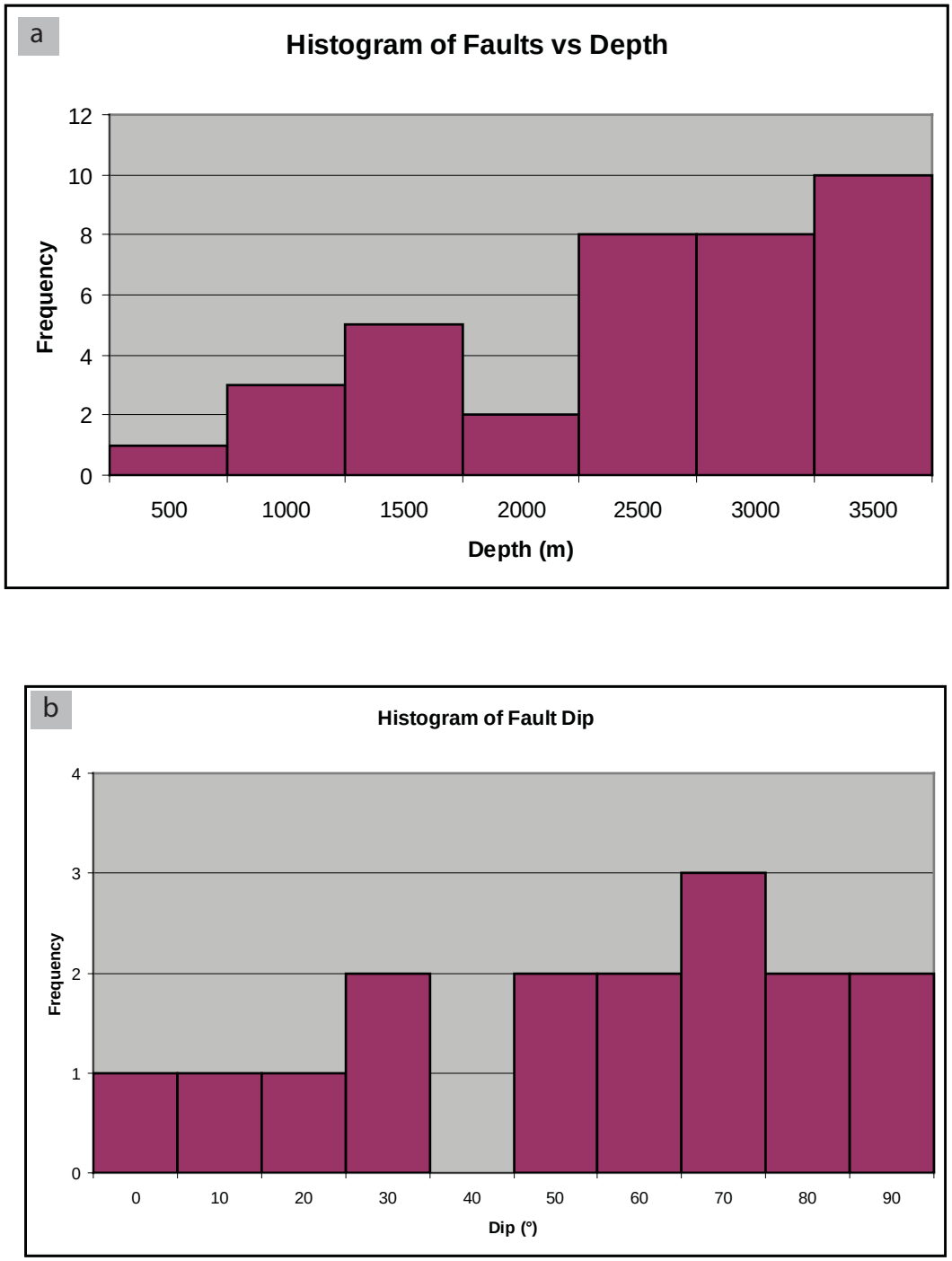

Figure 2-38. Histograms of faults in the Cajon Pass core. (a) Histogram of the frequency of faults at depth showing an overall increasing number of faults at depth with a low at 2000 m depth. (b) Histogram of fault dips.

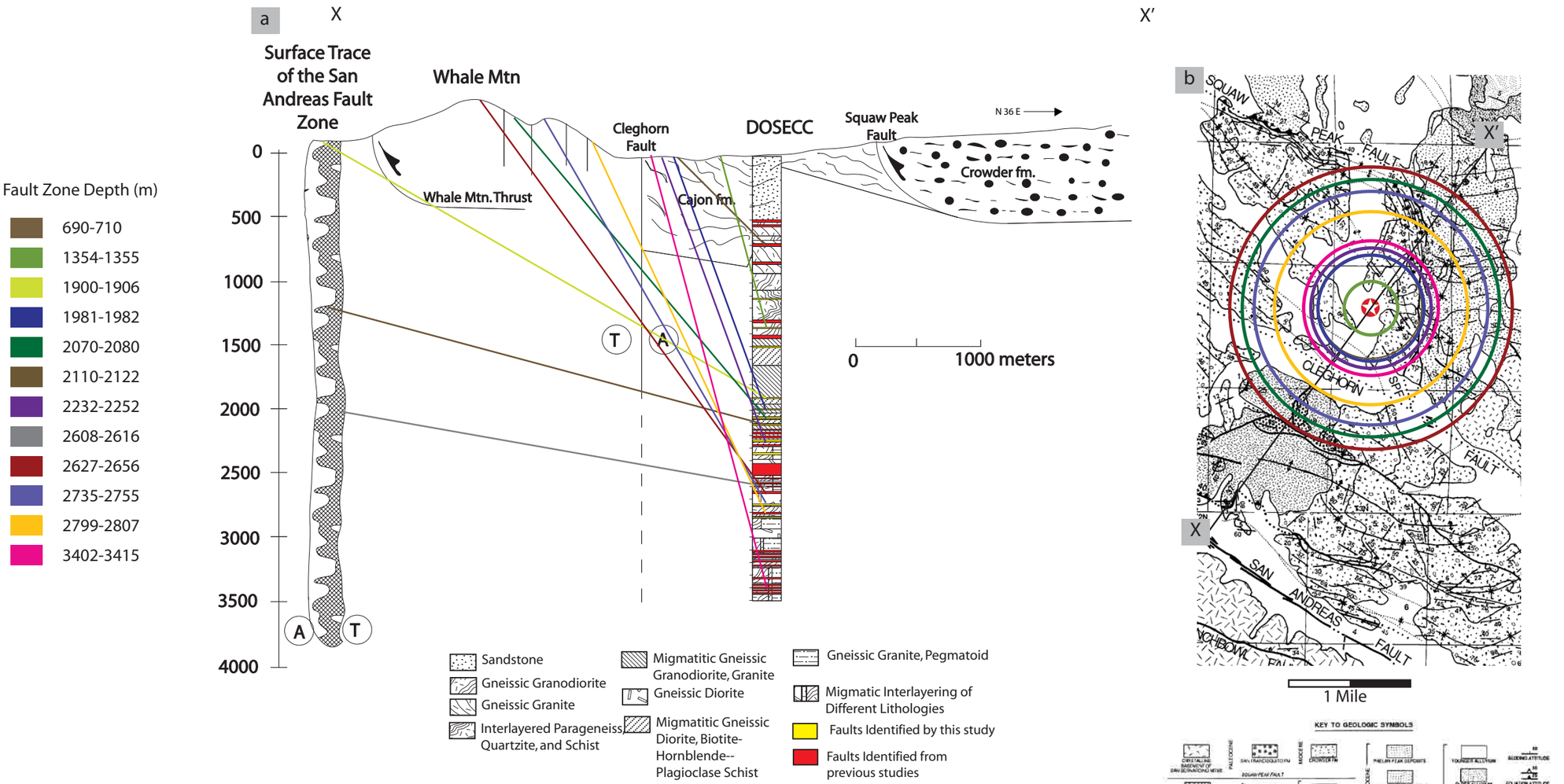

Figure 2-39. Cross-section and map displaying fault correlations in the Cajon Pass. (a) Cross section of the Cajon Pass with the extrapolation upward and southwestward of measurable faults in the borehole by assuming that the dips in the core are persist to the surface. Cross section modified from Zoback and Healy (1992). Each color represents a different fault at depth. Note the excellent correlation of the fault at 3402 m depth with the Cleghorn fault. A lithologic column modified from Vernik and Nur (1992) has been placed on the location of the borehole. T and A denote towards and away motion on the strike-slip faults. (b) Map of the Cajon Pass area modified from Meisling and Weldon (1989). Each colored circle represents an extrapolation of a fault from the core to a potential fault correlation location on the surface. The circles area appropriate because the core in unorientated, making the strike unknown. The colors of each circle correspond with the faults in the cross section.

Figure 2-40. Photograph of fully intact core of fault from 3402 m depth. Note the green and pink alteration and the distinct slip surface in the core. This core may be the Cleghorn fault.

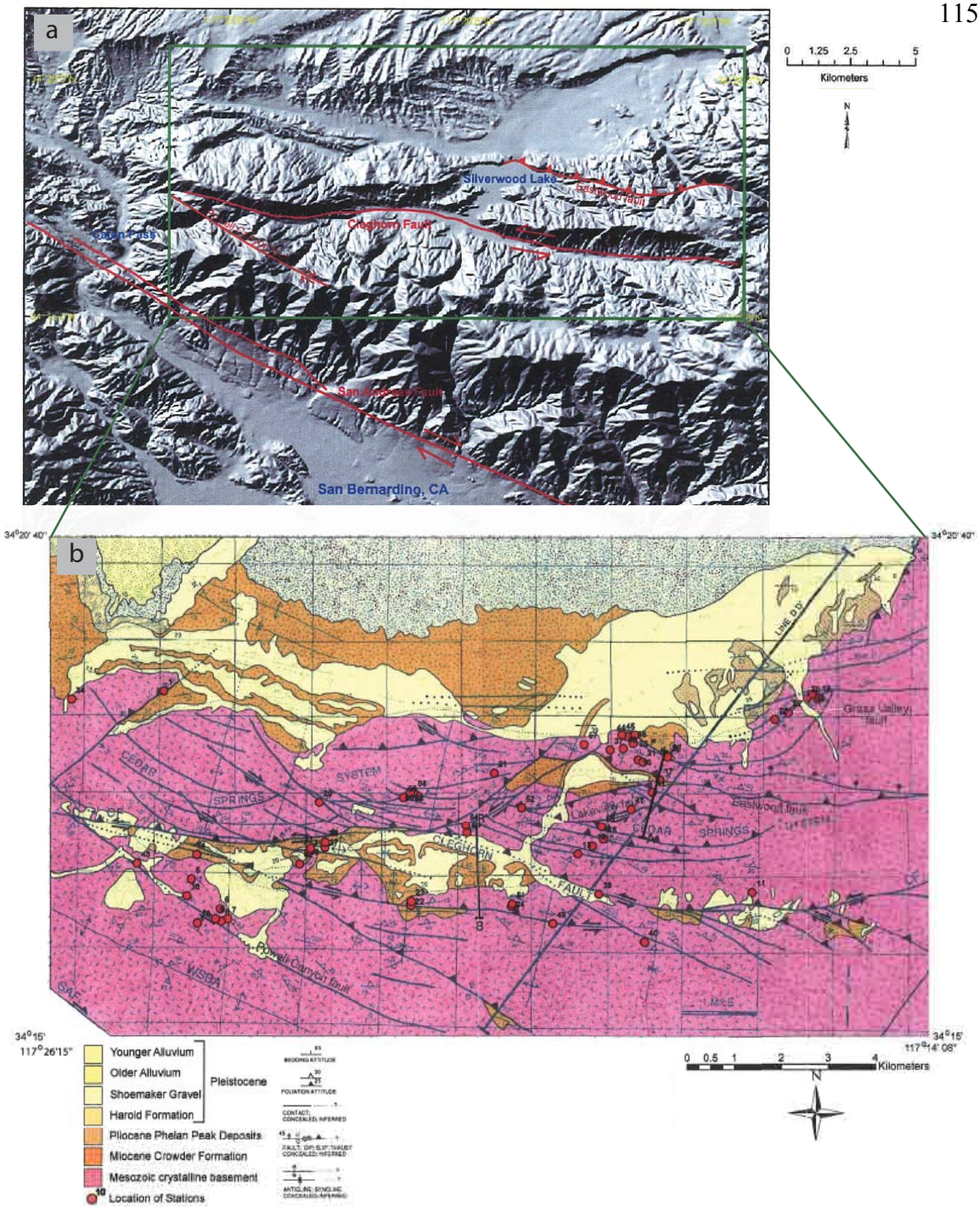

Figure 2-41. Map of the western San Bernardino Mountains, with sample locations from Jacobs (2005). (a) Shaded relief image of western San Bernardino Mountains with the major faults annotated in red and geographic locations in blue. (b) Geologic map of the Silverwood Lake Area from Meisling and Weldon (1989). The red circles represent stations from fieldwork by Jacobs (2005).

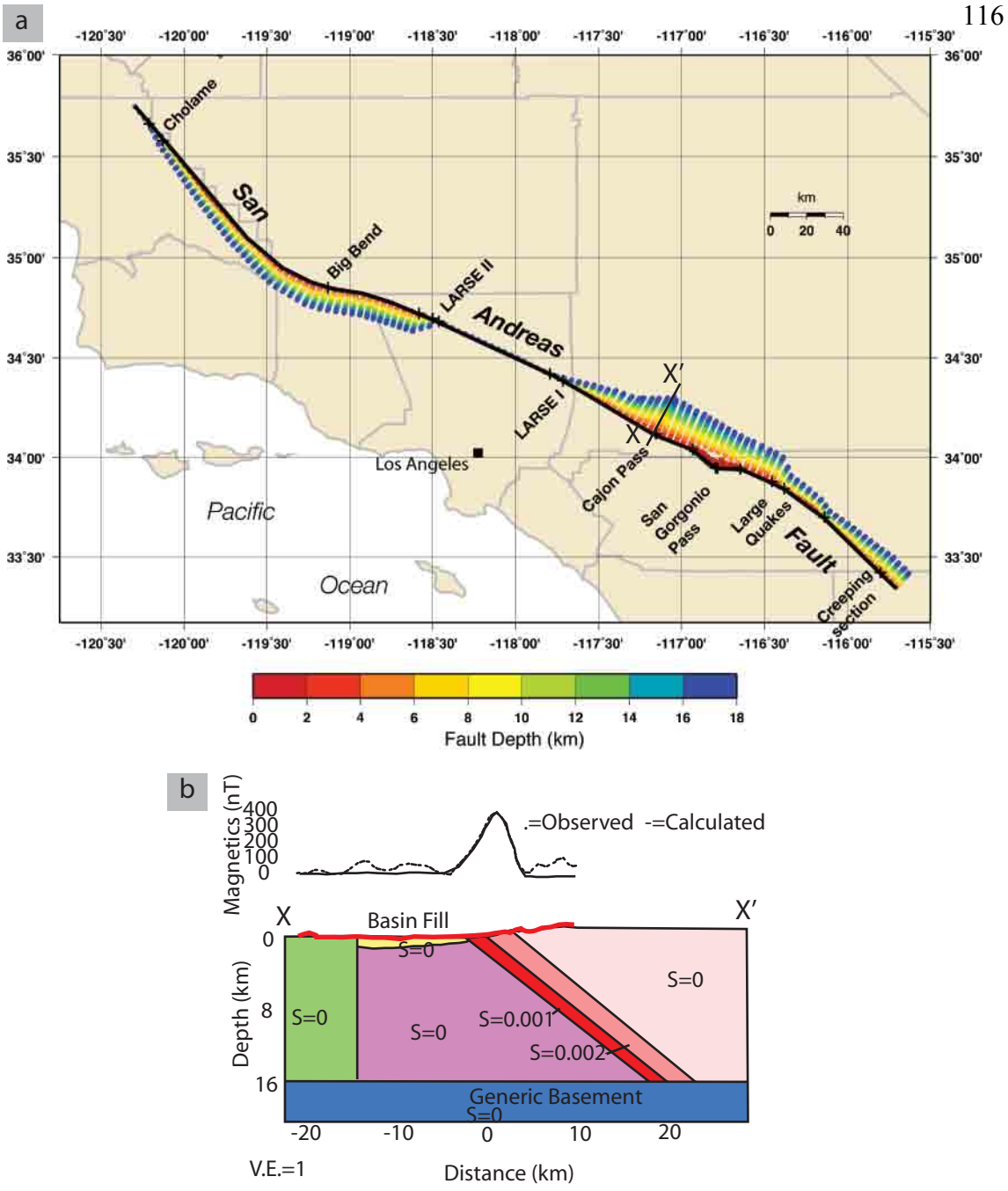

Figure 2-42. Image of the San Andreas fault dip and magnetic anomaly cross section of the Cajon Pass from Fuis et al. (2008). (a) Map of southern California showing the dip of the San Andreas fault. Warm colors correspond with shallower depths, cool colors are deep. (b) Cross section X-X', with magnetic anomaly of the Cajon Pass showing a 37° dipping SAF.

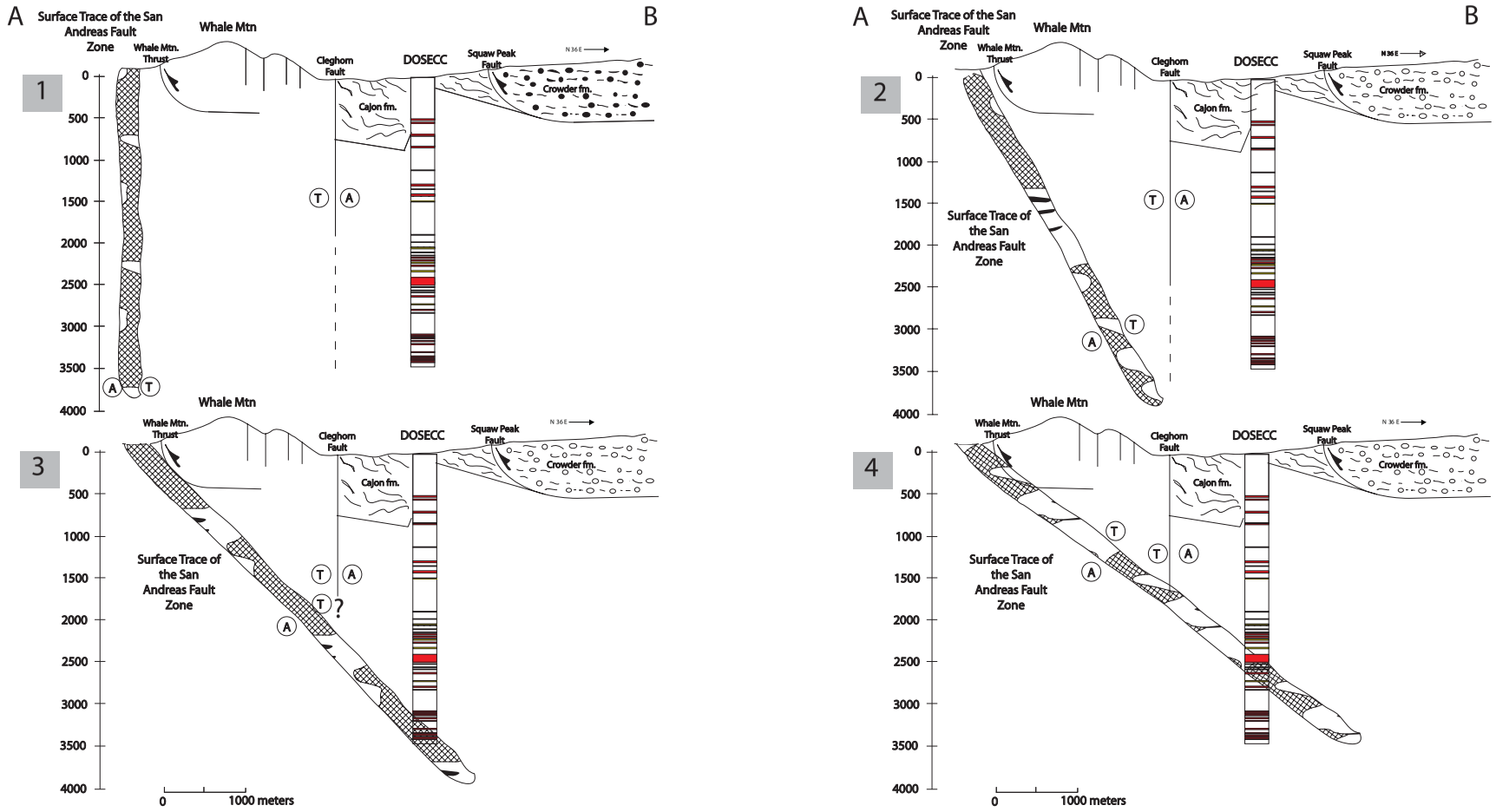

Figure 2-43. Four cross-sections showing various orientations of the SAF and its spatial relationship with the CPDDH. Revised cross section from Zoback and Healy (1992) with lithologic column by Vernik and Nur (1992). The location of the cross section line is shown on Figure 2-3. 1=SAF at 90°; 2=SAF at 60°; 3=SAF at 45°; 4=SAF at 37°.

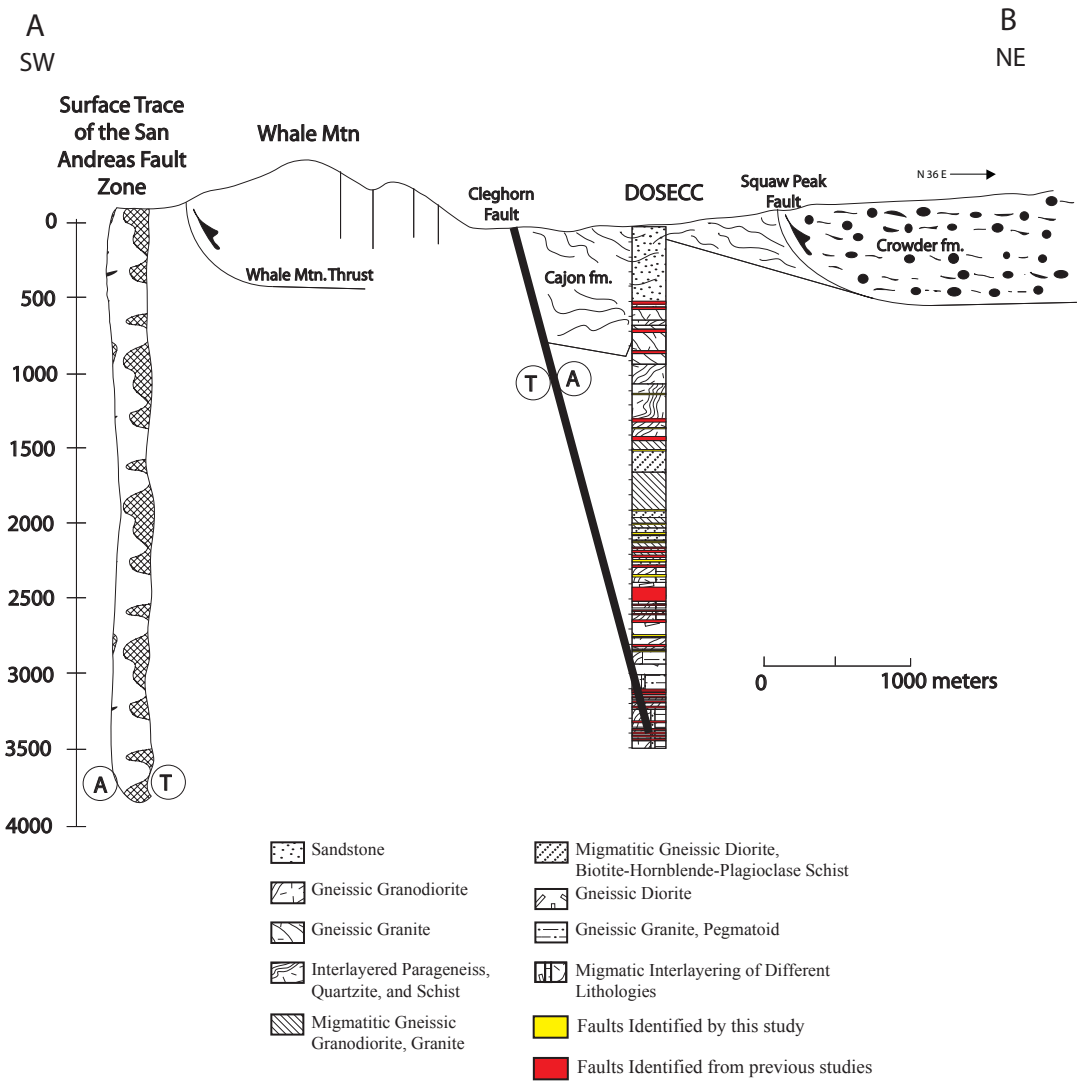

Figure 2-44. Simplified cross section of the Cajon Pass showing the relationship of the San Andreas fault, Whale Mountain thrust, Cleghorn fault, and Squaw Peak fault to the location of the borehole modified from Zoback and Healy (1992). The location of the cross section is on Figure 2-3. A lithoogic column modified from Vernik and Nur (1992) has been placed on the location of the borehole. T and A denote towards and away motion on the strike-slip faults. The Cleghron fault is drawn showing a 75° dip, and highlighting the correlation with the fault zone at 3402-3414 m depth, as suggested by this study as one possible correlation. Note the sense of movement is left-lateral, as opposed to the right-lateral San Andreas Fault.

CHAPTER 3

SEPARATION ACROSS THE CLARK FAULT, AND STRUCTURAL CHARACTERIZATION OF THE CLARK AND COYOTE CREEK FAULTS, CLARK VALLEY, COYOTE MOUNTAIN, SOUTHEAST SANTA ROSA MOUNTAINS, CALIFORNIA[1]

Abstract

We determined a revised right separation across the Clark fault along the Santa Rosa segment using a marker assemblage of biotite, hornblende-bearing tonalite – marble-bearing metasedimentary rocks - migmatite located in Coyote Mountain and the southeast Santa Rosa Mountains. Separation measured from this study is 16.8 km + 3.67 km / -6.03 km. Our measurement uses the updated location of the Clark fault in Clark Lake Valley and matches a distinctive lithologic contact across the fault instead of matching the diffuse western boundary of the Eastern Peninsular mylonite zone (Sharp, 1967). Our results are more robust because we calculate the errors associated with projecting the lithologic contacts across Quaternary cover to the trace of the Clark fault, and consider a range of plausible projections.

Additional strain may be present in folds and small faults within the damage zone of the San Jacinto fault zone. Two large map-scale folds deform the marker assemblage near the San Jacinto fault zone and we tested whether Cretaceous ductile deformation or brittle late Quaternary right slip in the San Jacinto fault zone produced the folds. Well developed ductile fabrics, a vertical to overturned western fold limb, and uncommon

[1] Coauthored by David H. Forand and Susanne U. Janecke

brittle fabric elements reflect the Cretaceous contractional origin of the anticline northeast of the Coyote Creek fault in the southeast Coyote Mountain. An anticline northeast of the Clark fault in the Santa Rosa Mountains has an east trend that is not consistent with formation as a drag fold in the Clark fault's damage zone, has limited lateral extent, is cut by latest Cretaceous to early Tertiary (?) brittle faults of the Palm Canyon fault system. It thus predates slip on the San Jacinto fault zone. Although our study rules out significant right separation partitioned into folded rocks, a dense population of brittle faults in the damage zone accounts for some additional right separation. Most of the slip is too distributed to quantify, except across the Mid Ridge fault zone, which is roughly half way between the Clark and Coyote Creek faults. The > 7 km long Mid Ridge fault zone was not identified as a continuous or significant structure by Sharp (1967) or Theodore and Sharp (1975) yet the zone produced a right separation of the marker assemblage of 0.5-3 km. The separation has a large uncertainty because the contact must be projected across a large expanse of Quaternary cover and into the hanging wall of a younger cross fault. Though many fairly long faults are present in the damage zone of the Clark fault in the SE Santa Rosa Mountains they do not have significant right lateral strain. More detailed maps are needed to verify this preliminary interpretation.

3-1. Introduction

3-1.1. Geologic Context

The San Jacinto fault zone, southern California, is approximately 300 km long, and produces the most small to moderate earthquakes of any active fault in the San

Andreas fault system in southern California (Sharp, 1967; Thatcher et al., 1975). The San Jacinto fault zone accommodates between 19 and 29 km of right separation of the transform plate boundary between the North American and Pacific plates (Bartholomew, 1970; Sharp, 1967; Dibblee, 1954; Hill, 1984; Sanders, 1989; Revenaugh, 1998; Janecke et al., 2005). It consists of several dextral strike-slip faults that together accommodate a large fraction of the plate motion in southern California. One of the longer faults in the zone is the Clark fault (Figure 3-1).

The Clark fault is a 145-150 km long active oblique dextral strike-slip fault with a minor southwest-down component of slip (Sharp, 1967; Sanders, 1989; Belgarde, 2007). It trends west-northwest and cuts metasedimentary and plutonic rocks of the Peninsular Ranges and late Cenozoic sedimentary rocks of the Salton Trough (Sharp, 1967) (Figure 3-1). This fault contains seven distinct segments from north of Hemet, California to the Extra fault in the southeast (Sharp, 1967; Sanders, 1989; Kirby et al., 2007; Belgarde, 2007). The Anza segment of the Clark fault has 23 km of right separation based on displacement of Cretaceous intrusive rocks (Sharp, 1967).

The two segments of the Clark fault (Figure 3-2) that are of interest to this study are the Clark Valley and Santa Rosa segments (Sanders, 1989). The Clark Valley segment is bounded on its northwest end by a 1 km step and 14º bend to the Horse Canyon segment to the northwest (Sanders, 1989). Towards the southeast, along the Santa Rosa segment, the right separation was thought to decrease to approximately 14.5 km (Sharp, 1967). The Santa Rosa and Clark Valley segments are 12 and 22 km long respectively (Sanders, 1989; Steely et al., 2009; Janecke et al., in revision).

South of the Clark fault is the Coyote Creek fault, which is an approximately 121-km long dextral strike-slip fault with a northwest strike that diverges southeastward from the Clark fault. The fault zone is comprised of interconnected fault step-overs and bends north of the junction with the Superstition Mountain segment in the southeast. The Coyote Creek fault is comprised of six main segments and separates similar rock types as the Clark fault in the study area. This fault is thought to be slightly younger than the Clark fault and has much less total separation (Sharp, 1967; Dorsey, 2002; Janecke et al., 2005; Janecke et al., in revision). The Coyote Creek fault accounts for approximately 1.0 - 4.8 km of right separation at Coyote and Borrego Mountains (Sharp, 1967; Janecke et al., 2005; Steely et al., 2005, Steely 2006).

The two segments of interest of the Coyote Creek fault (Figure 3-2) are the Coyote Ridge segment located northeast of Upper Borrego Valley and the Coyote Canyon segment located in Coyote Canyon. These two segments are the two most northern segments of the Coyote Creek fault and comprise approximately 32 km of its 80 km length. At its northernmost end, the Coyote Canyon segment of the Coyote Creek fault has a 5 km wide releasing step to the Horse Canyon segment of the Clark fault (Sanders, 1989). Right separation along the Coyote Ridge segment of the Coyote Creek fault was estimated to be approximately 5 km by Sharp (1967), and 6 km by Dorsey 2002 but this value has been revised downward to approximately 3.5 km (Janecke et al., 2005; Janecke et al., in revision).

Seismicity along the San Jacinto fault zone is well characterized by Sanders and Kanamori (1984), Sanders (1989), Sanders et al. (1986), and Sanders and Magistrale

(1997). New relocated earthquakes reveal much additional structure of the fault zone (Shearer et al., 2005; Lin et al., 2007).

3-1.2. Tectonic History

The ~300 km long San Jacinto fault zone initiated between ~1.5 and 1.1 Ma as a response to a change in the plate boundary motion (Morton and Matti, 1993; Kirby, 2005; Janecke et al., 2006; Lutz et al., 2006; Kirby et al., 2007). Between 19 and 29 km of right separation (Sharp, 1967; Bartholomew, 1970; Hill, 1984; Morton and Matti, 1993; Janecke et al., 2005) is accommodated by a series of dextral strike-slip faults that generally trend ~130°; but faults bend, branch, and diverge, forming a complex network of separate faults within the zone (Dibblee, 1954; Sharp, 1967, 1975; Sanders, 1989).

Sometime between 97 and 62 Ma, long before activation of the San Jacinto fault zone, the eastern Peninsular Ranges mylonite zone developed as a top-to-the-west thrust system (Sharp, 1979; Simpson, 1984; Todd et al., 1988). It contains marble-rich marker zones that are used in this study in the Santa Rosa and Coyote Mountains (Todd et al., 1988). During the late stages of its late Cretaceous – early Tertiary evolution the higher structural levels of the mylonite zone may have been cut near its top by a brittle low-angle fault system that may have normal or thrust slip across it (Erskine and Wenk, 1985; Goodwin, oral communication, 2009). Before 62 Ma, the mylonite zone was cut by the brittle low-angle faults that juxtaposed different structural levels of the mylonite terrane. This transition from ductile to brittle deformation may have accompanied uplift and unroofing in the latest Cretaceous to early Tertiary time (George and Dokka, 1994; Dickinson, 1981; Engel and Schultejann, 1984; Todd et al., 1988; Grove et al., 2003), but

this is controversial and some of the brittle faults might be late Cenozoic (Axen and Fletcher, 1998). The ductile structures were displaced and reactivated by the West Salton detachment fault during slip across the San Andreas transform fault in the Miocene and Pliocene (Axen and Fletcher, 1998).

3-1.3. Objectives

The study area is located in the Anza-Borrego Desert State Park, California, approximately 65 miles northeast of San Diego. The field area is comprised of two separate focus locations to meet the objectives of this study. They are the southeast Santa Rosa Mountains and Coyote Mountain (Figure 3-2). A marker zone present in each focus location was located, characterized, mapped, and used as an offset contact surface. The approximately 5.5 miles wide Clark Valley separates the two locations. Large parts of the Santa Rosa segment of the Clark fault are concealed in the alluvium of Clark Valley (Sharp, 1967; Theodore and Sharp, 1975; this study, Appendix I).

The objective of this study is to determine the displacement along the central traces of the Clark fault in the area of Clark Dry Lake, along the Santa Rosa segment, and to determine the nature of and how much strain is accommodated adjacent to the fault in the damage zone. The working hypothesis tested here is that similar large folds located northeast of the Coyote Creek fault and the Clark fault formed in the damage zone of the dextral faults and represent additional displacement across the San Jacinto fault zone.

A marble-rich zone and its enclosing rocks in these ranges along the Clark and Coyote Creek faults were mapped and described. Mapping for this study was used to find and characterize distinctive rock units to determine separation across the Clark fault.

Though geologic maps of portions of the study area were made and included here, updating and mapping the entire region of interest was beyond the scope of this study. These mountains are an excellent area to map the displacement and strain within the damage zone of two predominantly dextral strike-slip faults in crystalline rock. Specific questions for this study are:

1. Are folds in the damage zone of the Coyote Creek and Clark faults preexisting structures, or a result of dextral slip in the San Jacinto fault zone, or perhaps the result of both processes?
2. How much displacement is in the damage zone of the San Jacinto fault zone and how does it compare to strain across the main traces of the fault?
3. What is the displacement across the Clark fault zone and how well is this value known?

The significance of working in this area is two-fold: 1. Displacement has not been measured in this area since Sharp (1967) and Bartholomew (1970), except in an abstract by Janecke et al. (2005). 2. Recalculating displacement not only has implications for the geologic community but also to the populations living in proximity to these active faults. Working along the Clark and Coyote Creek faults in the Coyote and the Santa Rosa Mountains will be used to determine a more precise lifetime strain rate across the Clark and Coyote Creek faults by using the total accumulated strain of the entire San Jacinto fault zone and prior age estimates (Janecke et al., in revision). A marble–rich interval (Figure 3-3) located in the Santa Rosa and Coyote Mountains provides exposures that were used to measure right separation and strain in the damage zone of these faults and

the total right separation across the Coyote Creek and Clark strands of the San Jacinto fault zone.

Deformation, subsidiary smaller faults, and damage zone width were explored and noted in each location along with the lithology of rock units, the strike and dip of foliation, and orientation of lineations, if present. Quaternary fault scarps in each focus area were also mapped, as were relative ages of alluvium. The Clark fault in Clark Valley, along the Santa Rosa Mountains northwest to Rockhouse Canyon, was also examined using imagery and spot checks in the field.

Determining if deformation styles in the field are brittle or ductile can be used as a proxy for determining if strain is seismic or aseismic, late Cenozoic or Cretaceous. Brittle faults are shear surfaces that develop during elastic deformation of the rock when shear stress exceeds shear strength (Jaroszewski, 1980), typically characterized by a high density of irregular fractures and the formation of breccia or gouge. Ductile faults, shear zones, and folds on the other hand, are defined as shear surfaces which develop while the rock is undergoing permanent deformation, and occur in strain zones subjected to shearing that exceeds the ductility of the rock under the given conditions (Jaroszewski, 1980). Ductile shear zones could not have formed in the San Jacinto fault zone at the near surface conditions in the focus areas. We infer a Cretaceous age of deformations whenever there is evidence of ductile processes in shear zones and folds. The distinction between brittle and ductile structures is important because it allows potentially seismic deformation produced by the San Jacinto fault zone to be separated from preexisting deformation of the Eastern Peninsular Range mylonite zone.

3-1.4. Prior Work

The geology of bedrock adjacent to the Clark Valley, Santa Rosa, Coyote Canyon, and Coyote Ridge segments of the Clark and Coyote Creek faults is shown in a 1:63,360-scale strip map (Sharp, 1967). A much more detailed map of Coyote Mountain, in the Clark Lake Quadrangle, was produced at a 1:24,000 scale (Theodore, 1967; Theodore and Sharp, 1975). Sharp (1967) and Bartholomew (1970) produced generalized geologic maps of the Clark fault, as well as the Eastern Peninsular Ranges' mylonite zone in the Santa Rosa and Coyote Mountains. Bartholomew (1970) identified and collected data to suggest that the San Jacinto fault has a curvilinear surface trace and that the fault zone consists of three principal faults: the San Jacinto, Coyote Creek, and Clark faults. His interpretation has not been widely accepted. Dibblee (1954 and 1997) mapped a part of the Santa Rosa Mountains. Marble horizons were also mapped by Theodore (1967) and Theodore and Sharp (1975), but were not separated out and correlated across the faults. Janecke's unpublished mapping (2002-2007) shows that more than one marble-rich zone is likely to be present (Figure 3-3). Each zone needs to be fully characterized and traced laterally to faults and adjacent fault blocks to determine their lateral continuity and utility as marker units. Isoclinal folds and unrecognized duplication by thrust faults and shear zones, which were inferred but not well documented by Engel and Schultejann (1985), may repeat the marker zones. Only minimal mapping in the San Ysidro Mountains has been compiled by Rodgers (1963) and performed by Sharp (1967), Engel and Schultejann (1984), and Janecke (unpublished).

The marble-rich zone in the Santa Rosa Mountains was described by Sharp (1965) as a fine- to very coarse- grained calcite marble bed that constitutes a very small part of

the prebatholithic metamorphic country rock in the Santa Rosa and Coyote Mountains. The marble-rich zone is present throughout the Eastern Peninsular Ranges mylonite zone and is enclosed in zones of mylonitic deformation, which transect batholithic intrusive rocks as well as metasedimentary rocks (Sharp, 1965). Petrography performed on the marble in Coyote Mountain by Theodore (1970) shows that the majority of the marble has a calcite-dolomite- (diopside, tremolite) assemblage. The Santa Rosa Mountains may expose both calcite and dolomitic marbles (Theodore, 1967; B. Cox, personal communication).

Two notably marble-rich sections of metasedimentary rocks are exposed on the eastern slope of Coyote Mountain and at the south end of the Santa Rosa Mountains (Theodore and Sharp, 1967; Janecke, unpublished) (Figure 3-3). The structurally lower, western marble marker zone varies in thickness, but in most areas it is less than ~7 m thick (Sharp, 1965). The marble zone is associated with a metamorphic assemblage including reddish weathering quartzite, pegmatites, gabbroic, tonalitic, and adamellitic plutons (Sharp, 1965). This unique assemblage is present throughout the field area. These are prebatholithic rocks and are quartz-rich, carbonate-bearing metasedimentary rocks that are probably deformed and metamorphosed remnants of the Paleozoic miogeoclinal prism shed westward from the North American craton (Todd et al., 1988). It is not possible to reconstruct an original pre-metamorphic section because of complexity of the metamorphic bodies, interruption by intrusive bodies, and the lack of continuous lithologically distinctive units (Sharp, 1965), including the marble-rich zones.

Engel and Schultejann (1984) mapped locations in Coyote Mountain and in the Santa Rosa Mountains in an attempt to describe and interpret the complex deformation

that took place in the latest Mesozoic and Cenozoic. Their mapping, predominantly in Coyote Mountain, shows many thrust faults and they have identified the Santa Rosa mylonite zone as a series of complexly folded, faulted, and sheared gneiss, pegmatite, marble, feldspathized quartzite and amphibolite rocks. These authors suggest that thrusted and folded sections of metasedimentary rocks and gneisses up to several km thick are commonly misinterpreted as homogeneously sheared and foliated margins of plutons (Engel and Schultejann, 1984). The authors also identify at least one major (approximately 6 km amplitude) nappe in the Santa Rosa Mountains. These results are difficult to evaluate due to the schematic nature of their geologic maps, their scale, and missing topographic basemap. A geologic map of the southern Santa Rosa Mountains by Dibblee (1996) similarly lacks a base map and is at a large scale, but was found to be more accurate than the maps of Engel and Schultejann (1984).

3-1.4.1 Clark fault

The focus of this project is along the Clark Valley and Santa Rosa segments, which have a general strike of 300°, and the overall fault has a general strike of approximately 290-300°. Sharp (1967) measured 22 to 23 km of dextral offset of Cretaceous intrusive rocks along the Anza segment, and dextral offset of 19 km across the Clark Valley and Santa Rosa segments. Sharp (1967) also reported 14.3 km of right-lateral separation along the Santa Rosa segment using a mylonite in the area as an offset planar feature and there is a discrepancy between the separation he reports in the text and tables of Sharp (1967).

The Santa Rosa segment is identified by its relatively continuous fault traces in Clark Lake Valley and along the south-southwestern edge of the Santa Rosa Mountains (Sharp, 1967; Dorsey, 2002; Ryter, 2002; Belgarde, 2007). Northeast of Clark Dry Lake this segment steps approximately 1.6 km left and contains 1 to 3 major splays within a relatively narrow fault zone approximately 2 km wide. The main trace within this zone steps approximately 0.7 km to the east via 2 bends northwest of Lute Ridge and produces extensional strains there (Belgarde, 2007; this study). Faulting is distributed across a 1.5 km wide zone of fault scarps for approximately 5.4 km at and to the southeast of Lute Ridge until reaching the southernmost end of the Santa Rosa segment near Smoke Tree (Belgarde, 2007). The segment boundary is marked by a concentration of branch points that bend away from the Clark fault towards the southeast (Belgarde, 2007). To the southeast of the Santa Rosa Mountains, the Clark fault enters into the Salton Trough and cuts through approximately 3-4 km of sedimentary rocks on both its northeast and southwest side (Belgarde, 2007; Kirby et al., 2007).

The Clark Valley segment is bounded on its northwest end by a 1-km step and a 14º bend to the Horse Canyon segment. Its southeast end is buried by sediment, but may be the branch point of the East Coyote Mountain fault and the Clark fault. This same area may also have a left step of the main strands of the Clark fault zone (Figure 3-2).

3-1.4.2 Coyote Creek fault

The Coyote Creek fault is an approximately 80 km long dextral strike slip fault that strikes 315°. This fault is thought to be slightly younger than the Clark fault and has much less separation (Sharp, 1967; Dorsey, 2002; Janecke et al., 2005; Lutz et al., 2006).

The Coyote Creek fault accounts for approximately 1.6 - 4.8 km of right separation at Coyote and Borrego Mountains (Sharp, 1967; Janecke et al., 2005; Steely et al., 2005, Steely, 2006). It is comprised of eight different segments. From north to south they area: Coyote Canyon, Coyote Ridge, Borrego Badlands, Borrego Mountain, Central segment, Superstition Mountain, and Superstition Hills. The Coyote Ridge and Borrego Badlands segments are of interest because they border Coyote Mountain and are partially or completely located within the study area.

The Coyote Ridge segment of the Coyote Creek fault forms the southwest edge of Coyote Ridge, including Coyote Mountain, and extends in a southerly direction to its termination at the southern extent of Coyote Mountain (Janecke et al., in revision). This segment separated crystalline rocks in the northeast from basin fill southwest of the fault. The Borrego Badlands segment, southeast of there, cuts basin-fill deposits (Figure 3-2) (Janecke et al., in revision). To the north the Coyote Canyon segment of the Coyote Creek fault is present and is characterized by an irregular surface trace, four small basins southwest of its trace, and some thrust faults (Sanders, 1984). The southeast boundary of the Coyote Canyon segments and northwest boundary of the Coyote Ridge segment is a faulted bedrock block between Collins Valley and Upper Borrego Valley (see below).

3-2. Methodology

3-2.1. Field Methods

Additional geologic mapping of potential offset marker units and their enclosing rock units was conducted in order to upgrade and compile a 1:24,000 scale structural and geologic map of the south part of the Santa Rosa Mountains and all of Coyote Mountain.

Mapping was focused on identifying a feature to measure displacement across the Clark fault in Clark Lake Valley. The geological map produced here lies within the Fonts Point and Clark Lake 7.5 minute quadrangles. One-meter resolution orthophoto quadrangles, Landsat 7 multispectral data, topographic maps, Digital Elevation Models (DEMs), black and white aerial photographs at a scale of 1:40,000, color photos at a scale of 1:24,000, and Google Earth imagery aided field mapping. Data were recorded on paper maps produced in Environmental Systems Research Institute (ESRI) ArcMap by overlaying a Universal Transverse Mercator (UTM) grid onto one-meter resolution orthophoto quadrangles. These maps were printed at a 1:24,000 scale and used in the field. Stereographic color and black and white photographs at the 1:24,000 scale and higher resolution Google Earth imagery were also used in the field and laboratory to better constrain the locations and extent of geologic features. Mapping was focused on identifying, characterizing, tracing marker units and marker packages of rock, and identifying structures that have been active in the late Pleistocene and Holocene, as well as determining if they are related to dextral movement along the Clark fault.

Various mapping techniques, such as data collection along predetermined transects, were conducted to produce an accurate and detailed geologic map in targeted areas. A Garmin eTrex Venture CX model GPS was used to record the locations in North American Datum (NAD) 27 UTM projection. UTM locations, specific site details, written descriptions, and site identification numbers were recorded. A Brunton compass was used to measure orientations of lineations, foliations, contacts, faults, and other structural elements for structural analysis. Photographs were collected with an Olympus Stylus 710 digital camera. Photograph dates and numbers were recorded to correspond

with field sites. Notes about the field sites describe lithologies and orientations of foliations and structural features. Orientations of approximately 450 foliations, fault planes, slickenlines, folds, and contacts orientations are tabulated in Appendix K and plotted on Appendix I.

3-2.2. Data Analysis

The geological map of field area on Appendix I was produced using Adobe Illustrator and ESRI ArcMap. The topographic base with a NAD 27 projection, UTM grid, and strike and dip and trend and plunge measurements were plotted at their correct location using GPS coordinates in ESRI ArcMap. This map was imported into Adobe Illustrator. If needed, minor corrections to the locations of field data were made in Illustrator after cross-referencing field locations because steep topography precluded or modified a GPS measurement at some sites. Field maps were scanned in Adobe ImageReady and digitized using Adobe Illustrator. Contacts, fault traces, and lineations were compiled as line segments, and formations were developed into polygons.

Relocated microseismic data were acquired from Lin et al.'s 2007 catalog of relocated seismicity (http://www.geology.wisc.edu/~glin/LSH/). The data set contains relocated hypocenters of earthquakes with magnitudes ranging from Mw 0.1 to 6.4 that occurred between 1981 and 2005. Analysis of this data in the study area strengthens structural interpretations of both the Clark and the Coyote Creek faults by revealing seismically active and locked parts of the fault zone at depth. Earthquake foci were plotted using ArcMap software. Three-dimensional views and cross sections of hypocenters were developed in ArcScene. The orientations and alignments of the

relocated microseismic data were examined to determine fault geometries at depth and their correlations mapped to surface traces as well as the depth of the seismogenic zone.

Stereograms of the strike and dip of foliations were made using StereoWin (http://www.geo.cornell.edu/geology/faculty/RWA/programs.html). These stereograms were used to calculate fold axes orientations and interlimb angles, as well as to examine the trends of foliations. Fault planes and slickenline orientations were also analyzed using stereograms. Stereograms are located in Figure 3-14 and Figure 3-16 and are discussed in detail below.

Thin sections of the biotite-hornblende bearing tonalite were produced from different locations and used to compare the similarities of the plutonic rocks near the Clark fault.

3-3. Results

3-3.1. Domainal Context of Structures in Coyote Mountain

Coyote Ridge, the elongate fault block between the Clark fault and the Coyote Creek fault, is about 30 km long and broadens southeastward from 2.5 to 6 km wide. Coyote Mountain, at the southeast end of the ridge, and the focus of our study is a small part of the larger fault zone that strongly deforms Coyote Ridge. The northwest half of Coyote Ridge is cut and complexly deformed by northeast and north-northeast striking cross faults that Sharp (1967, 1972) interpreted as rotated normal and oblique faults. These developed a thrust-slip component with continued strain and rotation. Detailed mapping identified many rocks units and a few faults in the southeast end of Coyote Ridge at Coyote Mountain (Theodore and Sharp, 1975) but the middle portion of the

ridge is not well characterized. Analysis of aerial photographs, satellite imagery, topographic maps, and digital elevation models shows that the small number of faults mapped there (Sharp, 1967) are a small fraction of the cross faults that deform Coyote Ridge. This study thus shows that there are many unmapped faults with small to modest displacements that cut through Coyote Ridge and Coyote Mountain.

Detailed mapping of this complex structural array was beyond the scope of this study but photogeologic, image and topographic analysis allows many general trends to be identified in advance of field confirmation. For the purposes of this discussion we separate the Coyote Ridge fault block into three domains-the northwest domain, the southeast domain and a small domain in the extreme southeast tip of the Coyote Mountain, which we name Peg Leg domain after a local historic monument. The boundary of the northwest and southeast domains is roughly located along a northeast-trending line connecting the southeast edge of Jackass Flat and southeast edge of Collins Valley. At that point the dominant style of cross faulting changes from straight to curving east-northeast to northeast-striking cross fault (in the northwest domain) to a complex array of northwest to north-striking cross faults in the southeast domain. Straight to curving east-northeast to northeast-striking cross faults are uncommon in the southeast domain, which forms most of the current study area around Coyote Mountain. The Peg Leg domain at the extreme southeast end of Coyote Ridge has a different dominant structural style and contains mostly closely spaced east- to north-northeast striking cross faults. With additional mapping further subdivisions may become evident in the domains (Figure 3-4).

The northwest domain is a ridge of faulted plutonic and crystalline rocks. Quaternary deposits are quite localized where faulting blocked drainages. This produced small low areas at bends, steps and intersections of cross faults. The dominant fault set has a spacing between 0.5 and 1.75 km and faults are continuous between the Coyote Creek fault to the Clark fault. The elevation of the northwest domain is higher overall than the elevation of the southeast domain in part because the southeast domain exposes wide expanses of easily eroded Quaternary sedimentary rocks but also because the southeast domain is faulted down relative to the northwest domain (Figure 3-4). Faults in the northwest domain were not examined in the field, are of an unknown type, but are active based on the abundant microseismicity beneath this domain (Lin et al., 2007) and presence of some fault scarps (Sharp, 1972; 1975).

Faulted Quaternary sedimentary rocks and ubiquitous pediment-related deposits underlie 40% of the southeast domain, and the remainder consists of faulted and folded crystalline rocks (Sharp, 1967; Theodore, 1967; Theodore and Sharp, 1975; this study). The Quaternary units lie between the Box Canyon fault and the main traces of the Coyote Creek fault and west of the West Coyote Mountain fault (Figure 3-4). The southeast domain is deformed by a disorganized fault system and is far less regular in its fault patterns than the northwest domain. It contains many small and short discontinuous faults that are organized into broad fault zones. Few faults connect simply between the Clark and Coyote Creek faults and additional mapping is needed to completely characterize this web of small, interconnected faults.

The northeast and east-northeast striking faults that dominate the northwest domain are rare in the southeast domain. The north-northeast-striking West Coyote

Mountain fault is the only possible exception to this rule and its north-northeast-striking and large west-down vertical component of slip distinguishes it from the cross faults in the northwest domain, which do not have large vertical escarpments. Faults in the southeast domain strike mostly northwest to north-northwest and most have small displacements. They are organized in sets of faults, often bound diamond-shaped fault blocks, and in aggregate they form fault zones with moderate displacements.

Many of the faults in the southeast domains are subsidiary faults of the Coyote Creek fault that grossly parallel the Coyote Creek fault and lie on its northeast side. Vertical components across these subsidiary faults are mostly southwest down based on the topographic steps across the fault traces. The zone of numerous subsidiary faults northeast of the main trace of the Coyote Creek fault is consistently about 1-2 km wide. A similar damage zone might be present in the subsurface southwest of the main trace of the Coyote Creek fault but is not mappable because the active channels of Coyote Creek have covered all traces of deformation (Figure 3-4). It is difficult to quantify the total right slip within the damage zone of the Coyote Creek fault on its northeast side but it is likely to be 1 km or less because lithologic contact have small offsets (Theodore and Sharp, 1975).

Four other zones of cross faults are noteworthy in the southeast domain. These are the Butler Canyon fault array, the Mid Ridge fault zone, West Coyote Mountain and East Coyote Mountain fault zones. The Butler Canyon fault array diverges from the Clark fault in the northwest where Butler Canyon emerges southward from Jackass Flat and continues southeast to near the Coyote Creek fault. It is mostly west of the study area and

thus was not validated in the field. Its geometry suggests that the Butler Canyon fault array is an oblique-dextral array.

The Mid Ridge fault zone connects the south half of the East Coyote Mountain fault zone with the Clark fault, if incompletely mapped relationships around Buck Wash are correct. It crosses the West Coyote Mountain fault zone along the west edge of Coyote Mountain. There is abundant microseismicity beneath the southeast domain on Coyote Ridge except, notably, beneath the down-dip projection of the Mid Ridge fault zone and its probable northwestward continuation (Lin et al., 2007). It might be locked or simply inactive.

The West Coyote Mountain and East Coyote Mountain fault were known from prior mapping but their complexity and relative activity levels were not documented (Theodore and Sharp, 1975). Both consist of multiple strands and have significant vertical components of slip. These faults are described further in the results section.

The Peg Leg domain is the smallest domain and located in the southeast corner of Coyote Ridge. It is a complex area with many different rock types (Theodore, 1967; Theodore and Sharp, 1975) and many fairly closely spaced east- to northeast-striking faults and a conjugate set striking northwest. These faults cut crystalline rocks and form a clear domain of coherent faults. The Peg Leg fault domain may persist to the east into Clark Lake Valley where several lineaments, uplifting and exhuming deposits and anomalous drainage patterns in the Quaternary deposits southeast of Clark Lake are suggestive of steep north-northeast- to north-striking faults. The majority of the faults in the Peg Leg domain are steep, though some have a shallow map trace. Based on their steep dip, some faults have a strike-slip component as well as a normal component. Most

of these faults have short trace lengths, and do not obviously cross one another. Faults in this area range from 1.5 km to 300 m in length and have a general strike of approximately 305°, though many of the faults have a curvi-planar surface trace. A large number of these faults have a sinistral separation, though some do have apparent dextral offset. The northwest striking faults roughly parallel the larger northwest-striking faults of Coyote Ridge, including the Mid Ridge fault and the Citrus fault. Microseismicity (Figure 3-17 and Lin et al., 2007) defines one of the NE-striking faults in Clark Lake Valley and this domain produces many small earthquakes. The Peg Leg domain extends most of the way from the Coyote Creek fault in the southwest to the Clark fault in the northeast and therefore blocks the East Coyote Mountain fault and Mid Ridge faults from reaching the Coyote Creek fault at their southeast ends (Figure 3-17, Figure 3-18). The microseismicity is discussed in more detail below.

Rock units in the Peg Leg are not unique, and there was no marker, marker assemblage, or offset contact surface to use to determine offset along many of the smaller faults that populate the area. The units in this area are comprised of gneissic gabbro and amphilobite, garnet hornblende biotite tonalite gneiss, garnet bearing quartz monzonite, and an undifferentiated unit with some marbles and pegmatites scattered throughout (Appendix I). The rock units in this area of Coyote Mountain are not unique.

Many of the faults in the Peg Leg domain are not well developed into the kind of fault zones described by Chester et al. (1993) and slip indicators are rarely observable in exposures, despite the presence of many faults in this domain. Upon completion of the geological map, separations were measured in the Peg Leg domain based on the map pattern. Offset along these faults ranges from 72 m to 432 m (Figure 3-12). The sums of

separations across these smaller faults are 72 m right laterally and 912 m left laterally. It is likely that the left lateral faults define fault blocks that rotated in a clockwise sense. It is difficult to estimate the dextral slip represented by this fault array, however, because the original strike of the left-lateral fault is uncertain.

3-3.2. Faults and Breccias of the Southeast Santa Rosa Mountains and their Origin

The southeast Santa Rosa Mountains are a complex region as well, with many small to modest strike-slip to oblique slip -faults than previously recognized. The complexity has many sources (Figure 3-5). One source is that the Clark fault is fairly localized and although the most active deformation is concentrated in a central zone, there are many cross faults in the northeast and northwest that diverge from the Clark fault in the southeast Santa Rosa Mountains (Belgarde, 2007). The fault zone generally included faults that diverge from the Clark fault in a southeast direction - that is, on the northeast side of the fault subsidiary structures strike more easterly than the main trace and southwest of the fault they strike more southerly.

Second, the Santa Rosa fault merges with the Clark fault in the southeast Santa Rosa Mountains (Dibblee, 1954). This branch point is not simple because the Santa Rosa fault, like the Buck Ridge fault to the northwest, consists of many fault strands that are distributed across a broad zone (Belgarde, 2007; Janecke and Belgarde, 2008; this study). The deformation of the Buck Ridge and Santa Rosa fault zones is distributed across an area as much as 10-12 km wide northeast of the main trace of the Clark fault.

Several large enigmatic east-northeast dipping moderate to low-angle brittle faults within the crystalline rocks of the Santa Rosa Mountains represent the third source of

complexity. They grossly parallel the ductile fabrics in the range but in detail these faults cut across the older structures. Some parts of the fault zone are extremely irregular and rough. This family of structures is broadly similar to the Palm Canyon fault (Erskine and Wenk, 1985; Matti et al., 2002) and we tentatively correlate the two. The Palm Canyon-related brittle faults occur only in the southeast Santa Rosa Mountains and southward continuations have not been identified in the Coyote Mountain area. We infer that Coyote Mountain was once in the footwall of similar but now eroded faults, and this may explain its high metamorphic grade (Theodore, 1967) relative to other areas.

Northward the brittle faults of the Palm Canyon fault system merge into a single structure, and only the southern approximately 5 km of the Palm Canyon fault zone splays into 2-3 separate strands (Erskine and Wenk, 1985; Todd et al., 1988). Marble-rich metasedimentary rocks and migmatities are repeated across the brittle splay faults but normal or oblique displacement of metasedimentary rocks that were duplicated by numerous isoclinal nappes and folds is also possible. The brittle faults have been interpreted as Cretaceous normal faults (George and Dokka, 1994; Erskine and Wenk, 1985; Todd et al., 1988), Cretaceous thrust faults (Simpson, 1984, 1985; Esrkine and Wenk, 1985; Todd et al., 1988), and late Cenozoic normal faults coeval with the West Salton detachment fault (Axen and Fletcher, 1998). The latter seems least likely because nowhere do these faults displace late Cenozoic sedimentary rocks, but further work is needed to determine their kinematics, age and tectonic significance.

A fourth possible source of complexity in the southeast Santa Rosa Mountains are suspected sackung-related scarps and breccia masses. A sackung is an unusual type of landslide that forms when ridges collapse outward at the base and downward at their

crest, and produce diagnostic uphill facing scarps that parallel ridge crests in the process of spreading outward (McCalpin and Hart, 2002; Bovis, 1982) (Figure 3-6). Focusing of energy into ridge during earthquakes may produce this type of landslide and slip events on uphill facing scarps are suspected to record paleoseimsic events on nearby faults (McCalpin and Hart, 2002; Hart, 2008). The best examples of this process are east of the main traces of the Santa Rosa fault along the NNW-trending crest of the Santa Rosa Mountains. Fault scarps southwest of the Clark fault between Butler Canyon and Rockhouse Canyon, and northeast of the Clark fault centered around 33.3995°N and 116.347225°W may have a similar origin. These sets of uphill facing bedrock scarps align with the ridge crests, coincide with large areas of pervasive brecciation (on the scale of mountain sides or large ridges) and may have been produced by spreading the collapse of ridges during earthquakes. One prominent set of uphill facing scarp is near the crest or the Rattlesnake Ridge (the ridge west of Rattlesnake Canyon and east of the Santa Rosa fault). Rattlesnake Ridge is pervasively brecciated as well but not reorganized by the brecciation process. The internal structure of the rock masses in Rattlesnake Ridge are traceable from one breccia block to the next. There are a limited number of processes that could have produced this relationship and conventional landsliding is not one of them. Sharp (1967) concluded that landsliding explained the pervasive brecciation of rocks in the southeast Santa Rosa Mountains where we map discrete faults within a broad zone of brecciated crystalline rocks (due to sackung or fault-related deformation), and few conventional landslides. Dibblee (1954, 1984) originally mapped the southeast continuation of the Buck Ridge fault there and our mapping supports his interpretation,

while revealing multiple fault strands in place of his single strand, and probable sackung within parts of the fault zone.

A final possible source of complexity are conventional landslides marked by curving localized headscarps, rock falls, rock-sliding, slumping, and flows (e.g., Hart, 2008). We discriminate between sackung and conventional landsliding because their diagnostic morphologies are so different. Excellent small volume examples of conventional landslide masses are on the west slope of upper Rattlesnake Canyon around 33.344723° N and 116.205189° W (Appendix I) and there are at least two large landslides on the east side of the Santa Rosa Mountains in Martinez Canyon and the headwaters of Wonderstone Wash. These have identifiable headscarps, intact landslide masses with flow features of large translated blocks and lobate toes. These uncontroversial landslides have morphologies that are markedly different that those of most other areas inferred to be conventional landslide masses in the field areas (Hart, 2008).

We discount conventional landsliding as an important process in Coyote Mountains, in the broad pass between Coyote Mountain and Alcoholic Pass, in Buck Ridge, and along the west face of the Santa Rosa Mountains because downhill facing scarps are expected to outnumber uphill facing scarps, lobate toes regions should be preserved, and discrete amphitheaters should mark the headwall areas. Instead significant lateral expanses of proposed landslide headwalls have long linear escarpments (e.g. 33.322394° N 116.319871°W) instead of discrete curving headwalls. Other interpreted source regions of landslides, like the west face of the Santa Rosa Mountains east of Clark Lake, preserve up to 550 m high facetted spurs with intervening steep, V-

shaped erosional drainages instead of amphitheaters. Elsewhere, uphill-facing scarps are present where downhill-facing ones are predicted (Coyote Mountain and Alcoholic Pass), and lobate down-dip parts of proposed landslides are straight instead of curving and lobate (all along the SW margin of Coyote Mountain) (Figure3-8, Appendix I). The brecciated rock mass between the Buck Ridge and Clark fault (in the southeast part of Buck Ridge) has many landforms that resemble head scarps (Tom Rockwell, oral comm., 2008) but they form systematic NE and NW-striking sets and do not parallel contour lines. This latter pattern means that their geometry is inconsistent with their having formed as headscarps of landslides because motion would have been lateral at the upslope end instead of downslope. Conventional landsliding, though present, explains a minority of the brecciated rocks in the study area.

We disagree with Sharp's assessment (1967) that the Buck Ridge fault ends north of Clark Lake because there are many mappable fault zones in the southeast Santa Rosa Mountains in the Santa Rosa fault zone (Belgarde, 2007; this study), many low elevation fault scarps, few lobate toes of landslides, over a dozen facetted spurs indicative of tectonic processes, largely intact, mappable brecciated lithologic units in low lying areas, and limited numbers of arcuate regions that could be headscarps of conventional landslides. If conventional landsliding was a major process it must have occurred so long ago that the Santa Rosa and Buck Ridge fault zones have transformed the landscape into one strongly dominated by tectonic processes. We conclude that some of the pervasive brecciation in Coyote Mountain, Coyote Ridge, the SE Santa Rosa Mountains, and Buck Ridge resulted from sackung and that most of the remainder of the brecciations, faulting,

and landforms reflect distributed deformation in the damage zone of the San Jacinto fault zone (Appendix I).

3-3.3. Descriptions of Rock Units

3-3.3.1 Coyote Mountain

In Coyote Mountain, an east-northeast dipping, unfoliated to foliated stack of rock units is present. From bottom to top, the rock units are comprised of hornblende-biotite bearing tonalite, metasedimentary rocks, biotite-rich migmatites, mixed with metasedimentary rocks and mylonite in metaigneous protoliths. The metasedimentary rocks include marbles that range from white to gray-blue and vary from 0.5 to 140 m thickness, though most are between 1- 5 m thick. The upper metasedimentary succession is associated with several deformed metaigneous rocks (Theodore and Sharp, 1975). Of note is the succession of the biotite-hornblende-bearing tonalite to the southwest edge of the mountain. Mylonitic deformation is confined to rock units northeast and above the tonalite (Theodore and Sharp, 1975). Brittle faults cut all rock types and sometimes have small drag structures associated with them. Prominent alteration, gouge, and breccia is also present in some areas, though localized fault slip is often unrecognizable. Detailed descriptions of all rock units from Coyote Mountain are in Appendix J.

Most of the rock units mapped in Coyote Mountain and the Santa Rosa mountains are defined by the one main major rock type present in each unit, as many areas incorporate smaller volumes of other rock types, that are not mappable at the 1:24,000 sale. The only unit that contains few enclaves of other rocks is the biotite-hornblende bearing tonalite. Areas where many different rock types are present, but none dominate

at the 1:24,000 scale, have been mapped as an undifferentiated unit (Ku). The heterogeneous undifferentiated unit is the largest rock unit mapped in Coyote Mountain (Appendix I). This heterogeneous suite of rocks types is due to mixing during metamorphism, pluton emplacement in late Cretaceous and later mylonitization.

Rock unit descriptions and names determined by Theodore (1967) and Theodore and Sharp (1975) are the basis of the units described (Appendix J) for this study. Some rock units were modified or improved upon by the separating or combining units in different groupings based on field reconnaissance. We corrected and updated the detailed maps of Theodore (1967) and Theodore and Sharp (1975) of Coyote Mountain, with field data near the marker units and resolved discrepancies with the high-resolution imagery.

3-3.3.2 Southern Santa Rosa Mountains

In the southern Santa Rosa Mountains, a very similar east dipping, unfoliated to foliated stack of rock units is present. From west to east, these units are an weakly deformed to mylonitic biotite-hornblende bearing tonalite, metasedimentary rocks including an approximately 1-80 m thick marble-rich interval, biotite-rich migmatite with sills and dikes of mylonitic plutonic rocks, and more metasedimentary rocks with some marble and several types of metaigneous rocks. Beyond the crystalline and metasedimentary rocks to the east, in the hanging wall of the West Salton detachment fault and outside of our current study area, Tertiary conglomerates dominate the area and were mapped and described by Pettinga (1991) and Belgarde (2007). Detailed descriptions of all units in the southern Santa Rosa Mountains are in Appendix J.

Brittle faults cut the all the crystalline rocks in the Santa Rosa Mountains and consist of at least (3 or 4) geometric sets. The oldest set, based on cross cutting relationships, are the low to moderately east-northeast dipping faults of the Palm Canyon fault zone. As noted above, these faults may be latest Cretaceous to early Tertiary in age, either normal or thrust faults, and are poorly understood (Erskine and Wenk, 1985; Axen and Fletcher, 1998).

Similar to Coyote Mountain, the Santa Rosa Mountains contain biotite-hornblende bearing tonalite, metasedimentary rocks, mylonite, migmatite, and an undifferentiated unit. In the Santa Rosa Mountains, several additional map units are most likely present, but more detailed mapping is need to identify and break out distinct units. Despite the better mapping in the Coyote Mountain part of the study area, it is clear that the rock units are nearly identical in the two areas. There are fewer blue marbles observed in the Santa Rosa Mountains (Figure 3-3).

3-3.3.3 Biotite-hornblende-bearing tonalite

Late-Cretaceous biotite-hornblende bearing tonalite in each location in the study are part of the southern California batholith. These plutons, according to Sharp (1967), are mesozonal based on the characteristics of intrusive rocks and the higher grade of regional metamorphism observed in the present study area. Mesozonal to catazonal emplacement characterizes the eastern side of the batholith (Sharp 1967). Evidence for this is:

1. Generally, but not uniformly, concordant intrusive contacts with smooth curving boundaries
2. Foliated marginal phases of plutons

3. Local assimilation in marginal zones
4. No chill zones near contacts
5. Abundant pegmatites near border zones
6. Little contact metamorphism

Mesozonal plutons occur at depth intervals from 5-15 km depth and have characteristics that are transitional between those of the shallower epizone and the deeper catazone. The contacts may be sharp or gradational, discordant or concordant, have typically well developed contact metamorphic aureole, and may have foliated fabric along their margins (Winter, 2001). Conformable contacts between prebatholithic rocks and plutons are a general feature, except where faults juxtapose them (Sharp 1967).

Thin sections of the biotite-hornblende bearing tonalite were examined from three locations. Samples from locations from the pluton on the west side of Coyote Mountain near the feature known as Anza's Angel (UTM 11S 0561430, 3688004), along the northwest side of Coyote Mountain (UTM 11S 0562109, 3690894), and in the Santa Rosa Mountains sectioned (UTM 11S 0573796, 3687252) (Figure 3-7). All three locations displayed a medium crystalline, slightly to moderately shear biotite-hornblende bearing tonalite containing quartz, plagioclase, biotite, and hornblende. The location along the northwest side of Coyote Mountain contains fractured grains whereas the other two specimens did not. This is likely due to its being within a few 100 m of the Coyote Creek fault. This sample also displays a slightly lower percentage of hornblende than the other locations.

3-3.3.4 Comparison of rock units in the two areas

The rock units that are mapped in both Coyote Mountain and in the southeast Santa Rosa Mountains are identical or nearly identical in hand sample, in outcrop, in their thickness patterns, and in their pseudostratigraphic arrangement from west to east. We therefore correlate units across the intervening Clark Lake Valley. The main difference between the rocks in the two areas, aside from the scale of mapping, is the presence of sillimanite-bearing mylonites of Coyote Mountain and none with such a high grade in the Santa Rosa Mountains (Theodore, 1967; Sharp, 1967; this study). Sillimanite-bearing metamorphic rocks that indicate upper amphibolite facies deformation conditions developed in Coyote Mountain, whereas most of the mylonites of the Santa Rosa Mountains formed under lower to middle amphibolite facies conditions (Theodore, 1967; Anderson, 1983; Simpson, 1984, 1985). Regardless of this, there are strong similarities of rock suites throughout all of the Eastern Peninsular Ranges mylonite zone (Erskine and Wenk, 1985; Todd et al., 1988).

3-3.4. Description of Faults

3-3.4.1 Clark fault

Mapping refines the location and structural geology of the multiple traces of the Clark fault in Clark Lake Valley and adjacent areas and builds on Sharp (1972), Belgarde (2007) and the compilation in the Quaternary fault and fold database (Appendix I) (Figure 3-8). The Clark fault zone is approximately 2 km wide near the Santa Rosa Mountains and has many traces near Lute Ridge (UTM, 0574000, 3686000) (Belgarde, 2007; this study). There is an extensional bend from Lute Ridge northwestward to a low

series of hills of folded young sediment. The low hills formed in a contractional left step in the fault. Southeast of Lute Ridge there are branch points with splays to the northeast and southwest. As the Clark fault progresses southeast, the fault zone becomes more diffuse and up to 18 km wide in segments to the southeast (Belgarde, 2007). This change in fault zone geometry may be attributed to a change from rigid crystalline rocks enclosing the narrower part of the fault zone to mud-rich basinal deposits where the fault zone widens (Belgarde, 2007) (Appendix I). Conglomerate adjacent to the fault produced intermediate fault patterns. The Clark Valley and Santa Rosa segments of the Clark fault are predominantly in crystalline rock and narrower, whereas the Arroyo Salada segment cuts younger sedimentary rock, is wider, and is located southeast of the Santa Rosa segment (Belgarde, 2007).

The Clark fault has a simpler, more linear trace as it strikes through the crystalline rock of the Peninsular Ranges, and in the area of Lute Ridge it separates crystalline from sedimentary rocks. The number of strands of the Clark fault varies by location. The appearance of the Clark fault changes laterally along strike within the study area. The trace of the fault in Clark Valley has a far less visible damage zone than in areas further southeast. The main strand of the fault is buried in Clark Valley, and its mapped location is based on a few fault scarps, pop ups, sags and vegetation lineaments.

There is an abundance of Quaternary deformation along the Clark Fault everywhere within the study area. There are scarps ranging from a few meters to 2 km in length with up to approximately 10 m of vertical offset in places (Sharp, 1972; Le and Oskin, 2008). There are few scarps and geomorphic features resulting from slip on the Clark fault in Clark Valley, though there are lineaments and scarp like features located

within the Clark Valley basin, possibly due to subsidiary faults. Examples of such features include two north-northwest trending and one northeast vegetation lineaments in the study area associated with the Clark fault that were observed using air photographs, landsat digital elevation models, Google Earth, and gravity data (Figure 3-9).

Deflected drainages in the areas of Rattle Snake Canyon and Palo Verde Wash were measured by Le and Oskin (2008) to be 18 ± 2 m. Le and Oskin (2008) used cosmogenic dating to determine an age of 31 ± 6 ka for the offset surface, with a slip rate of 1.7 ± 0.4 mm/year for this single fault strand at their location.

3-3.4.2 Coyote creek fault

Much like parts of the Clark Valley and Santa Rosa segments of the Clark fault, the Coyote Canyon segment of the Coyote Creek fault is a fairly narrow, well defined fault zone that is mostly concealed in the study area (Sharp 1967, 1972) (Figure 3-8). There are only a few places where we observed lateral changes along the trace of the fault, and these are all immediately south of the southeast tip of Coyote Mountain. The active floodplain of Coyote Creek covers most of the fault northwest of there. The main trace at the southeast tip of Coyote Mountain strikes 310° and its northwest end it lays at the base of the bedrock. The scarp projects directly along the base of Coyote Mountain and aligns with the Quaternary-bedrock contact, which strikes 315° there (Figure 3-8, Appendix I).

We infer that the main strand of the fault is concealed at the northeast edge of Borrego Valley, with subsidiary strands and damage located in the southwest part of Coyote Mountain, Coyote Ridge and Borrego Valley. Small faults in Coyote Ridge have

a similar strike to that of the main strand of the Coyote Creek fault, range in length from 285 m to 1.5 km length and are concentrated in a zone approximately northeast of the trace of the Coyote Creek fault. Some of these strands have a down to the southwest component and some have northeast down components. The latter coincide with uphill facing fault scarps (this study).

The fault zone associated with the Coyote Creek fault has an uncertain width in the study area because half of the fault is buried in upper Borrego Valley. A concentration of northwest striking faults on the northeast side of the fault, in the southwest 2 km of Coyote Mountain and Coyote Ridge, is likely the damage zone immediately northeast of the Coyote Creek fault.

As noted above, there are few clearly defined scarps, vegetation lineaments, or deflected drainages along the main strand of the Coyote Creek fault near Coyote Mountain. We have identified fault traces using Google Earth imagery and LiDar (Light Detection and Ranging) data in the east edge of Borrego Valley. Late Quaternary to Holocene(?) alluvial fans along the southwest edge of Coyote Mountain are not faulted. There is no evidence of push-ups or pull-aparts resulting from slip along the Coyote Creek fault in the study area. At the southeast tip of Coyote Ridge there is a small patch of uplifted playa deposits on the northeast side of the Coyote Creek fault that defines the approximate trace of the fault to lie along the base of bedrock exposures northwest of there. A second small southwest-down step in the landscape approximately 0.5 km southwest of the main scarp is another strand of the Coyote Creek fault. The sense of vertical displacement matches that across the fault elsewhere.

3-3.4.3 Citrus fault

The largest of the subsidiary faults in the damage zone of the Coyote Creek fault is the approximately 2.5-km long Citrus fault (Figure 3-8, Figure 3-10). It strikes parallel to the main strand of the Coyote creek fault at (315° - 320°). It is unknown how much separation is associated with this fault or what type of offset it is. It has a strong component of southwest down slip based on a large cliff as well as some right lateral strike-slip. It has approximately 233 m of vertical relief across it. If dip slip dominates over strike slip on the Citrus fault it would reflect significant strain partitioning. The fault may terminate in the migmatite in the northwest or may continue northwestward to similar faults SE of Alcoholic Pass. In the SE the fault ends where E-striking faults of the Peg Leg fault domain cross it (Figure 3-10).

3-3.4.4 East Coyote Mountain fault

The East Coyote Mountain fault is a normal-oblique fault that bounds the east side of Coyote Mountain and is partially responsible for the formation of Clark Valley. The fault is approximately 7 km long, strikes 334° and can be identified by the many short scarps in the Quaternary deposits and vegetation lineaments near the eastern base of the mountain.

The East Coyote Mountain fault was inferred on the basis of gravity data by Sharp (1967), as well as associated scarps mapped by Theodore and Sharp (1975), and was interpreted by Bartholomew (1970) to be a dextral strike-slip fault that linked the Clark and southern Coyote Creek faults during the middle to late Pleistocene slip. Dorsey (2002) suggests that this is wrong, and that geomorphic features expressed along the east

side of Coyote Mountain do not indicate recent fault slip. Mapping for this study as well as observations made in the field and in air photo review document many short Quaternary fault scarps that have both vertical and dextral components. There is more than one strand, and possibly as many as four that cut late Pleistocene ± Holocene fans. The youngest deposits lap across the fault. To the north there are weakly defined fault scarps in Clark Valley at a slight east-down step in the valley floor, which suggest its connection with the Clark Fault at the boundary between the Clark Valley and Santa Rosa segments. At the southeast end there is no direct connection of the East Coyote Mountain fault to the Coyote Creek fault because northeast- and east-striking faults intervene (Figure 3-8, Figure 3-11, Figure 3-12, Appendix I).

The East Coyote Mountain fault zone is complex, with many branching, subparallel, and en echelon strands. The deepest part of Clark Lake abuts the east side of Coyote Mountain and east-side down motion across the East Coyote Mountain fault probably produced the gentle westward tilt of the valley floor.

3-3.4.5 West Coyote Mountain fault

The West Coyote Mountain fault is predominantly a normal fault with Quaternary rocks in its hanging wall along the west side of Coyote Mountain. It juxtaposes the crystalline basement rock that comprises Coyote Mountain against the Quaternary sedimentary rocks of Coyote Ridge. The fault is approximately 5 km long and is marked by approximately 500 m in vertical topographic relief. Northeast striking faults in this region are left lateral, so we suspect a left lateral component of slip across the Western Coyote Mountain fault.

Dorsey (2002) documented complex slickenline patterns in the West Coyote Mountain fault zone at its southern end. She proposes that the Santa Rosa fault, a normal dextral fault on the west side of the Santa Rosa Mountains (Dibblee, 1954), correlates with the West Coyote Mountain fault. This correlation suggests that this normal fault was active before the initiation and offset of the Clark fault, and that slip on the older fault was terminated by the initiation of the Clark fault.

Near the southwest end of the extent of the West Coyote Mountain fault, an uphill facing scarp lies west of the fault's main trace. Elsewhere, the trace of the fault is difficult to pinpoint due to the pediment and alluvial cover. It is cut by and cuts east and southeast-striking faults in Coyote Ridge. A drainage that parallels along the northwestern base of the bedrock of Coyote Mountain in the area may be partly aligned with the trace of the West Coyote Mountain fault.

We argue that it is more likely that the Western Coyote Mountain fault is coeval with the Coyote Creek and Clark faults because it has a similar strike to many of the crossing faults identified in Coyote Ridge between the Clark fault and the Coyote Creek fault in the northwest domain and because the Santa Rosa fault is a extensional part of the Buck Ridge fault system, rather than an earlier, unrelated normal fault (Sharp, 1967; Sharp, 1972; Belgarde, 2007 this study) (Figure 3-4).

3-3.4.6 Mid Ridge fault

A fault approximately 6 km in length cuts through the north half of Coyote Mountain at 320º and is referred to here as the Mid Ridge fault because of its location. This fault may represent 0.5 to as much as 3.9 km of dextral separation, based on the

offset of the western marble-rich zone at the eastern edge of the biotite-hornblende tonalite, or 1.7 km of sinistral separation, based on offset of the gneissic gabbro and amphibolite unit and garnet bearing quartz monzonite. The right lateral separation is based on projecting the marble and contact of the tonalite across the younger West Coyote Mountain fault, and the estimate is very uncertain due to the long distance of the projection and structural complexities. The possible left separation could reflect repetition of rocks types in the area, not a valid measurement. The Mid Ridge fault branches from the East Coyote Mountain fault along the eastern side of Coyote Mountain near a gravel pit and strikes northwest onto Coyote Ridge. The western termination of this fault is uncertain but likely to be the Clark fault near Jackass Flat (Figure 3-8, Figure 3-10).

3-3.4.7 Other faults in Coyote Mountain

Field mapping combined with photogeologic mapping located 10 to 14 other small faults northeast of the main trace of the Coyote Creek fault and southwest of the Citrus fault. They have an average spacing of 105 m and persist approximately 812 m southwest from the Citrus fault.

There are other faults in the area and along the eastern and southern portions of Coyote Mountain (Figure 3-8, Figure 3-12) within the heterogenous map unit that have no measurable offset due to the lack of marker units. Some of the faults cut Quaternary deposits along strike. Some smaller faults observed in the field display a dip-slip component, but net or apparent slip amounts are uncertain. The faults mapped in this area range in length from 200 m to 2 km and orientations vary from 250° to 350°, though

many of the faults have a surface trace that is generally subparallel to the strike of the Clark and Coyote Creek faults (Appendix I).

3-3.5. Damage Zones

The damage zones of both the Clark and Coyote Creek faults are of an indeterminable width because of the high density of faulting throughout the field area. Determining where one damage zone begins and where one ends in these locations is nearly impossible and it is likely that there is no undeformed protolith within the confines of the map areas. Therefore the term “damage zone” will be used in the general sense due to the extensive overlap of damage zones of the Clark, Coyote Creek, intervening dextral faults and connecting cross faults in the area. The damage zones of the faults are at least 6 km wide, which is the spacing between the Clark and Coyote Creek faults near Coyote Mountain. The damage zones in the crystalline rocks northeast of the Clark fault and northeast of the Coyote Creek fault are similar in style and types of deformation, except that the damage zones northeast of the Clark fault may be wider. This is expected for a fault with more slip.

The damage zones of these faults contain older, unrelated mylonitic deformation produced in the deep crustal thrust zone between 97 and 62 Ma (Sharp, 1967; Simpson, 1984; Goodwin and Renne, 1991). The second suite of deformation observed in some locations is the result of dextral faulting was ongoing since 1.4 and 1.1 Ma (Morton and Matti, 1993; Kirby, 2005; Janecke et al., 2006; Lutz et al., 2006; Kirby et al., 2007). Brittle deformation associated with the Pliocene West Salton Detachment fault was not significant in our area.

Small scale folding is present throughout the mylonite, with a few (5) larger folds observed in the eastern part of Coyote Mountain (Theodore, 1967). Small folds in the mylonite in average are 0.5 m to 5 m in wavelength (Theodore, 1967). Some of the folds in Coyote Mountain are associated with small thrust faults (Figure 3-13f).

Brittle faults populate the damage zones. Fractures and small splay faults within the damage zone have various orientations, but generally follow kinematic and strain partitioning structural models traditionally associated with strike-slip fault zones (Anderson, 1951; Wilcox et al., 1973; Withjack and Jamison, 1986). The faults within the damage zones range from 2 m to 1.5 km in length and many of the smaller faults are not mappable on a 1:24,000 scale map (Appendix I). In most cases these faults are brittle and show damage and or alteration independent of the associated major fault in the area (Figure 3-13). Some of the faults, particularly in the area of Anza's Angel in Coyote Mountain and immediately west of the central part of Palo Verde Wash within the Clark Fault zone, have well-defined fault cores as described by Chester et al. (1993), ranging from 3 to 8 cm wide. Some smaller faults have clay gouge in their cores.

Fractures are present in the damage zone, but no single set dominates the damage zone. Fractures, on average, vary in length from 2 cm to greater than 5 m. Theodore (1967) determined that joints are approximately normal to well-developed mullion structures in the mylonitic rocks in Coyote Mountain. No systematic analysis of joints was attempted for this study.

3-3.6. Is Folding at Coyote Mountain the result of Deformation Along the San Jacinto Fault Zone?

One large map-scale fold in the southern half of Coyote Mountain lies within the damage zone of the Coyote Creek fault (Theodore and Sharp, 1975). We hypothesized that it is the result of brittle deformation adjacent to the San Jacinto fault zone and we tested this concept in the field and built on the structural analysis of Theodore (1967). Theodore divided Coyote Mountain into 12 separate and distinct subareas based on their structure. Seven stereonets showed east-southeast plunging folds with an open form. A combination of all the strike and dip data plotted in Theodore and Sharp (1975) and data collected during this study produced the same result- a gently east-southeast plunging fold deforming the crystalline rocks (Figure 3-14). Lineations in Coyote Mountain are clustered and have a mean of plunge 37.2°. The attitude of the foliations and lineations in Coyote Mountain are like those elsewhere in the Eastern Peninsular Shear Zone (Simpson, 1984, 1985; Erskine and Wenk, 1985; Todd et al., 1988).

The map-scale fold that we investigated in south Coyote Mountains as a possible damage element plunges east and has northeast and southeast dipping units on opposite limbs (Figure 3-14, 3-15). The northeast-dipping limb is far steeper (and locally overturned) than the opposite limb, which makes it a top to the northeast fold. This is not an orientation that could be the result of slip on the San Jacinto fault zone. The asymmetric map-scale fold is clearly a Cretaceous structure because the rock units exhibit pervasive ductile deformation, thin and thicken laterally, were not faulted and fractured, and formed a subvertical to overturned limb. It may be related to thrust faults hypothesized to exist in Coyote Mountain (Engel and Schultejann, 1984) (Figure 3-15)

and is clearly much older than the brittle San Jacinto fault zone. Engel and Schultejann (1984) showed that there are folds with diverse vergences in the East Peninsular mylonite zone, despite the mylonite having an overall top to the west motion. The map-scale fold in Coyote Mountain is probably part of this family of "differently vergent" folds. In addition, the geometry of the fold matches to the overall geometry of smaller folds throughout Coyote Mountain, regardless of the way we grouped the data and regardless of the location relative to the San Jacinto fault zone (Figure 3-14). Therefore we conclude that there is one dominant set of ductile folds that plunge east in Coyote Mountain and they formed a long ago at depth.

3-5.7. Southeast Santa Rosa Mountains Folding Resulting from Clark Fault Displacement

Folds in the Santa Rosa Mountains are similar to those in Coyote Mountain and most are clearly old ductile structures of the Cretaceous mylonite zone. There is one fold in the damage zone in the southeast Santa Rosa Mountains that might be younger and we collected structural data to test this hypothesis (Figure 3-16). The fold, which is located approximately 2.5 km northeast of the trace of the Clark fault, is a weakly developed open anticline plunging 36º toward 101.6º. The fold has an interlimb angle of approximately 134.4°, the axial surface strikes 96.9° and dips 83.2° north, and represents approximately 8% north-south shortening. The fold is approximately 1.5 km long. The trend of the anticline is approximately 25º counterclockwise of the trace of the Clark fault.

Cross-cutting relationships show that the fold is older than the Clark fault and most likely Cretaceous. The fold is restricted to the heterogeneous undifferentiated map

unit and the migmatite and appears to be in one fault block beneath (west of) the Palm Canyon fault. The Palm Canyon fault is not folded (Figure 3-16) and the westward extension of the fold is not present in Rattlesnake Canyon. The anticline thus predates the Palm Canyon fault, which in turn predates the San Jacinto fault zone. It is likely that this anticline formed during Cretaceous thrusting and is a subsidiary structure of the mylonite zone. The fold is not the product of brittle fault slip in the damage zone of the San Jacinto fault.

No other statistically significant folds were evident in the strike and dips in or along Rattle Snake Canyon in the Santa Rosa Mountains. Mapping and image analysis, however, show that complex, mountain-scale inclined folds deform the southeast Santa Rosa Mountains a short distance north of the field area (Engel and Schultejann, 1984; Belgarde, 2007; Janecke, unpublished mapping).

3-3.8. Microseismicity of the Clark Fault and the Coyote Creek Fault Zones

3-3.8.1 Summary and general information

Microseismicity within the study area along the Clark fault and the Coyote Creek fault correlates with many of the structures mapped at the surface but not with others. The earthquakes reveal the presence of some important fault traces that are covered by unfaulted surficial deposits. In other areas the earthquakes show significant differences between the dominant structures at the surface and those at depth (Figure 3-17, Figure 3-18, Figure 3-19). Discrepancies in alignments of microseismicity and mapped faults are expected because of the short time period of earthquakes (1981-2007) and because most of the seismicity is localized at the base of the seismogenic zone, 10-14 km below the

mapped faults. Mapped short faults are unlikely to extend from 12 km depths to the surface or vice versa. As also observed farther east (Belgarde, 2007), there are fewer earthquakes between 5 and 10 km deep than above or below this depth. This pattern could be the result of an aseismic decollement in the subsurface (Belgarde, 2007). In the present field area this less seismic depth interval lies within crystalline rocks.

Seismic alignments have two dominant strikes. One is northwest parallel to the Clark and Coyote Creek faults and the other is northeast-roughly subparallel to cross faults in the area. Several seismic alignments differ in strike from the strike of their master fault at the surface. Northeast-striking faults are likely to be clockwise of adjacent surface faults, whereas a few northwest-striking dextral faults are counterclockwise of their master surface faults. The seismic patterns are even more discordant with the surface structure in the southeast fault domain on Coyote Ridge. Surface faults within this domain strike-clockwise of the San Jacinto fault zone whereas the concentration of earthquakes form a cloud of activity that is counterclockwise of the master fault. The explanation of this pattern is uncertain but may reflect crossing coeval faults.

The maximum depth of numerous earthquakes changes southeast of Clark Lake Valley along the Clark fault and at the southeast tip of Coyote Mountain for the Coyote Creek fault. Southeast of there the maximum depth is less than 12 km (Fig. 17). This shallowing of the base of seismicity is well known (Sanders and Kanamori, 1984; Sanders, 1989; Sanders and Magistrale, 1997).

There are many correlations between mapped faults and aligned earthquakes in the study area, particularly between the more significant faults and the seismicity. The Coyote Creek and Clark dextral faults produced many small earthquakes. Cross sections

indicate that almost all of the identifiable seismic alignments down dip of northwest striking faults define steeply northeast dipping fault planes (Fig. 3-17, 3-20).

One striking feature of the seismicity in the study area is the wide spread of microseismicity perpendicular to the fault traces (in map view), particularly around Coyote Mountain and Coyote Ridge (Figure 3-17, 3-18, and 3-19). The Coyote Creek fault zone produced small earthquakes there across a zone at least 7 km wide, and there are alignments that persist northeast to the Clark fault, north of Clark Lake, that broaden the fault zone even farther. The seismic expression of the Coyote Creek fault widens to the southeast along Coyote Ridge (Figure 3-17).

The Clark fault also widens to the southeast and is especially broad in the San Felipe Hills, southeast of our study area (Belgarde, 2007). Its microseismic expression is up to 4 km wide seismically in the study area and has a few gaps in seismic activity. Altogether, the San Jacinto fault zone near Coyote Mountain produces earthquakes across a damage zone about 6-9 km wide perpendicular to its main traces.

3-3.8.2 Microseismicity of the Coyote Creek fault zone

There are two prominent alignments of microseismicity near the Coyote Creek fault that have a northwest to west-northwesterly strike. Locally a third alignment is present but it is less laterally continuous. The three faults are approximately 1-2 km apart and there were few earthquakes between the three faults. We interpret these as seismically active parts of the Coyote Creek fault zone.

The microseismic alignment down dip of the main trace of the Coyote Creek fault is the northeasternmost of the three alignments. It is approximately 12 km long and 1.5

km wide in plan view. The alignment of earthquakes downdip of the main trace of the Coyote Creek fault dips between 80° and 60° northeast and diverges from the surface trace of the Coyote Creek fault southeastward. The northeasternmost alignment is 0.5 m northeast of the Coyote Creek fault in the Coyote Ridge segment and up to 3.5 km northeast of the main fault trace under Coyote Mountain. This northeasternmost alignment is most active at 10-14 km depth. It ends beneath Coyote Mountain where northeast-striking alignments of earthquakes diverge from its tip and/or cross it beneath the Peg Leg fault domain. A southeastward decrease in the amount of dip explains the more easterly strike of the seismic alignment relative to the northwest strike of the surface trace of the Coyote Creek fault.

The southwestmost northwest-striking microseismic alignment near the Coyote Creek fault zone lies roughly beneath the surface trace of the Coyote Creek fault at 10 to 14 km depth. Because this southwest fault zone dips steeply northeast it projects to the surface within the alluvium of Upper Borrego Valley 2-3 km southwest of the main fault's surface trace (Figure 3-17, Figure 3-18, Figure 3-20 A-A', and B-B'). The southwestmost seismic alignment is the main evidence for a buried fault strand there that is at least 23 km long. This southwestmost fault strand terminates close to the southernmost tip of Coyote Mountain where northeast to east-northeast striking seismic alignments beneath the Peg Leg fault domain cross its trace (Figure 3-18, Figure 3-19).

3-3.8.3 Microseismicity of the Clark fault zone

Seismicity associated with the Clark fault also defines steeply northeast dipping fault planes. In cross section, the area shows two to three closely spaced well-defined

alignments in the upper to mid crustal levels (10-13 km) that dip between 70°-85° to the northeast and lie about 1-2 km apart (Figure 3-20, E-E'). The alignment of earthquakes farther to the northeast is more continuous than the southwest one. If one assumes a constant dip and projects the alignment that lies farther to the northeast to the surface from 10-14 km depth, it projects close to the Clark fault at Lute Ridge and the southwestern traces of the Clark fault zone in Clark Lake Valley. The fault strands are most active between 8 and 12 km and form an approximately 2 km thick zone perpendicular to its plane (Figure 3-20 D-D'). 12 km is the base of the seismogenic zone in Clark Lake Valley.

3-3.8.4 Comparisons of microseismicity of the Coyote Creek and Clark fault zones

The microseismic alignments along deep parts of the Coyote Creek and Clark faults have concordant changes in strike from northwest to southeast and cannot be explained by simple northwest-striking fault zones (Fig. 3-17 to 3-21). The deflection of the alignments beneath the Clark fault has a similar shape as the deflections of earthquake alignments beneath the Coyote Creek fault. Matching concave and convex deflections align in a northeast direction. Interestingly, the same area has the most numerous and densest population of northeast-striking alignments. We suspect that interactions with the conjugate fault sets may have deformed both the Coyote Creek and Clark faults of the San Jacinto fault zone at depth.

Though there are alignments of earthquakes along several faults, there are many faults that have little or no associated earthquakes. In particular the West and East Coyote Mountain faults produced few earthquakes since 1981. The East Coyote Mountain fault is

probably locked because there are abundant faults along the eastern side of Coyote Mountain that we interpret as forming during ancient earthquakes. No earthquakes coincide with the down dip projection of the Mid Ridge fault. As expected, the Palm Canyon fault in the San Rosa Mountains and the West Salton detachment fault occur in areas with almost no microearthquakes (Figure 3-17, Figure 3-18, Figure 3-19). These two faults are interpreted to be inactive ancient structures.

The volume of rock beneath east Coyote Mountain, Clark Lake Valley and western Borrego Badlands has an unusually large number of short alignments of earthquakes with northeast trends (Fig. 3-17). This area may be more structurally complex than adjacent areas due to the intersection with major active sinistral faults that penetrate into the dextral San Jacinto fault zone from the southwest.

Northeast to east-northeast trending alignments of earthquakes in Coyote Mountain and Clark Lake Valley are approximately 1 km wide and up to 3.5 km long. One such alignment beneath Upper Borrego Valley and Coyote Mountain crosses the southeast northwest-trending alignment of the Coyote Creek fault.

In the central part of Coyote Mountain (Figure 3-17, 3-20, C-C') there are many earthquakes clustered in a zone at approximately 12-15 km depth below Coyote Mountain. The zone has a depth extent of at least 5 km and shows two strong alignments of earthquakes that dip moderately to steeply to the northwest. These faults appear to project upward to some of the crossing faults mapped in western Clark Lake Valley.

The Peg Leg domain produces many small earthquakes and there are some northeast-trending lineaments of seismicity within this dense cloud of events. Thus the

faults within the Peg Leg domain must be active since they produced small earthquakes during the last 28 years.

The subsurface beneath Clark Lake itself is devoid of microseismicity. Cross faults produce abundant earthquakes beneath the remainder of Clark Lake Valley farther to the east. Some of the northeast-striking earthquake alignments underlie areas of where there are few mapped northeast-striking fault. The up dip projection of one of the longer northeast-striking alignments beneath Clark Lake Valley, however, coincides with a series of topographic, soil and vegetation anomalies southeast of Clark Lake that suggest active faulting. It is mainly active between 8-10 km depth. The northeast striking faults are conjugate to the San Jacinto fault zone and probably connect the Coyote Creek fault and the Clark fault.

Farther to the southeast of Coyote Mountain beneath the western Borrego Badlands, a diffuse alignments of earthquakes trends northeast-southwest and terminates at the base of the Santa Rosa Mountains near Lute Ridge along the Clark fault. The zone is approximately 10 km long and 4 km wide. This zone is nearly perpendicular to the trace of the Clark and Coyote Creek fault and does not extend northeast of the Clark fault.

3-3.9. Geological Evidence Used for Measurement of Right Separation Across the Clark Fault

Offset was measured using a marker assemblage of a biotite-hornblende bearing tonalite, a metasedimentary package of rocks that contains a mappable marble, (and sometimes an orange weathering quartzite), and overlain by a thick biotite-rich migmatite (Figure 3-21). The marble is not always present in the assemblage. It is usually close to

the contact between the biotite-hornblende bearing tonalite on the west and the migmatite on the east when it is present, so the tonalite-migmatite contact is also a reliable contact in the marker suite. The marble waxes and wanes throughout the assemblage ranging from not present to greater than 10 m thick and ranges from 5 m to 20 m long between the tonalite and migmatite. This marker assemblage is located in several locations: on the southwest side of Coyote Mountain at a geographic feature know as Anza's Angel; along the northwestern part of Coyote Mountain in an outcrop belt approximately 100 m in length; and along both sides of Rattle Snake Canyon in the Santa Rosa Mountains, along a belt of nearly continuous contacts approximately 7.5 km long in a series of large marble pods that individually extend approximately 500 m in north-south and varying in thickness from approximately 0-30 m.

3-4. Discussion

3-4.1. Clark Fault Separation

Separation across the Clark fault in Clark Valley has been previously estimated to be approximately 14.5 km right laterally (Sharp, 1967). Sharp (1967) used the west base of the Eastern Peninsular Ranges mylonite zone as his offset contact surface. The mylonite zone is a broad diffuse deformational boundary and is a poor marker because of the variety of characteristics of the mylonitic rocks with different protoliths as well as the difficulty to identify the mylonite and its contacts. No error was reported in his study.

Our new estimate of right separation across the Clark fault depends on the projection used to extend the marker assemblage to the trace of the Clark fault, the location of the main strand of the Clark fault, and the location of the marker assemblage

in the Santa Rosa Mountains (Figure 3-20, Figure 3-22). There is 3.8 km ± 1 km of cover between the marker and the Clark fault in the Coyote Mountain area. We must also compensate for the West Coyote Mountain fault, which displaces much of the marker assemblage into the subsurface along 72% of the edge of the Coyote Mountain.

In Coyote Mountain, the marker assemblage is projected from its northernmost location in five different ways. It is projected using the local 27° strike of the contact between the marble and biotite hornblende tonalite northward to the trace of the Clark fault; from its location using the mean strike of the foliations nearby in Coyote Mountain to the trace of the Clark fault; using the average trend of the foliation of the rocks in the immediate area in two different ways. Finally the marker is projected in a “concave-to-the-southeast” form from its location, honoring changes in the strike of foliation nearby.

In the southeast Santa Rosa Mountains, the marker assemblage is located on the northeast side of Rattlesnake Canyon and is projected four different ways. The marker is projected to the trace of the Clark fault as a plane using the local strike of the contact (172°) between the biotite-hornblende bearing tonalite and migmatite at its southernmost exposure. The marker assemblage is projected in a “concave-northwest” form to parallel the strikes of foliations in outcrops in the vicinity in two different ways that honor the map data. The marker is projected as a plane using the mean strike of the foliations of the area. Lastly the marker is projected at the most deflected possible angle that honors all the map data. The different projections are used to determine separation and are included in the error analysis (Figure 3-20).

3-4.2. Separation

Our estimate of 16.8 km +3.67 km / -6.03 km of right separation is higher than the separation measured by Sharp in 1967 of 14.4 km across the main trace of the Clark fault, yet the tow measurements overlap within error. The wide expanse of cover and the range of possible attitudes of the marker sequence beneath the cover result in a fairly high error in our estimate, but are ultimately more robust. Our results account for error analysis, which was not considered by Sharp, and he thus projected greater certainty than was warranted.

3-4.3. Off Fault Deformation and Deformation Between the Coyote Creek and the Clark Faults

Deformation within the damage zone is comprised of fault scarps and damaged rock relating to fault movements from both the main fault and subsidiary faults located within the damage zone. The presence of fault scarps along faults in the damage zone and fault zone of the Clark fault indicate that some of the deformation in the damage zone was produced by large surface-rupturing earthquakes, and is therefore seismic.

The fault and damage zones of the Coyote Creek fault in the crystalline rocks of the study area have no fault scarps, and no Quaternary deformation observed. Brittle faulting examined in Coyote Mountain adjacent to the main trace of the fault suggests surface-breaking ruptures as well, but the absence of any offset Quaternary deposits in the area makes it difficult to prove late Quaternary activity across these faults. Nearby identical faults along strike of the Coyote Creek fault, northwest of the study area

displace Quaternary deposits however, so we infer that all the northwest-striking faults were active at that time.

Many of the subsidiary faults within the damage zones of both the Coyote Creek fault and the Clark fault are brittle and display a developed fault core containing fault gouge, as well as highly damaged rock surrounding the main trace of the subsidiary fault.

3-4.4. Strain

The Clark fault is thought to have approximately 14.5 km of right lateral offset in Clark Valley based on the work of Sharp (1967). We have reexamined and remapped areas surrounding the Clark fault in the southeast Santa Rosa Mountains and in Coyote Mountain and have identified additional strain that has been unaccounted for by Sharp 1967. Offset lithologic contacts are displaced as much as 21 km or as little as 11.6 km. This estimate does not include strain of 1-2 smaller dextral faults within Coyote Mountain with possible separations of 1-3 km, though uncertainty is large due to the lack of a correlatable offset units and structural complexities. The Mid Ridge and Citrus faults are the largest faults of this type. The minimum value of additional strain in the fault block between the Clark and Coyote Ridge faults is 0.5 km of dextral separation. These faults branch from Clark fault in the northwest and merge with domains of east-west faults in the southeast. Overall their strikes are clockwise of the Clark and Coyote Creek fault.

An additional domain of smaller faults located in the southeast section of Coyote Mountain may also be accommodating unaccounted strain. Rock units in the southern half of Coyote Mountain in the proximity of the cultural feature know as Peg Leg Smiths

Monument were not mapped in enough detail to determine offset along many of the smaller faults that populate the area. It is uncertain whether these faults have any impact on total separation of the Clark or the Coyote Creek fault. These faults may represent as much as 1 ± 0.5 km of sinistral separation and 0.2 ± 0.1 km of dextral separation and an unknown amount of block rotation. The largest strains would accrue if there was significant block rotation in this fault domain-as is likely given the easterly strikes of the left-lateral fault there.

Altogether we document more separation within the Clark fault zone (16.8 km +3.67 km / -6.03 km) than Sharp (1967) but the uncertainties are large. Little strain is localized within folds in the damage zone, in contrast to our working hypothesis of strain accumulation in drag folds along the trace of the Clark fault. The suspected drag folds were shown to be preexisting folds of the Eastern Peninsular mylonite zone.

3-4.5. Implications for Hazards

Fault scarps and diverted drainages and the abundance of microseismicity in the region provide conclusive evidence that there is a highly active fault zone within the study area. As the science of earthquake predictions advances, structural studies and characterizations in this area may augment understanding of geologically similar actively deforming regions near metropolitan areas. This study has refined the measured offset along the Clark fault to 16.8 km +3.67 km / -6.03 km and accommodated for error not previously considered. Also, the identification of fault strain in the damage zone requires consideration as does the possible linkage of faulting when revising earthquake hazards. Currently, very few people will be affected by a large-scale earthquake on the Clark fault,

but as southern California's population continues to grow and extend eastward, seismic risk and hazards will need to be accounted for in this region. Similar interpretations of microseismicity in active tectonic regimes with poor exposure in or around densely populated areas may prove to be a more efficient and a noninvasive way to assess risk.

3-5. Conclusions

The Clark fault has a measured right lateral separation of 16.8 km +3.67 km / -6.03 km within the study area, and is 2.4 km higher than previous measurements by Sharp (1967). A unique marker package of biotite-hornblende bearing tonalite – marble – migmatite was used as an offset contact surface. Located both in Coyote Mountain and the Santa Rosa Mountains, this offset contact surface was projected from its outcrops to the main trace of the Clark fault, located in Clark Valley. A variety of projections were used at both the Coyote Creek and Santa Rosa Mountains field sites. This analysis allows us to incorporate error.

The previous and accepted measurement by Sharp (1967) did not include an error analysis on his separation. Our results are therefore more robust because of the error as well as using a more finite offset contact surface as opposed to the diffuse mylonite zone used by Sharp (1967).

Additional strain was also observed in smaller faults in the damage zone in Coyote Mountain that had previously been unaccounted for by Sharp (1967) or Theodore and Sharp (1975). 1-2 smaller faults ranging in lengths of 1-6 km in the eastern and western sections of Coyote Mountain have a combined separation of 1-3 km ± 2 km, though there is much uncertainty with this value. A zone of smaller faults in the southeast

portion of Coyote Mountain display a strong combined sinistral separation of 1 ± 0.5 km and 0.2 ± 0.1 km of dextral strain. Though many faults strike through the Santa Rosa Mountains, no separation was discernible.

Contrary to our initial hypothesis, no strain is located in drag folds related to dextral movement of the Clark fault because there are no drag folds. Foliations and outcrop attitudes do not show any evidence for drag folding, and are in general agreement with the overall attitude of the Eastern Penisular Shear Zone.

Off-fault deformation in both Coyote Mountain and the southeast Santa Rosa Mountains within the field area is seismic. The presence of fault scarps, deflected drainages, and complex brittle subsidiary faults within the damage zone are evidence for this.

The separation across the Clark fault implies a lifetime slip rate of 16.8 km/1.1 m.y. This translates into a rate of 15.3 mm.yr. Adjacent small faults increase this value slightly but their rates are difficult to quantify.

Microseismicity and earthquakes within the study area correlate with many of the structures mapped at the surface, but not others. The earthquakes reveal the presence of some fairly long fault traces that are covered by surfical deposits. The major dextral faults in the area produce most of the small earthquakes but there is much seismicity along crossing structures as well. Seismic correlations suggest that most northwest striking faults dip steeply to the northeast. The microseismicity also outlines complex structures and relationships. Particularly, bands of seismicity perpendicular to the traces of large faults in and near Coyote Mountain and Coyote Ridge may reflect crossing coeval faults.

References

Anderson, E.M., 1951, The dynamics of faulting and dyke formation with applications to Britain, 2nd ed.: Oliver and Boyd, Edinburgh, 198 p.

Anderson, E.C., 1983, Petrology of a portion of the eastern Peninsular ranges mylonite zone, southern California: Contributions to Mineralogy and Petrology, v. 84, p. 253-271.

Axen, G.J., and Fletcher, J.M. 1998, Late Miocene-Pleistocene extensional faulting, northern Gulf of California, Mexico and Salton Trough, California: International Geology Review, v. 40, p. 217-244. Reprinted in Ernst, W.G., and Nelson, C.A., eds., Integrated Earth and environmental evolution of the southwestern United States, The Clarence Hall, Jr. volume: Bellwether Publishing, Ltd. for the Geological Society of America, p. 365-392.

Bartholomew, M.J., 1970, San Jacinto Fault zone in the Imperial Valley, California: Geological Society of Bulletin, v. 81, p. 3161-3166.

Belgarde, B.E., 2007, Structural characterization near the se end of the Clark Fault, Salton Trough California [m.s. thesis]: Logan, Utah State University.

Bovis, M.J., 1982, Uphill-facing (antislope) scarps in the Coast Mountains, southwest British Columbia: Geological Society of America Bulletin, no. 93, p. 804-812.

Chester, F.M., Evans, J.P, Biegal, R.L., 1993, Internal structure as weakening mechanisms of the San Andreas Fault: Journal of Geophysical Research, v. 98, p. 771-786.

Dibblee, T.W., 1954, Geology of the Imperial Valley Region, California. In: Jahns, R.H., ed., Geology of Southern California: California Division of Mines Bulletin, v. 170, p. 21-28.

Dibblee, T.W., 1984, Stratigraphy and tectonics of the San Felipe Hills, Borrego Bandlands, Superstition Hills, and vicinity, *in*: Rigsby, C.A. ed, The Imperial Basin; tectonics, sedimentation and thermal aspects 40, Pacific section SEPM Field Trip Guidebook, p. 31-44.

Dibble, T.W., 1996, Stratigraphy and tectonics of the San Felipe hills, Borrego Badlands, Superstition hills and Vicinity, *in* Abbott, P.L., and Seymour, D.C., eds., Sturzstorms and detachment faults, Anza-Borrego Desert State Park California: South Coast Geological Society Annual Field Trip Guide Book Number 24, p. 45-58.

Dibblee, T.W., 1997, Geology of the southeastern San Andreas fault zone in the Coachella Valley area, southern California, In: Baldwin, J., Lewis, L., Payne, M., Roquemore, G., eds., Southern California San Andreas fault-white water to Bombay beach, Salton Trough, California, South Coast Geoloigical Society Field trip guidebook 24.

Dickinson, W.R., 1981, Plate tectonic evolution of the southern Cordillera, in Dickinson, W.R., and Payne, W.D., eds., Relations of tectonics to ore deposits in the southern Cordillera: Arizona Geological Society Digest, v. 14, p. 113-135.

Dorsey, R. J., 2002. Stratigraphic record of Pleistocene initiation and slip on the Coyote Creek fault, lower Coyote Creek, southern California. In: Barth, A. ed., Tectonic Evolution Southern and Baja California, Sonora and Environs, Geological Society of America, Special Paper 365, 251-269.

Engel, A.E.J., and Schultejann, P.A., 1984, Late Mesozoic and Cenozoic Tectonic History of South Central California: Tectonics, v.3, no.6, p. 659-675.

Erskine, B.G., and Wenk, H.R., 1985, Evidence for Late Cretaceous Crustal Thinning in the Santa Rosa mylonite zone, Southern California: Geology, v.13, p.274-277.

George, P.G., and Dokka, R.K., 1994, Major Late Cretaceous Cooling Events in the Eastern Peninsular Ranges, California, and their Implications for Cordilleran Tectonics: Geological Society of America Bulletin, v. 106, p.903-914.

Goodwin, L.B., and Renne, P.R., 1991, Effects of progressive mylonitization on AR retention in biotites from the San Rosa mylonite zone, California, and thermochronologic implications: Controbutions to Mineralogy and Petrology, v. 108, n. 3, p. 283-297.

Grove, M., Lovera, O, and Harrison, M., 2003, Late Cretaceous Cooling of the East-Central Peninsular Ranges Batholith (33N): Relationship to La Posta Pluton Emplacement, Laramide Shallow Subduction, and Forearc Sedimentation. in Johnsin, S.E., Paterson, S.R., Fletcher, J.M., Grity, G.H., Kimbrough, D.L., and Martin-Barajas, A., eds., Tectonic Evolution of Northwestern Mexico and Southwestern USA, Geological Society of America Special Paper 374, p.355-379.

Hart, M.W., 2008, Structural and geomorphic characteristics of landslides at Coyote Mountain, Anza-Borrego Desert State Park, California. Environmental & Engineering Geoscience, vol. 14, no.2, p.81-96.

Hill, R.I., 1984, Petrology and Petrogenesis of Batholithic Rocks, San Jacinto Mountains, Southern California, [PhD Thesis]: Pasadena, California Institute of Technology, 700 p.

Janecke, S. U., and Belgarde, B. E., 2008, Detecting hidden, high-slip rate faults: Southern San Jacinto fault zone: Final Report for NEHRP Grant 06HQGR0031, 96 p.

Janecke, S.U., Kirby, S.M., Langenheim, V.E., Steely, A.N., Dorsey, R.J., Housen, B., Lutz, A., 2005, High Geologic Slip Rates on the San Jacinto Fault zone in the SW Salton Trough, and Possible Near-Surface Slip Deficit in Sedimentary Basins: Geological Society of America Abstracts with Programs 37, no. 7, p. 257.

Janecke, S. U., Kirby, S., Steely, A., Lutz, A., Dorsey, R., Housen, B., Langenheim, V., 2006, Early Pleistocene emergence of new dextral faults SW of the southern San Andreas fault, Salton Trough: Abstracts for NSF MARGINS program, Workshop on Rupturing of Continental Lithosphere. Ensenada Mexico, 46 p.

Janecke, S.U., Dorsey, R.J., Steely, A.N., Kirby, S.M., Lutz, A., Housen, B.A., Belgrade, B., Langenheim, V., Tirrenhour, T., and Forand, D., In revision. High Geologic slip rates since early Pleistocene initiation of the San Jacinto and San Felipe fault zones in the San Andreas fault system: Southern California, USA.

Jaroszewski, W., 1980, Fault and fold tectonics, Kirk, W.L. (trans); Ellis Horwood Limited, Chichester, England, 565 p.

Jennings, C. W., 1977, Geologic Map of California: California Division of Mines and Geology Geologic Data Map No. 2, scale 1:750,000.

Kirby, S. M., 2005, The quaternary tectonic and structural evolution of the San Felipe Hills, California [m.s. thesis]: Logan, Utah State University, 200 p.

Kirby, S. M., Janecke, S. U., Dorsey, R. J., Housen, B. A., Langenheim, V. E., McDougall, K. A., and Steely, A. N., 2007, Pleistocene Brawley and Ocotillo Formations: Evidence for Initial Strike-Slip Deformation along the San Felipe and San Jacinto Fault zones Southern California. Journal of Geology 115, 43-62.

Le, K., and Oskin, M., 2008, The southern San Jacinto fault zone: SoSAFE field trip, 8p.

Lin, G., Shearer, P. M., and Hauksson, E., 2007, Applying a three-dimensional velocity model, waveform cross correlation, and cluster analysis to locate southern California seismicity from 1981 to 2005: Journal of Geophysical Research, 112, B12309.

Lutz, A. T., Dorsey, R.J., Housen, B. A., Janecke, S. U., 2006, Stratigraphic record of Pleistocene faulting and basin evolution in the Borrego Badlands, San Jacinto fault zone, southern California. Geological Society of America Bulletin 118, 1377-1397.

Magistrale, H., 2002, The relation of the southern San Jacinto fault zone of the Imperial and Cerro Prieto faults. In: Barth, A., ed., Contributions to Crustal Evolution of the Southwestern United States: Geological Society of America Special Paper 365, p. 271-278.

Matti, J.C., Cox, B.F., Morton, D.M., Sharp, R.V., and King, T., 2002, Fault-bounded Neogene sedimentary deposits in the Santa Rosa Mountains, southern California: crustal stretching or transpressional uplift?: Abstracts with Programs, Geological Society of America, vol.34, no.6, p. 124.

McCalpin, J.A., and Hart, E.W., 2002, Ridgetop spreading features and relationships to earthquakes, San Gabriel mountains region, southern California – Part A: Distribution and description of ridgetop depressions (sackungen): National Earthquake Hazards Reduction Program, Improved Final Technical Report 1434-HQ-GR-1026.

Morton, D. M., and Matti, J. C., 1993, Extension and contraction within an evolving divergent strike-slip fault complex: the San Andreas and San Jacinto fault zones at their convergence in southern California. In: Powell, R. E., Weldon, R. J., Matti, J. C., eds., The San Andreas Fault System: Displacement, Palinspastic Reconstruction, and Geologic Evolution: Geological Society of America, Memoir 178, 217-230.

Pettinga, J.R., 1991, Structural styles and basin margin evolution adjacent to the San Jacinto fault zone, southern California: Geological Society of America Abstracts with Programs, v. 23, no. 257.

Revenaugh, J., 1998, Seismic estimation of cumulative offset on the San Jacinto fault zone: EOS, Transactions, American Geophysical Union, v. 79, F593.

Rodgers, T.H., 1963, 30X60 Geologic map of California: Santa Ana Sheet: California Division of Mines and Geology, 1:250000.

Ryter, D.W., 2002, Late Pleistocene kinematics of the central San Jacinto fault zone, southern California [Ph.D. dissertation]: Eugene, University of Oregon 137 p.

Sanders, C. O., 1989, Fault segmentation and earthquake occurrence in the strike-slip San Jacinto fault zone, California. In: Schwartz, D. P.; Sibson, R. H. eds., Proceedings of Conference XLV; a workshop on Fault segmentation and controls of rupture initiation and termination, U. S. Geological Survey Open-File Report OF 89-0315, p. 324-349.

Sanders, C. O., and Kanamori, H., 1984, A seismotectonic analysis of the anza seismic gap, San Jacinto fault zone, southern California: Journal of Geophysical Research, v. 89(B7), p. 5873–5890.

Sanders, C. O., and Magistrale, H., 1997, Segmentation of the northern San Jacinto fault zone, southern California: Journal of Geophysical Research, v. 102(B12), p. 27,453–27,467.

Sanders, C.O., Magistrale, H., and Kanamori, H., 1986, Rupture patterns and preshocks of large earthquakes in the southern San Jacinto fault zone: Bulletin of the Seismological Society of America, v. 76(5), p. 1187-1206.

Sharp, R.V., 1965, Geology of the San Jacinto Fault zone in the Peninsular Ranges of Southern California [PhD thesis]: Pasadena, California Institute of Technology, 182 p.

Sharp, R.V., 1967, San Jacinto Fault zone in the Peninsular Ranges of Southern California: Geological Society of America Bulletin, v. 78, p. 705-729.

Sharp, R. V., 1972, Map showing recently active breaks along the San Jacinto fault zone between the San Bernardino area and the Borrego Valley, California. U. S. Geological Survey Miscellaneous Geologic Investigations Map I-0675, scale 1:24,000.

Sharp, R.V., 1975, En echelon fault patterns of the San Jacinto fault zone, *in* Crowell, J.C., ed., Sam Andreas fault in southern California: California division of Mines and Geology Special Report 118, p. 147-152.

Sharp, R.V., 1979, Some characteristics of the eastern Peninsular Ranges mylonite zone, in Proceedings, Conference VIII, Analysis of Actual Fault Zones in Bedrock: U.S. Geological Survey open file report, 79-1239, p. 258-267

Shearer, P., E. Hauksson and G. Lin, 2005, Southern California hypocenter relocation with waveform cross-correlation, Part 2: Results using source-specific station terms and cluster analysis, Bulletin of the Seismological Society of America, v. 95, p. 904-915.

Simpson, C., 1984, Borrego Springs-Santa Rosa mylonite zone: A Late retaceous West-Directed Thrust in Southern California: Geology, v. 12, p. 8-11.

Simpson, C., 1985, Deformation of granitic rocks across the brittle-ductile transition, Journal of Structural Geology, v. 7, no. 5, p. 503-511.

Steely, A. N. 2006, The evolution from late Miocene west Salton detachment faulting to cross-cutting oblique strike-slip faults in the southwest Salton Trough, California [m.s. thesis]: Logan, Utah State University, 253 p. 3 plates.

Steely, A.N., Janecke, S.U., Axen, G., and Dorsey, R., 2005, Pleistocene (~1 MA) transition from West Salton detachment faulting to cross-cutting dextral strike-slip faults in the SW Salton Trough: Geological Society of America Abstracts with Programs, v. 37, no. 7, p. 274.

Steely, A.N., Janecke, S.U., Dorsey, R.J., and Axen, G.J., 2009, Early Pleistocene initiation of the San Felipe fault zone, SW Salton Trough, during reorganization of the San Andreas fault system: Geological Society of America Bulletin, v. 121, no. 5-6, p. 663-687.

Thatcher, W., Hileman, J.A., Hanks, T.C., 1975, Seismic slip distribution along the San Jacinto Fault zone, southern California and its implications: Geological Society of America Bulletin, v. 86, p. 1140-1146.

Theodore, T.G., 1967, Structure and petrology of the gneisses and mylonites at Coyote Mountain, Borrego Springs, California [Ph.D. thesis]:, Los Angeles, University of California, 268 p.

Theodore, T.G., 1970, Petrogenesis of mylonites of high metamorphic grade in the Peninsular ranges of southern California: Geological Society of America Bulletin, v. 81, p.435-450.

Theodore, T.G., and Sharp, R.V., 1975, Geologic map of the Clark Lake quadrangle, San Diego county, California: U.S. Geological Survey Miscellaneous Field Studies Map MF-0644, scale 1:24000, 1 sheet.

Todd, V.R., Erskine, B.G., and Morton, D.M., 1988, Metamorphic and tectonic evolution of the northern Peninsular ranges batholith, southern California, *in* Ernst, W.G., ed., Metamorphism and Crustal Evolution of the Western United States (Rubey Volume VII): Englewood Cliffs, Prentice-Hall, p. 894-937.

Wilcox, R.E., Harding, T.P., Seely, D.R., 1973, Basic wrench tectonics. In: Sylvester A.G. (ed.), Wrench fault tectonics: American Association of Petroleum Geologists.

Withjack, M.O., and Jamison, W.R., 1986, Deformation produced by oblique rifting: Tectonophysics, v. 126, p.99-124.

Winter, J.D., 2001, An introduction to igneous and metamorphic petrology, 1st edition, Prentice Hall, New Jersey, 697 p.

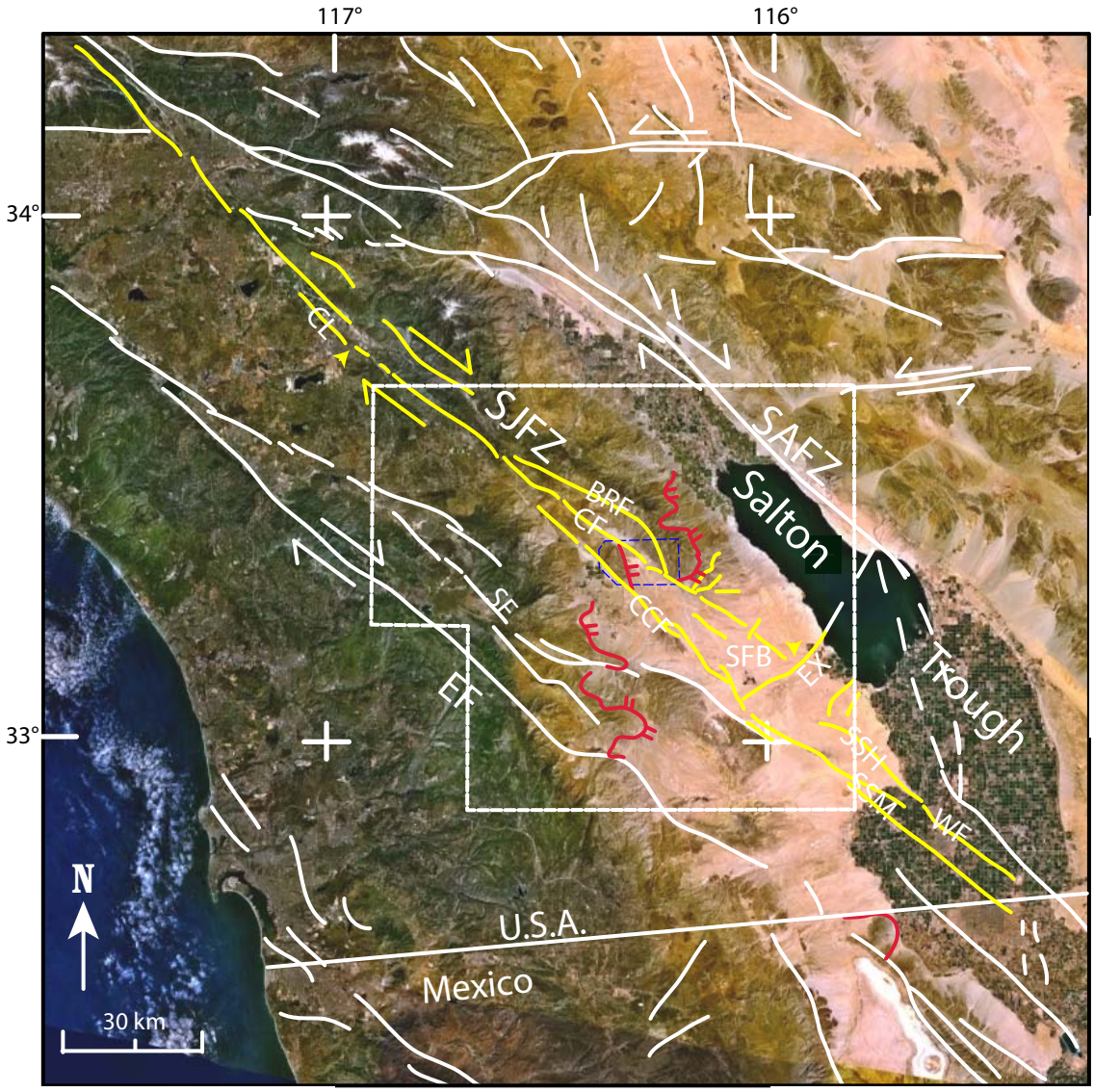

Figure 3-1. NASA Learning Technologies Landsat 7 image of southern California showing major fault traces. White dashed line is the outline of Figure 3-2. Blue dashed outline is the study area. Yellow lines are the major faults associated with the San Jacinto fault zone (SJFZ). Yellow arrows show the beginning and end of the Clark fault. Red line is the Western Salton detachment fault; bars are on the hanging wall. BRF-Buck Ridge Fault; EX-Extra fault zone, SAFZ-San Andreas Fault Zone; SSH-Superstition Hills Fault; SSM-Superstition Mountain Fault; SF-San Felipe fault zone; SFB-San Felipe-Borrego subasin; WF-Wienert Fault. Fault locations compiled from Sanders (1989), Magistrale (2002), and Jennings (1977.) Image modified from Belgarde (2007).

Figure 3-2. Important active faults of southern California overlain on a shaded relief map. The study area is indicated by the black dashed lines, Segments along the Clark Fault are color coded. BB-Borrego Badlands; BM-Borrego Mountain; BR-Buck Ridge; BRF-Buck Ridge Fault; CCF-Coyote Creek fault; CF-Clark Fault; EVFZ-Earthquake Valley fault zone; FCM-Fish Creek Mountains; FCMF-Fish Creek Mountains fault; FCVB-Vallecito-Fish Creek basin; OB-Ocotillo Badlands; SM-Superstition Mountain; TF-Truckhaven fault; VM-Vallecito Mountains; WSDF-West Salton detachment fault; YR-Yaqui Ridge. Faults and segments are compiled and modified from rogers, 1965; Jennings, 1977; Sanders, 1989; Kennedy and Morton, 2004; Kirby, 2005; Lutz, 2005; Steely et al., 2007; Belgrade, 2007.

Figure 3-2

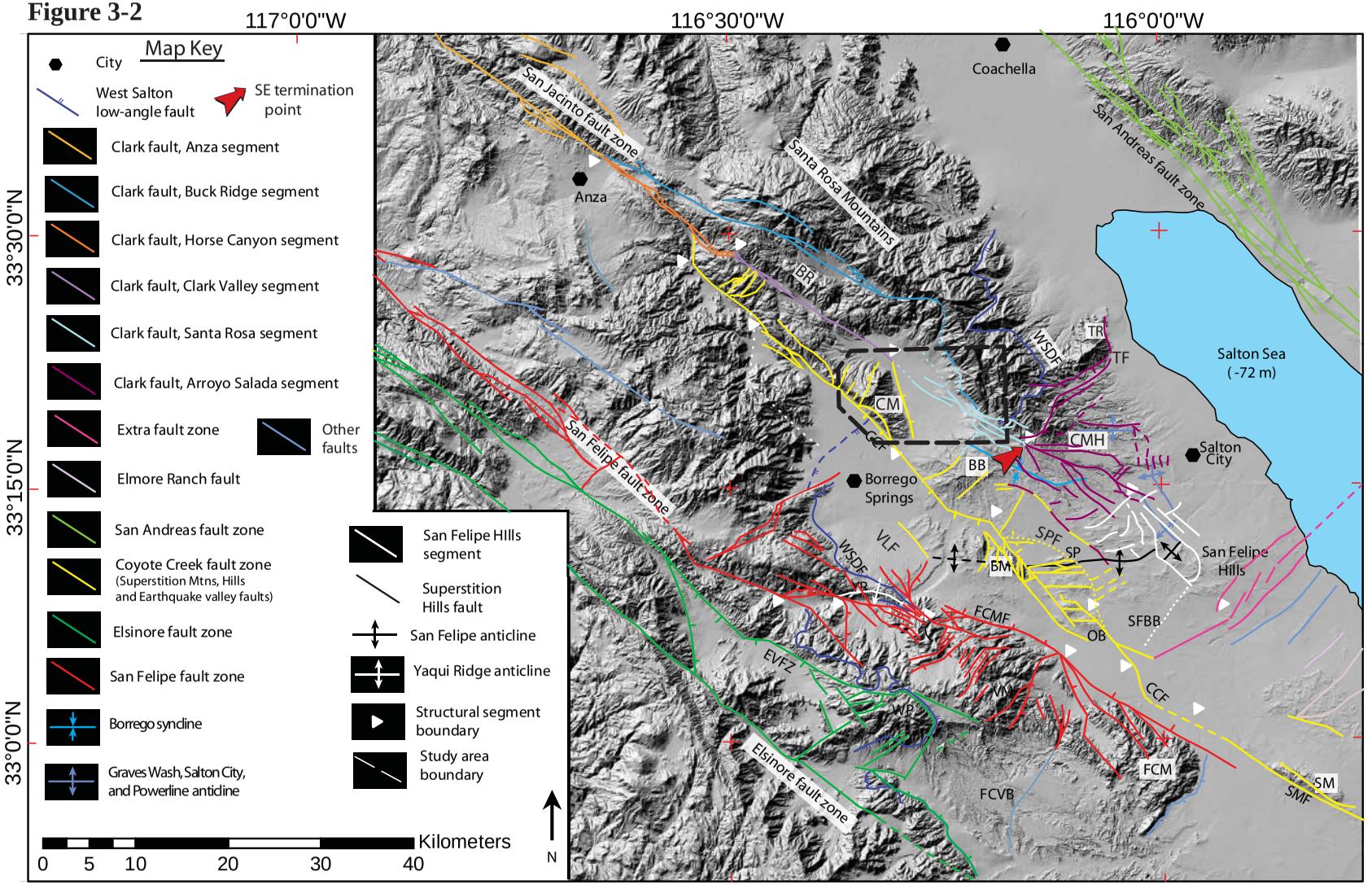
117°0'0"W
116°30'0"W
116°0'0"W
33°30'0"N
33°15'0"N
33°0'0"N
Map Key
City
West Salton low-angle fault
SE termination point
Clark fault, Anza segment
Clark fault, Buck Ridge segment
Clark fault, Horse Canyon segment
Clark fault, Clark Valley segment
Clark fault, Santa Rosa segment
Clark fault, Arroyo Salada segment
Extra fault zone
Other faults
Elmore Ranch fault
San Andreas fault zone
Coyote Creek fault zone (Superstition Mtns, Hills and Earthquake valley faults)
Elsinore fault zone
San Felipe fault zone
Borrego syncline
Graves Wash, Salton City, and Powerline anticline
San Felipe HIlls segment
Superstition Hills fault
San Felipe anticline
Yaqui Ridge anticline
Structural segment boundary
Study area boundary
Kilometers
0 5 10 20 30 40
N
San Jacinto fault zone
Santa Rosa Mountains
San Andreas fault zone
Coachella
Anza
BR
WSDF
TR
TF
Salton Sea (-72 m)
CM
CCF
CMH
BB
Salton City
Borrego Springs
San Felipe fault zone
VLF
SPF
SP
BM
San Felipe Hills
YR
FCMF
SFBB
OB
EVFZ
WP
CCF
FCM
SM
SMF
FCVB
Elsinore fault zone

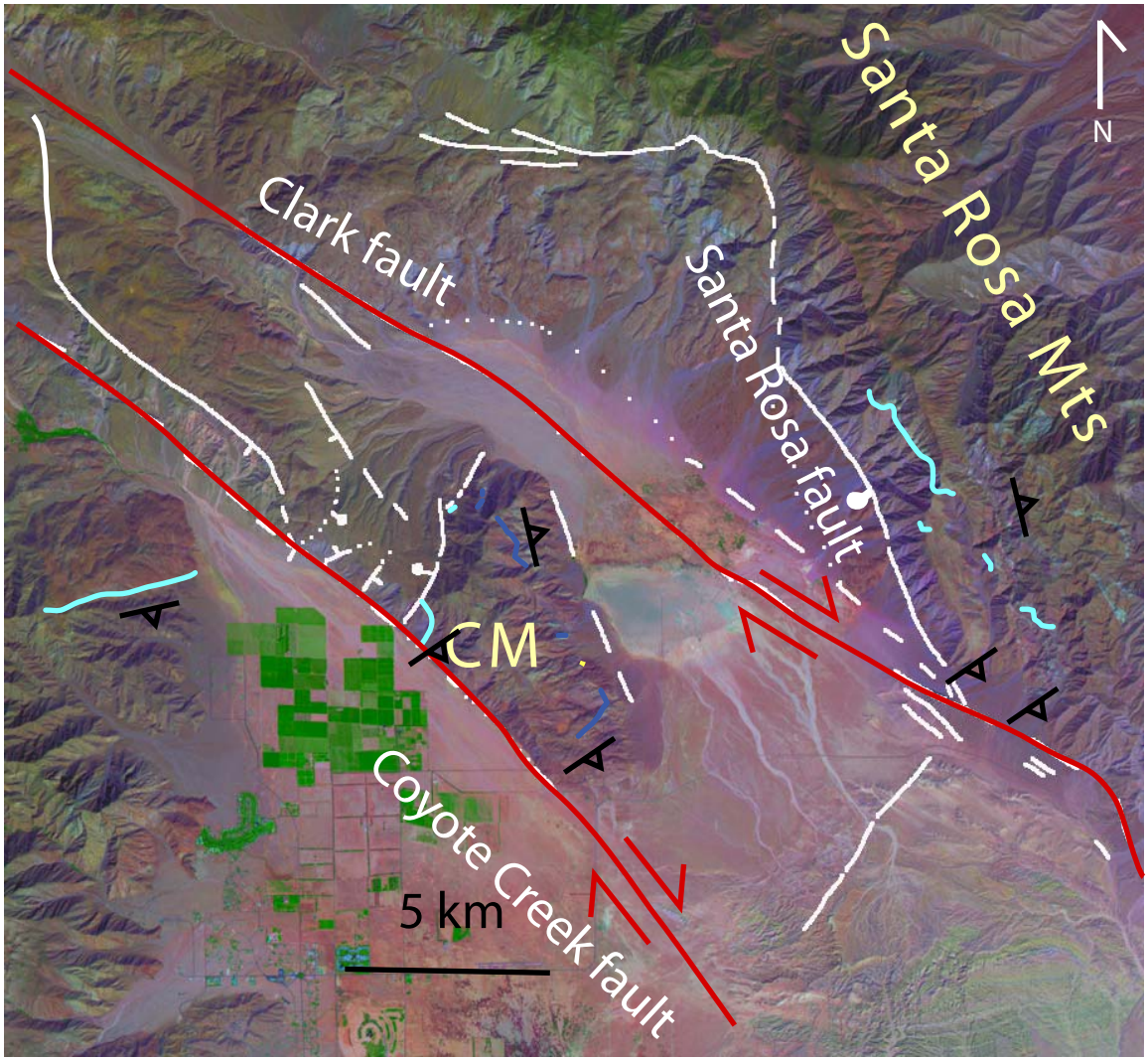

Figure 3-3. Processed Landsat image of the Clark and Coyote Creek faults (red) showing marbles in the adjacent crystalline rocks that correlate across the Clark Fault. Foliations are from Theodore and Sharp (1975), Sharp (1967), and S.U. Janecke, inplubished mapping. CM-Coyote Mountain. The blue represents the locations of marble and marble rich zones with the structurally higher zone being dark blue. Modified from S.U. Janecke

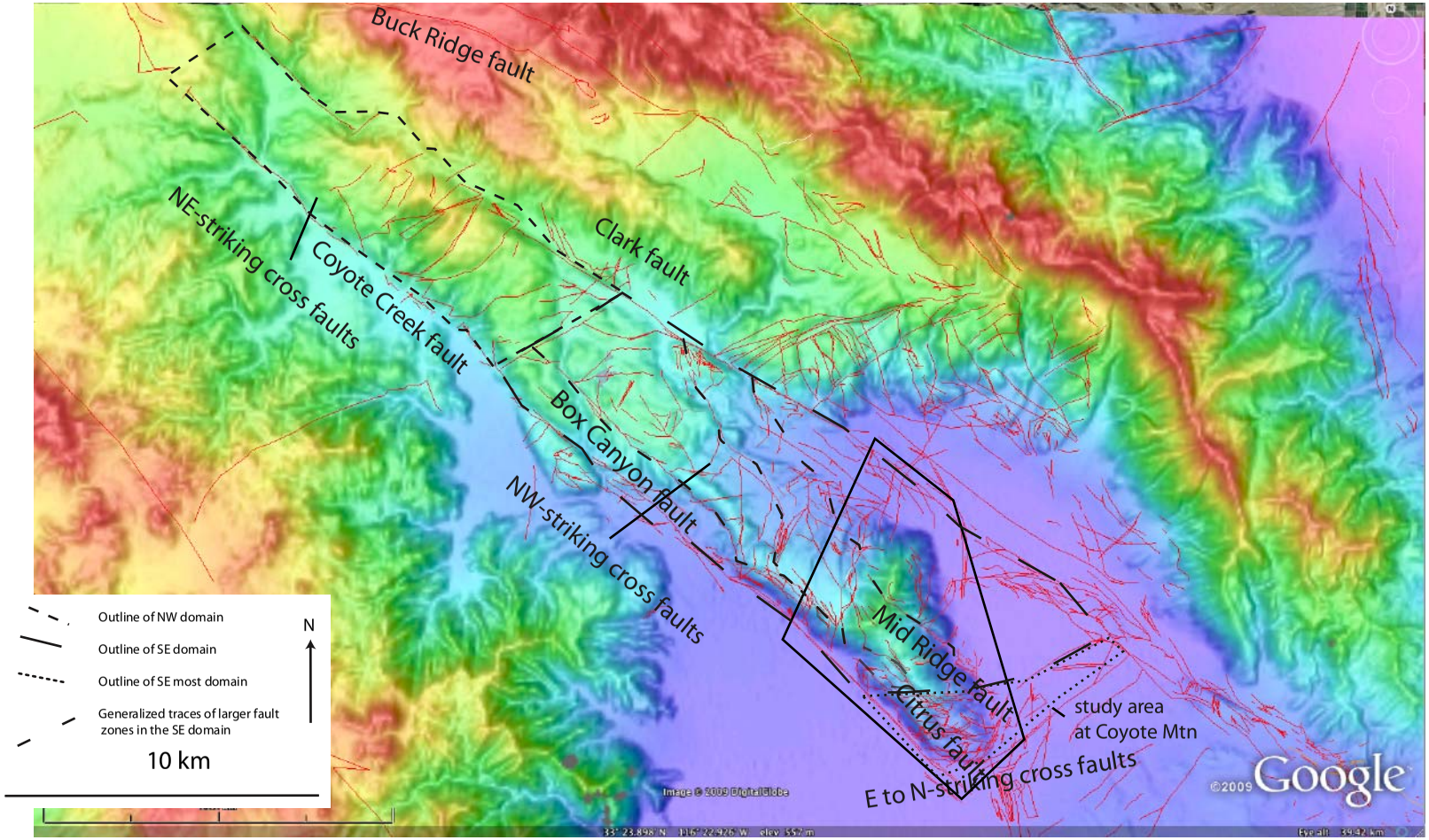

Figure 3-4. Google Earth image with DEM overlain showing the Coyote Ridge structural domains. There are four different domains. Warm colors of the DEM represent higher elevations and cooler colors represent lower elevations. Note the complexity of faulting in the area. By. S. Janecke.

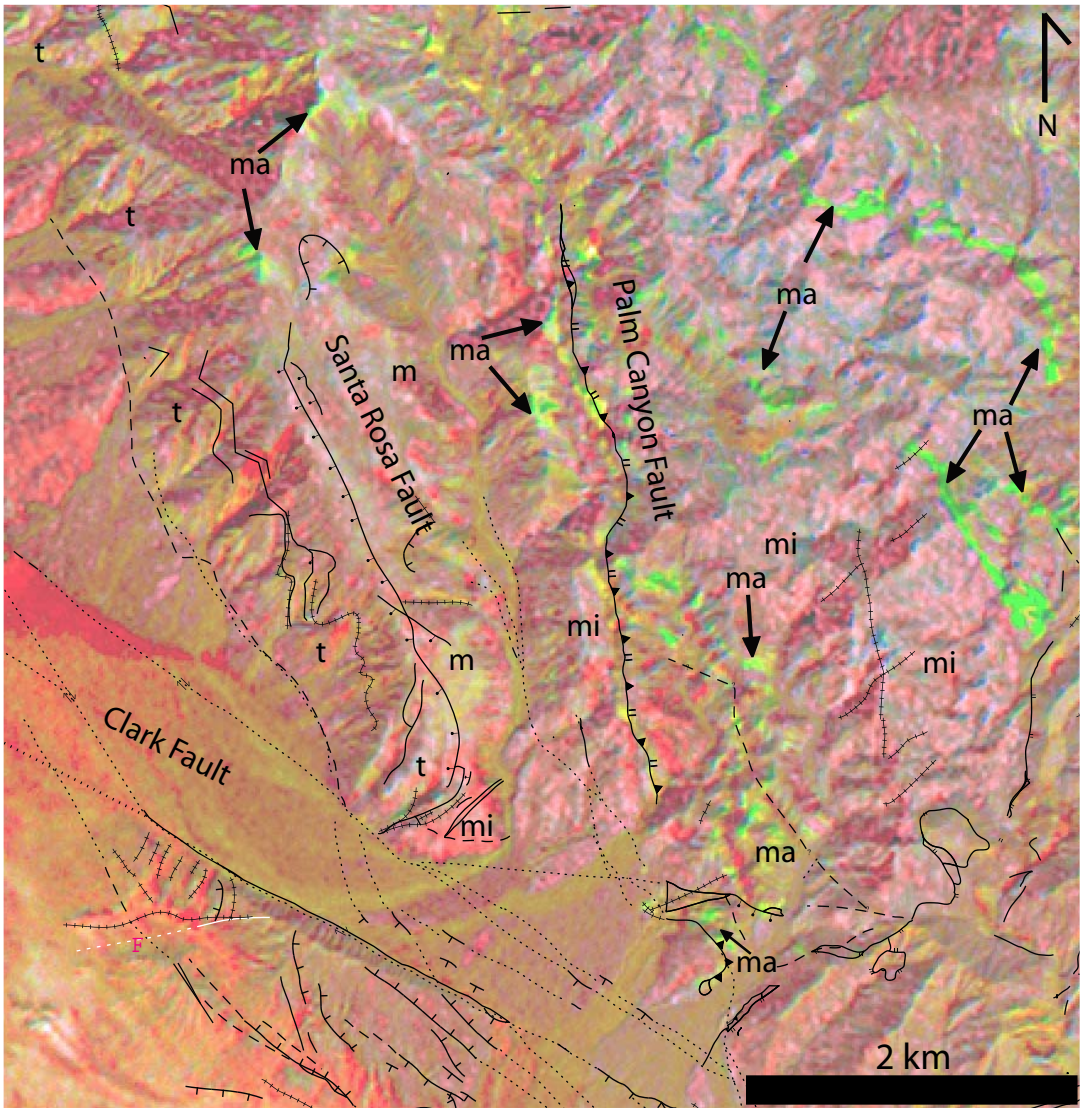

Figure 3-5. Processed Landsat image of the southeast Santa Rosa Mountains with faults mapped from this study shown. Note the complexity of faulting. Greens and yellows represent marble and marble rich zones, light pinks are migmatites, and dark pinks and reds are biotite hornblende bearing tonalite and orange is mylonite. T = tonalite; mi = migmatite; m = mylonite; ma = marble.

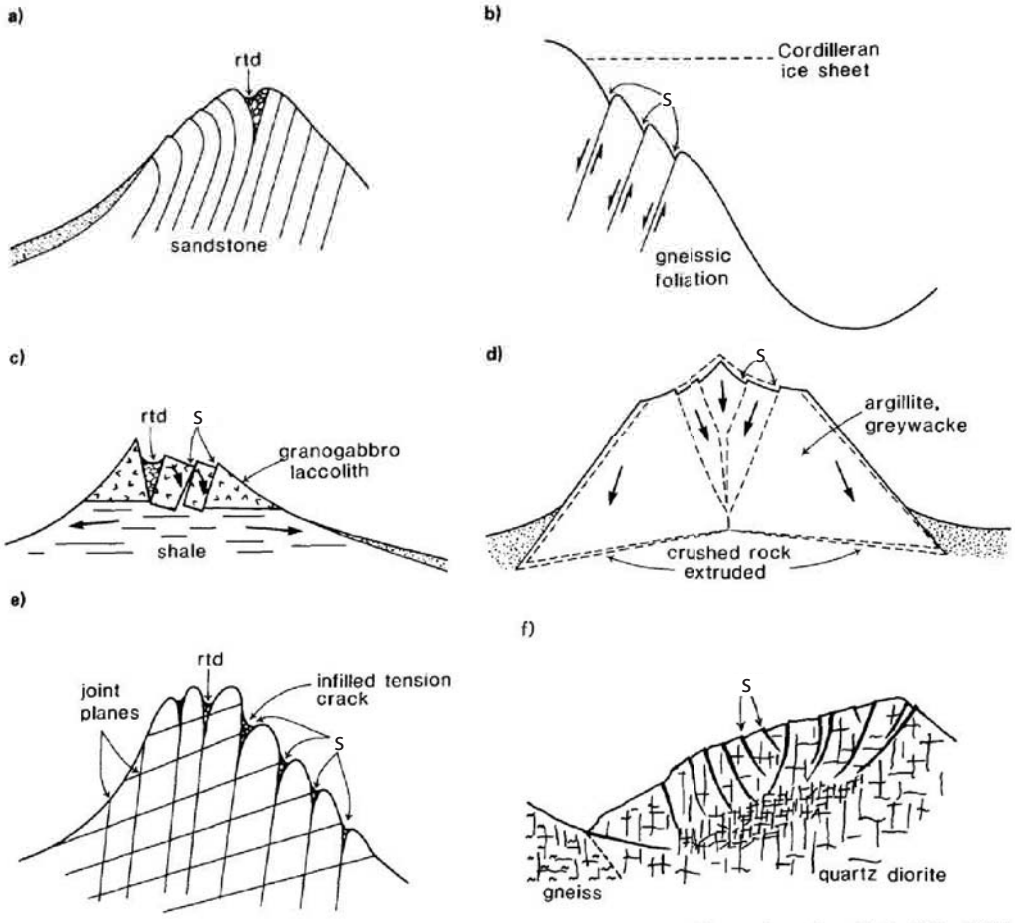

Figure 3-6. Figures showing different styles of sackung type landslides and their mechanics. a) sackung attributed to slow downslope bending of strata under gravity. b) sackung caused from variations in isostatic rebound. c) sackung created from horizontal spreading causing tensional failure and subsidence. d) sackung attributed from foundering of a ridge core, causing an outward and downward motion of the valley side masses along low angle shear planes. e) sackung attributed to ridge spreading in areas of high relief causing modified tension cracks. f) sackung caused from steeply inclined slip planes on which the rock behaves dilatantly on account of low effective normal stress. rtd=ridge top depression; s= sackung. Figure modified from Bovis (1982).

Figure 3-7. Simplified geologic map of the study area showing the locations significant features and locations of field photographs. Letters correspond with photographs from figures 3-9, 3-11, and 3-15.of the unique assemblage used to measure separation across the Clark fault, as well as the locations of field photos. Red dots mark the locations of thin section locations. The biotite hornblende tonalite is gray, the migmatite is green and the mylonite and mylotinized rocks are blue.

Figure 3-7

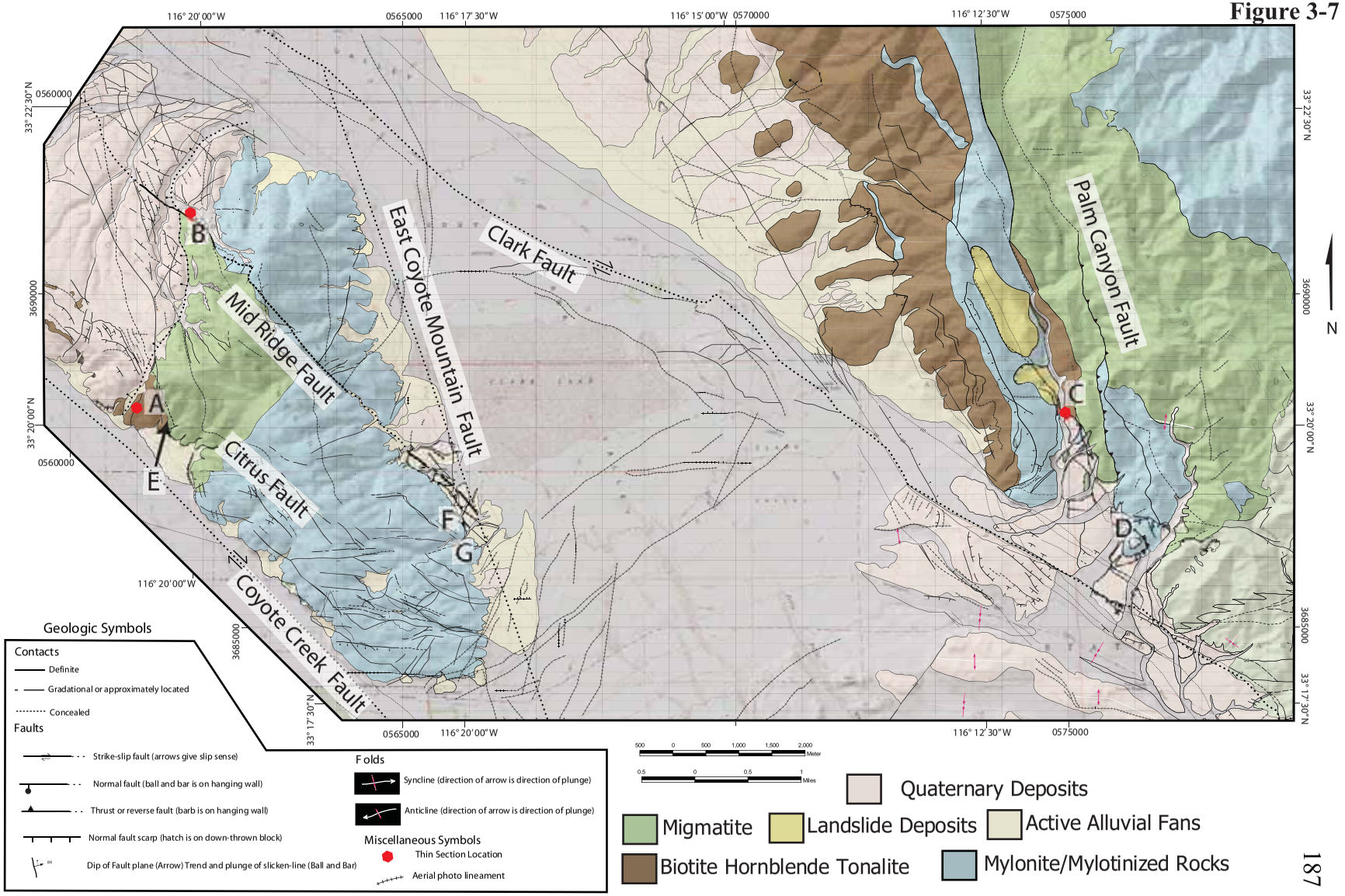
116° 20' 00" W
0565000
116° 17' 30" W
116° 15' 00" W
0570000
116° 12' 30" W
0575000
33° 22' 30" N
0560000
3690000
33° 20' 00" N
3685000
33° 17' 30" N
East Coyote Mountain Fault
Clark Fault
Palm Canyon Fault
Mid Ridge Fault
Citrus Fault
Coyote Creek Fault
A
B
C
D
E
F
G
N
Geologic Symbols
Contacts
Definite
Gradational or approximately located
Concealed
Faults
Strike-slip fault (arrows give slip sense)
Normal fault (ball and bar is on hanging wall)
Thrust or reverse fault (barb is on hanging wall)
Normal fault scarp (hatch is on down-thrown block)
Dip of Fault plane (Arrow) Trend and plunge of slicken-line (Ball and Bar)
Folds
Syncline (direction of arrow is direction of plunge)
Anticline (direction of arrow is direction of plunge)
Miscellaneous Symbols
Thin Section Location
Aerial photo lineament
500 0 500 1,000 1,500 2,000 Meter
0.5 0 0.5 1 Miles
Quaternary Deposits
Migmatite
Landslide Deposits
Active Alluvial Fans
Biotite Hornblende Tonalite
Mylonite/Mylotinized Rocks

Figure 3-8. Simplified map of the study area showing all faults and folds. Notice the complexity of faulting in Coyote Mountain as well as the northeast trending faults in the northern section of Clark Valley. The biotite hornblende tonalite is gray, the migmatite is green and the mylonite and mylotinized rocks are blue.

Figure 3-8

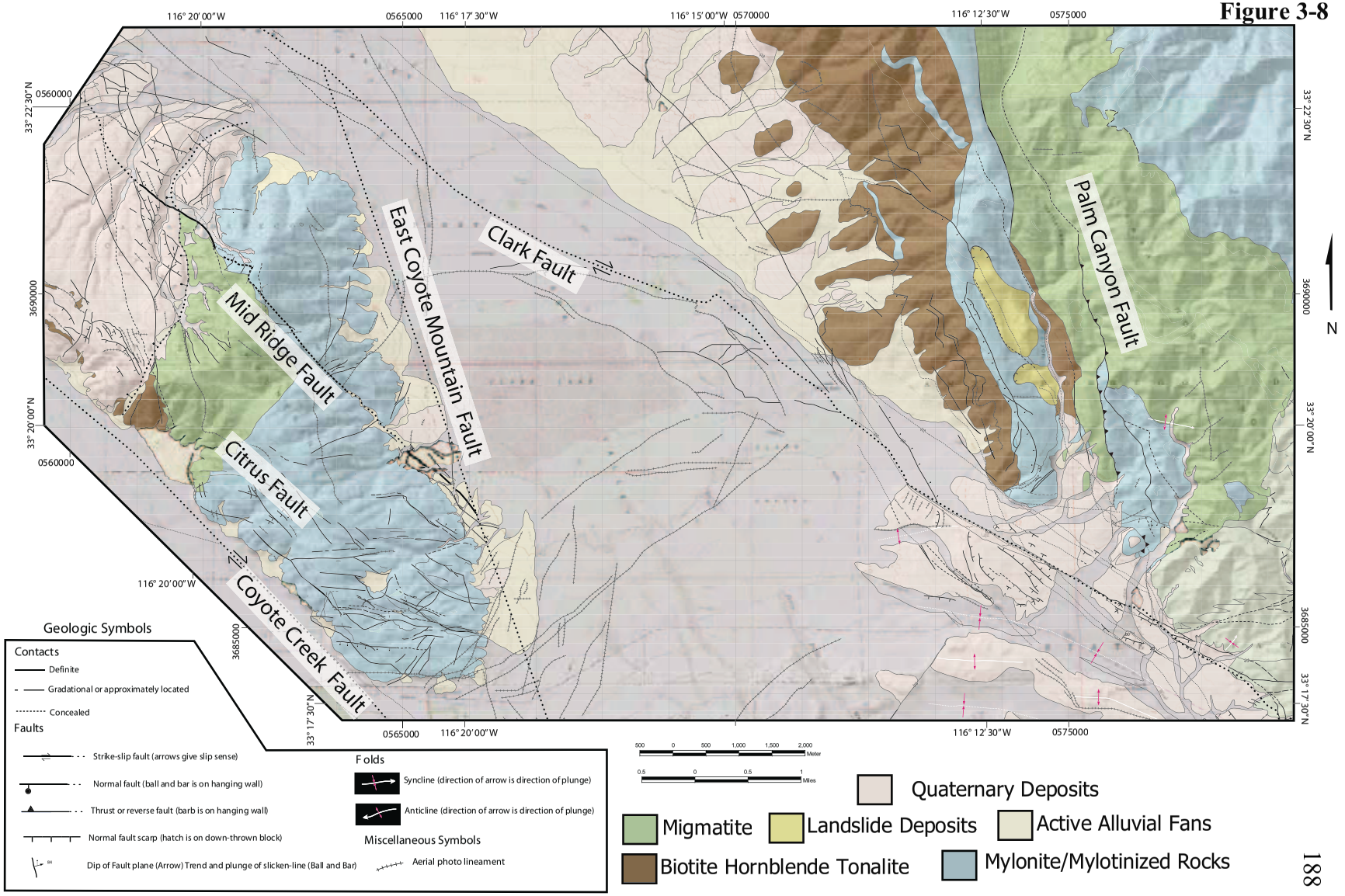
116° 20' 00" W
0565000
116° 17' 30" W
116° 15' 00" W
0570000
116° 12' 30" W
0575000
33° 22' 30" N
0560000
3690000
33° 20' 00" N
3685000
33° 17' 30" N
East Coyote Mountain Fault
Clark Fault
Palm Canyon Fault
Mid Ridge Fault
Citrus Fault
Coyote Creek Fault
N
Geologic Symbols
Contacts
Definite
Gradational or approximately located
Concealed
Faults
Strike-slip fault (arrows give slip sense)
Normal fault (ball and bar is on hanging wall)
Thrust or reverse fault (barb is on hanging wall)
Normal fault scarp (hatch is on down-thrown block)
Dip of Fault plane (Arrow) Trend and plunge of slicken-line (Ball and Bar)
Folds
Syncline (direction of arrow is direction of plunge)
Anticline (direction of arrow is direction of plunge)
Miscellaneous Symbols
Aerial photo lineament
500 0 500 1,000 1,500 2,000 Meter
0.5 0 0.5 1 Miles
Quaternary Deposits
Migmatite
Landslide Deposits
Active Alluvial Fans
Biotite Hornblende Tonalite
Mylonite/Mylotinized Rocks

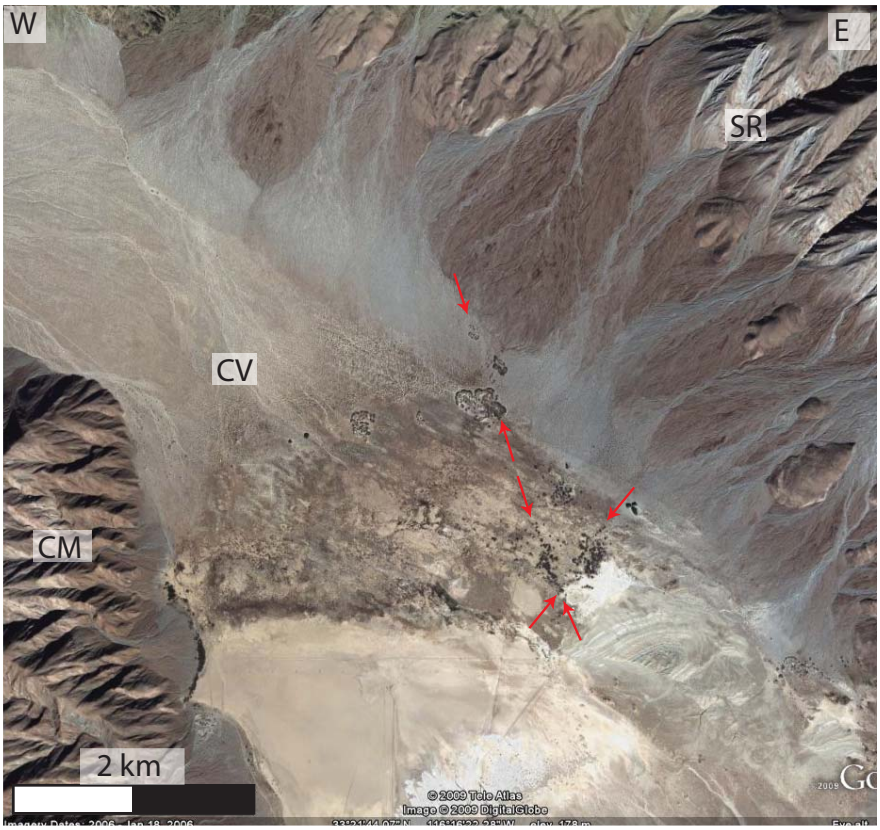

Figure 3-9. Google earth image with the various vegetation lineaments along the Clark Fault. The red arrows mark the ends of the lineaments. CM-Coyote Mountain; CV-Clark Valley; SR-Santa Rosa Mountains.

Figure 3-10. 1:24,000 map showing the Mid Ridge and Citrus fault in Coyote Mountain. See Appendix J for descriptions of the units. Complex faulting along with various potential piercing points make identifying separation along this fault difficult. Two possible piercing points are obvious showing opposite sense of motion. Marbles towards the northern part of the fault show approximately 3.6 km of dextral separation, where as a gneissic gabbro and amphibolite – adamellite contact show 1.7 km of sinsitral separation.

Figure 3-10

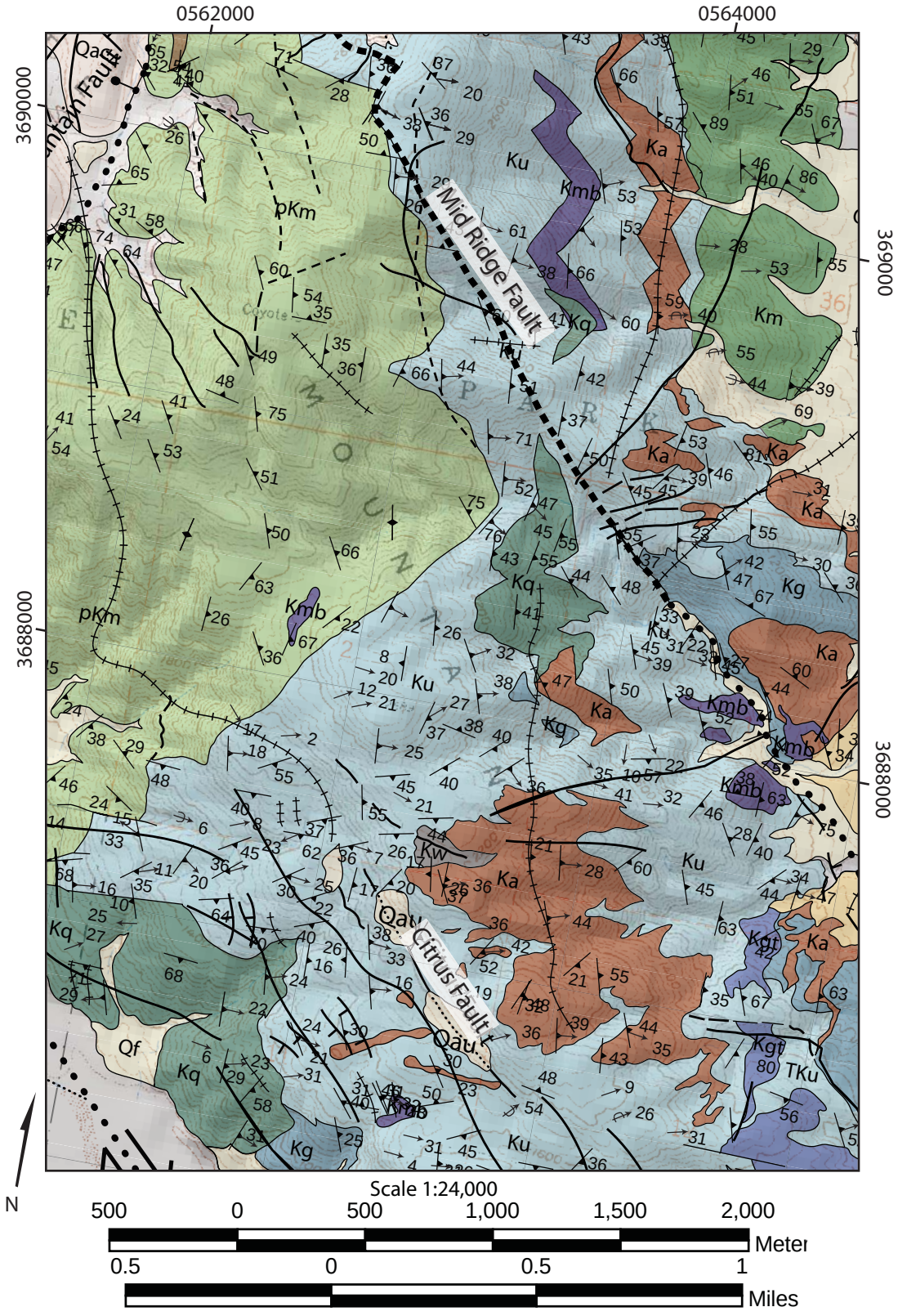
0562000
0564000
3690000
3688000
369000
3688000
Mid Ridge Fault
Citrus Fault
Qac
pKm
Ku
Kmb
Ka
Km
Kq
Kw
Kg
Kgt
Qau
Qf
TKu
N
Scale 1:24,000
500 0 500 1,000 1,500 2,000
Meter
0.5 0 0.5 1
Miles

Figure 3-11. 1:41,600 map showing the East Coyote Mountain fault in Clark Lake Valley. See Appendix J for descriptions of the units. Note the scarps in the Quaternary deposits and the complexity.

Figure 3-11

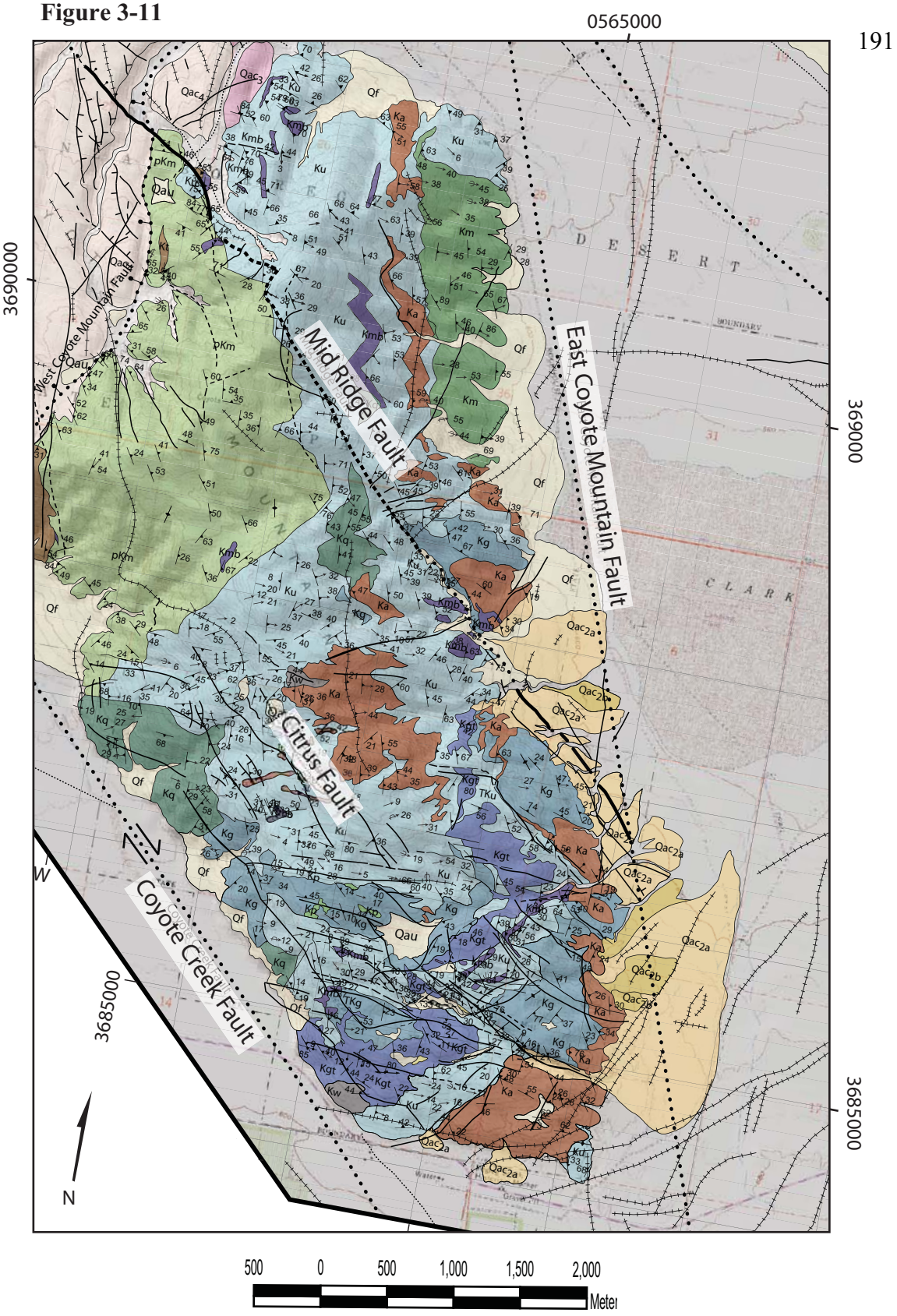
0565000
369000
3685000
West Coyote Mountain Fault
Mid Ridge Fault
East Coyote Mountain Fault
Citrus Fault
Coyote Creek Fault
D E S E R T
C L A R K
W
N
500 0 500 1,000 1,500 2,000
Meter

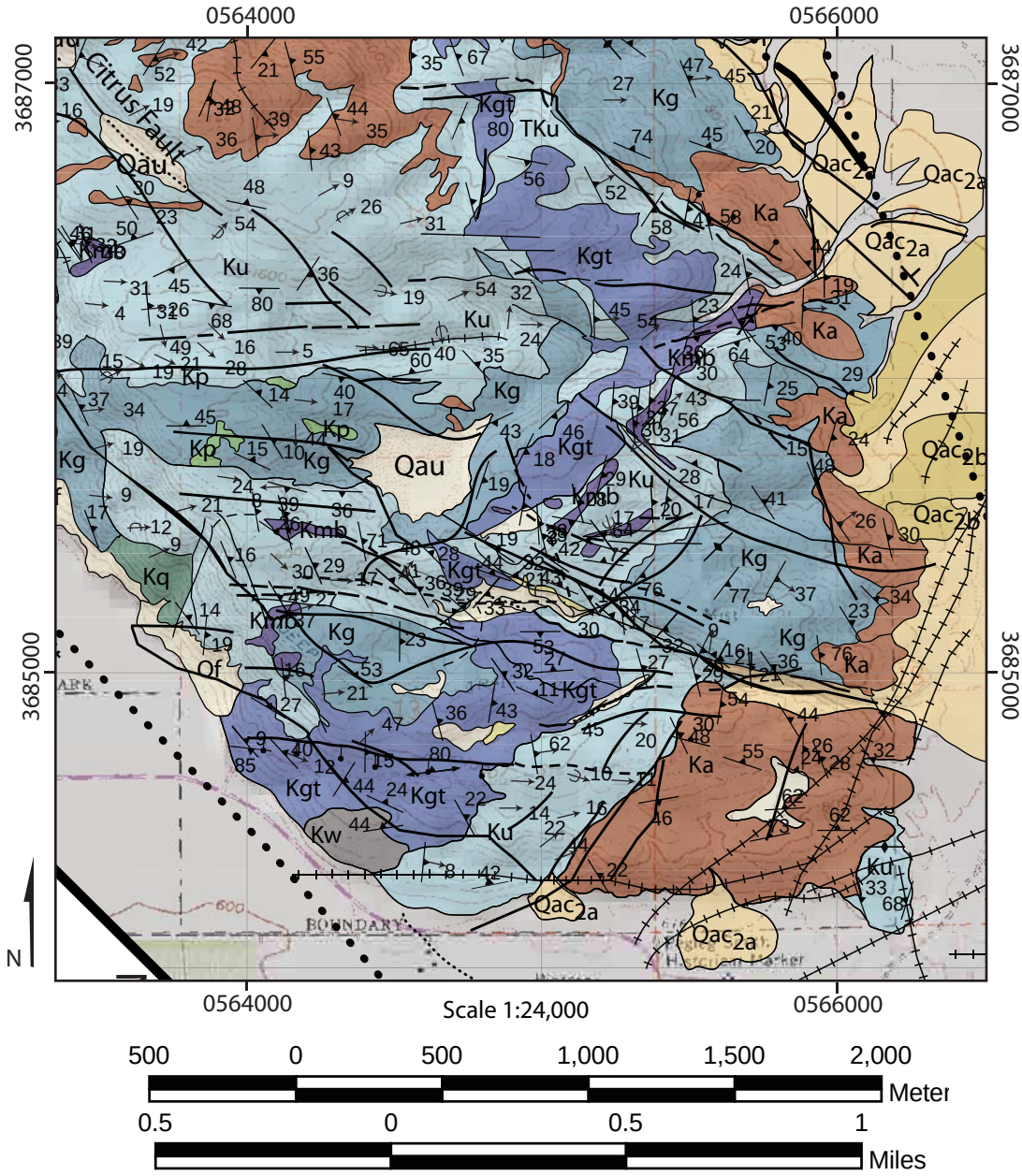

Figure 3-12. 1:24,000 map showing some the complex faulting in Coyote Mountain in the Peg Leg domain. See Appendix J for descriptions of the units. Note the complexity of faulting in the area and the apparent sinsitral and dextral separation along many of these faults.

Figure 3-13. Field photographs of brittle faults in the Santa Rosa Mountains, and Coyote Mountain. (d) Photograph of two small thrust faults in the Santa Rosa Mountains looking northeast (UTM 0576112, 3686773). The two faults have developed gouge and display down to the SE slip. Hammer is for scale. (e) Photograph of a brittle fault in Coyote Mountain looking northeast (UTM 0561499, 3688290). The fault is located in the migamtite (pKm) unit near the location of Anza's Angel. The white line represents the fault and is 20 m long. (f) Photograph of a small thrust in Coyote Mountain looking northeast (UTM 0565557, 3686646). The small thrust has some drag folding associated with it. Hammer for scale.

Figure 3-13

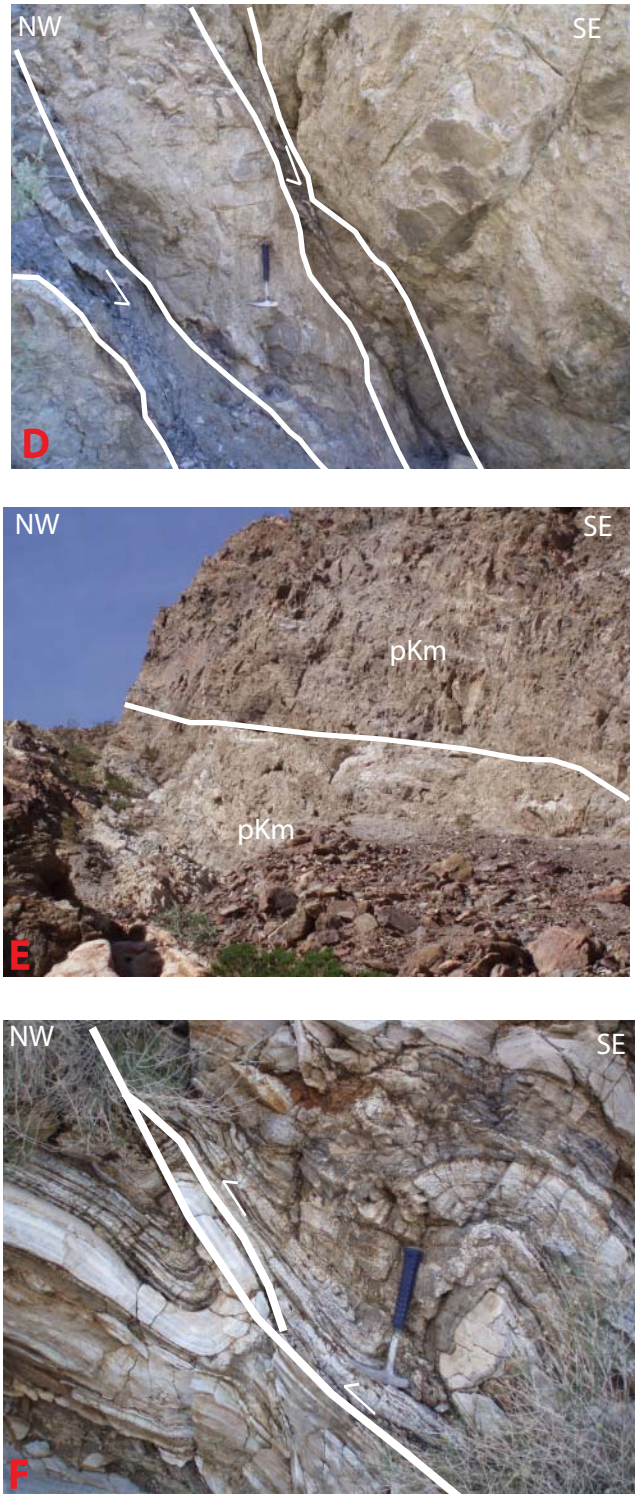

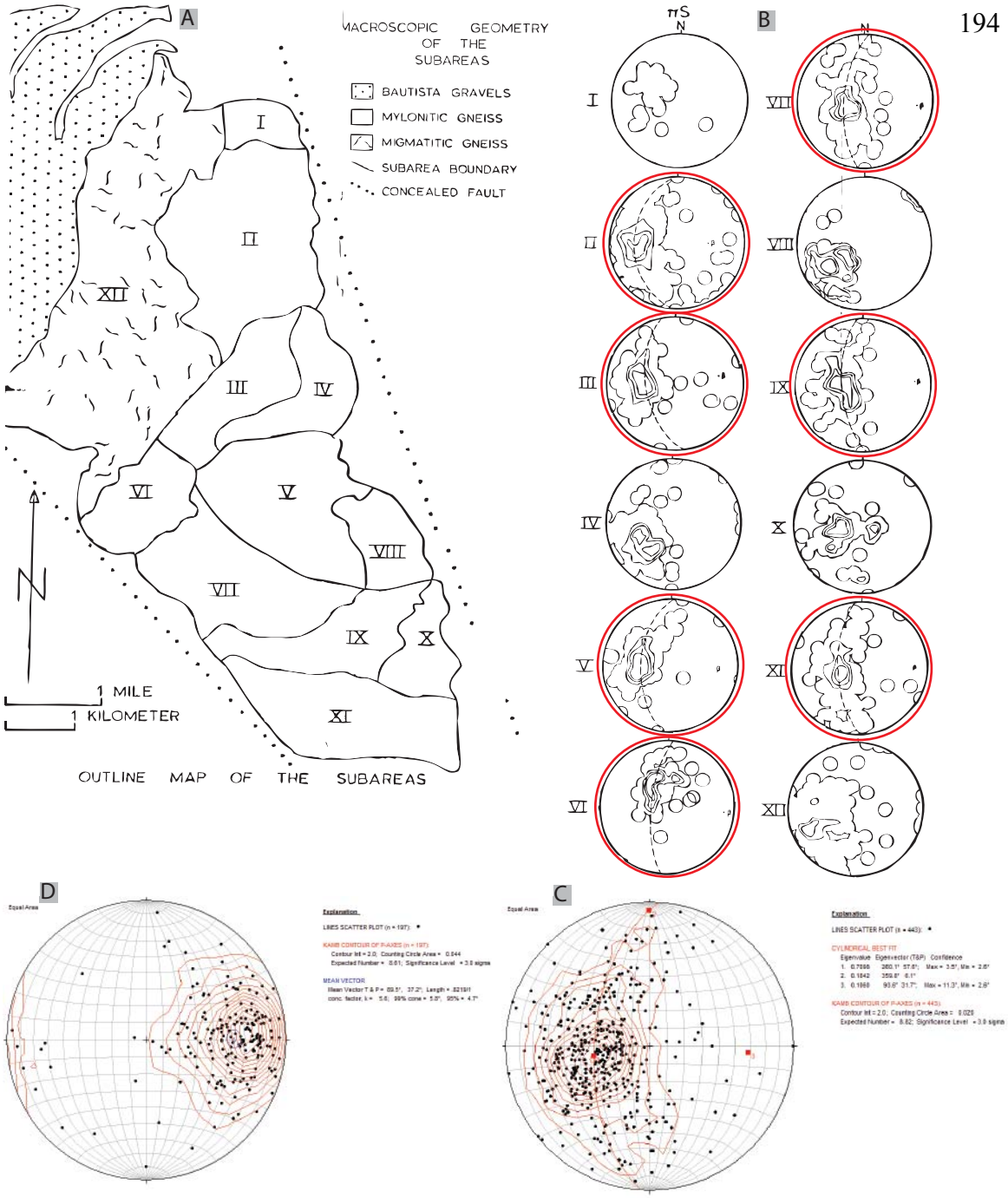

Figure 3-14. Structural domains and stereonets of lower hemisphere projections of poles to foliation and lineations of Coyote Mountain. A. Generalized geologic map of Coyote mountain subdivided into 12 different areas. B. Stereonets of poles to foliations of the subareas of Coyote mountain by Theodore (1967). Seven of the subareas (II, III, V, VI, VII, IX, XI; labeled in red) show folds with a general east-southeast trend. C. Stereonet of all Coyote mountain poles to foliation from B as well as all data collected for this study. Note the similarity of the fold in C as with the folds in B. D. Lower hemisphere projection of all lineations from Theodoere (1967) and this study. They cluster in the same area and have a mean trend of 89.5° and plunge 37.2°.

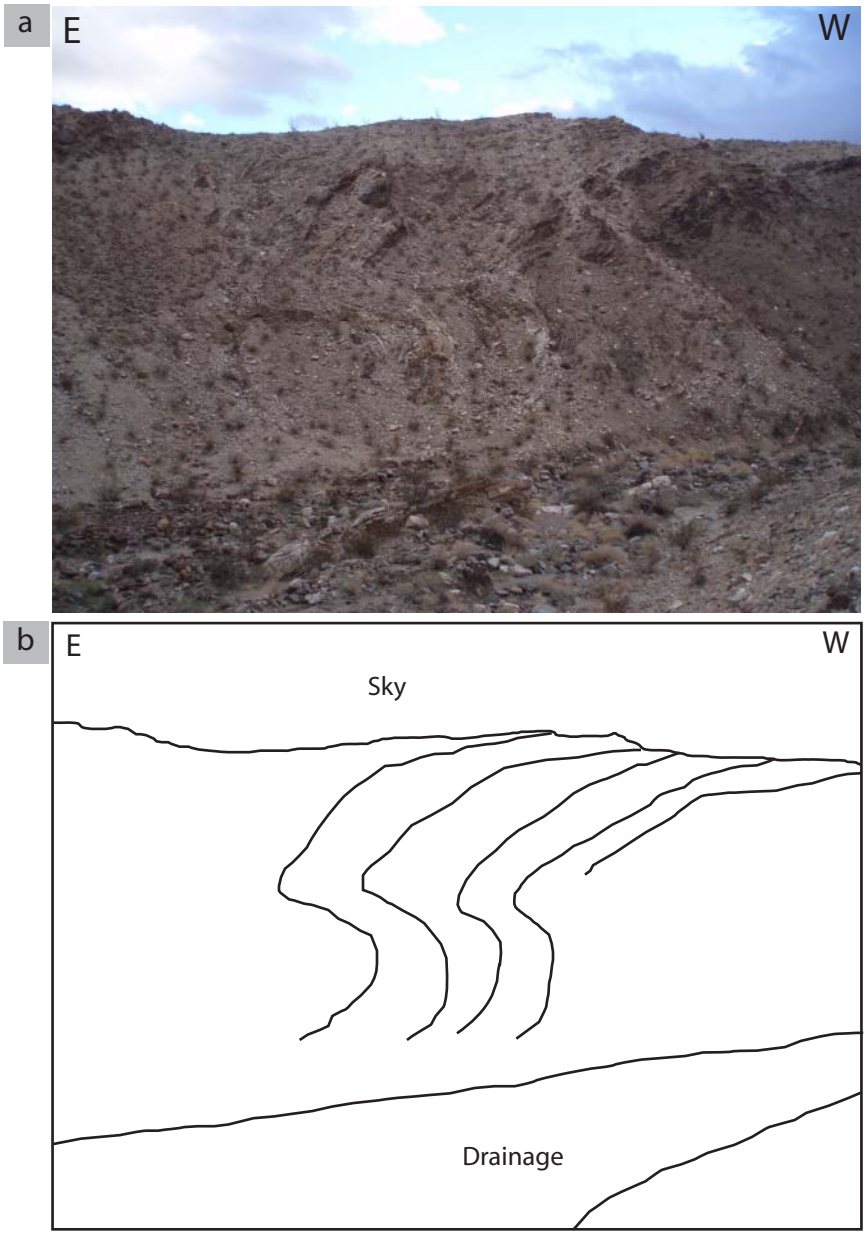

Figure 3-15. Field photograph of the east directed fold related to a thrust fault in Coyote Mountain. The photograph is looking south (UTM 056599, 3686409). The cliff face is approximately 80 m tall. (a) Picture. (b) Sketch of fold.

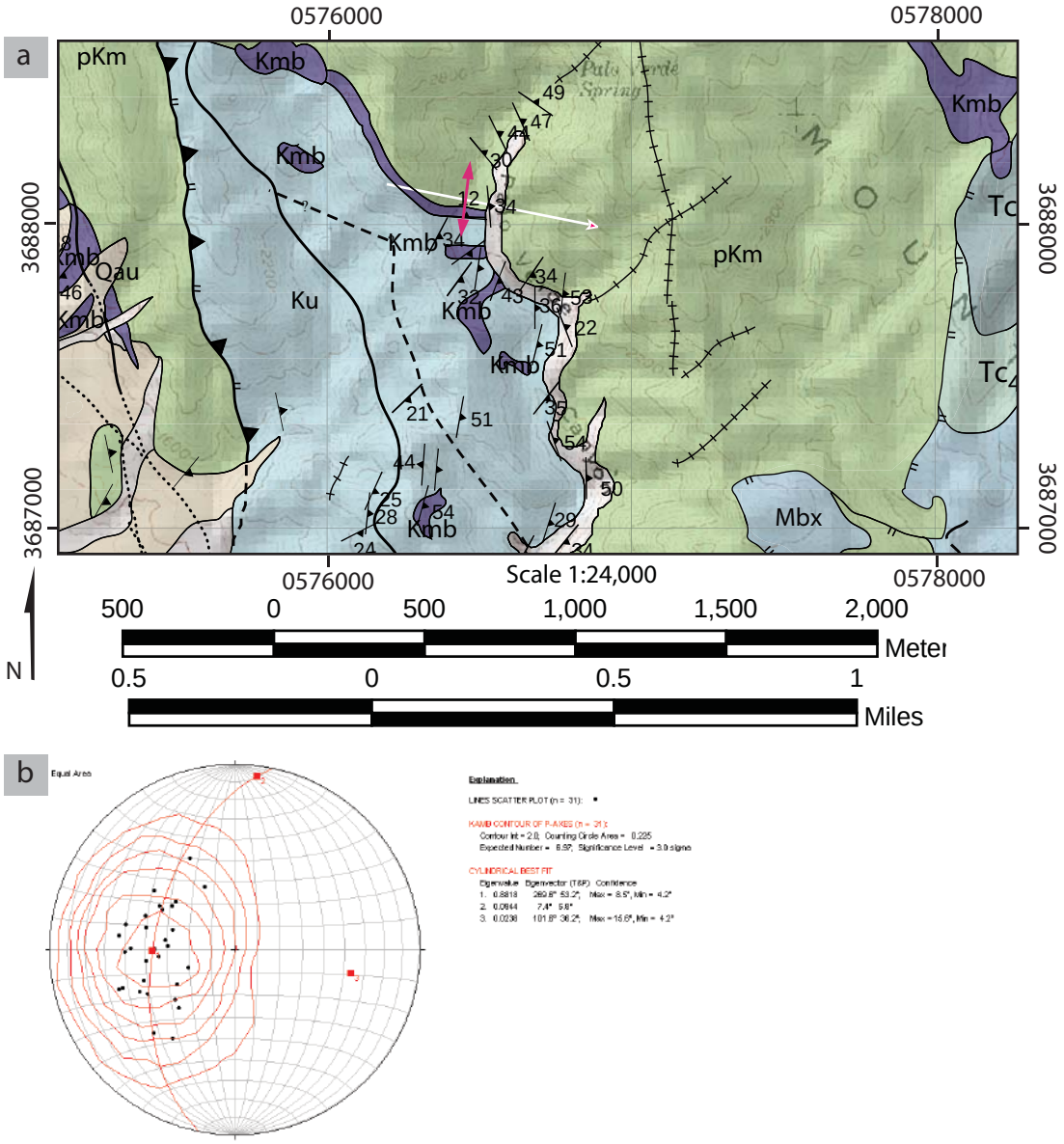

Figure 3-16. 1:24,000 map showing the fold in the Santa Rosa Mountains. See Appendix J for descriptions of the units. (a) The fold is poorly developed and likely not due to movement along the Clark Fault. (b) The accompanying stereonet displaying its trend and plunge is also shown. Note the lack of faulting cutting the fold, and its near confinement to one unit.

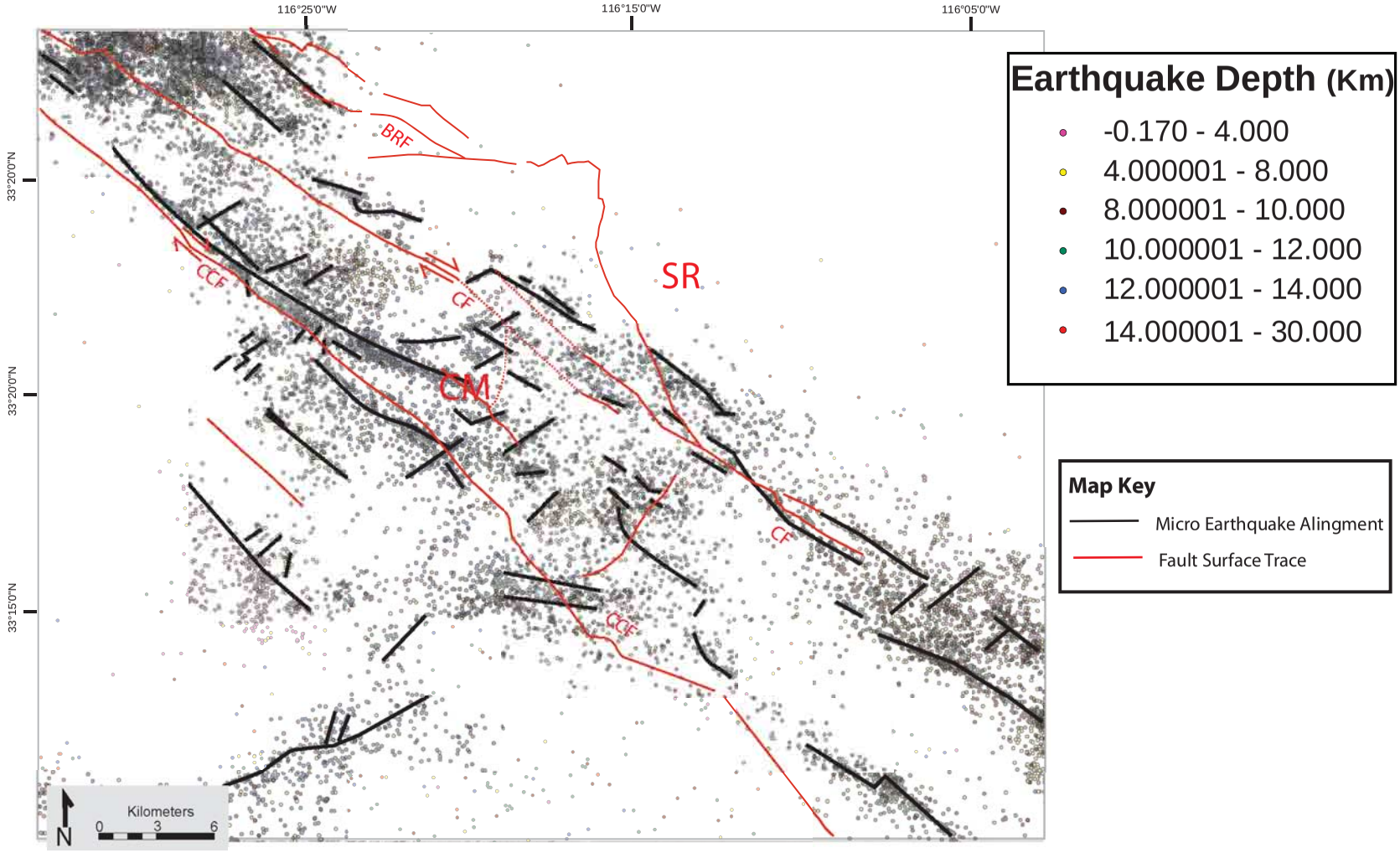

Figure 3-18. Interpretation of earthquake epicenters of the Clark and Coyote Creek fault zones. Dataset from Lin et al. (2007) plotted by depths. Alingments of earthquakes are shown as black lines. Fault surface traces are shown as red lines. CM-Coyote Mountain; SR-Santa Rosa Mountains CF-Clark Fault; CCF-Coyote Creek Fault; BRF-Buck Ridge Fault. From S.U. Janecke.

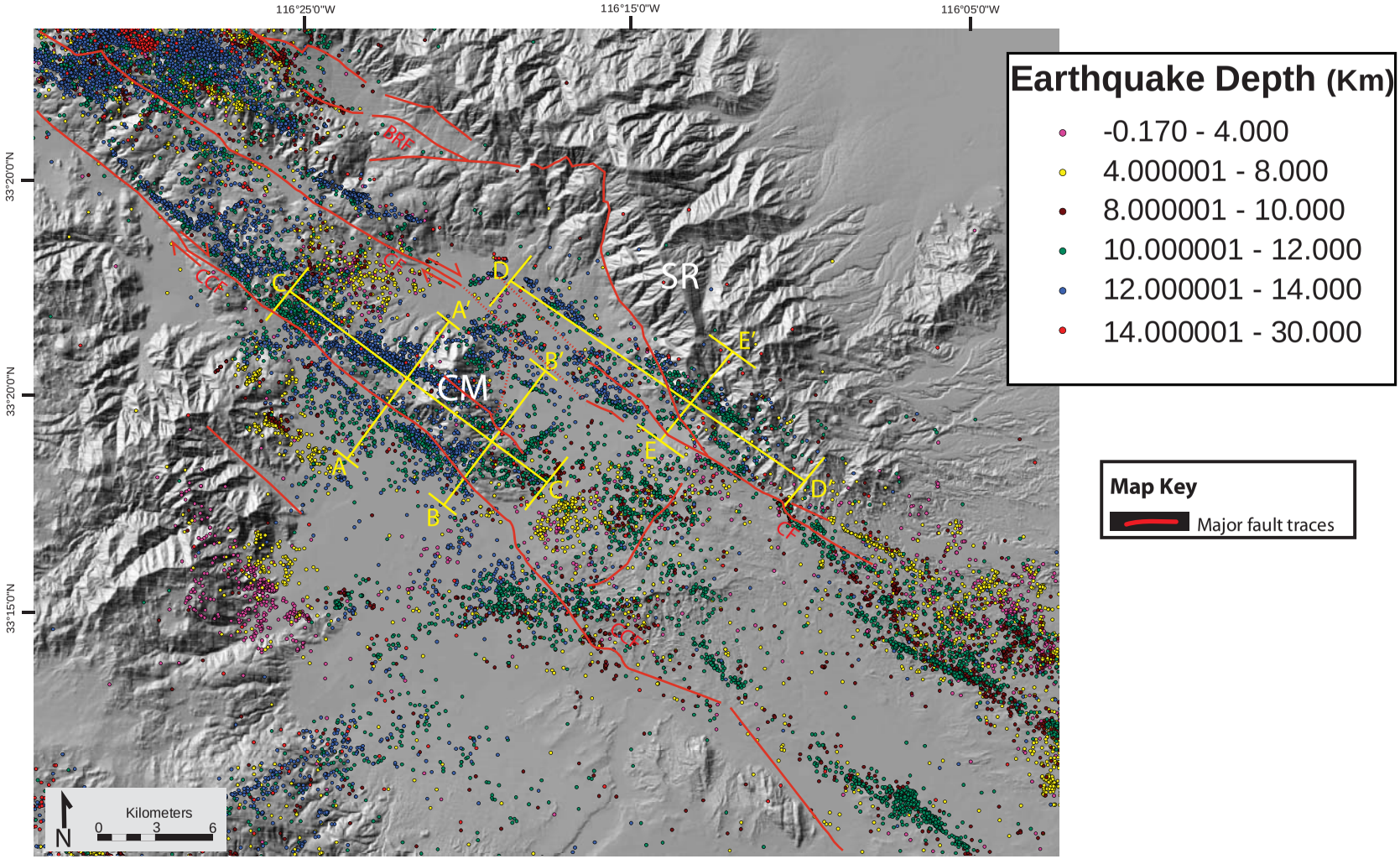

Figure 3-17. Interpretation of earthquake epicenters of the Clark and Coyote Creek fault zones. Dataset from Lin et al. (2007) plotted by depths. Locations of the faults are noted. Note the correlation between the earthquake alignments and fault traces. Cross sections from Figure 3-20 are plotted in yellow. CM-Coyote Mountain; SR-Santa Rosa Mountains; CF-Clark Fault; CCF-Coyote Creek Fault. BRF-BuckRidge Fault

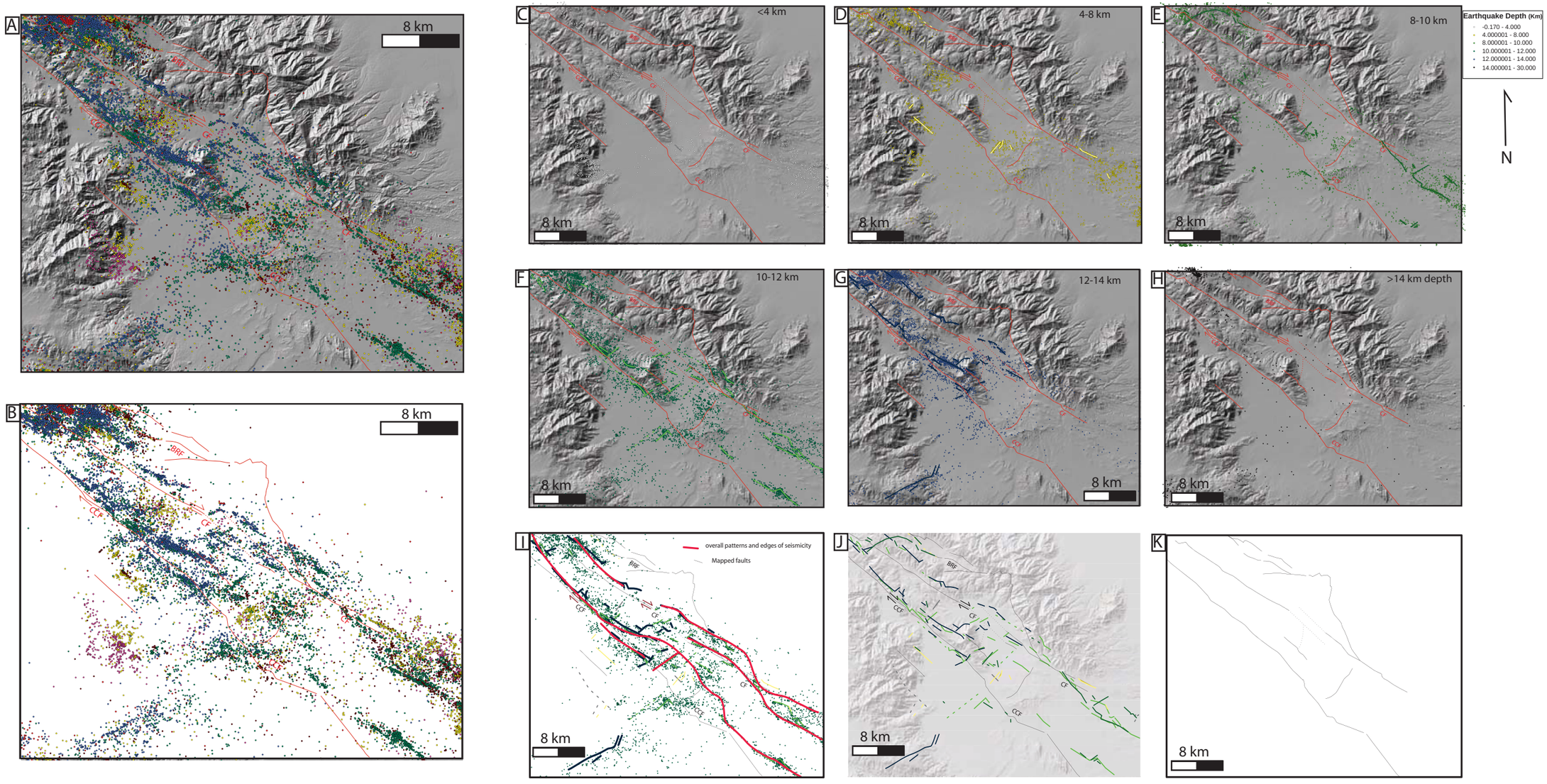

Figure 3-19. Microseismicity of the field area plotted according to depth. Dataset from Lin et al (2007). Fault surface locations are red. CF=Clark fault, CCF= Coyote Creek fault, BRF=Buck Ridge fault. A) Shaded relief map with all microseismicity plotted and colored according to depth. B) All microseismicity plotted with no shaded relief map displayed. C) Map of microseismicity less than 4 km depth with earthquake alignments identified. D) Map of microseismicity 4-8 km depth with earthquake alignments identified. E) Map of microseismicity 8-10 km depth with earthquake alignments identified. F) Map of microseismicity 10-12 km depth with earthquake alignments identified. G) Map of microseismicity 12-14 km depth with earthquake alignments identified. H) Map of microseismicity greater than 14 km depth with earthquake alignments identified. I) Map of microseismicity displaying mapped faults and major microseismicity alignments. J) Shaded relief map showing the mapped faults and individual alignments from figures C-H. K) Map of the field area showing the major mapped faults.

Figure 3-20. Cross sections of microseismicity along the Clark and Coyote Creek fault zones. Red lines are parallel to earthquake alignments, green denotes the base of the seismogenic zone, black indicates where fault traces from the geologic map intersect the central trace of each cross section, and major fault traces are labeled, CF-Clark fault; CCF-Coyote Creek fault, MRF-Mid Ridge fault. Widths of the selection zones for each cross section are: A-A': 1.3 km, B-B': 1.7 km; C-C': 3.8 km; D-D': 3.4 km; E-E': 3.1 km.

Figure 3-20

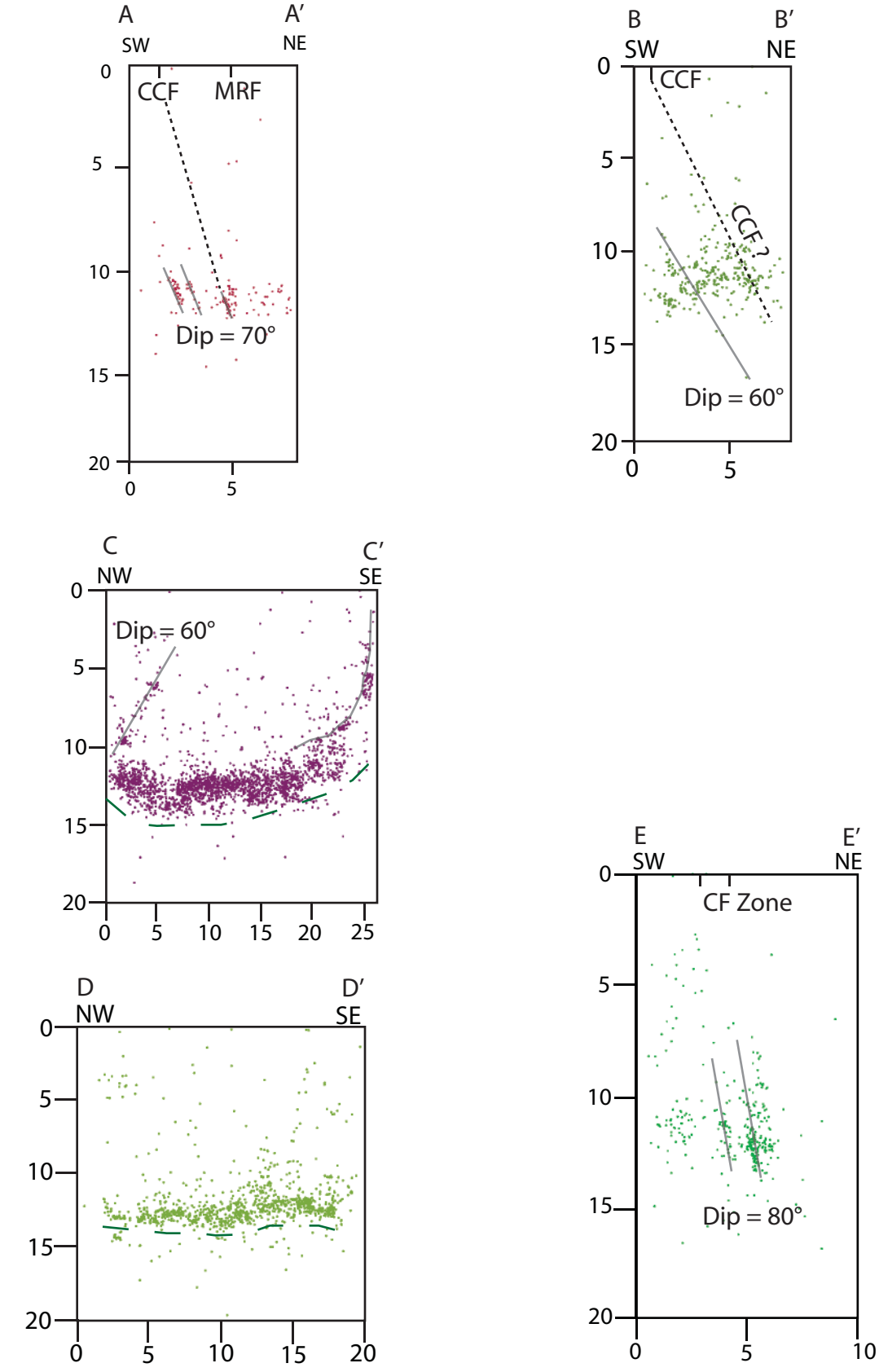
A
A′
SW
NE
CCF
MRF
Dip = 70°
B
B′
SW
NE
CCF
CCF ?
Dip = 60°
C
C′
NW
SE
Dip = 60°
D
D′
NW
SE
E
E′
SW
NE
CF Zone
Dip = 80°

Figure 3-21. Field photographs of the biotite hornblende bearing tonalite, marble, migmatite, assemblage used for determining separation of the Clark fault. (a) Photograph of the cultural feature known as Anza's Angel looking southeast (UTM 0561312, 2688830). The contact of the marble with the biotite hornblende bearing tonalite below and the migmatite above is shown in white. The thickest part of the marble is 7 meters for scale. (b) Photograph taken along the northwestern side of Coyote Mountain looking south (UTM 0561999, 3691217). The contact of the marble with the biotite hornblende bearing tonalite below and the migmatite above is shown in white. The assemblage at this location is noticeably smaller than at Anza's Angel. (c) Photograph of the assemblage on the south side of Rattlesnake Canyon looking southeast (UTM 0575075, 2688414). The contact of the marble with the biotite hornblende bearing tonalite below and the migmatite above is shown in white. In this location the marble is in thick pods that pinch and swell with in the assemblage.

Figure 3-21

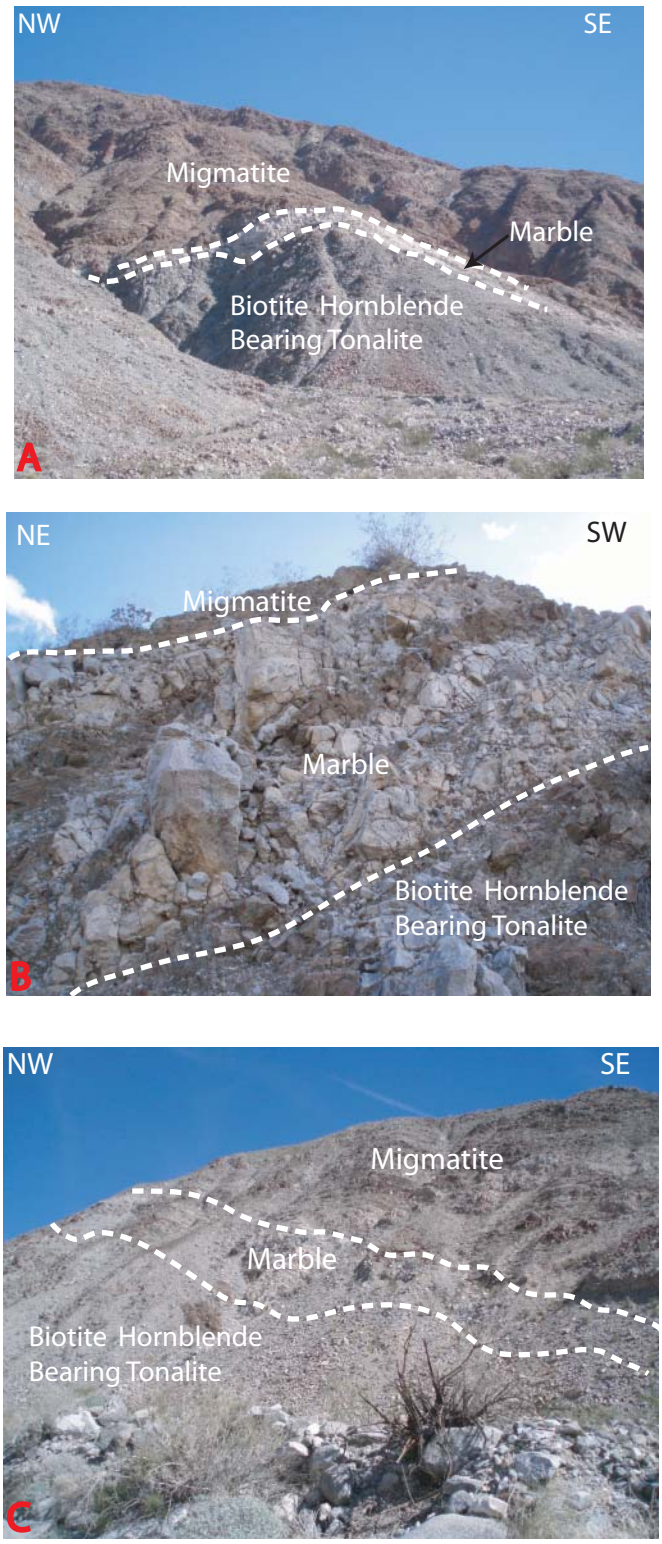
NW
SE
Migmatite
Marble
Biotite Hornblende
Bearing Tonalite
A
NE
SW
Migmatite
Marble
Biotite Hornblende
Bearing Tonalite
B
NW
SE
Migmatite
Marble
Biotite Hornblende
Bearing Tonalite
C

Figure 3-22

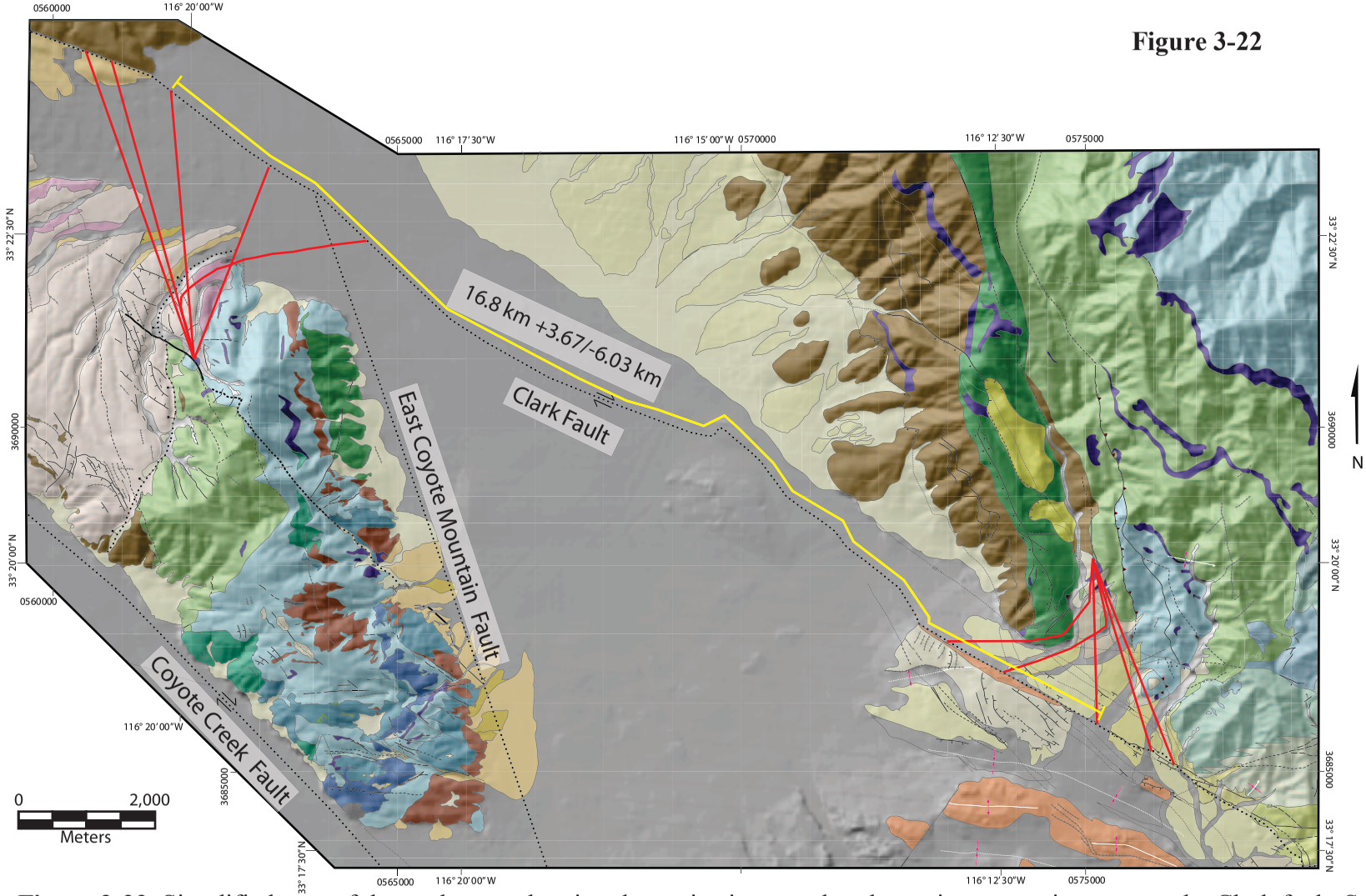

Figure 3-22. Simplified map of the study area showing the projections used to determine separations across the Clark fault. See Appendix J for descriptions of units. The Projections used are in red, and the preferred measurement is in yellow.

CHAPTER 4

CONCLUSIONS

Damage zone rock and their associated structures from two locations in southern California along major strike-slip faults in southern were examined. A unique set of questions was posed for each area. In the previous two chapters, emphasis was placed on structural characterization and determining its significance to the tectonic regime in each area.

4-1. Cajon Pass

Based on the structural analysis conducted on the crystalline core from the Cajon Pass, 11 new faults were identified in the Cajon Pass Core. By combining the detailed analysis of the core with wireline log data and previously published core analysis, an organized and complete distribution of deformation in the core as well as the borehole was determined. The majority of the faults captured by the core are small (~9 m thick average of fault and damage zone), and contain laumontite precipitation and alteration. The faults range in dip, have a small fault core, and uncertian offset. This is due to the limited core available as well as the small sample size.

Deformation mechanisms vary complexly with respect to depth or fault zones. Styles, geochemical features of fault zone, and microscopic features do not vary with respect to depth or to fault zones. The extent of deformation varies within the core, and is controlled by the size of the fault zones intersected by the core.

The frequency of faults in the core increases 5-fold with depth, and fractures within the core have greater populations around fault zones, however, statistically, the

fracture density does not increase in depth because of the presence of non- fault related fractures. This may be due to the variation in the size of the fault zones, with larger fault zones having a higher and wider fracture density than smaller ones or fault zones forming out of fractures. Another potential reason for this is that some faults could be inactive dip slip faults from older deformational events with some later strike-slip reactivation, thus increasing the fracture density in areas.

We propose that the fault zone intersected by the core at 3402 m that dips approximately 75° directly correlates with the nearby left-lateral strike-slip Cleghorn fault. The Cleghorn fault dips approximately 70 –90° to the northeast and is located approximately 1 km to the west of the borehole. The range of dip, combined with the concealed nature of the fault, allow for a reasonable up dip projection. This correlation suggests that all but the lower ~ 100m of the borehole lies in the hanging wall of the Cleghorn fault and therefore separated from the SAF by a major active left-lateral fault. The Cleghorn fault probably produced the fault rock in the lower 250-300 m of the borehole. Subsequently, stress measurement interpretations from deep within the borehole are likely to reflect stresses around the Cleghorn fault.

Microstructures in these fault zones primarily include shear fractures containing a matrix of laumontite with angular to sub-angular clasts within the matrix. Sense and amount of movement is not always discernable, but the microstructures in the vicinity of the fault zones may record evidence of seismic stress cycles. Evidence for this includes their damage zone alteration, style and types of fracture fillings, and textures. Intense microstructural damage, grain size reduction, fractured and cracked grains, and secondary mineral precipitation characterizes these damage zones. Samples in other parts of the core

are more likely created by distributed crustal deformation occurring around the pass, such as the antiforms being created in the area (Weldon, 1986); though at some depths, the core in undeformed. Predominant laumontite minerals in the fault and damage zones indicate of moderate- to high- temperature fluid interacting with the rocks. The small size of the faults observed as well as the laumontite signature can be interpreted as fluid interaction occurring as faults are rupturing or shortly thereafter. Fracture fills, both in and out of the damage zones, also predominantly return laumontite signatures.

Comparisons of faults at depth with faults examined by Jacobs (2005) in the San Bernardino Mountains show that faults at depth within the core are predominantly laumontite, whereas faults examined at the surface in the San Bernardino Mountains contain more clays than laumontite. Microstructural deformation styles are similar regardless of the amount of clay present. The variation in laumontite content is hypothesized to be due to a combination of differences in water-rock interaction, lack of stability of clay at deeper crustal levels, and the considerable uplift and weathering of the San Bernardino Mountains as described by Spotila et al. (2002) and Blythe et al. (2002). Also, uplift is required to explain the lack of clay in fault zones and dominance of laumontite from 500 m to 3500 m.

Data presented here were used to test the Fuis hypothesis (2007, 2008) of a gently to moderately dipping San Andreas Fault in the area of the Cajon Pass. The data do not preclude a northeast dipping SAF, but appear to rule out a dip less than 45° because there are no demonstrable rock types from southwest of the SAF in the core. Furthermore, the dip of the Cleghorn fault and dip of a major fault at 3402 m depth matches within error and projects towards one another.

4-2. Clark Fault

The Clark fault has a measured right-lateral separation of 16.8 km +3.67 km / -6.03 km within the study area, and is 2.4 km higher than previous measurements by Sharp (1967). A unique marker package of biotite-hornblende bearing tonalite – marble – migmatite was used as an offset contact surface. Located both in Coyote Mountain and the Santa Rosa Mountains, this offset contact surface was projected from its outcrops to the main trace of the Clark fault, located in Clark Valley. A variety of projections were used at both the Coyote Creek and Santa Rosa Mountains field sites locations. This variation allows us to incorporate error.

The previous and accepted measurement by Sharp (1967) did not include an error analysis on his separation. Our results are therefore more robust because of the error as well as using a more finite offset contact surface as opposed to the diffuse mylonite zone used by Sharp (1967).

Additional strain was also observed in smaller faults in the damage zone in Coyote Mountain that had previously been unaccounted for by Sharp (1967) or Theodore and Sharp (1975). 1-2 smaller faults ranging in lengths of 1-6 km in the eastern and western sections of Coyote Mountain have a combined separation of 1-3 km ± 2 km, though there is much unceritinity with this value. A zone of smaller faults in the southeast portion of Coyote Mountain display a strong combined sinistral separation of 1 ± 0.5 km and 0.2 ± 0.1 km of dextral strain. Though many faults strike through the Santa Rosa Mountains, no separation was discernible.

Contrary to our initial hypothesis, no strain is accumulated in drag folds related to dextral movement of the Clark fault because there are no drag folds. Foliations and

outcrop attitudes do not show any evidence for drag folding, and are in general agreement with the overall attitude of the Eastern Pennisular Shear Zone.

Off-fault deformation in both Coyote Mountain and the southeast Santa Rosa Mountains within the field area is seismic. The presence of fault scarps, deflected drainages, and complex brittle subsidiary faults within the damage zone are evidence for this.

The separation across the Clark fault implies a lifetime slip rate of 16.8 km/1.1 m.y. This translates into a rate of 15.3 mm.yr. Adjacent small faults increase this value slightly but their rates are difficult to quantify.

Microseismicity and earthquakes within the study area correlate with many of the structures mapped at the surface, but not others. The earthquakes reveal the presence of some important fault traces that are covered by surfical deposits. The largest faults in the area have the best map correlation. The major dextral faults in the area produce many small earthquakes and in cross section, all northwest striking faults dip steeply to the northeast. The micorseismicity also outlines complex structures and relationships. Particularly, bands of seismicity perpendicular to the traces of large faults in and near Coyote Mountain and Coyote ridge may reflect crossing coeval faults.

Our separation and strain results within the damage zones of the Clark fault do not significantly change estimates of total displacement. The high density and complexity of faulting in the study area was not foreseen at the start of this study, thus our damage zone displacement and strain should be thought of as preliminary. Accurate measurements of offset and strain, particularly in the Santa Rosa Mountains would require multiple field seasons and resources, that were out of the scope of this study.

4-3. Summary

The two studies have their own unique conclusions but share some basic principals. There are some similarities that shed insight into damage zone architecture and raise questions for continued studies.

Combined, the two studies represent an in depth review of how deformation is distributed and its characterization of major strike slip faults in southern California. Each study exhibits varying stages and sizes of faulting in the vicinity of the major fault and each shows characteristics of damage as precipitated by Chester and Logan (1987), Chester et al. (1993), and Kim et al. (2004). The complexity of deformation along strike slip faults is well documented in both the Cajon Pass and near the Clark fault. The work conducted in the Cajon Pass focused on meso- and micro- scale deformation and than related that to the tectonic regime of the area. In the vicinity of the Clark fault, the focus was on larger scaled damage zone deformational features and how they relate to separation measurements.

Though the scales of examination of the two studies are different, the architecture of the damage zones follow a similar model similar to that conceived by Chester et al. (1993). Their model is comprised of a centralized layer of ultracatalasite within a narrow zone of foliated cataclasites that makes up the fault core. A thicker zone of damaged rock binds the fault core, showing a decrease in the intensity of damage the further away you are removed from the fault core. This architecture has been well documented in Cajon Pass drill core at both the meso (cm)- and microscopic (mm) scales (Appendix H). Jacobs (2005) identified the same architecture in surface exposures of the Cleghorn fault in the San Bernardino Mountains at the outcrop scale.

Likewise, this architecture was identified at the outcrop scale in some of the subsidiary faults within the damage zone of the Clark and Coyote Creek faults. This architecture is also crudely seen at the map scale near the Clark and Coyote Creek faults. Based on mapped relationships, it appears that the subsidiary faults of the Clark and Coyote Creek fault diminish in size and frequency the further away from their main strands (or fault cores) (Appendix I).

Deformation also varies vertically near strike slip faults. As noted in the Cajon Pass drill core, faults intersected by the borehole are sometimes separated by intact and undeformed crystalline rock. This is counterintuitive because of the size of the San Andreas fault, its capability to produce large earthquakes, and the proximity of the borehole to the fault (~4 km to the southwest). Though there are areas that are undeformed, the styles of deformation are the same throughout the core as stated above

One aspect of uncanny similarity in each investigation is that each area shows evidence of, or may support a hypothesis of a moderately to steeply dipping strike slip fault. This implication may potentially be far reaching. In the Cajon Pass, the lack of any dipping fault within the core may be interpreted that the dipping San Andreas fault dips between 45° and 90° to the northeast. Using the interpretation of microseismicity in the Anza Borrego Desert State Park region, the Clark and Coyote Creek faults are shown both dipping in a general easterly direction. At depth the CCF fault appears to be dipping between ~60°-70° and the Clark fault appears to be dipping ~80°. These three faults, which are major plate boundary faults, are dipping in a generally easterly direction, and this may represent more than a coincidence. More work is needed to properly constrain

the dip of the San Andreas fault, as well as to determine the mechanics and kinematics of dipping strike-slip faults.

The presence and attitude of structures located within the damage zone of major faults needs to be well understood before concrete conclusions can be made about regional tectonics, separation, slip rates, and mechanics. This study highlights how revisiting previous studies and conclusions can lead to greater insight to the structure and tectonics of an area as well as add and improve upon previous published work.

References

Blythe, A.E., House, M.A., and Spotila, J.A., 2002, Low-temperature thermochronology of the San Gabriel and San Bernardino Mountains, southern California: constructing structural evolution, *in* Barth, A., ed., Contribution to crustal evolution of the southwestern United States: Boulder, Colorado, Geological Society of America Special Paper 365, p. 231-250.

Chester, F.M., and J.M. Logan, 1987, Composite planar fabric of gouge from the Punchbowl Fault, California: Journal of Structural Geology, no. 9, p. 621-634.

Chester, F.M., Evans, J.P., and Biegel, R.L., 1993, Internal structure and weakening mechanisms of the San Andreas Fault: Journal of Geophysical Research, v. 98, no. B1, p.771-786.

Fuiss, G.S, Scheirer, D.S., Langenheinm V.E., and Kohler, M.D., 2007, The San Andreas fault in southern California is almost nowhere vertical-implications for tectonics: Geological Society of America Abstracts with programs, v. 39, no. 6, p.279.

Fuiss, G.S., Scheirer, D.S., Langenhein, V.E., Kohler, M.D., 2008, The San Andreas Fault in southern California has a “propeller” shape-implications for tectonics and seismic hazard: Geological Society of America Abstracts with programs, v. 40, no. 6, p.326.

Jacobs, J.R., 2005, Examination of Exhumed Faults in the Western San Bernardino Mountains, California: Implications for Fault Growth and Earthquake Rupture [m.s. thesis]: Logan, Utah State University.

Kim, Y.S., Peacock, D.C.P., and Sanderson, D.J., 2004, Fault damage zones: Journal of Structural Geology, no. 26, p. 503-517.

Sharp, R.V., 1967, San Jacinto Fault zone in the Peninsular Ranges of Southern California: Geological Society of America Bulletin, v. 78, p. 705-729.

Spotila, J.A., House, M.A., Blythe, A.E., Niemi, N.A., and Bank, G.C., 2002, Controls on the erosion and geomorphic evolution of the San Bernardino and San Gabriel Mountains, southern California, *in* Barth, A., ed., Contribution to crustal evolution of the southwestern United States: Boulder, Colorado, Geological Society of America Special Paper 365, p. 205-230.

Theodore, T.G., and Sharp, R.V., 1975, Geologic map of the Clark Lake quadrangle, San Diego county, California: U.S. Geological Survey Miscellaneous Field Studies Map MF-0644, scale 1:24000, 1 sheet.

Weldon, R.J., 1986, The late Cenozoic geology of Cajon Pass: Implications for tectonics and sedimentation along the San Andreas fault [Pd.D. thesis]: Pasadena, California Institute of Technology, 400p.

APPENDICES

APPENDIX A: Core measurements

Core	Segment	Depth to top (feet)	Depth to bottom (feet)	Meters	Meters	Total meters
1	ALL	NM	NM	265.2	273.4	8.2
2 &3	ALL	NM	NM	321	328.9	7.9
4	4	1,575.00	1,577.20	480.06	480.73	0.67
	3	1,577.20	1,579.00	480.73	481.28	0.55
	2	1,579.30	1,580.90	481.37	481.86	0.49
	1	1,581.00	1,583.40	481.89	482.62	0.73
5	11	1,710.00	1,712.10	521.21	521.85	0.64
	10	1,712.60	1,714.90	522.00	522.70	0.70
	9	1,714.90	1,716.90	522.70	523.31	0.61
	8	1,717.00	1,718.30	523.34	523.74	0.40
	7	1,718.30	1,721.20	523.74	524.62	0.88
	6	1,721.40	1,724.10	524.68	525.51	0.82
	5	1,724.20	1,726.80	525.54	526.33	0.79
	4	1,727.00	1,729.10	526.39	527.03	0.64
	3	1,729.40	1,731.78	527.12	527.85	0.73
	2	1,732.00	1,734.50	527.91	528.68	0.76
	1	1,734.60	1,737.00	528.71	529.44	0.73
6	4	1,950.00	1,951.00	594.36	594.66	0.30
	3	1,951.00	1,953.80	594.66	595.52	0.85
	2	1,953.80	1,956.40	595.52	596.31	0.79
	1	1,956.70	1,958.00	596.40	596.80	0.40
7	2	2,297.80	2,299.20	700.37	700.80	0.43
	1	2,299.40	2,302.00	700.86	701.65	0.79
NO CORE 8						0.00
9	4	2,310.00	2,312.00	704.09	704.70	0.61
	3	2,312.00	2,314.80	704.70	705.55	0.85
	2	2,315.10	2,317.30	705.64	706.31	0.67
	1	2,317.30	2,318.80	706.31	706.77	0.46
10	5	2,439.00	2,440.80	743.41	743.96	0.55
	4	2,440.90	2,442.00	743.99	744.32	0.34
	3	2,442.50	2,444.00	744.47	744.93	0.46
	2	2,444.50	2,446.60	745.08	745.72	0.64
	1	2,446.60	2,447.90	745.72	746.12	0.40
11	1	2,822.00	2,822.80	860.15	860.39	0.24
12	2	2,823.00	2,825.00	860.45	861.06	0.61
	1	2,825.00	2,827.00	861.06	861.67	0.61
13	5	3,350.00	3,352.50	1,021.08	1,021.84	0.76
	4	3,352.60	3,354.90	1,021.87	1,022.57	0.70
	3	3,355.00	3,357.80	1,022.60	1,023.46	0.85
	2	NO SEGMENT 2				0.00
	1	NO SEGMENT 1				0.00
14	1	3,360.50	3,362.80	1,024.28	1,024.98	0.70
15	4	3,734.00	3,736.60	1,138.12	1,138.92	0.79
	3	3,736.00	3,738.60	1,138.73	1,139.53	0.79
	2	3,738.75	3,741.30	1,139.57	1,140.35	0.78
	1	3,741.40	3,743.00	1,140.38	1,140.87	0.49
16	4	4,210.00	4,212.50	1,283.21	1,283.97	0.76
	3	4,212.60	4,215.00	1,284.00	1,284.73	0.73
	2	4,215.00	4,217.40	1,284.73	1,285.46	0.73
	1	4,217.40	4,219.00	1,285.46	1,285.95	0.49
	9	4,433.00	4,434.60	1,351.18	1,351.67	0.49
	8	4,434.60	4,436.50	1,351.67	1,352.25	0.58
	7	4,436.50	4,437.70	1,352.25	1,352.61	0.37
	6	4,438.41	4,440.10	1,352.83	1,353.34	0.52

17	5	4,440.11	4,442.90	1,353.35	1,354.20	0.85
	4		NO SEGMENT 4			0.00
	3	4,445.16	4,446.70	1,354.88	1,355.35	0.47
	2	4,447.00	4,448.75	1,355.45	1,355.98	0.53
	1		NO SEGMENT 1			0.00
18	3	4,920.00	4,921.50	1,499.62	1,500.07	0.46
	2	4,921.83	4,923.40	1,500.17	1,500.65	0.48
	1	4,923.50	4,925.70	1,500.68	1,501.35	0.67
19	8	5,419.41	5,422.30	1,651.84	1,652.72	0.88
	7	5,422.30	5,425.00	1,652.72	1,653.54	0.82
	6	5,425.08	5,426.80	1,653.56	1,654.09	0.52
	5	5,426.80	5,428.30	1,654.09	1,654.55	0.46
	4	5,428.88	5,431.80	1,654.72	1,655.61	0.89
	3	5,431.80	5,434.40	1,655.61	1,656.41	0.79
	2	5,434.60	5,437.30	1,656.47	1,657.29	0.82
	1	5,437.70	5,438.90	1,657.41	1,657.78	0.37
20	3	5,712.00	5,714.90	1,741.02	1,741.90	0.88
	2	5,715.50	5,718.40	1,742.08	1,742.97	0.88
	1	5,718.40	5,721.25	1,742.97	1,743.84	0.87
21	2	6,050.70	6,052.00	1,844.25	1,844.65	0.40
	1	6,052.00	6,054.00	1,844.65	1,845.26	0.61
22	1	6,059.00	6,059.70	1,846.78	1,847.00	0.21
23	2	6,083.30	6,085.10	1,854.19	1,854.74	0.55
	1	6,085.20	6,087.00	1,854.77	1,855.32	0.55
24	1	6,150.00	6,152.20	1,874.52	1,875.19	0.67
25	1	6,180.00	6,182.00	1,883.66	1,884.27	0.61
26	6	6,240.80	6,242.70	1,902.20	1,902.77	0.58
	5	6,242.80	6,245.10	1,902.81	1,903.51	0.70
	4	6,245.20	6,247.60	1,903.54	1,904.27	0.73
	3	6,247.68	6,249.90	1,904.29	1,904.97	0.68
	2	6,250.00	6,251.90	1,905.00	1,905.58	0.58
	1	6,252.10	6,254.00	1,905.64	1,906.22	0.58
27	1	6,500.00	6,502.00	1,981.20	1,981.81	0.61
28	3	6,503.77	6,506.60	1,982.35	1,983.21	0.86
	2	6,506.70	6,508.70	1,983.24	1,983.85	0.61
	1	6,508.80	6,509.80	1,983.88	1,984.19	0.30
29	3	6,510.00	6,512.30	1,984.25	1,984.95	0.70
	2	6,512.35	6,515.00	1,984.96	1,985.77	0.81
	1	6,515.00	6,517.10	1,985.77	1,986.41	0.64
30	4	6,700.00	6,703.10	2,042.16	2,043.10	0.94
	3	6,703.10	6,706.00	2,043.10	2,043.99	0.88
	2	6,706.00	6,707.00	2,043.99	2,044.29	0.30
	1	6,707.50	6,708.80	2,044.45	2,044.84	0.40
31	6	6,740.00	6,743.00	2,054.35	2,055.27	0.91
	5	6,743.00	6,745.66	2,055.27	2,056.08	0.81
	4	6,745.66	6,747.90	2,056.08	2,056.76	0.68
	3	6,747.90	6,750.20	2,056.76	2,057.46	0.70
	2	6,750.50	6,752.10	2,057.55	2,058.04	0.49
	1	6,752.50	6,755.10	2,058.16	2,058.95	0.79
NO CORE 32						0.00
33	5	6,813.00	6,814.10	2,076.60	2,076.94	0.34
	4	6,814.50	6,816.30	2,077.06	2,077.61	0.55
	3	6,816.40	6,818.70	2,077.64	2,078.34	0.70
	2	6,818.80	6,820.50	2,078.37	2,078.89	0.52
	1	6,820.70	6,822.30	2,078.95	2,079.44	0.49
34	3	6,932.30	6,932.80	2,112.97	2,113.12	0.15
	2	6,933.30	6,935.50	2,113.27	2,113.94	0.67
	1	6,936.90	6,938.00	2,114.37	2,114.70	0.34

35	9	7,160.00	7,161.35	2,182.37	2,182.78	0.41
	8	7,161.75	7,164.00	2,182.90	2,183.59	0.69
	7	7,164.00	7,165.90	2,183.59	2,184.17	0.58
	6	7,166.40	7,169.00	2,184.32	2,185.11	0.79
	5	7,169.16	7,171.16	2,185.16	2,185.77	0.61
	4	7,171.50	7,173.89	2,185.87	2,186.60	0.73
	3	7,173.90	7,176.27	2,186.60	2,187.33	0.72
	2	7,176.53	7,179.00	2,187.41	2,188.16	0.75
	1	7,179.00	7,181.00	2,188.16	2,188.77	0.61
36	6	7,370.00	7,371.50	2,246.38	2,246.83	0.46
	5	7,371.79	7,373.66	2,246.92	2,247.49	0.57
	4	7,373.66	7,375.91	2,247.49	2,248.18	0.69
	3	7,375.91	7,377.70	2,248.18	2,248.72	0.55
	2	7,377.70	7,380.00	2,248.72	2,249.42	0.70
	1	7,380.00	7,382.00	2,249.42	2,250.03	0.61
37	4	7,502.00	7,504.00	2,286.61	2,287.22	0.61
	3	7,504.10	7,506.90	2,287.25	2,288.10	0.85
	2	7,507.00	7,509.00	2,288.13	2,288.74	0.61
	1	7,509.00	7,511.40	2,288.74	2,289.47	0.73
38	2	7,712.00	7,713.77	2,350.62	2,351.16	0.54
	1	7,713.77	7,717.50	2,351.16	2,352.29	1.14
39	7	7,958.00	7,960.50	2,425.60	2,426.36	0.76
	6	7,960.50	7,962.90	2,426.36	2,427.09	0.73
	5	7,963.00	7,965.80	2,427.12	2,427.98	0.85
	4	7,965.80	7,968.30	2,427.98	2,428.74	0.76
	3	7,968.40	7,971.00	2,428.77	2,429.56	0.79
	2	7,971.00	7,973.80	2,429.56	2,430.41	0.85
	1	7,973.80	7,976.50	2,430.41	2,431.24	0.82
NO CORE 40						0.00
41	1	8,250.00	8,250.40	2,514.60	2,514.72	0.12
42	1	8,543.00	8,545.20	2,603.91	2,604.58	0.67
43	1	8,557.00	8,558.10	2,608.17	2,608.51	0.34
44	3	8,640.00	8,641.30	2,633.47	2,633.87	0.40
	2	8,641.80	8,643.50	2,634.02	2,634.54	0.52
	1	8,643.50	8,645.80	2,634.54	2,635.24	0.70
45	5	8,790.00	8,791.00	2,679.19	2,679.50	0.30
	4	8,791.00	8,793.30	2,679.50	2,680.20	0.70
	3	8,793.40	8,796.10	2,680.23	2,681.05	0.82
	2	8,796.10	8,798.30	2,681.05	2,681.72	0.67
	1	8,798.30	8,800.80	2,681.72	2,682.48	0.76
46	7	8,995.00	8,997.60	2,741.68	2,742.47	0.79
	6	8,997.60	8,999.70	2,742.47	2,743.11	0.64
	5	9,000.00	9,002.00	2,743.20	2,743.81	0.61
	4	NO SEGMENT 4				0.00
	3	9,004.80	9,007.56	2,744.66	2,745.50	0.84
	2	9,007.57	9,010.20	2,745.51	2,746.31	0.80
	1	NO SEGMENT 1				0.00
47	1	9,205.70	9,206.60	2,805.90	2,806.17	0.27
48	6	9,350.00	9,352.37	2,849.88	2,850.60	0.72
	5	9,352.37	9,354.60	2,850.60	2,851.28	0.68
	4	9,354.60	9,357.00	2,851.28	2,852.01	0.73
	3	9,357.00	9,359.40	2,852.01	2,852.75	0.73
	2	9,359.40	9,361.45	2,852.75	2,853.37	0.62
	1	9,361.45	9,363.00	2,853.37	2,853.84	0.47
49	3	9,470.00	9,471.00	2,886.46	2,886.76	0.30
	2	9,471.00	9,473.50	2,886.76	2,887.52	0.76
	1	9,473.50	9,475.90	2,887.52	2,888.25	0.73
	7	9,890.00	9,892.00	3,014.47	3,015.08	0.61

50	6	9,892.00	9,893.58	3,015.08	3,015.56	0.48
	5	9,894.33	9,897.00	3,015.79	3,016.61	0.81
	4	9,897.00	9,899.87	3,016.61	3,017.48	0.87
	3	9,899.87	9,902.40	3,017.48	3,018.25	0.77
	2	9,902.40	9,905.00	3,018.25	3,019.04	0.79
	1	9,905.00	9,906.00	3,019.04	3,019.35	0.30
51	3	10,445.00	10,446.90	3,183.64	3,184.22	0.58
	2	10,446.90	10,448.70	3,184.22	3,184.76	0.55
	1	10,448.70	10,450.50	3,184.76	3,185.31	0.55
52	1	10,970.00	10,972.30	3,343.66	3,344.36	0.70
53	5	11,160.00	11,161.90	3,401.57	3,402.15	0.58
	4	11,162.00	11,162.79	3,402.18	3,402.42	0.24
	3	11,164.62	11,166.90	3,402.98	3,403.67	0.69
	2	11,167.00	11,169.41	3,403.70	3,404.44	0.73
	1	11,169.80	11,172.00	3,404.56	3,405.23	0.67
NO CORE 54						0.00
55	3	11,501.00	11,503.30	3,505.50	3,506.21	0.70
	2	11,503.60	11,505.20	3,506.30	3,506.78	0.49
	1	11,505.20	11,506.20	3,506.78	3,507.09	0.30

APPENDIX B: Previous samples collected from the Cajon Pass Core

Core	Segment	Depth (ft)	Depth (m)	Worker(s)	Use
35	9	7161	21826.73	MCW	
		7160.1	21823.98	TGB	
		7160.6	21825.51	BP/SP	
	8	7162	21829.78	MCW; Sass	
		7162.75	21832.06	TB; RS	
		7163.4	21834.04	TB; RS	Vein and shear
		7163.8	21835.26	Sass	avoid vert vein
		7164	21835.87	TB; RS	
	7	7164.1	21836.18	Mcw	
		7165	21838.92	TB; RS	
	6	7167.1	21845.32	Sass	Axial Plug
		7167.8	21847.45	TB; RS	Shear zone in chlorite
		7168.2	21848.67	Lev	Axial and 2 horiziontal
		7168.4	21849.28	MCW	
		7168.5	21849.59	TB; RS	Fold and cross cutting
		7168.5	21849.59	TB	Small fold
		7168.7	21850.20	MCW	
	5	7169.7	21853.25	Sass	Axial Plug
		Unknown		LTS; EJ	Remainder
		Unknown		Silver, James	
	2	7176.5	21873.97	LTS; EJ	
		7178	21878.54	TB; RS	
		7178.6	21880.37	Lev	Axial Plug
		7178.6	21880.37	MCW	Plug though remainder
	1	7180	21884.64	MCW	
		7179	21881.59	TB; RS	
		7179.3	21882.51	Sass	Axial
36	6	7371.1	22467.11	TB; RS	
	5	7372	22469.86	Sass	Axial
		7372.5	22471.38	Sass	Orthogonal Set
		7372.6	22471.68	MCW	
		7372.6	22471.68	LTS, EWJ, SC	Entire Slab
	3	7376.5	22483.57	Sass	
		7376.8	22484.49	MCW	
		7376.9	22484.79	MCW	
		7377.1	22485.40	TB; RS	
		7377.8	22487.53	TB; RS	
37	4	7502.4	22867.32	Sass	Axial
		Unknown		Lev	
		Unknown		LTS, EWJ, SC	1/2 Slab
		Unknown		MCW	
	3	7504.7	22874.33	TB; RS	Vert Veins
		7505.9	22877.98	MCW	
		7506	22878.29	MCW	
		7506.3	22879.20	Sass	Orthogonal Set
		7507	22881.34	TB; RS	Both sides of fracture
		7504.7-7506.3		LTS	Possible Slab?
	2	7507	22881.34	Sass	Axial
		7508	22884.38	TB	Slicken surface?
		7509	22887.43	TB; RS	Wraped
	1	7509.5	22888.96	MCW	
		7509.7	22889.57	MCW	
		7510	22890.48	Sass	Axial
		7510.4	22891.70	MCW	

			7510.5	22892.00	TB; RS	Folds
38	2		7712	23506.18	Sass	Axial
			7712.3	23507.09	TB; RS	
			7712.5	23507.70	MCW	
			7713.1	23509.53	Sass	Orthogonal Set
	1		7714.1	23512.58	Sass	Axial
			7714.5	23513.80	MCW	
			7714.7	23514.41	TB; RS	Fracture
			7715	23515.32	Lev	
		7713.8-7715			Lev	Slab
		Bottom Chunck			TB; RS	Slab
39	7		7958.1	24256.29	Sass	Axial
			7958.3	24256.90	TB; RS	Low angle
			7959.2	24259.64	Lev	
			7959.5	24260.56	MCW	
			7960	24262.08	Sass	Orthogonal Set
			7960.4	24263.30	TB; RS	
	6		7961	24265.13	MCW	
			7962.1	24268.48	Sass	Axial
			7962.5	24269.70	MCW	
	5		7934	24182.83	TB; RS	
			7934.3	24183.75	MCW	
			7934.5	24184.36	MCW	
			7935.2	24186.49	Sass	Axial
	4		7960	24262.08	Sass	
		Entire Core			JLK	
	3		7969.2	24290.12	Sass	Axial
			7970	24292.56	MCW	
			7970.2	24293.17	MCW	
	2		7972.6	24300.48	MCW	
	1		7974.3	24305.67	Sass	Orthogonal Set
			7975	24307.80	MCW	
			7976	24310.85	Lev	
			7976.7	24312.98	TB; RS	Bag
41	1	Unknown			LTS	K-Feld
		Unknown			TB; RS	Fractures
42	1		8343.2	25430.07	Lev	
			8343.2	25430.07	Sass	Orthogonal Set
			8543.5	26040.59	MCW	
			8544	26042.11	TB; RS	
			8544.2	26042.72	TB; RS	Bags
			8544.6	26043.94	TB; RS	
			8545	26045.16	Sass	Axial
		Unknown			Silver gets all	
43	1		8557.4	26082.96	TB; RS	Both sides of fracture
			8557.7	26083.87	TB; RS	Both sides of fracture
			8557.9	26084.48	Sass	Orthogonal Set
44	3	Unknown			TB; RS	Bag
		Unknown			TB; RS	Entire piece
	2	Top				
			8642.4	26342.04	TB; RS	Bag
			8642.5	26342.34	MCW	
		Unknown			Sass	Orthogonal Set
	1		8643.9	26346.61	Sass	Axial
			8643.2	26344.47	MCW	
			8643.5	26345.39	Lev	

		8645.8	26352.40	TB; RS	
45	4	8792	26798.02	MCW	
		8793	26801.06	TB; RS	
		8794.8	26806.55	Sass	Axial
	2	8796.3	26811.12	Sass	Axial
		8796.8	26812.65	MCW	
		8798	26816.30	MCW	
	1	8798.1	26816.61	MCW	
		8800	26822.40	MCW	
46	7	8896.3	27115.92	MCW	
		8896.5	27116.53	AMAP	
	6	8998.8	27428.34	MCW	
		8999	27428.95	MCW	
		8999.7	27431.09	Sass	Axial
	2	9007.7	27455.47	Sass	Axial
		9008.4	27457.60	MCW	
		9009.6	27461.26	MCW	
47	1	9206.3	28060.80	Sass	
48	5	9357.5	28521.66	Sass	Orthogonal Set
		9353.2	28508.55	Sass	Orthogonal Set
		9354.4	28512.21	Sass	Axial
	4	9355	28514.04	Sass	Orthogonal Set
	3	9357.8	28522.57	Sass	Orthogonal Set
		9358.2	28523.79	Sass	Axial
		9359.4	28527.45	Sass	Orthogonal Set
	2	9360.8	28531.72	Sass	Redial
		9361.4	28533.55	Sass	Axial
	1	9362	28535.38	Sass	Axial
		9362.8	28537.81	Sass	Orthogonal Set
49	3	9470	28864.56	Sass	Orthogonal Set
	2	9471	28867.61	Sass	Orthogonal Set
		9472	28870.66	Sass	Axial
		9472.6	28872.48	Sass	Orthogonal Set
	1	9473.6	28875.53	Sass	Orthogonal Set
		9473.8	28876.14	Wang	3" Slab
		9474.2	28877.36	Byerlee	3 perpendicular plugs
		9474.8	28879.19	Sass	Orthogonal Set
		9475.7	28881.93	Sass	Axial
50	6	9893	30153.86	Sass	Orthogonal Set
	5	9895.2	30160.57	Sass	Orthogonal Set
		9896.2	30163.62	Sass	Axial
	4	9898.4	30170.32	Sass	Orthogonal Set
		9898.5	30170.63	Sass	Axial
	3	9900.8	30177.64	Sass	Orthogonal Set
		9901.8	30180.69	Sass	Orthogonal Set
	2	9903	30184.34	Sass	Orthogonal Set
		9904.3	30188.31	Byerlee	3 perpendicular plugs
		9904.7	30189.53	Wang	
	1	9905.2	30191.05	Sass	
53	2	11167.8	34039.45	Sass	Axial
		11169.4	34044.33	Sass	Orthogonal Set
		11169.5	34044.64	Wang	3" Slab
		11169.65	34045.09	Byerlee	3 perpendicular plugs
	1	11170.7	34048.29	Sass	Orthogonal Set
		11172	34052.26	Sass	Axial

APPENDIX C: Record of samples taken for this study from the Cajon Pass Core

Core	Segment	Depth (feet)	Depth (meters)	Feature	Picture Number	Thin Section	XRD	XRF
6	2	1540	469.39	Protolith				
4	1	1582.8	482.44	Fracture	628125			
5	4		0.00	Protolith				x
5	9		0.00	Slicks				
5	11	1710	521.21	Cataclasite	628127	x	x	
5	11	1710.9	521.48	Cataclasite	628126	x		x
5	10	1713.4	522.24	Slicks				
7	1,2	2299.2	700.80	Cataclasite	628128	x	x	
9	3	2314.4	705.43	Micro Fractures	628129			
9	1	2317.9	706.50	Fracture	628130			
10	5	2440	743.71	Fracture	628131			
12	2		0.00	Protolith				x
12	2	2823	860.45	Fracture				x
14	1	3362	1024.74	Fracture FIll			x	
14	1	3362.8	1024.98	Fracture	628120			
15	4	3734.6	1138.31	Fracture	628114			
15	3	3736.7	1138.95	Fault Zone		x	x	
15	2	3741	1140.26	Fracture	628115			
16	4	4211.5	1283.67	Fracture	628112			
16	3	4213.9	1284.40	Fracture	628122			
16	2	4215.6	1284.91	Fracture Surface	628124		x	
16	2	4217.2	1285.40	Fracture	628123	x		
16	1	4218.9	1285.92	Fracture	628113	x		
17	9	4434	1351.48	Fracture	628107			
17	4	4443.3	1354.32	Fracture		x	x	
17	3	4446.5	1355.29	Fracture	628121			
17	1	4449.5	1356.21	Fracture	628108-111			
18	3		0.00	Slip Surface				
18	2	4922.6	1500.41	Protolith				x
18	2	4923.1	1500.56	Fracture fill				x
18	2	4923.1	1500.56	Fracture/Slip	628106		x	
18	1		0.00	Slip Surface			x	
19	7	5425	1653.54	Protolith		x		
21	2	6051.8	1844.59	Fracture	628105			
23	1	6086.1	1855.04	Fracture	628097			
24	1	6150	1874.52	Protolith				
25	1	6180.7	1883.88	Fracture				
25	1	6181	1883.97	Fracture fill			x	
25	1	6181	1883.97	Fracture	628099			
25	1	6181.4	1884.09	Fracture	628098			
26	6	6241.2	1902.32	Fracture	628103			
26	5	6243	1902.87	Fracture	628102		x	
26	4	6246.6	1903.96	Fracture	628101		x	
26	1	6254	1906.22	Fracture and fill	628100		x	
29	1	6517.4	1986.50	Fracture	628104			
30	3	6705.7	2043.90	Fracture	615021			
30	1	6706.11	2044.02	Fracture	615021			
30	1	6707.25	2044.37	Fracture	619002			
30	1	6708.8	2044.84	Fracture	619001			
31	6	6743.16	2055.32	Fracture	615022			
31	4		0.00	Protolith		x		x
31	1	6755.1	2058.95	Fracture	615019-020		x	x
33	3	6818.62	2078.32	Fracture	615015			
33	1	6831.66	2082.29	Fracture	615018	x		
34	4	In Seg 4	#VALUE!	Protolith				
34	2	6934.9	2113.76	Fracture fill			x	
34	1	6937.2	2114.46	Fracture	615016		x	
34	2	6937.9	2114.67	racture with gouge f	615017			
35	8	7163.4	2183.40	Fracture	619107			
35	7	7164.4	2183.71	Fracture	619105	x		
35	6	7167.4	2184.62	Fracture	619104			
35	7	7167.5	2184.65	Fracture	619106			
35	6	7168.5	2184.96	Fracture/fold	619103			
35	5	7170.8	2185.66	Fracture	619102			
35	2	7177	2187.55	Fracture	619101			
35	2	7178	2187.85	Fracture				
35	1	7180	2188.46	Fracture	619100			
36	6	7370.1	2246.41	Protolith				x
36	6	7371.2	2246.74	Fracture	619099			x
36	5		0.00	Fracture				
36	5	7372	2246.99	Fracture	619098			

36	3	7377.7	2248.72	Fracture	619097				
36	4	7378.5	2248.97	Fracture	619096				
36	4	7378.8	2249.06	Fracture Fill					
36	4	7379	2249.12	Fracture	619095	x			
36	4	7379	2249.12	Fracture					
36	1	7380.7	2249.64	Fracture	628132			x	
37	4	7502.5	2286.76	Fracture	619083				
37	4	7502.8	2286.85	Fracture	619082				
37	4	7504.2	2287.28	Fracture	619081				
37	1	7509	2288.74	Fracture	619093			x	
37	2		0.00	Fracture fill					
37	2	7509.2	2288.80	Fracture	619094				
38	2		0.00	Protolith					
38	2	7712	2350.62	Fracture	619092				x
38	1	7715	2351.53	Fracture	619080			x	
38	1	7717.5	2352.29	Fracture	619079				
39	7	7958.6	2425.78	Fracture	619091				
39	6	7961	2426.51	Fracture	619090				
39	6	7962.3	2426.91	Fracture	619088				
39	6	7962.8	2427.06	Fracture	619089				
39	5	7963.8	2427.37	Fracture Fill				x	
39	4	7968	2428.65	Fracture	619087				
39	3	7969	2428.95	Fracture	629005				
39	2	7972.3	2429.96	Fracture	619086				
39	1	7976	2431.08	Fracture	619084				
39	1	7976.7	2431.30	Fracture	619085				
42	1		0.00	Fracture	621005			x	
42	7		0.00	Fracture					
43	1	8557	2608.17	Fracture	629001	2X3		x	
43		8557.5	2608.33	Fault					
43	1	8557.5	2608.33	Fracture	629006				
44	3	8640.2	2633.53	Fracture	621004	x			
44	3	8640.9	2633.75	Fracture	621003	x			
44	2	8642	2634.08	Fracture	621001				
44	2	8643	2634.39	Fracture	621002	x			
44	1		0.00	Fracture		x			
44	1	8645.1	2635.03	Fracture	629002			x	
45	4	8792.6	2679.98	Fracture					
45	1	8799.5	2682.09	Fracture	625084				
46	7	8995	2741.68	FaultFracture	625083				
46	7	8995	2741.68	Fracture	629007				
46	7	8995.2	2741.74	Fracture	625082?	x			
46	7	8996.4	2742.10	Slicks	625082			x	
46	7	8997	2742.29	Fracture	625082	x			
46	5	9000.9	2743.47	Fracture	625083				
46	5	9002.1	2743.84	Fracture fill				x	
47	1		0.00	Fracture	629008			x	
48	5	9354.3	2851.19	Fracture	625079				
48	4	9355.5	2851.56	Fracture	625080				x
48	3		0.00	Protolith		x			x
48	2		0.00	Fracture					
48	2	9360	2852.93	Fracture	625078				
48	2	9361.4	2853.35	Fracture	625077	x			
48	1	9361.5	2853.39	Fracture fill				x	
48	1	9362.5	2853.69	Fracture	625076				
49	3	9470.3	2886.55	Protolith					x
49	2	9475.5	2888.13	Fracture	625075	x			x
50	6	9894	3015.69	Protolith					
52	1	10971	3343.96	Protolith		x			x
53	5	11161	3401.87	Fracture	629003				
53	5	11161	3401.87	Fracture	625069				
53	5	11161.7	3402.09	Fracture	625070	2X3 X			x
53	5		0.00	Fracture					
53	3	11165.8	3403.34	Fracture	625074	x			
53	3	11166	3403.40	Fracture	625073	x		x	x
53	2	11167.4	3403.82	Fracture	629004	2X3		x	
53	2	11168	3404.01	Fracture fill				x	
53	2	11167.4	3403.82	Fracture	625072				
53	2		0.00	Fracture fill					
55	3	11501.6	3505.69	Fracture	625071				

APPENDIX D: Thin section descriptions

Sample ID	Core	Segment Number	Depth (m)	Mineralogy	Fabric
1701	5	11	518.46	Qtz, plagioclase, k-spar, biotite	High damage; cataclasite rock with fracture grains and remnant clasts, some areas have greater grain size reduction than others
1710.9	5	11	521.48	Qtz, plagioclase, k-spar, biotite	High damage; cataclasite rock with fracture grains and remnant clasts, some areas have greater grain size reduction than others
2299.2	7	1	700.80	Plagioclase, qtz, biotite, hornblende	High damage; cataclasite rock with fractured grains and remnant clasts
3736.7	15	3	1138.95	Qtz, plagioclase, biotite,	High damage; laumontite shear zone with hematite slip surfaces bordering it, show multiple episodes of movement, fractured and shattered grains are throughout the thin section
4217.2	16	2	1285.40	Qtz, k-spar, biotite, muscovite	Light damage; microcracks, some areas of feldspar alteration into laumontite(?)
4218.9	16	1	1285.92	Qtz, plagioclase, muscovite, biotite	Light damage; anastomosing mode I fractures with laumontite fill, some microcracks and fractured grains along laumontite filled fracture
4443.3	17	4	1354.32	Qtz, k-spar, biotite, plagioclase, hornblende	High damage; shear zone with calcite and laumontite, shear fractures with hematite slip surfaces, fractured and shattered grains and feldspar alteration, few open fractures
4923.1	18	2	1500.56	Qtz, plagioclase, green hornblende, biotite,	High damage; laumontite shear zones with multiple episodes of movement with well developed hematite slip surfaces within the shear zone; open fractures are present as well as some shattered grains and reduction in grain size throughout.
5425	19	7	1653.54	Qtz, plagioclase, hornblende, biotite	Little to no damage
6181.4	25	1	1884.09	Qtz, plagioclase, biotite, muscovite, k spar	Medium damage; mode I fracture with cataclasite flow contains protolith (qtz, plag, minor biotite,), Main fracture braches into thinner fractures with same fill.
6242	26	6	1902.56	Qtz, plagioclase, biotite,	Medium damage; Mode II fractures with laumotite fill, some microcracks and fractured grains
6707.3	30	1	2044.39	Qtz, k-spar, biotite, green hornblende, plagioclase	High damage; partitioned shear zone, with laumontite crystal growth bordering poorly developed hematite slip surfaces. Fine laumontite cataclasite in the shear zone. Hematite not always present in shear zone. Etched, fractured, and altered grains border shear zones
31.4	31	4	-	Qtz, plagioclase, k-spar, hornblende, biotite	Light damage; few mode I fractures with fill
33.1	33	1	-	Qtz, plagioclase, k-spar, biotite, twinned calcite	High damage; defined zone of ultracataclasite surrounded by laumontite and calcite, some fractured grains surround zone
7164.4	35	7	2183.71	Qtz, biotite, plagioclase, hornblende, twinned calcite	Light damage; calcite vein with biotite in the vein, some mode I fractures with calcite are also present
7167.4	35	6	2184.62	Qtz, plagioclase, biotite, hornblende	Light damage; one large calcite vein
7378.5	36	4	2248.97	Qtz, hornblende, twinned calcite, biotite, plagioclase, k-spar	Light damage, some micro cracks, poorly developed gneissic fabric.
7379	36	4	2249.12	Qtz, plagioclase, biotite, hornblende, calcite	High damage; laumontite shear fractures and altered calcite filled fractures, fractured grains, areas of grain size reduction
7380.7 (2x3)	37	2	2249.64	Hornblende, biotite, twinned calcite, plagioclase	High damage; shear zones with laumontite fill that surround ultracataclasite with hematite slip surfaces and foliated gouge (?), and pronounced reduction of grain size shows multiple epsiodes of slip and/or transtension, some fractured and shattered grains, and feldspar alteration
7713.5	38	1	2351.07	Qtz, plagioclase, biotite, calcite,	Light damage; some micro cracks and anastomosing micro mode I with a quartz and plagioclase fill.
38.2	38	2	-	Qtz, calcite, plagioclase, biotite	Light damage; few mode I fractures with fill and fractured grains
7972.3	39	2	2429.96	Qtz, plagioclase, green hornblende, biotite	Light damage, some micro cracks, and thin mode I fractures
8557 (2x3)	43	1	2608.17	Twinned calcite, qtz, plagioclase, k-spar, biotite	High damage; shear zones with laumontite fill that surround ultracataclasite with hematite slip surfaces and pronounced reduction of grain size, many fractured and shattered grains, mode I fractures filled with laumontite, some open fractures, and feldspar alteration
8557.5 (2x3)	43	1	2608.33	Twinned calcite, k-spar,biotite,	High damage; shear zones with laumontite fill that surround ultracataclasite with hematite slip surfaces and pronounced reduction of grain size, many fractured and shattered grains, mode I fractures filled with laumontite, some open fractures, and feldspar alteration
44.1	44	1	-	Qtz, k-spar, calcite, plagioclase, biotite, hornblende	High damage; zones of cataclasite to ultra cataclasite with hematite slip surfaces, fractured grains and fine grain laumontite zones near cataclasite
8640.2	44	3	2633.53	Qtz, k-spar, hornblende, biotite, plagioclase	Light damage; few mode I fractures with laumontite fill, some calcite in fractures as well
8640.9	44	3	2633.75	Hornblende, biotite, qtz, plagioclase	Light damage; anastomosing mode I fracture with laumontite and chlorite (?) fill

8643	44	2	2634.39	Qtz, k-spar, biotite, plagioclase, hornblende	Medium damage; laumontite shear fracture with multi stages of movement, hematite slip surfaces is in some areas of shear fracture. Fractured grains border the shear zone.
8645.1 (2x3)	44	1	2635.03	Qtz, plagioclase, biotite, calcite,	High damage; shear zones with laumontite fill that surround ultracataclasite with hematite slip surfaces and pronounced reduction of grain size, many fractured and shattered grains, mode I fractures filled with laumontite, some open fractures, and feldspar alteration
8792.6	45	4	2679.98	Qtz, plagioclase, k-spar, green hornblende	Light Damage; some fractured grains, epidote (?) through thin section
8995.2	46	7	2741.74	Twinned calcite, k-spar, plagioclase, chlorite, biotite	Medium damage; laumontite filled mode I fractures, fractured grains, altered feldspar grains
8997	46	7	2742.29	Qtz, biotite, hornblende, plagioclase	High damage; laumontite shear zone, show multiple episodes of movement and tension, fractured and shattered grains are throughout the thin section, filled mode I fractures are present
47.1 (2x3)	47	1	-	Qtz, plagioclase, k-spar, twinned calcite, biotite	High damage; shear zones with laumontite fill that surround ultracataclasite with hematite slip surfaces and pronounced reduction of grain size, many fractured and shattered grains, mode I fractures filled with laumontite, some open fractures, and feldspar alteration
9361.4	48	2	2853.35	Qtz, plagioclase, biotite, hornblende	Light damage; laumontite filled shear fracture with hematite in areas, some areas of grain size reduction, fractured grains
48.2	48	2	-	Qtz, Plagioclase, biotite	Light damage; open fractures and microcracks.
48.3	48	3	-	Qtz, plagioclase, biotite	Little to no damage
9475.5	49	2	2888.13	Qtz, plagioclase, k-spar, biotite,	Medium damage; mode I fractures with laumontite fill, some fractured grains and microcracks
10971	52	1	3343.96	Qtz, plagioclase, biotite, k-spar	Light damage; few open fractures, and fractured grains, few microcracks
11161.7 (2x3	53	5	3402.09	Qtz, plagioclase, k-spar, biotite, twinned calcite	High damage; shear zones with laumontite fill that surround ultracataclasite with hematite slip surfaces and pronounced reduction of grain size, many fractured and shattered grains, mode I fractures filled with laumontite, some open fractures, and feldspar alteration
11161.7	53	5	3402.09	Qtz, k-spar, plagioclase, biotite	Light damage; some laumontite filled fractures, few open fractures and microcracks
11165.8A	53	3	3403.34	Qtz, plagioclase, biotite	Medium damage; high density of fractured grains and shattered grains in areas appear protocataclasite, laumontite filled mode I fractures
11165.8B	53	3	3403.34	Qtz, plagioclase, biotite	Medium damage; high density of fractured grains and shattered grains in areas appear protocataclasite, laumontite filled mode I fractures
11166	53	3	3403.40	Qtz, plagioclase, biotite, k-spar, hornblende	Medium damage; laumontite shear fracture with multi stages of movement/transtension, few fractured grains and open fractures
11167.3 (2x3	53	2	3403.79	Qtz, twinned calcite, plagioclase, biotite,	Medium damage; laumontite filled shear fractures, many fractured grains and few shattered grains, some microcracks and mode I fractures, some altered feldspar
53.3	53	3	-	Qtz, plagioclase, biotite	High damage; shear zone with laumontite and some hematite slip surfaces, fractured and shattered grains and feldspar alteration, few open fractures
11501.6	55	3	3505.69	Qtz, plagioclase, biotite	Light damage; mode I fractures filled with fine laumontite, some microcracks are present
CP2FW			NA	Qtz, k-spar, twinned calcite, biotite, hornblende	Light damage; some open fractures
CP2HWA			NA	Qtz, plagioclase, twinned calcite, biotite,	Light damage; some open fractures, fractured grains, and minor amounts of laumontite is some fractures
CP2HWB			NA	Twinned calcite, plagioclase, biotite, hornblende	Medium damage; laumontite filled shear fractures with some hematite slip surfaces, open fractures, fractured grains
CP4			NA	Qtz, twinned calcite, k-spar, hornblende, biotite	Light damage; fractured grains and few microcracks
CP5			NA	Qtz, twinned calcite, plagioclase, hornblende, biotite	Light damage; fractured grains and few microcracks, some alteration of feldspars

APPENDIX E: X-ray diffraction patterns

Diffraction patterns are in order of sample number. The patterns are from a Philips X-pert PRO PANalytical machine with the accompanying X-Pert Highscore software. Sample numbers are in the upper left portion of each plot.

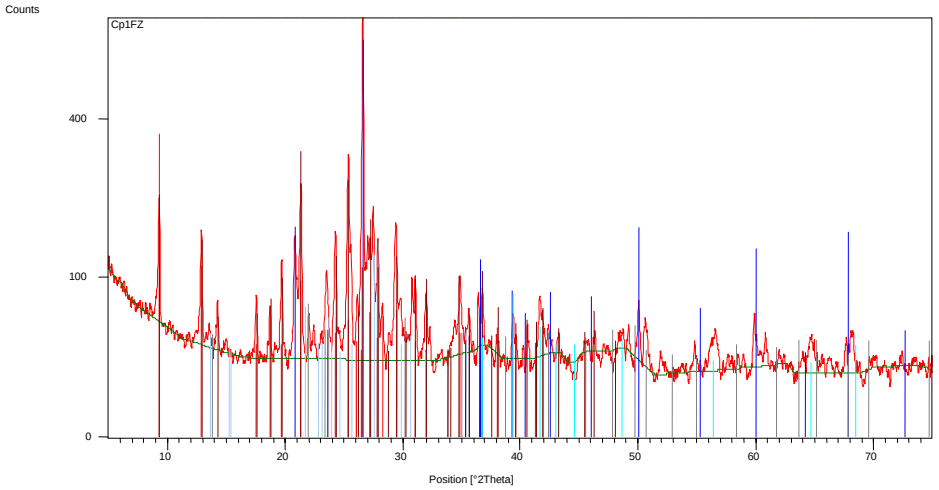
Counts
Cp1FZ
400
100
0
10
20
30
40
50
60
70
Position [°2Theta]

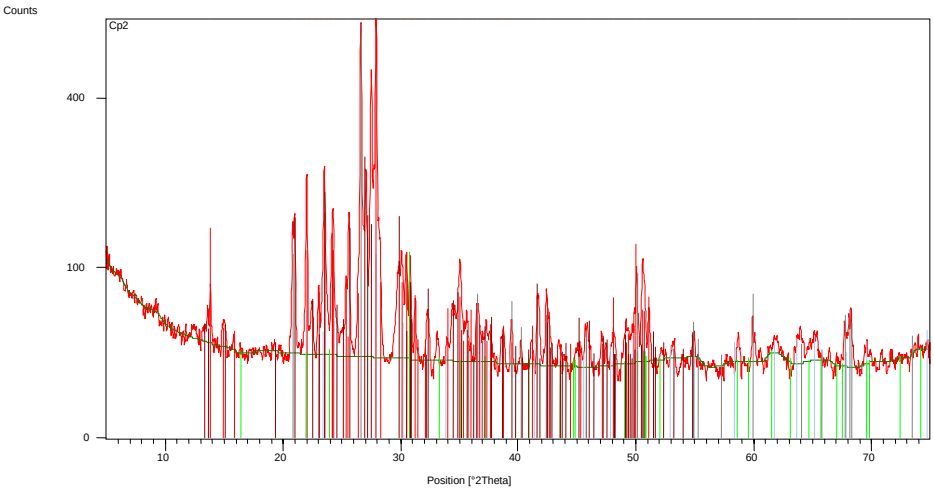
Counts
Cp2
400
100
0
10
20
30
40
50
60
70
Position [°2Theta]

\

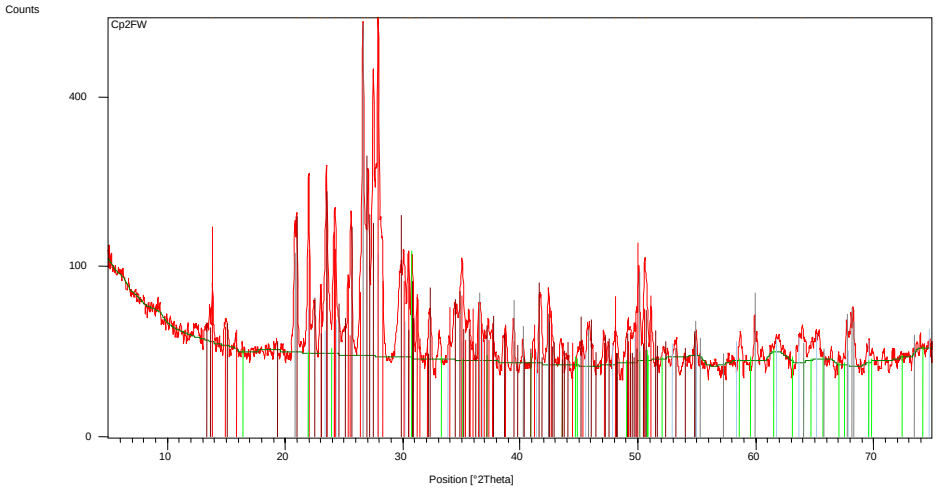
Counts
Cp2FW
400
100
0
10
20
30
40
50
60
70
Position [°2Theta]

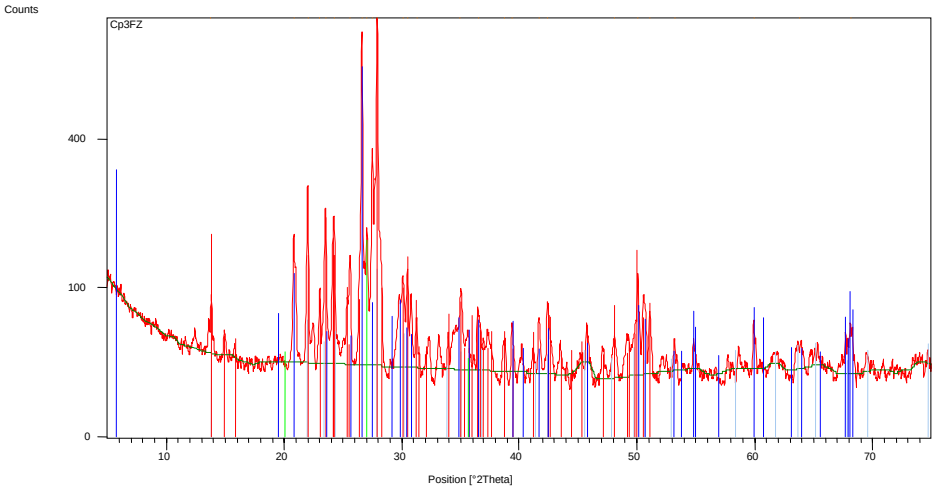
Counts
Cp3FZ
400
100
0
10
20
30
40
50
60
70
Position [°2Theta]

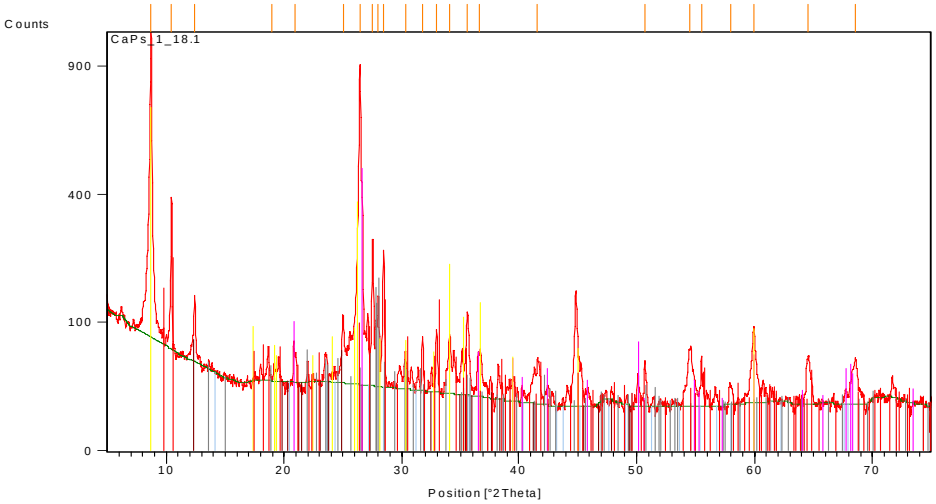
Counts
CaPs_1_18.1
900
400
100
0
10
20
30
40
50
60
70
Position [°2Theta]

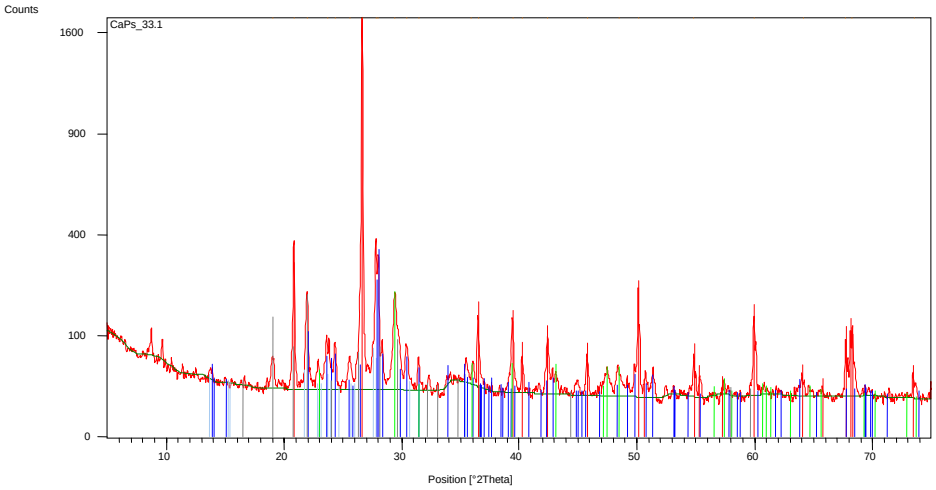
Counts
CaPs_33.1
1600
900
400
100
0
10
20
30
40
50
60
70
Position [°2Theta]

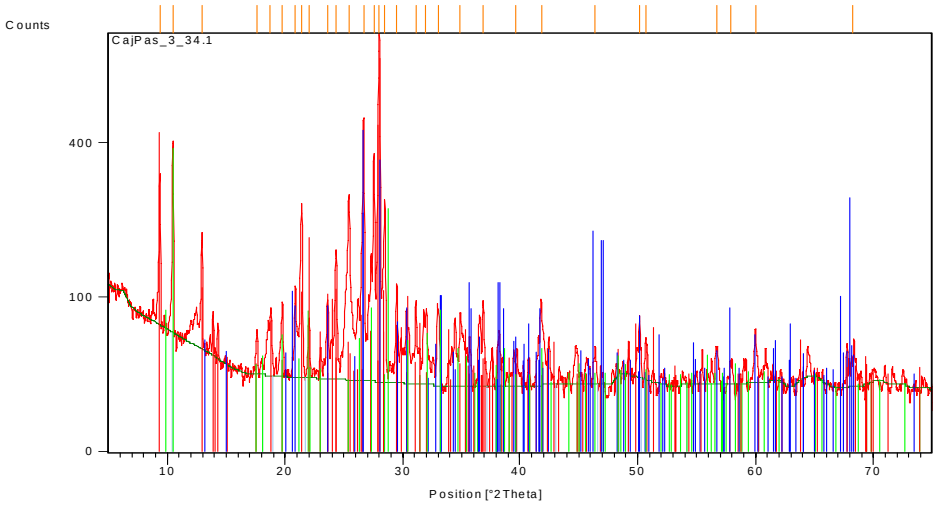
Counts
CajPas_3_34.1
400
100
0
10
20
30
40
50
60
70
Position [°2Theta]

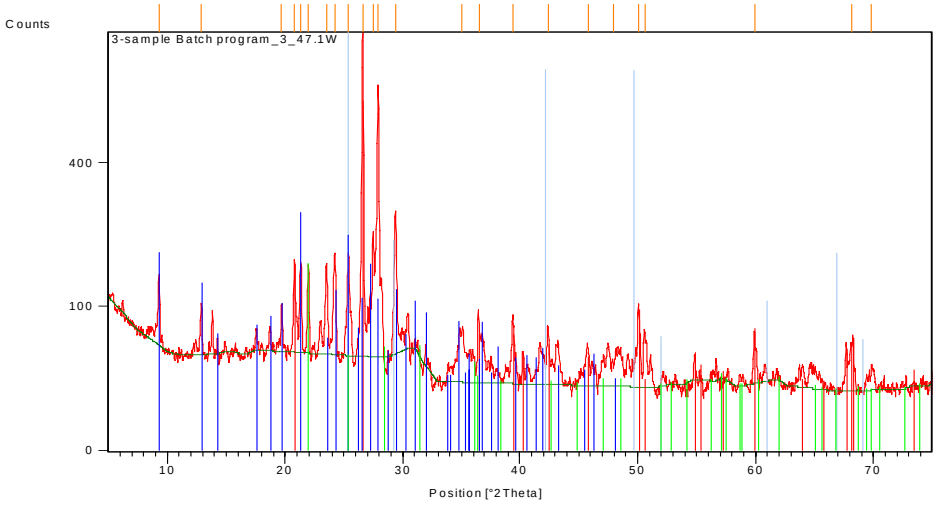
Counts
3-sample Batch program_3_47.1W
400
100
0
10
20
30
40
50
60
70
Position [°2Theta]

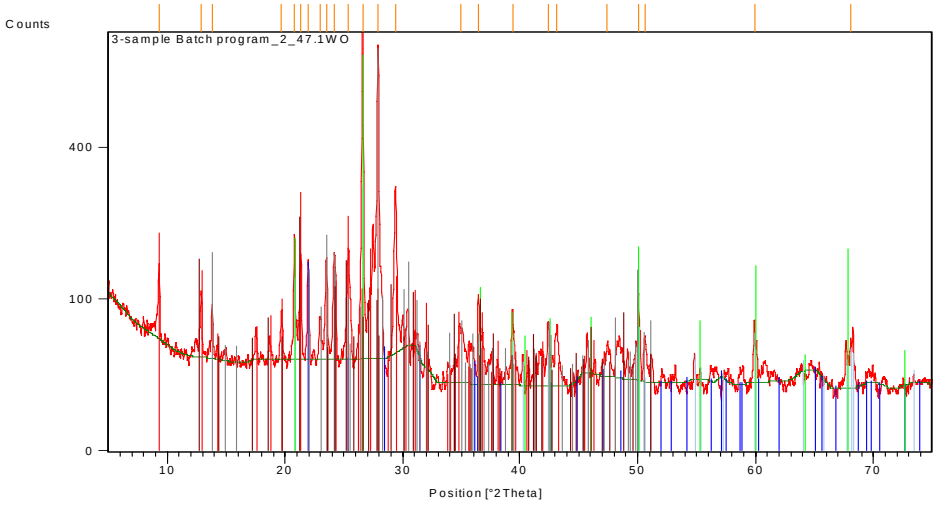
Counts
3-sample Batch program_2_47.1WO
400
100
0
10
20
30
40
50
60
70
Position [°2Theta]

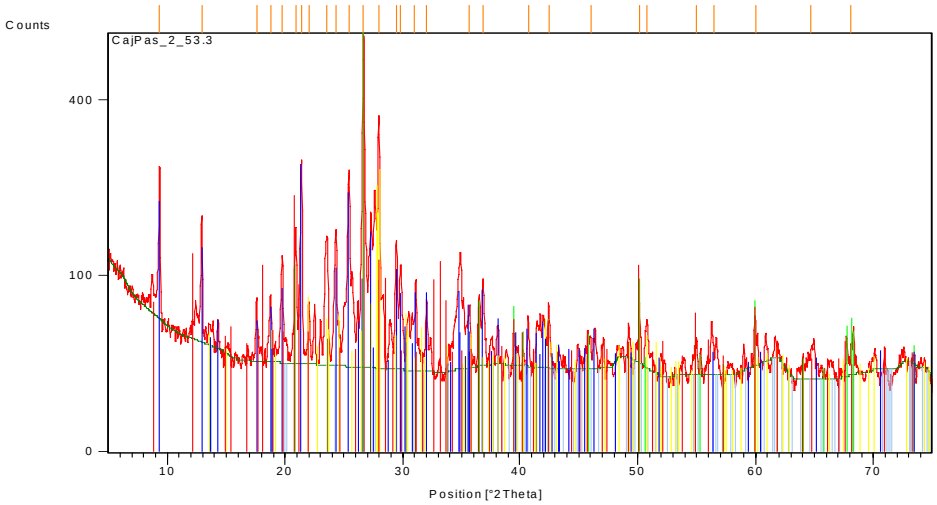
Counts
CajPas_2_53.3
400
100
0
10
20
30
40
50
60
70
Position [°2Theta]

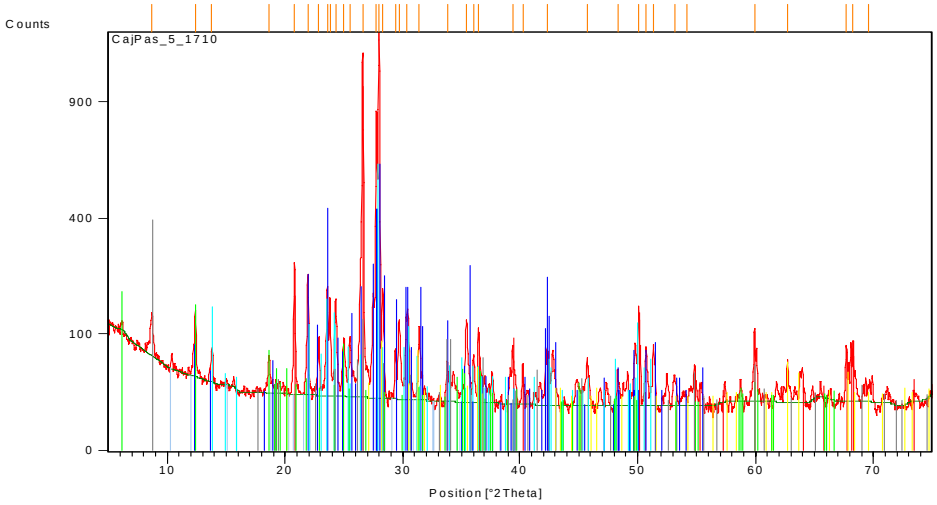
Counts
CajPas_5_1710
900
400
100
0
10
20
30
40
50
60
70
Position [°2Theta]

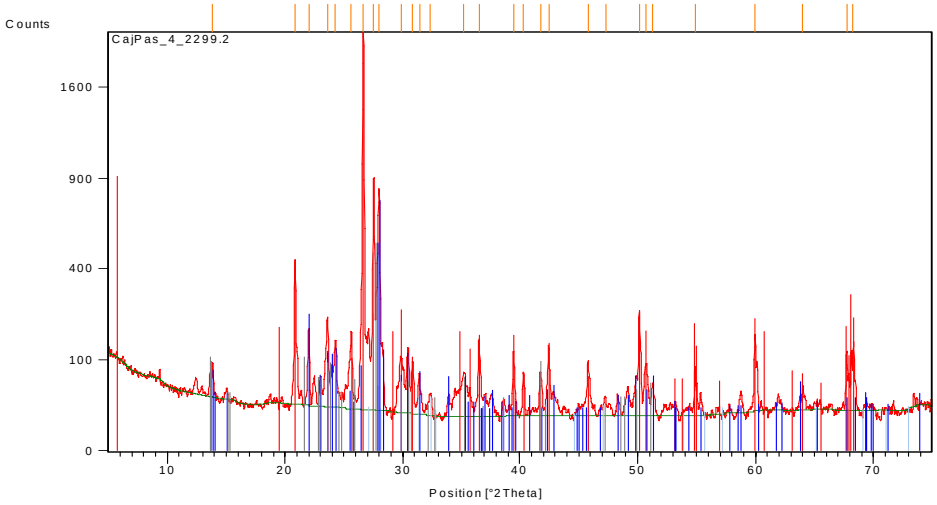
Counts
CajPas_4_2299.2
1600
900
400
100
0
10
20
30
40
50
60
70
Position [°2Theta]

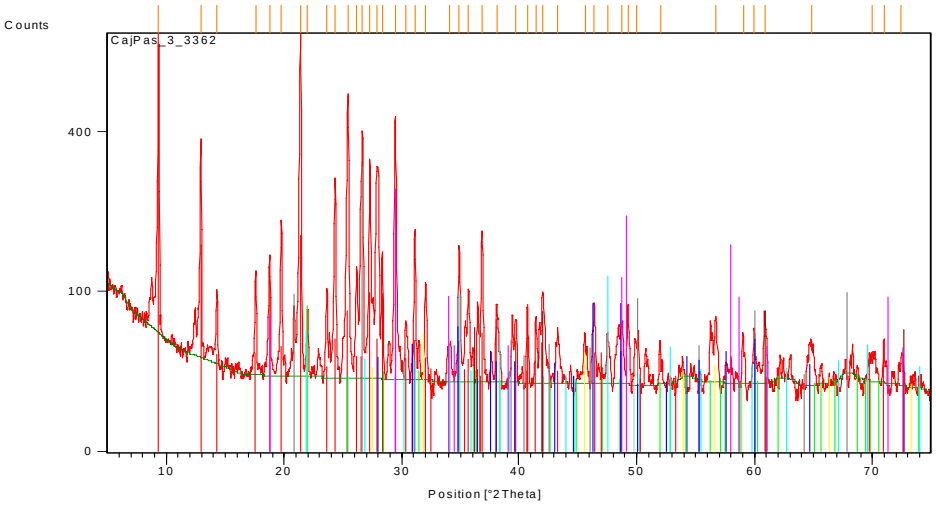
Counts
CajPas_3_3362
400
100
0
10
20
30
40
50
60
70
Position [°2Theta]

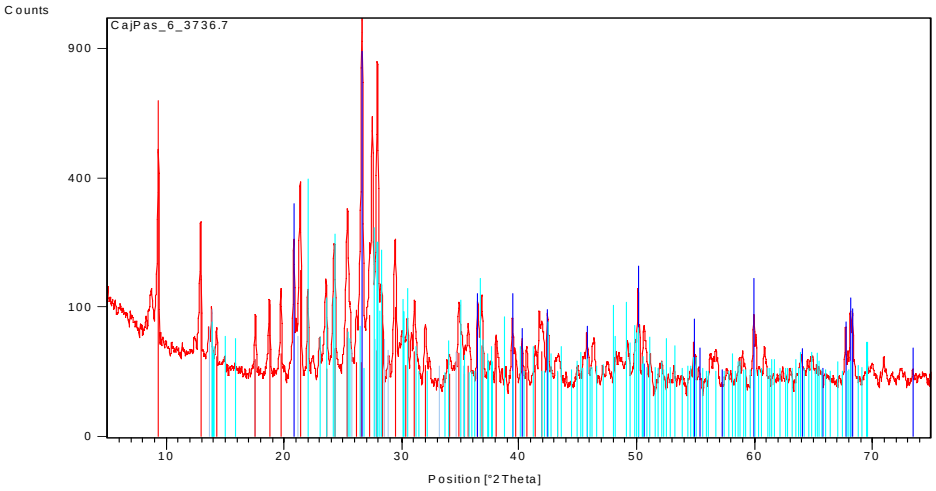
Counts
CajPas_6_3736.7
900
400
100
0
10
20
30
40
50
60
70
Position [°2Theta]

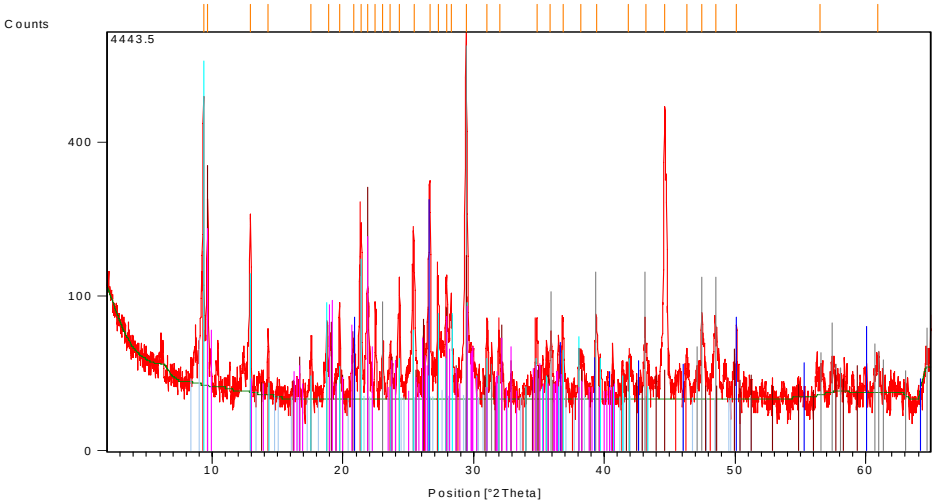
Counts
4443.5
400
100
0
10
20
30
40
50
60
Position [°2Theta]

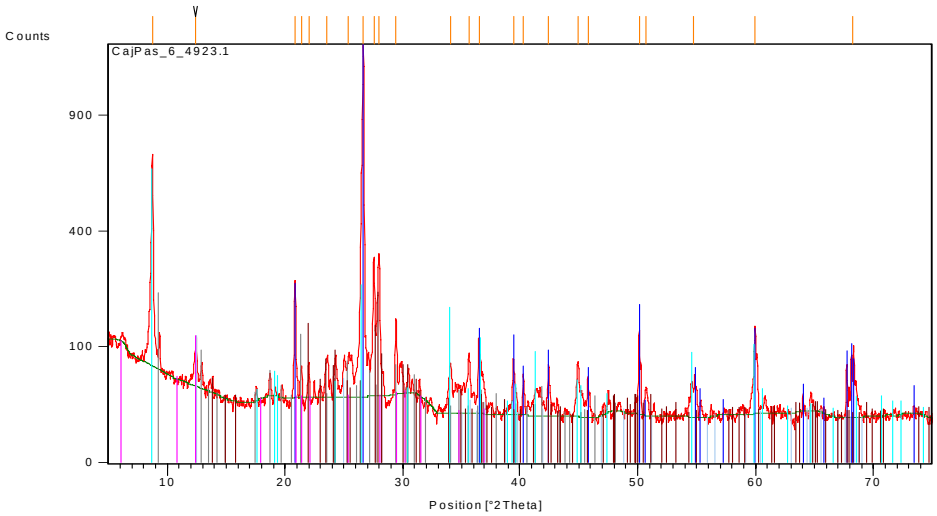
Counts
CajPas_6_4923.1
900
400
100
0
10
20
30
40
50
60
70
Position [°2Theta]

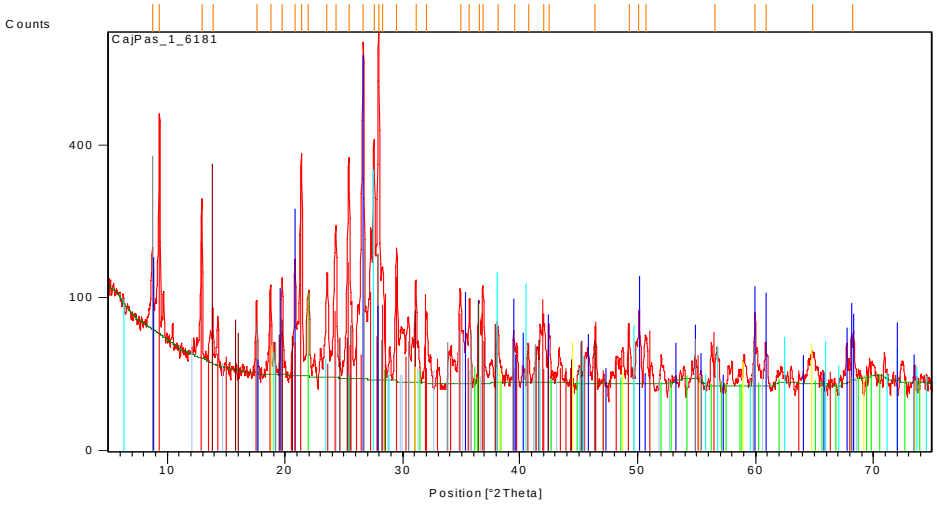
Counts
CajPas_1_6181
400
100
0
10
20
30
40
50
60
70
Position [°2Theta]

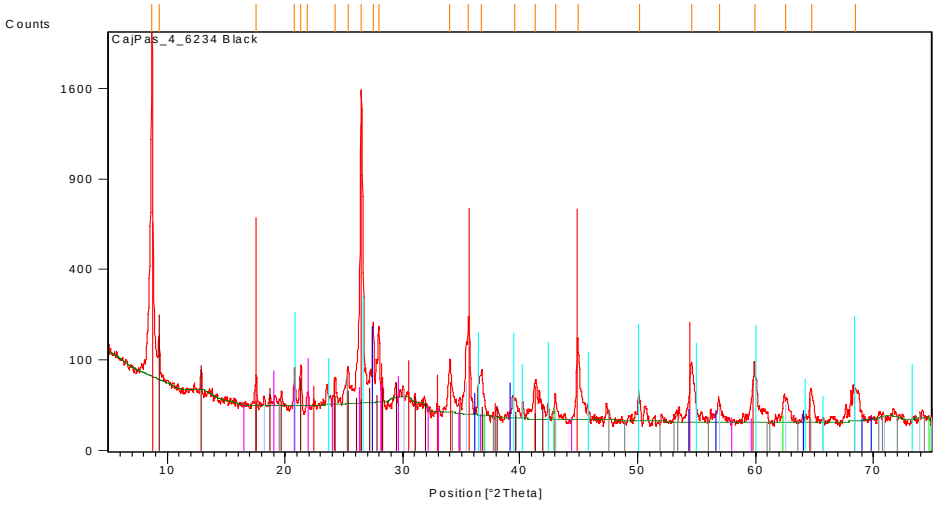
Counts
CajPas_4_6234 Black
1600
900
400
100
0
10
20
30
40
50
60
70
Position [°2Theta]

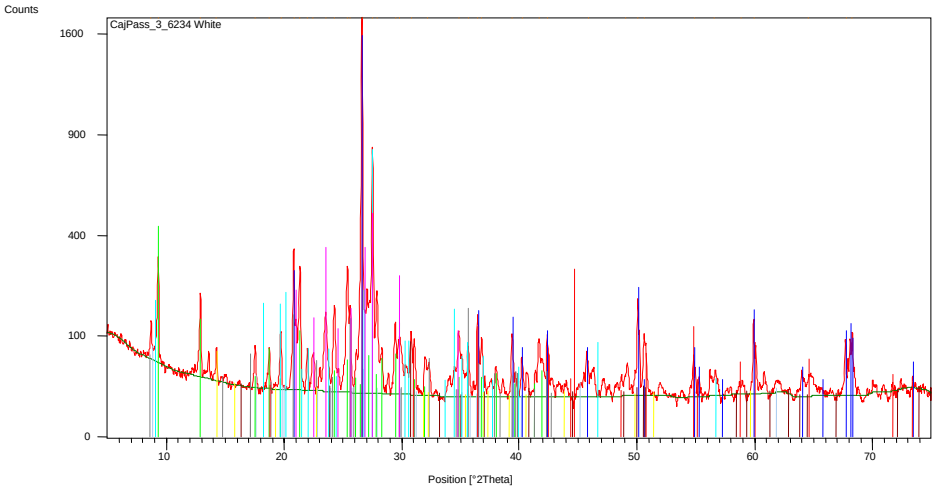
Counts
CajPass_3_6234 White
1600
900
400
100
0
10
20
30
40
50
60
70
Position [°2Theta]

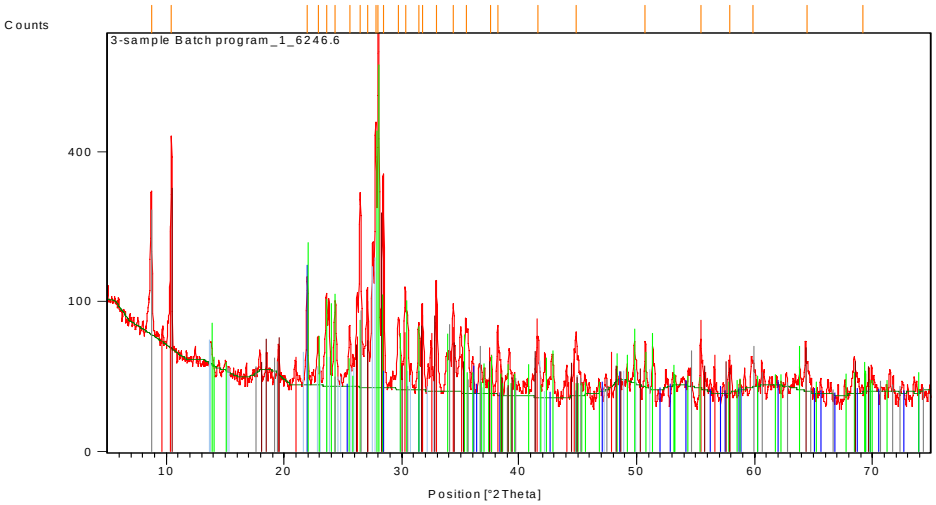
Counts
3-sample Batch program_1_6246.6
400
100
0
10
20
30
40
50
60
70
Position [°2Theta]

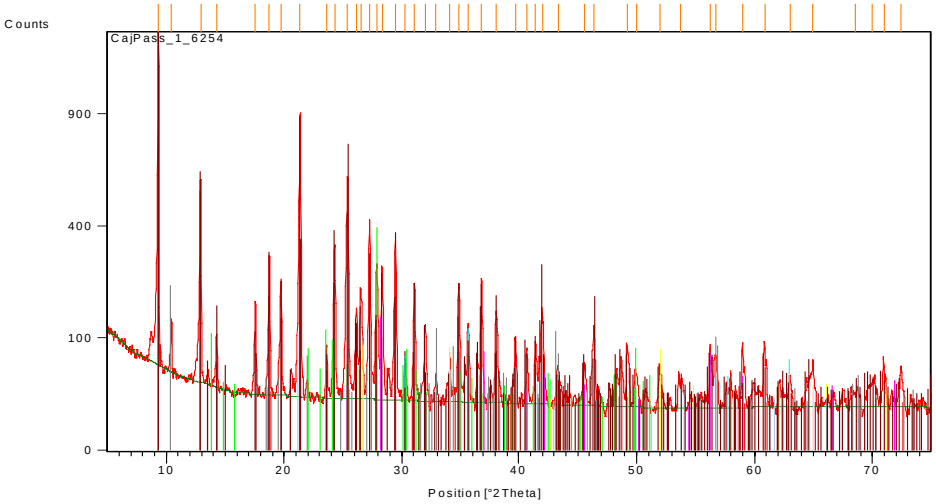
Counts
CajPass_1_6254
900
400
100
0
10
20
30
40
50
60
70
Position [°2Theta]

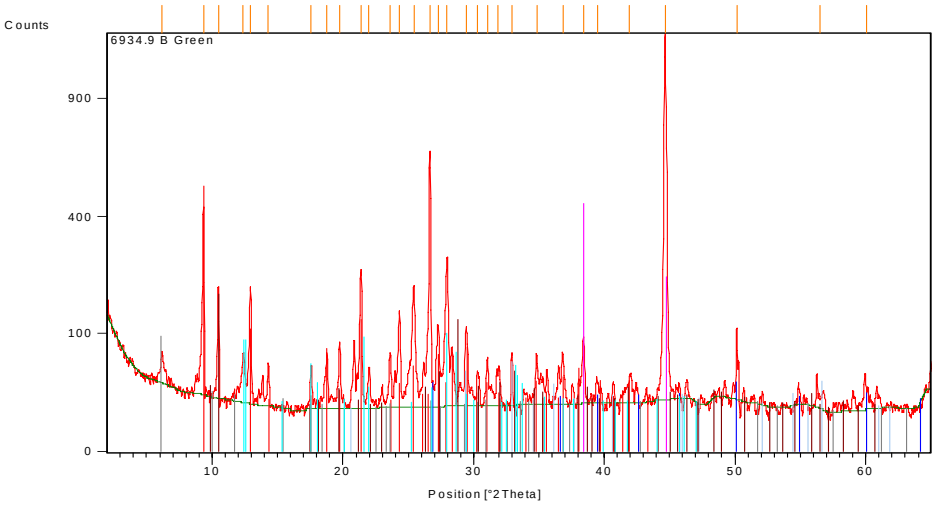
Counts
6934.9 B Green
900
400
100
0
10
20
30
40
50
60
Position [°2Theta]

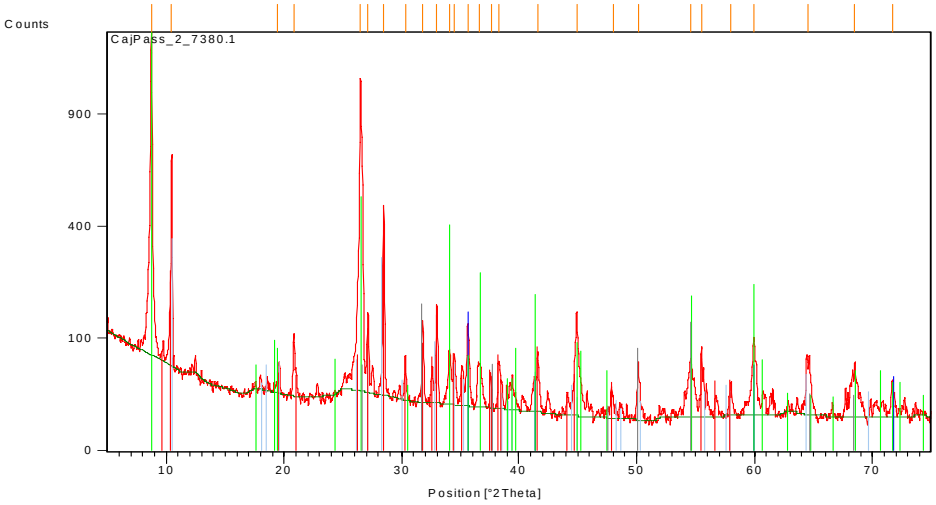
Counts
CajPass_2_7380.1
900
400
100
0
10
20
30
40
50
60
70
Position [°2Theta]

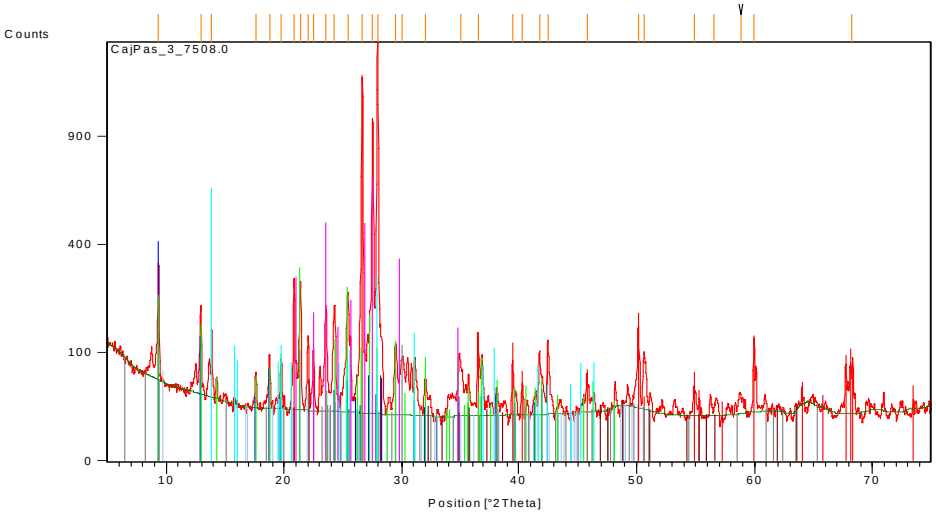
Counts
CajPas_3_7508.0
900
400
100
0
10
20
30
40
50
60
70
Position [°2Theta]

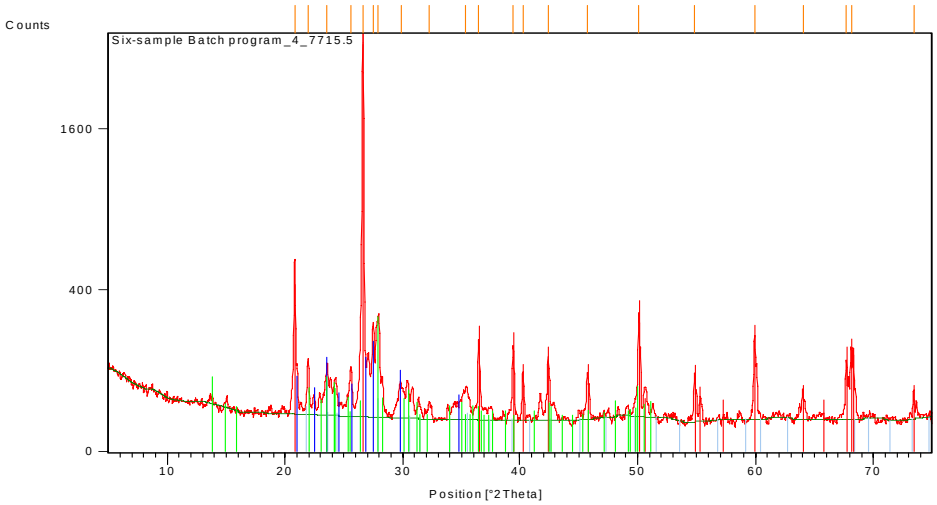
Counts
Six-sample Batch program_4_7715.5
1600
400
0
10
20
30
40
50
60
70
Position [°2Theta]

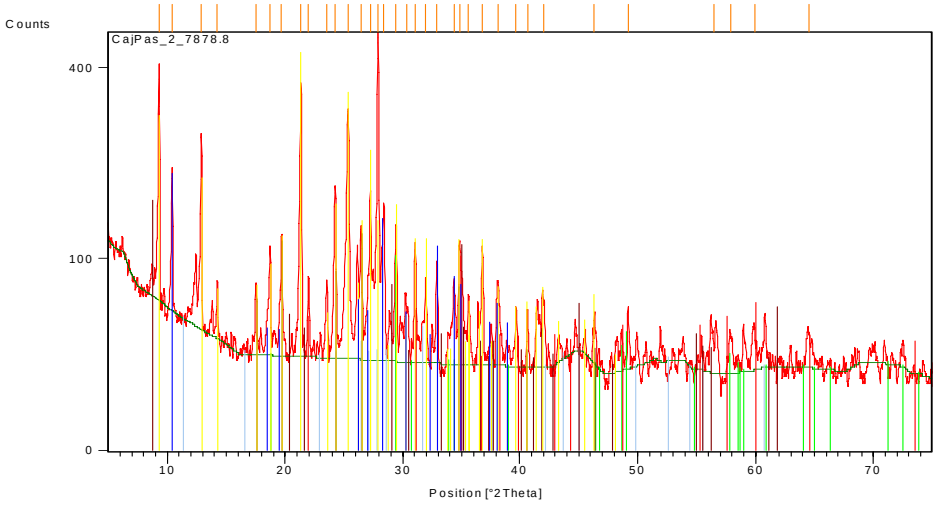
Counts
CajPas_2_7878.8
400
100
0
10
20
30
40
50
60
70
Position [°2Theta]

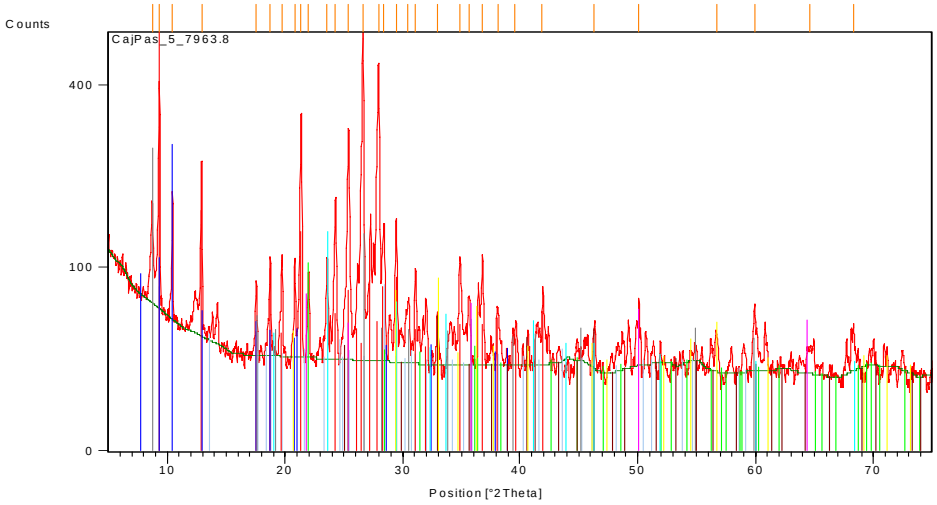
Counts
CajPas_5_7963.8
400
100
0
10
20
30
40
50
60
70
Position [°2Theta]

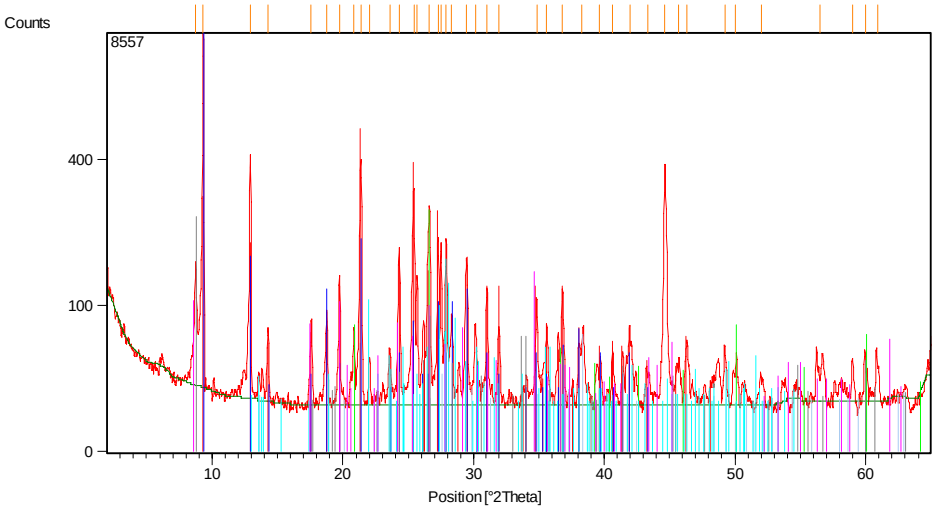
Counts
8557
400
100
0
10
20
30
40
50
60
Position [°2Theta]

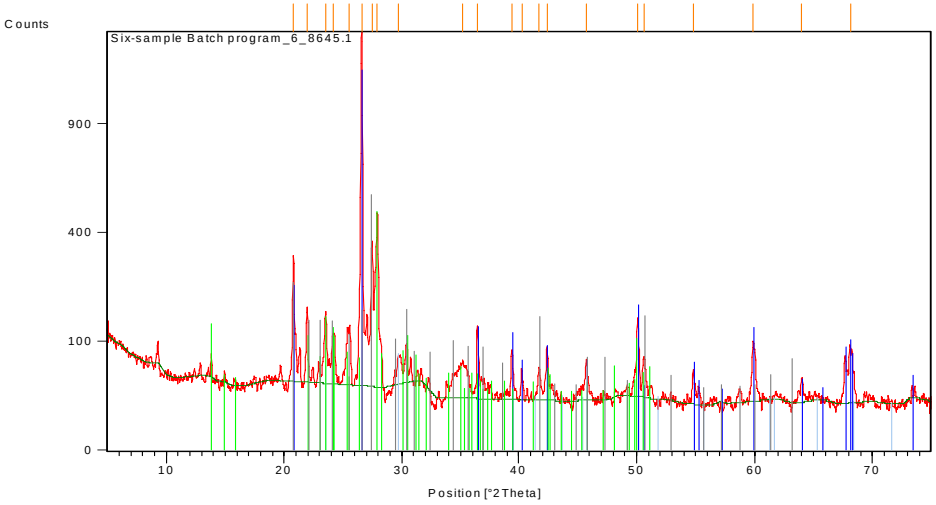
Counts
Six-sample Batch program_6_8645.1
900
400
100
0
10
20
30
40
50
60
70
Position [°2Theta]

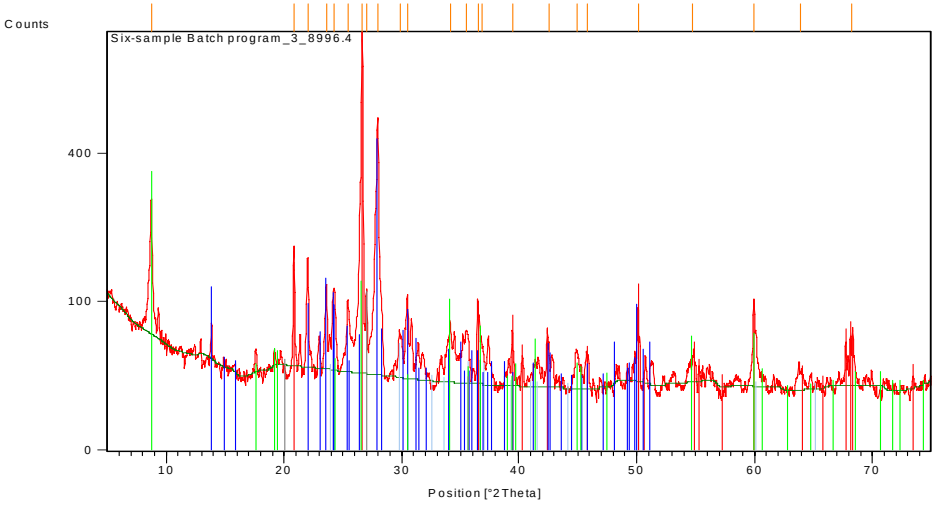
Counts
Six-sample Batch program_3_8996.4
400
100
0
10
20
30
40
50
60
70
Position [°2Theta]

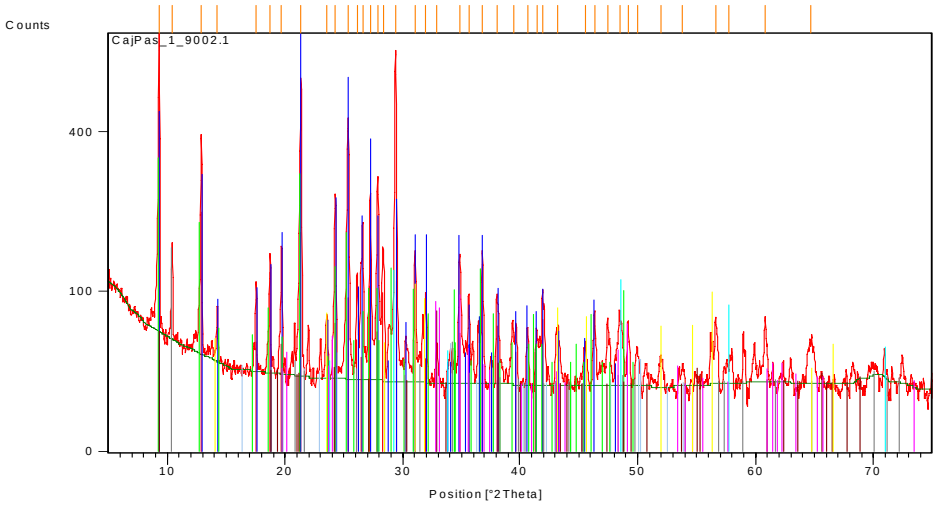
Counts
CajPas_1_9002.1
400
100
0
10
20
30
40
50
60
70
Position [°2Theta]

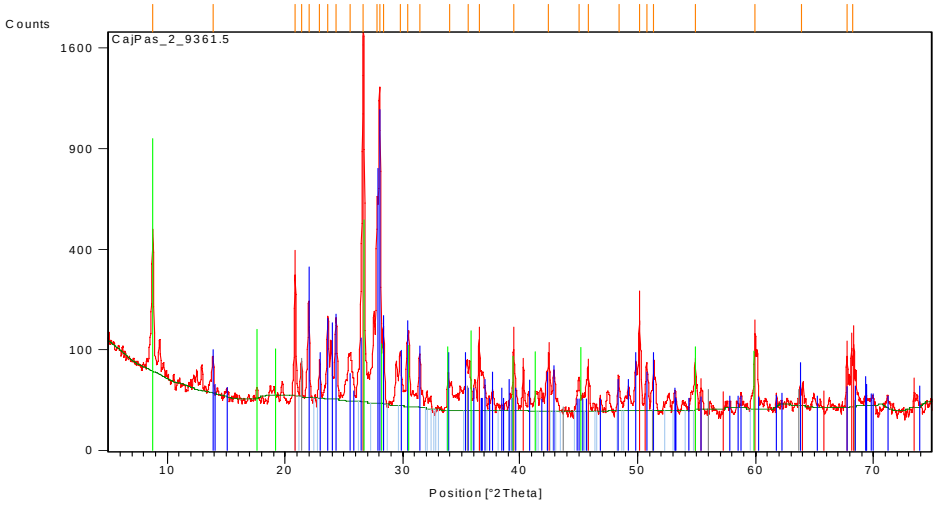
Counts
CajPas_2_9361.5
1600
900
400
100
0
10
20
30
40
50
60
70
Position [°2Theta]

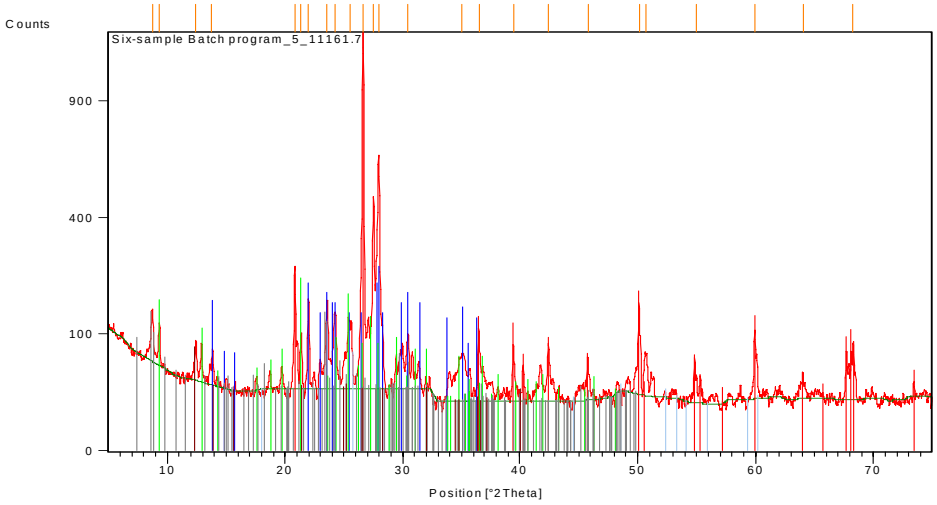
Counts
Six-sample Batch program_5_11161.7
900
400
100
0
10
20
30
40
50
60
70
Position [°2Theta]

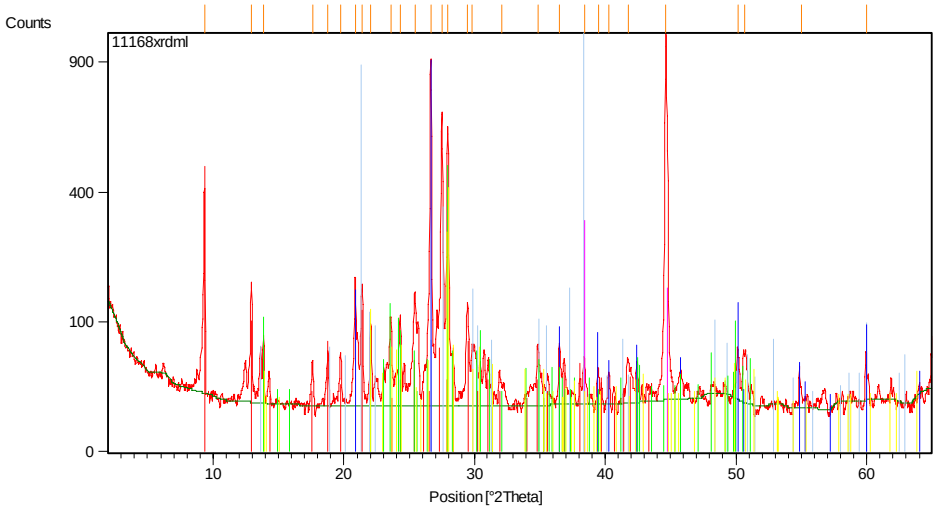
Counts
11168xrdml
900
400
100
0
10
20
30
40
50
60
Position [°2Theta]

APPENDIX F: Whole-rock geochemistry raw data

RE08002333 - Finalized
CLIENT : " Department Of Geology"
# of SAMPLES : 19
DATE RECEIVED : 2008-01-08 DATE FINALIZED : 2008-02-04
PROJECT : "Cajon Pass"
CERTIFICATE COMMENTS : ""
PO NUMBER : " "

SAMPLE DESCRIPT	WEI-21 Recvd Wt. kg	ME-XRF06 SiO2 %	ME-XRF06 Al2O3 %	ME-XRF06 Fe2O3 %	ME-XRF06 CaO %	ME-XRF06 MgO %	ME-XRF06 Na2O %	ME-XRF06 K2O %	ME-XRF06 Cr2O3 %	ME-XRF06 TiO2 %	ME-XRF06 MnO %	ME-XRF06 P2O5 %	ME-XRF06 SrO %	ME-XRF06 BaO %	ME-XRF06 LOI %	ME-XRF06 Total %
48.3	0.11	61.92	17.1	5.27	4.47	2.35	4.16	2.08	<0.01	0.68	0.11	0.221	0.04	0.04	1.34	99.8
9470.3	0.04	70.05	14.42	2.6	2.69	0.97	3.31	4.21	<0.01	0.24	0.05	0.064	0.05	0.13	1.16	99.94
9355.6	0.07	58.69	16.44	7.85	5.05	3.28	3.35	2.32	<0.01	0.81	0.17	0.263	0.05	0.07	1.52	99.85
7370.1	0.02	68.53	12.51	7.22	3.2	2.03	2.36	1.93	0.01	0.71	0.13	0.041	0.04	0.11	0.93	99.74
4922.6	0.1	48.03	19.63	10.16	7.99	4.64	3.7	2.55	<0.01	1.28	0.14	0.359	0.07	0.09	1.27	99.91
31.1	0.08	53.7	16.91	8.57	6.25	3.56	3.49	4.37	0.01	0.9	0.16	0.308	0.06	0.19	1.2	99.69
4923.1	0.06	59.65	14.65	7.23	3.74	3.34	2.88	3.17	0.01	0.94	0.1	0.19	0.04	0.08	3.69	99.71
31.4	0.03	63.45	16.98	3.71	4.45	1.26	4.43	3.86	<0.01	0.38	0.08	0.129	0.08	0.16	0.99	99.96
9475.5	0.04	73.62	13.52	1.62	2.24	0.34	3.51	3.34	0.01	0.09	0.02	<0.001	0.04	0.08	1.24	99.67
12.2	0.03	72.2	14.1	2.29	2.04	0.56	3.72	3.78	<0.01	0.27	0.04	0.049	0.03	0.13	0.54	99.74
53.3	0.04	57.01	17.44	3.8	5.46	1.38	2.1	3.81	0.01	0.4	0.05	0.136	0.03	0.08	8.24	99.94
38.2	<0.02	67.66	15.57	3.44	2.3	0.66	3.71	4.28	0.01	0.23	0.04	0.069	0.07	0.17	1.71	99.92
2823	0.06	72.16	13.98	2.31	1.81	0.58	3.29	4.61	0.01	0.34	0.05	0.067	0.03	0.15	0.49	99.86
7371.2	0.07	58.16	15.85	10.88	3.93	2.75	2.69	2.95	0.01	1.21	0.19	0.179	0.04	0.12	0.84	99.8
11161.7	0.02	61.25	17.37	4.54	4.1	1.84	3.74	3.4	0.01	0.53	0.07	0.212	0.06	0.11	2.45	99.68
10971	0.02	65.05	15.64	3.62	3.77	1.03	3.93	2.5	<0.01	0.3	0.05	0.217	0.03	0.06	2.9	99.1
5.4	0.02	65.12	15.55	4.56	3.8	1.4	3.61	2.97	<0.01	0.56	0.08	0.183	0.05	0.08	1.65	99.62
1710.9	0.09	61.57	17.39	4.64	4.86	1.66	4.21	2.12	<0.01	0.89	0.07	0.296	0.08	0.1	1.82	99.71
7712	0.05	70.07	15.2	1.89	2.04	0.56	3.53	4.8	<0.01	0.18	0.03	0.083	0.06	0.18	1.22	99.84

APPENDIX G: Principal component analysis

PRINCIPAL COMPONENTS ANALYSIS

Data file - C:\Documents and Settings\Dave\Desktop\MVSP Files\All Data.mvs

Analysis begun: Thursday, May 21, 2009 1:02:36 PM

Analysing 14 variables x 19 cases

Data log(10) transformed

Tolerance of eigenanalysis set at 1E-007

Data standardized

Transformed data

	521.62	526.52	860.67	860.67	1500.79	1500.95	2056.59	2058.69								
	2246.98	2247.32	2351.22	2351.22	2852.32	2852.74	2887.29	2888.87								
	3344.82	3402.96	3403.85													
SiO2	1.796	1.820	1.865	1.864	1.690	1.783	1.809	1.738	1.842	1.772	1.837	1.852	1.776	1.799	1.852	1.873	1.820
	1.794	1.764															
Al2O3	1.265	1.219	1.179	1.176	1.314	1.195	1.255	1.253	1.131	1.227	1.219	1.210	1.242	1.258	1.188	1.162	1.221
	1.264	1.266															
Fe2O3	0.751	0.745	0.517	0.520	1.048	0.915	0.673	0.981	0.915	1.075	0.647	0.461	0.947	0.797	0.556	0.418	0.665
	0.744	0.681															
CaO	0.768	0.681	0.483	0.449	0.954	0.676	0.736	0.860	0.623	0.693	0.519	0.483	0.782	0.738	0.567	0.511	0.679
	0.708	0.810															
MgO	0.425	0.380	0.193	0.199	0.751	0.637	0.354	0.659	0.481	0.574	0.220	0.193	0.631	0.525	0.294	0.127	0.307
	0.453	0.377															
Na2O	0.717	0.664	0.674	0.632	0.672	0.589	0.735	0.652	0.526	0.567	0.673	0.656	0.638	0.713	0.634	0.654	0.693
	0.676	0.491															

K2O	0.494	0.599	0.679	0.749	0.550	0.620	0.687	0.730	0.467	0.597	0.723	0.763	0.521	0.489	0.717	0.637	0.544	0.643	0.682
Cr2O3	0.004	0.004	0.004	0.004	0.004	0.004	0.004	0.004	0.004	0.004	0.004	0.004	0.004	0.004	0.004	0.004	0.004	0.004	0.004
TiO2	0.276	0.193	0.104	0.127	0.358	0.288	0.140	0.279	0.233	0.344	0.090	0.072	0.258	0.225	0.093	0.037	0.114	0.185	0.146
MnO	0.029	0.033	0.017	0.021	0.057	0.041	0.033	0.064	0.053	0.076	0.017	0.013	0.068	0.045	0.021	0.009	0.021	0.029	0.021
P2O5	0.113	0.073	0.021	0.028	0.133	0.076	0.053	0.117	0.017	0.072	0.029	0.035	0.101	0.087	0.027	0.000	0.085	0.084	0.055
SrO	0.033	0.021	0.013	0.013	0.029	0.017	0.033	0.025	0.017	0.017	0.029	0.025	0.021	0.017	0.021	0.017	0.013	0.025	0.013
BaO	0.041	0.033	0.053	0.061	0.037	0.033	0.064	0.076	0.045	0.049	0.068	0.072	0.029	0.017	0.053	0.033	0.025	0.045	0.033
LOI	0.450	0.423	0.188	0.173	0.356	0.671	0.299	0.342	0.286	0.265	0.433	0.346	0.401	0.369	0.334	0.350	0.591	0.538	0.966

Similarity matrix

	SiO2	Al2O3	Fe2O3	CaO	MgO	Na2O	K2O	Cr2O3	TiO2	MnO	P2O5	SrO	BaO	LOI
SiO2	1.000													
Al2O3	-0.803	1.000												
Fe2O3	-0.812	0.426	1.000											
CaO	-0.933	0.797	0.755	1.000										
MgO	-0.877	0.530	0.949	0.835	1.000									
Na2O	0.091	0.326	-0.241	0.002	-0.155	1.000								
K2O	0.286	-0.135	-0.524	-0.450	-0.492	-0.015	1.000							

Cr2O3 0.000 0.000 0.000 0.000 0.000 0.000 0.000 0.000

TiO2 -0.804 0.469 0.943 0.739 0.930 -0.158 -0.541 0.000 1.000

MnO -0.689 0.310 0.936 0.643 0.881 -0.214 -0.461 0.000 0.876 1.000

P2O5 -0.860 0.811 0.708 0.864 0.798 0.259 -0.422 0.000 0.763 0.604 1.000

SrO -0.308 0.521 0.163 0.341 0.199 0.528 0.038 0.000 0.201 0.099 0.373 1.000

BaO 0.186 -0.133 -0.207 -0.322 -0.271 0.075 0.745 0.000 -0.230 -0.120 -0.276 0.397 1.000

LOI -0.343 0.339 0.078 0.376 0.153 -0.367 -0.073 0.000 0.021 -0.158 0.238 -0.132 -0.421 1.000

	SiO2	Al2O3	Fe2O3	CaO	MgO	Na2O	K2O	Cr2O3	TiO2	MnO	P2O5	SrO	BaO	LOI

Eigenvalues

	Axis 1	Axis 2	Axis 3
Eigenvalues	6.861	2.221	1.634
Percentage	52.778	17.082	12.570
Cum. Percentage	52.778	69.860	82.430

PCA variable loadings

	Axis 1	Axis 2	Axis 3
SiO2	0.357	-0.074	-0.077
Al2O3	-0.269	0.318	0.334

Fe2O3	-0.350	-0.106	-0.251
CaO	-0.355	0.062	0.172
MgO	-0.364	-0.063	-0.142
Na2O	0.017	0.492	0.148
K2O	0.211	0.277	-0.065
Cr2O3	0.000	0.000	0.000
TiO2	-0.350	-0.065	-0.229
MnO	-0.313	-0.097	-0.398
P2O5	-0.343	0.161	0.147
SrO	-0.111	0.554	-0.008
BaO	0.128	0.407	-0.400
LOI	-0.091	-0.208	0.592

PCA case scores

	Axis 1	Axis 2	Axis 3
521.62	-0.434	0.361	0.236
526.52	-0.023	-0.057	0.104
860.67	0.800	-0.044	-0.155

860.67 0.820 -0.036 -0.287

1500.79 -1.249 0.298 0.032

1500.95 -0.365 -0.417 0.033

2056.59 0.080 0.650 -0.023

2058.69 -0.695 0.404 -0.356

2246.98 0.045 -0.652 -0.537

2247.32 -0.581 -0.282 -0.541

2351.22 0.559 0.394 -0.002

2351.22 0.782 0.371 -0.041

2852.32 -0.687 -0.177 -0.084

2852.74 -0.403 -0.147 0.192

2887.29 0.599 0.048 -0.065

2888.87 0.932 -0.198 0.151

3344.82 0.100 -0.233 0.460

3402.96 -0.166 0.212 0.241

3403.85 -0.114 -0.495 0.640

APPENDIX H: Photographs of previously identified faults from the Cajon Pass Core


Fault Zone from 500-515 m
Top of Core
Fault Zone from 500-515 m
Top of Core
CM

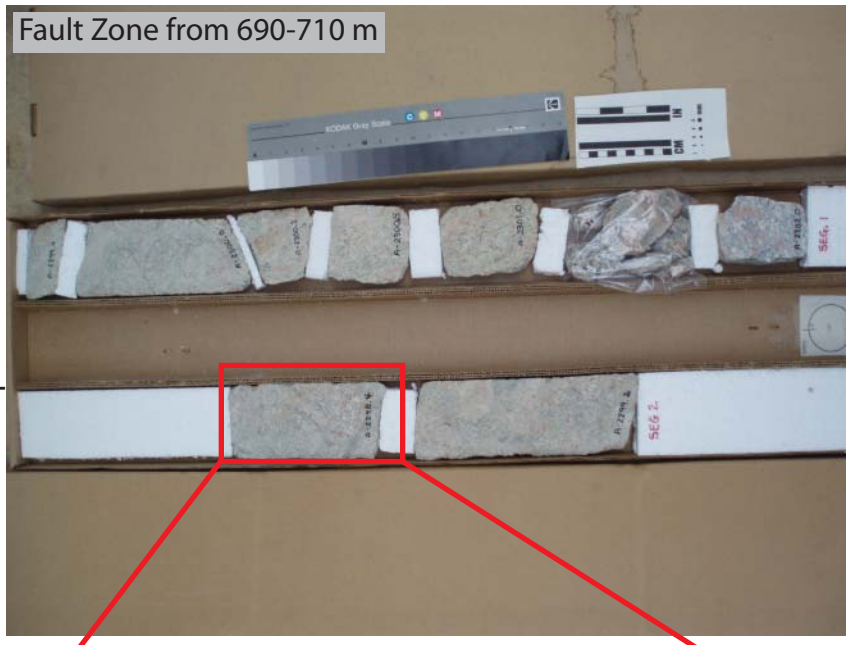
Fault Zone from 690-710 m
Top of Core

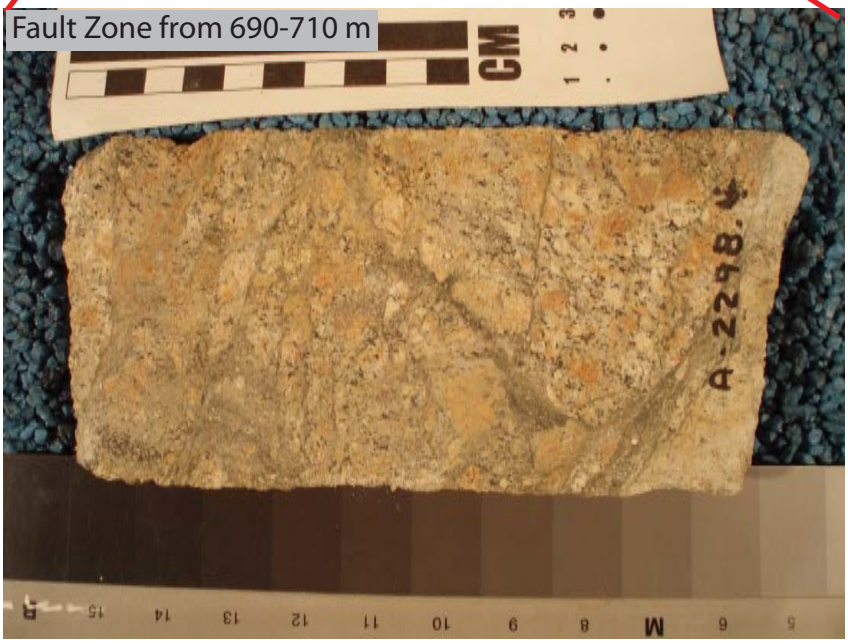
Fault Zone from 690-710 m
Top of Core
CM
A-2298

Top of Core

Top of Core

Top of Core

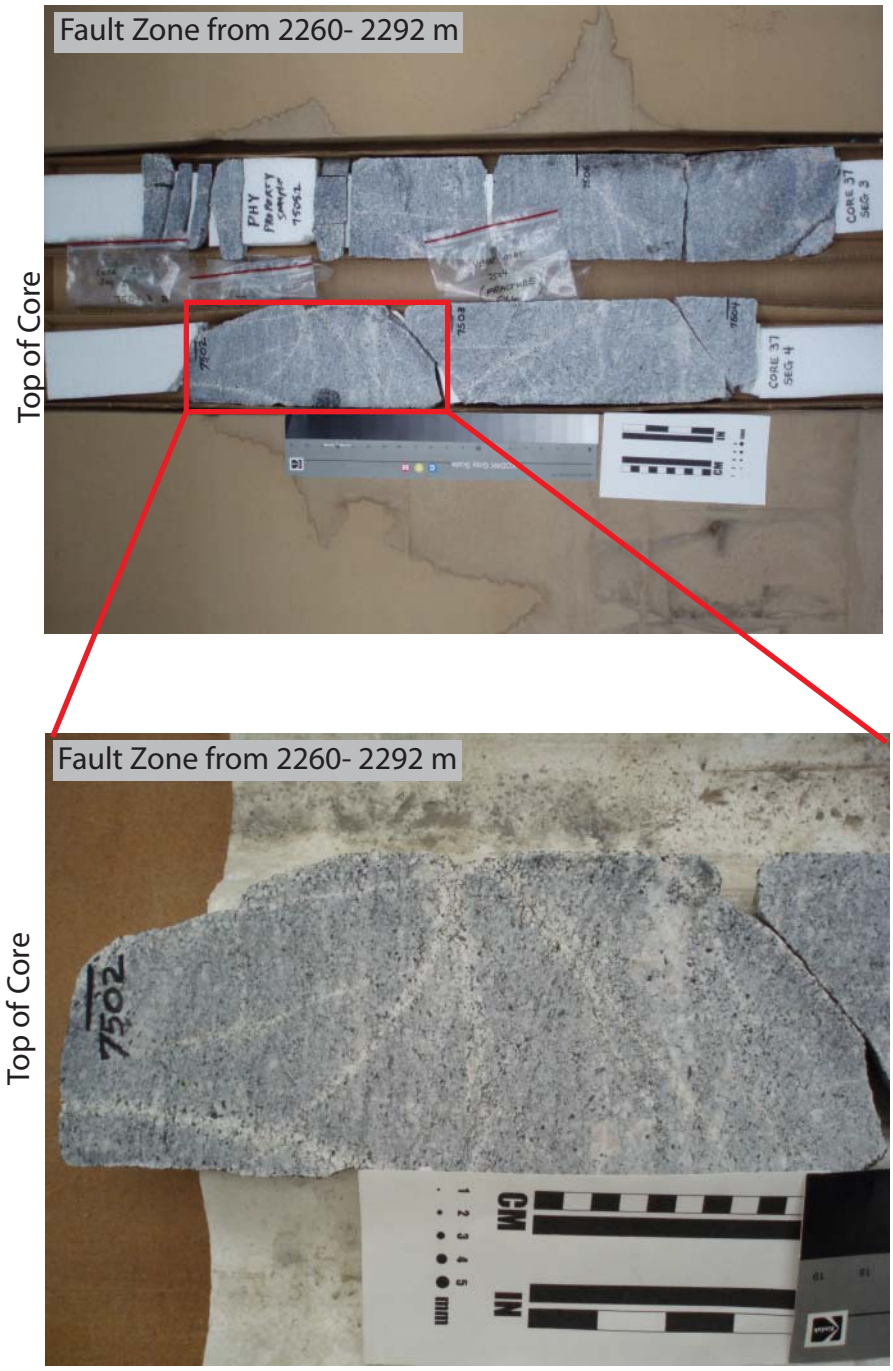
Fault Zone from 2260- 2292 m
Top of Core
Fault Zone from 2260- 2292 m
Top of Core
7502
CM
IN

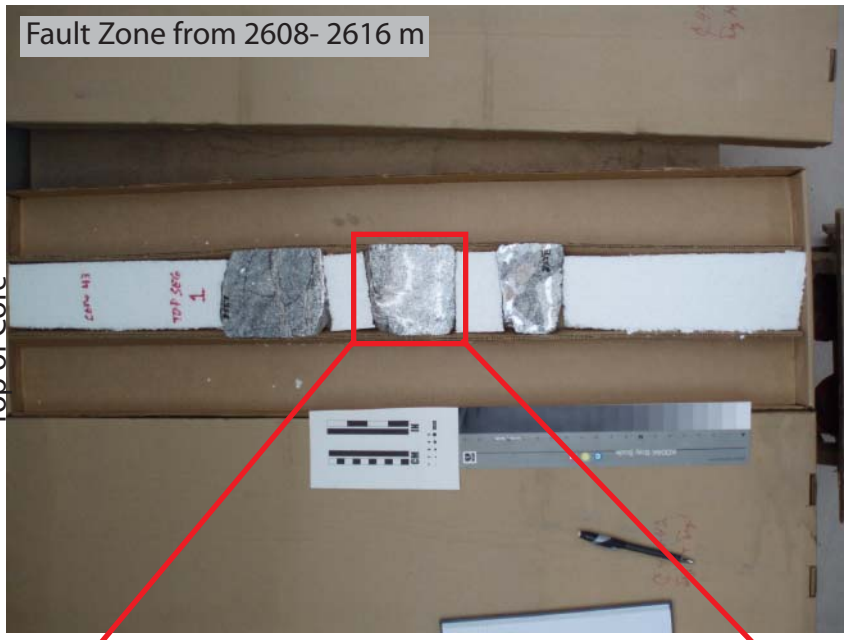
Fault Zone from 2608- 2616 m
Top of Core


Fault Zone from 2608- 2616 m
Top of Core
CM

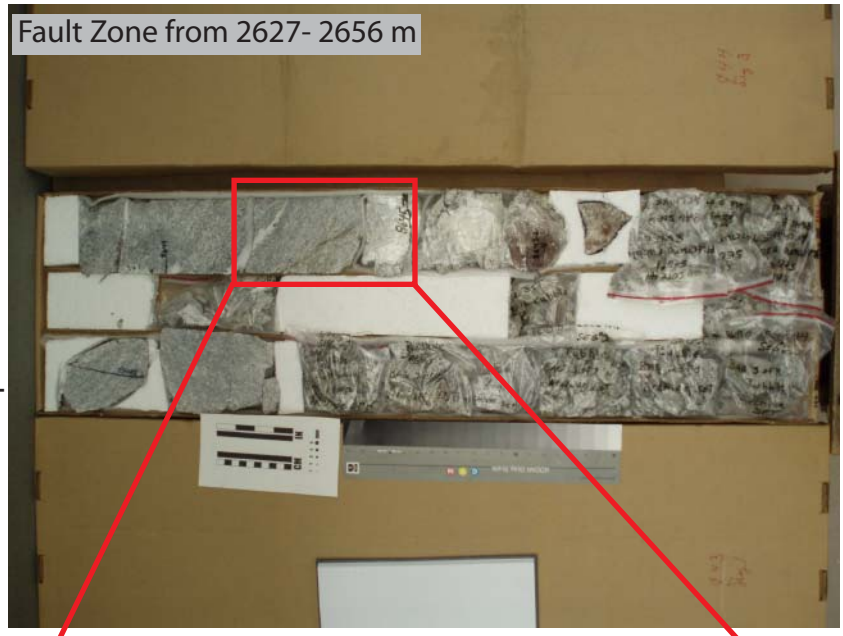

* This is the underside of the core marked identified in the top photograph with the red box.*


Fault Zone from 2779- 2807 m
Top of Core


Fault Zone from 2779- 2807 m
Top of Core
CM

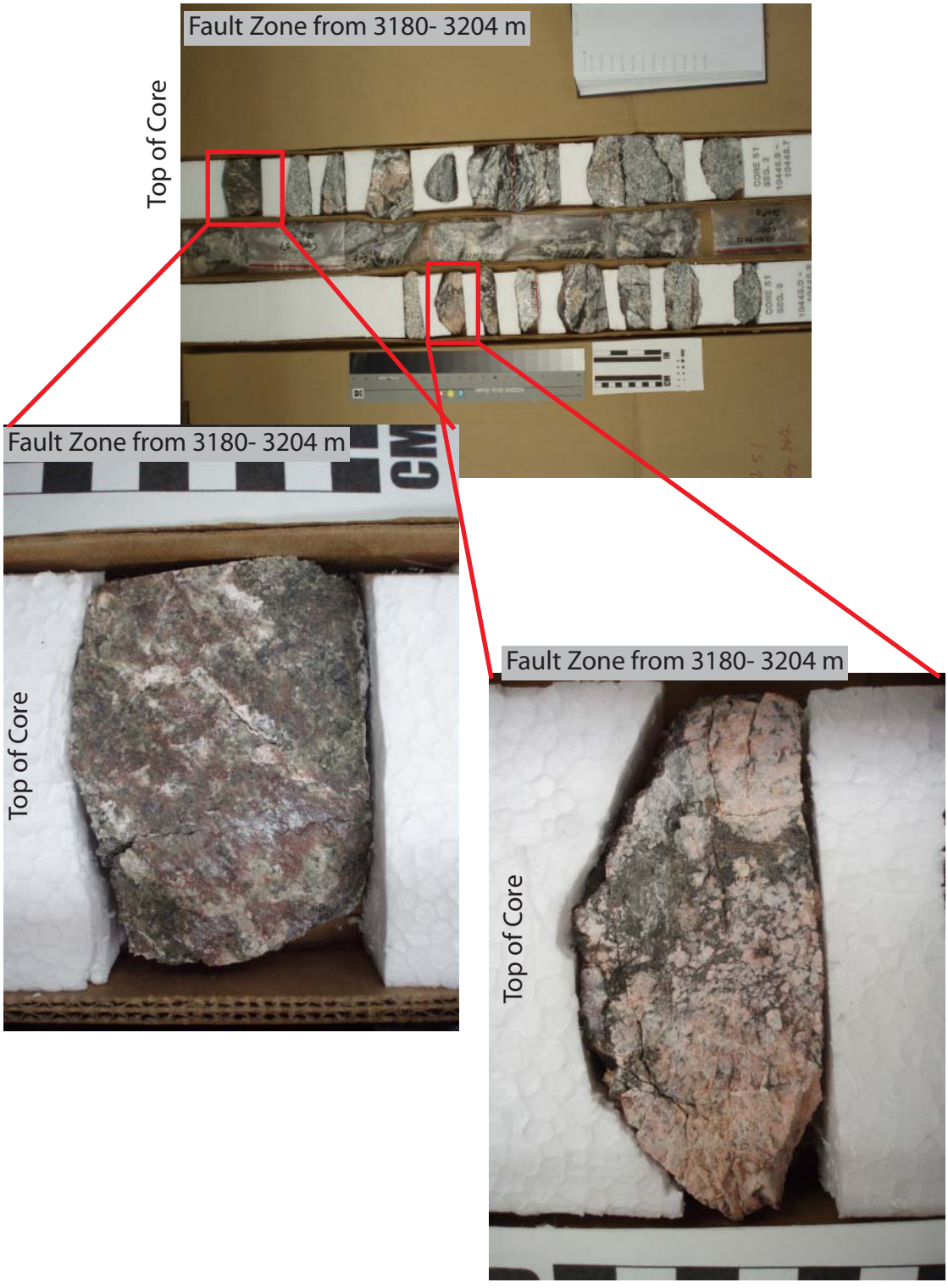
Fault Zone from 3180- 3204 m
Top of Core
Fault Zone from 3180- 3204 m
Top of Core
Fault Zone from 3180- 3204 m
Top of Core

APPENDIX I: Geologic map of Coyote Mountain and the southeast Santa Rosa Mountains

Geologic Map of Coyote Mountain and the Santa Rosa Mountains

By D.H. Forand and S.U. Janecke 2008

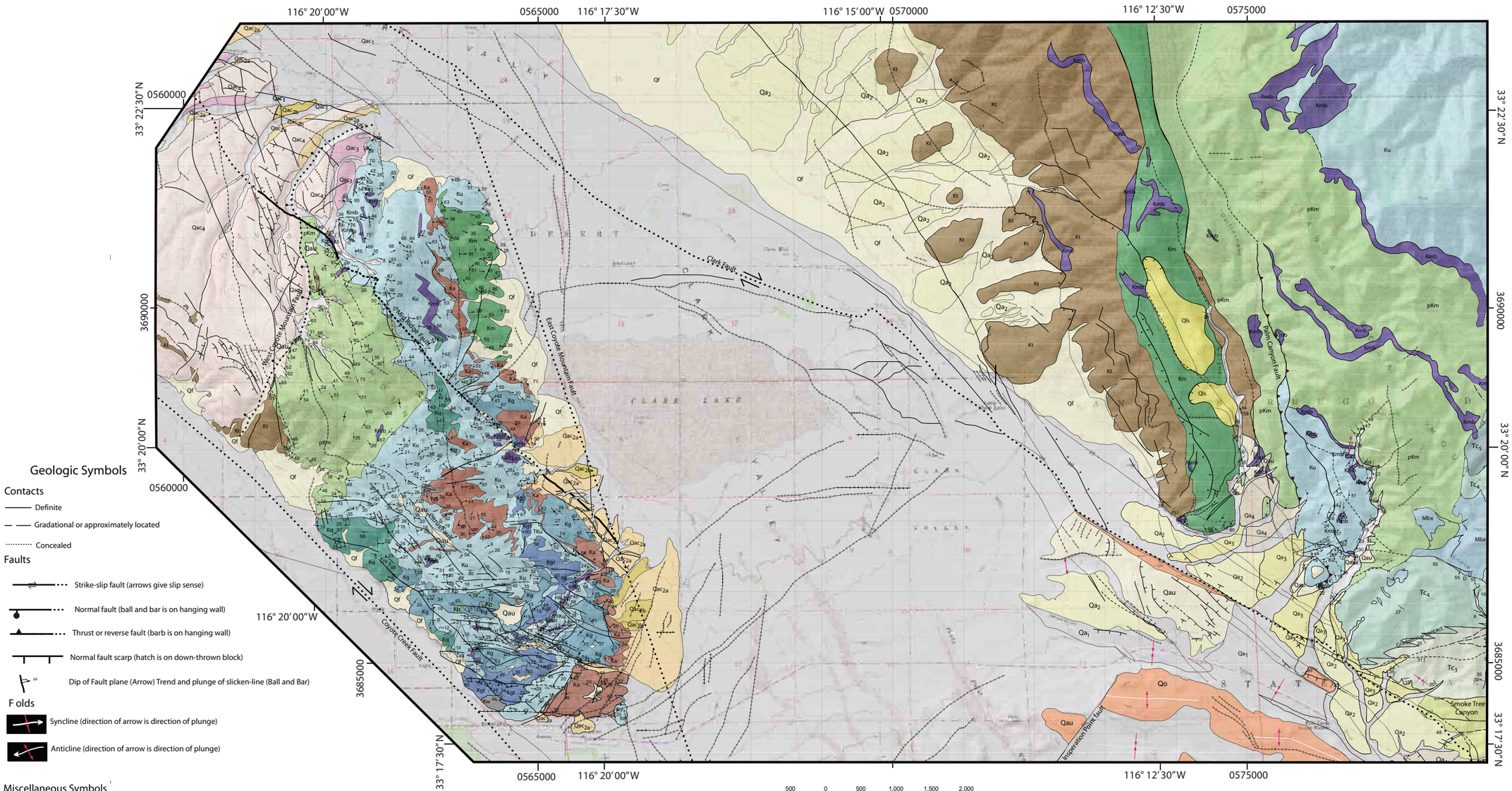

APPENDIX J: Correlation of units

Qau

Undifferentiated alluvium (Qau)

Qa_1

Active Wash (Qa1)

Active wash and drainage gullies. Contains a poorly sorted mixture of sand-sized particles with boulder- and cobble-sized clasts. These are unconsolidated sediments.

Qa_{2L} Qa_2

Young Alluvium (Qa2, Qa2L)

Previously active washes or dryland channels forming terraces above the active wash. These deposits contain a mixture of poorly sorted sand- to boulder-sized clasts. A lesser amount of sand-sized particales are present in this unit.

Qa_3

Old Alluvium (Qa3)

Light gray to brown continuous fluvial surfaces with well rounded pebble- to bolder-sized clasts . The clasts are dominantly biotite-tonalite, with minor amounts of meta-sedimentary clasts. Very little desert varnish and weathering of the surface exposure distinguishes this fluvial deposit from the alluvial pediment deposits.

Qa_4 Qa_5

Alluvial Pediment (Qa4ab, Qa5ab)

Gently sloping Northwest gradients to flat-lying, continuous surfaces comprised of locally derived clasts that are dominantly biotite-tonalite with minor amounts of meta-sedimentary clasts. Fluvial channel fills and finer sandstone lenses are present. Total thickness of this deposit varies from 2-20 meters thick. The surfaces of the pediments are generaly dark brown in color due to desert varnish. Large boulder sized clasts near surface are weathering down into a desert pavement.

Qo

Ocitillo Formation (Qo)

Pebble- to coble-sized conglomerate alluvial fan deposits ineterbedded with distal overbank and fluvial sandstones and siltstones deposits. Conglomerate beds are primarily light gray to green. Clasts are sub angular, locally derived, and matrix supported. Clast composition are dominantly igneous with metamorphic and quartz grains. Bedding thickness varies from 20-50 cm thick. The distal deposits of sandstone and siltstones are brown-red to orange in color. Bedding thickness varies from 5-30 cm thick.

Tc_5
Tc_4
Tc_3
Tc_2
c_1

Canebrake Formation (Tc1, Tc2, Tc3, Tc4, Tc5)

Light gray to brown alluvial fan conglomerate deposits. Large coble to mega-boulder conglomerate comprised of well rounded biotite-tonilite clasts with minor amounts of mafic and meta-sedimentary clasts make up the dark brown-chocolate brown weathering unit Tc1. Interbedded light gray, coble to boulder conglomerates, with finer pebble to coarse sandstones ranging from 2-5 m thick distinguishes the Tc2 unit. Conformably to slightly unconformably above Tc2, Tc3 is distinguished in the east by a basal boulder conglomeratic layer with lesser amounts of the finer interbedding. These units grade laterally to the west and vertically into one indistinguishable coarse boulder conglomerate. Unconformably above lies Tc4, Tc5, light brown weathering boulder to coble sized conglomerates

Mbx

Mega Breccia (Mbx)

Dark gray-green to rust-brown brecciated meta-sedimentary and meta plutonic rocks. Blocks of basement rock vary in size from clasts size to blocks 20 m wide. Locally derived calcite veins.

Qac1

Qac2a

Qac2b

Qac3

Qac4

Qac5

Ocotillo Conglomerate (Qac1-5)
Gravel, gravelly sand, coarse sand, and sparse silt and clay. Poorly consoliated, locally strongly deformed

Qf

Active Alluvial Fan (Qf)

Kgt

Garnet Hornblende Biotite Tonaitle Gneiss (Kgt)
White to gray, contains garnet, biotite, hornblende, plagioclase. Garnet porphoclasts range from 2 mm to 20 mm in a fine crystalline matrix of pladioclase and biotite. Garnet comprises 15-50% of rock. Contains more dark minerals than Ka. Unit is slightly sheared, but some areas look more massive. Apparent thickness: 71-380 m. Located in southern and eastern section of Coyote Mountain.

Ka

Garnet Bearing Quartz Monzonite Gneiss (Ka)
White to light gray, contains quartz, potassium feldspar, biotite, muscovite, garnet porpoclasts; Garnet ranges from 1mm to 10mm; Garnet is imposed on fine to med crystalline matrix; mafic minerals make up <5% of most of the unit; distribution of crystal size is bimidal, with garnet coarser than everything; unit is foliated and well linieated; outcrops throughout the mylonite zone; the unit is present throughout Coyote Mountain. Apparent thickness: 10-900 m.

Kq

Quartsofeldspathic Gneiss (Kq)
Gray, medium to coarse crystalline; contains biotite, quartz, muscovite, plagioclase; augen gneiss; foliation defined by parallelism of biotite; some areas are massive; coarser feldspar augens can be present; mylonitization or hearing is variable, ranging from incipient development of a cataclastic texture to a well developed blastomylonitic texture; shear dikes, small marbles, quartzites, and amphibolites are present. Apparent thickness: 70-400 m.

Kg

Gneissic Gabbro and Amphilbolite (Kg)
Gray, Fine crystalline; Contains biotite, hornblende, plagioclase; Hornblende is dimensionally oriented and is dominant mineral; a coarse, unsheared crystalline gabbro outcrops in southwestern section of Coyote Mountain; western outcrop also contains a fine to medium amphibolite, a coarse crystalline leucocratic gabbro is sometimes present along contacts(Theodore 1967); some smaller metamorphosed marble lenses interfinger with other units. Apparent thickness: 47-83 m.

Kp

Pegmatite (Kp)
White; quartz, potassium feldspar, small amounts of mica, and garnet?; coarse to medium crystalline, massive; located as pods or stingers throughout the mylonite and migmatie zone; few large outcrops are shown on the map, smaller outcrops are more prevalent in most areas

Kmb

Marble (Kmb)
White to gray to blue; medium to coarse crystalline; can contain biotite, though less than 5% of total rock; recrystallized fossils (crinoids stems?) in lighter colored marbles; blue marbles have darker calcite preserved fossils; some areas are deformed looking with elongated calcite crystals, present throughout the entire mylonite zone in small lensoidal bodies ranging from 1-3m in length; marble is also on pluton borders and in migmatite. Apparent thickness: 0.5-140 m.

Kw

Marble that contains abundant in Wollastonite (Kw)
Gray to white to tan, some areas of unit contain abundance of wollastonite, calc-silicates, small amounts of garnet, diopside, pyroxene are seen in some areas of the unit (Theodore, 1967); resistant blocks of calc-silicates form erosional remnants among the easily eroded marble; pock mark surface in areas; strong foliation in some areas of the unit, some folds are present; located in SE Coyote Mountain. Apparent thickness: 45-238m

Km

Mylonite with plutonic protolith (Km)
Gray, contain bands of alternating colors of material; feldspar, mica; same composition as a pelitic gneiss; range from fine to coarse crystalline, depending on degree of mylonitization; lineations and foliation are almost always present in outcrops; weathers brown to rust color; weathers to more gentle slope than other mapped units; outcrop in northeastern part of Coyote Mountain; has small marbles, sheared igneous rocks and amphibolites throughout (Theodore, 1967). Apparent thickness: 45-600m

Ku

Undifferentiated metasedimentary and metaigneous (Ku)
Heterogenous combination of all other units; metasedimentary in nature; all degrees of mylonitic texture present, largest unit mapped in Coyote Mountain; (Theodore)

pKm

Biotite Rich Migmatite (pKm)
Gray to rust to brown; fine to medium crystalline; quartz, sillimanite, biotite, muscovite, potissuim feldspar, oligoclase; This is the thickest rock unit at Coyote Mountain has irregularly alternating lepidoblastic folia of mica and granoblastic domains of quartz and feldspar; small scale isoclinal folds have axial planes parallel to predominant local foliation; dikes throughout the unit cut across and are at a high angle to foliation; located in the southwest portion of Coyote Mountain; small marbles, pegmatite dikes, quartzite, and amphibolite are also present in the unit. This is the thickest unit in Coyote Mountain, ~2000m.

Kt

Biotite-Hornblende Bearing Tonalite (Kt)
Grey to white; contains biotite, horblende, quartz, plagioclase; med to coarse crystalline, average grain size 1.5-2.0mm. 20-35% is hornblende and biotite; ranges from massive to semi foliated; stronger foliation appears at contacts with overlying metasedimentarty rocks; these are mesozonal plutonic rocks; located in western Santa Rosa mountains, and northwestern area of Coyote Mountain, weathers to a brown color

APPENDIX K: Foliation measurements and fault planes

Waypoint	Position	Strike	Dip	Dip Direction	Notes	Lineation		
						Trend	Plunge	Plunge Direction
1	11 S 576223 3686154	301	20.5	N				
2	11 S 576205 3686114	44	28	E				
3	11 S 576101 3686108	344		E				
4	11 S 576110 3686141	194	90					
5	11 S 576132 3686179	249	49	N				
6	11 S 576079 3686082	51	18	E	BAD MEASURMENT			
7	11 S 576225 3686172	159	37	W				
8	11 S 576229 3686174	335	1	E				
9	11 S 576546 3686568	29	30.5					
10	11 S 576377 3687149	5		E				
11	11 S 576341 3687085	89	54	SE				
12	11 S 576169 3686528	47	20	E				
13	11 S 576128 3686536	57	13	E				
14	11 S 576175 3686373				LOCATION OF FLOAT			
15	11 S 576205 3686162	91	8	E				
16	11 S 576179 3686129	24	22	E				
17	11 S 576120 3686123	21	56	E				
18	11 S 576056 3686129	174			HIGH UNCERINITY			
19	11 S 576091 3686104	41	42	E				
20	11 S 576104 3686104	35	60	E				
21	11 S 576105 3686108	331	66	E	DRAG FROM SMALL FAULT?			
22	11 S 576103 3686096				LOCATION OF FOLD OR FAULT STRUCTURE			
23	11 S 576102 3686088	35	69	E				
24	11 S 576201 3685929	295			POSSIBLE FAULT			
25	11 S 576206 3685932	98	41	S				
26	11 S 576177 3685911	72	29	S				
27	11 S 576239 3685962	104	30	S				
28	11 S 576056 3686035	26	46	E				
29	11 S 576045 3686102	111	16	S				
30	11 S 576042 3686124	174		S	MAY BE FLOAT?			
31	11 S 575786 3686361	84	14	S				
32	11 S 575920 3686433	4	19	E				
33	11 S 576052 3686451	73	23	S				
34	11 S 576060 3686448	73	23	S				
35	11 S 576063 3686435	73	23	S				
36	11 S 576051 3686406	26	22	E				
37	11 S 576047 3686394	64	14	E				
38	11 S 575998 3686420	68	36	S				
39	11 S 575991 3686427	68	36	S				
41	11 S 576098 3686444	84	9	S				
42	11 S 576113 3686448	72	21	S				
43	11 S 576118 3686453	9	19	S				
44	11 S 576141 3686485	26	9	E				
45	11 S 576068 3686471	24	67	E				
46	11 S 576028 3686485	61	12	E				
47	11 S 575947 3686500	335	44	W				
48	11 S 576052 3686021	69	22	E				
50	11 S 576275 3686185	341	19	E				
51	11 S 576334 3686237	347	37	E				
52	11 S 576346 3686257	359	26	E				
53	11 S 576504 3686425	52	34	E				
54	11 S 576518 3686537	64	59	E				
55	11 S 576651 3686874	29	16	E				
56	11 S 576579 3686706	26	29	E				
57	11 S 576720 3687390	38	35	E				
58	11 S 576502 3688021	274	12	N				
59	11 S 576456 3687874	54	41	S				
60	11 S 576044 3686567	39		E				
61	11 S 576033 3686577	291	11	N				
62	11 S 576053 3686602	344	38	E				
63	11 S 576096 3686611	334	22	E				
64	11 S 576164 3686665	296	69	S	FAULT PLAIN			
65	11 S 576181 3686693	238	26	E				
66	11 S 576211 3686720	18	28	E				

67	11 S 576244 3686760	13	31	E				
68	11 S 576250 3686772	4	57	E				
69	11 S 576092 3686958	63	24	E				
70	11 S 576148 3687005	6	28	E				
71	11 S 576157 3687080	24	25	E				
72	11 S 576326 3687030	15			BAD OUTCROP			
73	11 S 576320 3687237	184	44	E				
74	11 S 576365 3687920	28	34	E				
75	11 S 576432 3687779	36	32	E				
76	11 S 576452 3687323	10	51	E				
77	11 S 576255 3687391	46	21	E				
78	11 S 562588 3692263	45		E				
79	11 S 561977 3691021	68	76	E				
80	11 S 562008 3690945	309	68	N				
81	11 S 562595 3692216	56	37	E	ALSO 026, 64E			
82	11 S 564309 3691477	47	39	SE				
83	11 S 576048 3686087				SAMPLE LOCATION			
84	11 S 576306 3686672	67	62	SE				
85	11 S 576352 3686528	128	12	S				
86	11 S 576288 3686633	209	48	NE	FAULT			
87	11 S 576263 3686602	76	33	SE				
88	11 S 576164 3686616	81	21	S	FAULT			
89	11 S 565967 3686305	1	11	E		86	11	E
90	11 S 565979 3686300	359	19	E	39,19 SE	89	22	E
91	11 S 565632 3686119	16	19	E		105	20	
92	11 S 565702 3686168	19	28	SE				
93	11 S 565707 3686153	331	52	NE				
94	11 S 565703 3686160	40	45	E				
95	11 S 565729 3686121	341	22	NE		84	40	
96	11 S 565721 3686118	21	26	E				
97	11 S 565716 3686110	6	53	NE		94	53	
98	11 S 565709 3686117	324	53	NE				
99	11 S 565673 3686135	66	64	SE				
100	11 S 565605 3686109	84	31	SE				
101	11 S 565603 3686106	40	39	E				
102	11 S 565511 3686057	80	29	SE				
103	11 S 574750 3686898	70	60		RAKE =10W			
104	11 S 574655 3686907	205	29	NE				
105	11 S 571974 3691668	158	77	W	FAULT RAKE =76			
106	11 S 572288 3691625	304	61	NE				
107	11 S 565503 3686118	78	36	SE				
108	11 S 565833 3686345				FAULT			
109	11 S 565506 3686533	10	41	E	FAULT			
110	11 S 565562 3686495	136	90		FAULT			
111	11 S 565587 3686488	351	32	E	FAULT	81	32	
112	11 S 573797 3687252	94	38	SE	FAULT	104	31	
113	11 S 573897 3687119	330		NE	?			
114	11 S 573954 3687084	25	31	E				
115	11 S 574042 3687019	68	75	SE				
116	11 S 574066 3687010	14	47	SE				
117	11 S 574095 3686978	355	32	E		87	44	S
118	11 S 574109 3686957	4	36	E				
119	11 S 574132 3686928	356	8	E				
121	11 S 574444 3686849	335	59	NE				
122	11 S 574519 3686881	102	15	S		224	14	
123	11 S 574544 3686885	126	24	S		209	24	
124	11 S 574669 3686904	31	14	SE				
125	11 S 574894 3687797	18	32	E				
126	11 S 574908 3687837	48	16	SE				
127	11 S 574894 3687976	29	16	E		88	19	
128	11 S 574864 3688132	328	11	E				
129	11 S 574903 3688331	285	16	NE		76	19	
130	11 S 574948 3688478	341	58	E				
131	11 S 574933 3688544	331	44	NE				
132	11 S 561430 3688004	358	54	E				
133	11 S 561448 3688004	67	52	SE		246	14	
134	11 S 561503 3687965	119	84	N	FAULT RAKE = 43			
135	11 S 561596 3688092	246	46	E	FAULT			
136	11 S 561452 3689119	319	52	NE				

137	11 S 561574 3689492	304	57	N				
141	11 S 574416 3689922	106	29	S		257	10	
142	11 S 562714 3692377	349	24	E				
143	11 S 562580 3692241	36	39	SE		119	39	
144	11 S 562577 3691849	134	33	S				
145	11 S 562571 3691724	110	79	S				
146	11 S 562625 3691605	292	63	N				
147	11 S 562586 3692222	42	0		FAULT FROM SUSANNE			
148	11 S 562540 3691245	284	42	N		114	27	
149	11 S 562154 3690775	255	49					
150	11 S 562166 3690740	330	65	NE				
151	11 S 562262 3690570	204	49	W				
152	11 S 562258 3690568	344	46	E				
153	11 S 562240 3690575	319	45	NE				
154	11 S 562219 3690594	335	44	NE				
155	11 S 562188 3690645	219	65	W				
156	11 S 562152 3690660	269	77	NW				
157	11 S 562146 3690699	103	85	S				
158	11 S 562145 3690710	285	50	NE				
159	11 S 562139 3690741	386	56	N				
160	11 S 562109 3690894	354	55	E				
166	11 S 575082 3687945	21	58	E				
167	11 S 575125 3687795	39	46	NE				
168	11 S 574910 3687622	0	33	E				
169	11 S 564897 3688052	334	34	NE		74	34	
170	11 S 564630 3688125	240	74	SE				
171	11 S 564397 3688319	344	45	E		81	45	
172	11 S 564666 3688005	32	52	E				
173	11 S 561905 3690230	55	41	SE				
174	11 S 561927 3690209	356	40	E				
175	11 S 563874 3685085	5	19	E				
176	11 S 563986 3684730	97	85	S	FAULT RAKES = 71	E NOTEBOOK		
177	11 S 564033 3684741	320	9	E	FAULT			
178	11 S 564420 3684690	1	15	E				
181	11 S 564054 3685506	351	19	E				
182	11 S 564077 3685489	332	46	NE				
183	11 S 564157 3685499	342	46	NE		81	24	
184	11 S 564846 3685566	103						
185	11 S 564144 3685221	329	49	NE				
186	11 S 564164 3685445	346	60	NE				
187	11 S 565009 3685463	357	38	E				
188	11 S 565137 3685426	70						
189	11 S 565245 3685437	323	64	NE				
190	11 S 565395 3685537	357	20	E				
191	11 S 565244 3685655	331	31	NE				
192	11 S 565151 3685538	344	28	NE				
193	11 S 565074 3685509	101	23	S				
194	11 S 565343 3685855	5	37	NE				
195	11 S 565334 3685807	355	30	E				
196	11 S 565383 3685885	3	37	NE				
197	11 S 565654 3686018	246	28	NW		74	23	
198	11 S 562220 3691223	114	64	S				
199	11 S 562338 3691143	9	76	NE				
200	11 S 562352 3691059	21	19	E				
201	11 S 562332 3690976	46	59	SE				
202	11 S 562097 3690862	309	54	NE				
203	11 S 562025 3691039	29	53	NE				
204	11 S 561895 3691109	340	46	NE				
205	11 S 561845 3691098	40	41	SE				
206	11 S 561787 3691135	270	54	N				
207	11 S 564831 3688976	2	39	E		88	39	
208	11 S 563483 3686420	343	32	NE				
209	11 S 563377 3686413	271	31	N				
210	11 S 563436 3686424	324	46	NE				
212	11 S 564891 3685397	304	19	NNE		80	21	
213	11 S 564808 3685232	41	33	NE				
214	11 S 564952 3685341	47	21	E				
215	11 S 564957 3685312	296	32	NE				

216	11 S 565147 3685184	69	30	SE				
217	11 S 565194 3685222	326	14	NE				
218	11 S 565277 3685170	311	34	NE				
219	11 S 564905 3684963	325	32	NE		44	23	
220	11 S 565906 3684699	1	26	E		74	26	
221	11 S 565907 3684652	294	24	NE		90	24	
222	11 S 565549 3684763	284	30	N		316	34	
223	11 S 565529 3685000	36	20	E				
224	11 S 565543 3685035	26	26	E				
225	11 S 565603 3685008	29	11	E				
226	11 S 565686 3684987	289	21	N		274	4	
227	11 S 565729 3684976	356	21	E				
228	11 S 565540 3685069	301	64	NE				
229	11 S 565412 3685112	41	32	E		89	20	
230	11 S 564739 3685228	231	39	NE		91	19	
231	11 S 564614 3685250	331	36	NE				
232	11 S 564531 3685288	310	41	NE				
233	11 S 564258 3685328	336	29	NE				
234	11 S 565151 3684836	55	45	SE		92	32	
235	11 S 565372 3684548	81	46	SE		81	4	
236	11 S 562295 3691479	327	52	NE				
237	11 S 562290 3691508	276	84	N				
238	11 S 574831 3687407	44	33					
239	11 S 574793 3687411	31	32			54	12	
240	11 S 574853 3687567	35	40	NE		80	36	
241	11 S 576751 3686952	18	29	E		69	28	
242	11 S 576804 3687004				FAULT			
243	11 S 576857 3687049	1	47	E		81	47	
244	11 S 576874 3687123	359	50	E		82	50	
245	11 S 576770 3687222	162			FAULT			
246	11 S 576779 3687250	341	54	NE		84	51	
247	11 S 576687 3687403	36	45	SE		81	41	
248	11 S 576703 3687563	13	51					
249	11 S 576732 3687694	0	36					
250	11 S 576569 3687772	21	43	SE				
251	11 S 576513 3687813	8	31	E				
252	11 S 576541 3688172	329	30	NE				
253	11 S 576555 3688206	320	35	NE				
254	11 S 576597 3688263	333	44	NE		54	44	
255	11 S 576675 3688350	314	53	NE				
256	11 S 576730 3688379	305	49	NE				
257	11 S 576670 3688303	336	47	NE				
258	11 S 576605 3688172	314	36	NE				
259	11 S 576557 3688019	355	34	NE				
260	11 S 576595 3687838	30	39	SE				
261	11 S 576670 3687797	35	34	SE				
262	11 S 576792 3687730	7	53	E				
263	11 S 576815 3687625	339	22					
264	11 S 576771 3687346	29	37	NE				
265	11 S 576820 3687268	3	30	E				
266	11 S 576912 3687144	341	56					
267	11 S 576873 3687025	1	36	E		86	36	
268	11 S 576849 3686998	14	41					
269	11 S 576781 3686919	39	34	SE		116	31	
270	11 S 576689 3686743	64	31					
271	11 S 576570 3686532	64	46	SE				
272	11 S 565076 3685363	304	42	NE				
273	11 S 563430 3687372	172	17	NW				
274	11 S 563512 3687294	1	26	E				
275	11 S 563870 3686909	24	32					
276	11 S 563687 3686205	354	31					
	11S 0562684 3962021	89	21	S				
	11S 0562582 3692238	71	72		FAULT RAKE = 135			
		353	40					